This is to certify that the

dissertation entitled

DESIGN AND FLOW ANALYSIS OF VOLUTES FOR CENTRIFUGAL COMPRESSORS

presented by

Fahua Gu

has been accepted towards fulfillment
of the requirements for

Ph.D. degree in Mechanical Engineering

Major professor

Date 11-27-2000

DESIGN AND FLOW ANALYSIS OF VOLUTES FOR CENTRIFUGAL COMPRESSORS

By

Fahua Gu

A DISSERTATION

Submitted to
Michigan State University
in partial fulfillment of requirements
for the degree of

DOCTOR OF PHILOSOPHY

Department of Mechanical Engineering

2000

DESIGN AND FLOW

ABSTRACT

DESIGN AND FLOW ANALYSIS OF VOLUTES FOR CENTRIFUGAL COMPRESSORS

By

Fahua Gu

Centrifugal compressors are widely used in applications where the mass flow is lower and installation space is limited. The centrifugal compressor volute is the last component that collects the exit flow of the diffuser and delivers it to the pipeline. The volute is a unique component in the compressor because the flow can be decelerated or accelerated inside the volute at off-designs. The volute passage pressure, therefore, is circumferentially distorted, resulting in the flow distortion in the vaneless diffuser and impeller. The compressor efficiency and stable work range are seriously reduced.

In this dissertation, a volute design system was first developed to be applicable to both turbine and compressor volute design. Two volute design approaches were compared theoretically to assess the compressibility on the volute geometry and flow. The comparison is based on a turbine volute because the flow in turbine volutes is compressible. Numerical simulations revealed the deviation of the turbine volute flow from the free vortex pattern.

Extensive study w

nmental and theoretical a

nd the interaction betwee

odels were employed :

Model performs circumfe

mbine inflow for the va

lently depends on the

low is similar to a torn

low. One the other han

ular vortex structure w

odel was proposed t

Frozen Rotor, was use

he volute at off-des

ressure at the impel

This explains why th

This model also rev

Non-uniformly distri

ree dimensional an

mprovement of ac

he matching of vo

Extensive study was made on a single-stage centrifugal compressor. Both numerical and theoretical analyses are employed to understand the volute flow structure and the interaction between volute and impeller at off-design conditions. Two numerical models were employed to simulate the flow in the compressor. The first one, Stage Model, performs circumferential averaging at impeller exit to provide a circumferentially uniform inflow for the vaneless diffuser. It was observed that the volute secondary flow heavily depends on the inlet axial distribution. For design and higher mass flows, the flow is similar to a tornado with a core of forced vortex flow and a shell of free vortex flow. One the other hand, only forced vortex flow was found for the lower mass flow. A twin vortex structure was also found after tongue for the higher mass flow. A theoretical model was proposed to explain the difference of the flow structures. The second model, Frozen Rotor, was used to study the response of the impeller to the flow distortion due to the volute at off-design conditions. It was found that the circumferentially increased pressure at the impeller exit in the rotation direction is detrimental to the impeller flow. This explains why the impeller shows a significant efficiency drop at lower mass flows. This model also revealed the impeller responses to the distorted downstream pressure by non-uniformly distributing the mass flow into each passage. Based on this observation, a one dimensional analysis model was developed to simulate the distorted flow. With an improvement of accuracy, this model has the potential to optimize volute geometries and the matching of volutes with other components.

In memory of my mother

The author is

guidance, support and

Sincere thanks go to

Prof. Lamm for the

to Mr. Mike Cave a

ork and for financial

ance Karman Institu

Sayant and helpful di

The author is al

Mr Jonathan Maguire

ks Mr. Paul Haley

ive encouragement

reading this dissert

umerous criticism, a

dents at the turbom

Craig, Gayle Patrick

ks Dr. Fengjun Liu a

Last but not le

ve and support, his s

ACKNOWLEDGMENTS

The author is very grateful to his advisor, Professor Abraham Engeda, for his guidance, support and encouragement throughout the course of the research work. Sincere thanks go to Professors John McGrath, Craig Somerton, Chichia Chiu and Patricia Lamm for their advices, discussions and interest in this work. Particular thanks go to Mr. Mike Cave and Dr. Jean-Luc Di Liberti at Solar Turbines Inc. for initiating this work and for fruitful discussions. Special thanks go to Professor Van den Braembussche at von Karman Institute for Fluid Dynamics and Professor Tom Shih at MSU for their frequent and helpful discussion.

The author is also very thankful to Mr. Edward Benisek, Mr. Geoffrey Bruce and Mr. Jonathan Maguire at BorgWarner Automotive for their support and experimental data, Mr. Paul Haley at Trane Company, and Mr. Ron Aungier at Elliott Company for their encouragement. Mr. Craig Gunn at MSU is specially acknowledged for his help in preparing this dissertation and related publications. The author also appreciates the numerous criticism, assistance and great friendship from Mr. Yunbae Kim and all other students at the turbomachinery lab at Michigan State university: Joscelyn Pereire, Marc Ludwig, Gayle Patrick and Hooman Rezaei. The author also had very helpful discussions with Dr. Fengjun Liu at Western Michigan University and Dr. Bin Zhu at MSU.

Last but not least, the author would like to thank his wife, Qiangwei Fu, for her love and support, his son, Mingsi Gu for his love.

TABLE OF CONTENTS

CHAPTER 4: COMPARATIVE STUDY OF DESIGN APPROACHES

CHAPTER 5: VOLUTE FLOW STRUCTURES

CHAPTER 6: STEADY-STATE VOLUTE/IMPELLER INTERACTION

CHAPTER 7: ONE DIMENSIONAL MODELING OF COMPRESSOR FLOW

LIST OF TABLES

LIST OF FIGURES

FIGURE 2.12 V

FIGURE 2.13 L

FIGURE 2.14 C

FIGURE 2.15 C

FIGURE 2.16 C

FIGURE 2.17 C

FIGURE 2.18 S

FIGURE 2.19 M

DEN BRAEN

FIGURE 2.20 M

DEN BRAEN

FIGURE 2.21 M

BRAEMBUSS

FIGURE 2.22 S

BRAEMBUSS

FIGURE 2.23 S

MASS FLOW

A
AR
b
C
C_f
C_L
c
c_f
D
F
f
g
k
L
M
m
PS
p
Q
R
R_0
r
S
SS
S_T
T
U
V
W
X,Y,Z

NOMENCLATURE

A	area
AR	area ratio
b	passage width
C	absolute velocity
C_p	specific heat at constant pressure
C_v	specific heat at constant volume
c	sound speed
c_p	pressure recovery
D	diameter
F	force
f	frequency, friction
g	gravity acceleration
k	specific heat ratio
L	length
M	Mach number, Momentum
m	mass flow rate
PS	pressure side
p	pressure
Q	volume flow rate
R	gas constant
Ro	Rossby number
r	radius
S	width of volute
SS	suction side
Sr	Strouhal number
T	temperature
U	blade speed
V	velocity
W	relative velocity
X,Y,Z	coordinate system

Z:

Greek

α

β

δ

ε

Γ

Φ

λ

η

θ

ρ

μ

Ω

ω

Ψ

Superscripts

0

n

r

s

-

Subscripts

0

1

2

3

.

Z_R	Number of impeller blades

Greek

α	absolute flow angle from radial or axial
β	relative flow angle from radial or axial
δ	slip factor
ε	coefficient
Γ	circulation
Φ	flow coefficient
λ	swirling factor
γ	specific heat ratio
η	efficiency
θ	azimuth angle of volute section
ρ	density
μ	dynamic viscosity, load coefficient
Ω	rotational speed
ω	total pressure loss coefficient, impeller rotating speed
Ψ	isentropic head coefficient

Superscripts

0	stagnation
n	iteration
r	rotor
s	stator
-	average

Subscripts

0	stagnation, tongue
1	inlet of impeller, critical surface for turbine volute
2	exit of impeller, exit of turbine volute
3	inlet of diffuser
4	grid interface between impeller and diffuser
5	diffuser exit

7	critical surface, θ=0
8	exit flange of the compressor
com	compressible
e	exit
f	friction
hyd	hydraulic
i	inlet
inc	incompressible
ip	local interface pressure
isen	isentropic
k	volute centriod
loss	loss
MVDL	meridional velocity dump loss
m	meridional
n	normal
nodal	nodal
o	outlet
p	pressure gradient
r	radial
ref	reference condition
rotor	rotor
s	swirling flow
stator	stator
TVDL	tangential velocity dump loss
t	tangential, through flow
tip	tip of the impeller
t-t	total-to-total
u	tangential
z	axial
θ	tangential

1.1 Brief History

Chapter 1

INTRODUCTION

1.1 Brief History of Turbomachinery

Wilson (1993) gave a review on the history of the turbomachinery development. The Romans introduced paddle-type water wheels, pure "impulse" wheels, in around 70 B.C. for grinding grain. Through succeeding centuries, water wheels of the impulse or gravity-fed types can be seen in texts about grinding mills, water supply, or mining. The movement toward modern turbomachinery really started in eighteenth century. In 1705 Denis Papin published full descriptions of the centrifugal blowers and pumps he had developed. Bernard Forest de Belidor, describing waterwheels with curved blades, published four volumes on "Architecture hydraulique" in France in the period from 1737 to 1735. These were also called "tub wheels" and were precursors of what are now called radial inflow or Francis turbines. The Swiss mathematician Leonhard Euler (1707—1783), then at the Berlin Academy of Sciences, analyzes Hero's turbine and carried out experiments in the period around 1750. He published his application of Newton's law to turbomachinery, new universally known as "Euler's equation," in 1754 and thereby immediately permitted a more scientific approach to design than the previous cut-and-try methods.

The major fluid mechanics problem in turbomachinery is the design of compressors because of the adverse pressure gradient in the passage. It is hard to know the efficiencies of Denis Papin's centrifugal blowers (1705), but it is evident that there was little development until 1884 when Charles Parsons patented an axial-flow

compressor. The

ientation. In t

percent efficienc

Adjusted Rated

turbocompressor

1970 gave an incenti

The develo

gentrician and

jet-reaction mac

engine was the s

1881 and follow

The first steam t

Charles Parsons

ship at 18,000 r

12 Classification

Turboma

continuously flow

word *turbo* is o

expansion enthal

a pump, the en

extracted from th

these liquid rock

compressor. Three years later he designed a three-stage centrifugal compressor for ship ventilation. In 1899 he made an eighty-one-stage axial compressor which attained 70 percent efficiency. The other major pioneer working on compressors at that time was Auguste Rateau, who published a major paper on turboblowers in 1892. However, a turbocompressor he designed to give a pressure ratio of 1.5 at 12,000 rpm and tested in 1902 gave an isentropic efficiency of only 56 percent.

The development of turbines can be traced back to A.D. 62, when the Greek geometrician and inventor Hero of Alexandria devised the first steam-powered engine, a pure-reaction machine. It was only a toy having no power output. The first useful steam turbine was the spinning-arm reaction (Hero's) turbine of William Avery (U.S.) who in 1831 and following years made about fifty as drivers for circular saws and similar duties. The first steam turbine that had a major impact on the engineering world was that of Charles Parsons (1854—1931), who made a multistage axial-flow reaction turbine giving 10 hp at 18,000 rpm in 1884.

1.2 Classification of Turbomachinery

Turbomachines are devices in which energy is transferred either to or from a continuously flowing fluid by the dynamic action of one or more moving blade rows. The word *turbo* is of Latin origin, meaning, "that which spins." The rotor changes the stagnation enthalpy, kinetic energy, and stagnation pressure of the fluid. In a compressor or pump, the energy is imparted to the fluid by a rotor. In a turbine, the energy is extracted from the fluid. Turbomachinery is a major component in (a) aircraft, marine, space (liquid rockets), and land propulsion systems, (b) hydraulic, gas and steam turbines,

of industrial p

pumping plants.

ndustrial compre

The turb

romachinery.

romachinery, th

nd partially radia

ne advantages a

with many times

achines. This

esirable to redu

achines also h

ultistage axial

low to become s

low machinery

ultistage axial

ne for axial ma

In contra

ciently drops

fication of rad

nufacturing co

special cases w

rbochargers.

(c) industrial pipeline and processing equipment such as gas petroleum, and water pumping plants, and (d) a wide variety of other applications (e.g., heart-assist pumps, industrial compressors and refrigeration plants).

The turbomachine is classified according to the type of flow path. In axial flow turbomachinery, the meridional flow path is axial. In radial or centrifugal turbomachinery, the flow path is predominantly radial. If the flow path is partially axial and partially radial, the device is called mixed-flow turbomachinery. Each type has its own advantages and disadvantages. The radial flow pump or compressor can be designed with many times the head or enthalpy rise per stage than is possible with axial flow machines. This gives radial flow compressors and pumps an advantage where it is desirable to reduce the number of stages in an application to minimum. Radial flow machines also have very large cost, and even possibly efficiency, advantages over multistage axial machines when the size is small enough for the Reynolds number of the flow to become small, and when the blade tip clearances become relatively large. Radial flow machinery in almost every size will cost less to manufacture than the equivalent multistage axial machinery. In the larger sizes the efficiencies will be, in general, lower than for axial machines.

In contrast, radial flow turbines are shown to produce generally lower head or enthalpy drops per stage than is possible with axial flow machines. The areas of application of radial flow turbines are limited predominantly to those in which the lower manufacturing cost of small, single-stage radial turbines is of overriding importance and to special cases where the configuration is advantageous, such as the small automotive turbochargers.

1.3 Configurati

A single

diffuser non-rot

nozzle to direct th

the flow by mod

sweep the kine

decelerating the f

the periphery of t

achieve the comp

essentially a diver

typical configuratio

Figure 1.

1.3 Configuration of Radial Flow Turbomachinery

A single stage centrifugal compressor consists of an impeller (the rotating part), a diffuser (non-rotating) and a volute. Inlet guide vanes are sometimes used in front of the rotor to direct the flow to the impeller inducer. The impeller is used to impart energy to the flow by increasing the velocity and pressure of the fluid. The diffuser is used to convert the kinetic energy available at the impeller exit into static pressure by decelerating the fluid. The diffuser is followed by a volute which collects the fluid from the periphery of the diffuser. Usually an exit cone is connected to the volute exit to delivery the compressed fluid to the pipeline of desired application. The exit cone is essentially a divergent device where the fluid is further diffused. Figure 1.1 shows a typical configuration of a single stage centrifugal compressor.

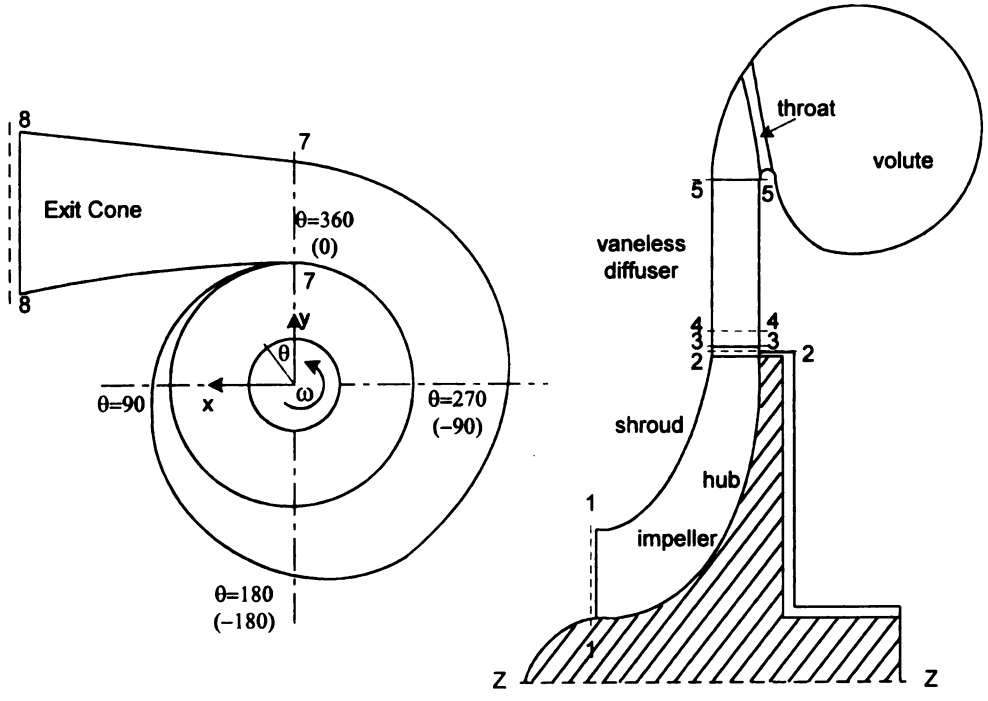

Figure 1.1 Configuration of a single stage centrifugal compressor

A radial

the cone guide

zone. The volute

periphery of the

zone uniform di

system in the wh

wheel shaft. Figure

Section 4

A radial inflow turbine is composed of an inlet cone, a volute and a wheel. The inlet cone guides the fluid to the volute. A slight acceleration can happen in the inlet cone. The volute serves both accelerating the fluid and distributing the fluid to the periphery of the wheel. In the case of overhung volutes, guide vanes are used to obtain more uniform discharge flows. The fluid is further accelerated (relative coordinate system) in the wheel passage and the thermal energy of the fluid is transformed to the wheel shaft. Figure 1.2 is a typical configuration of the radial inflow turbines.

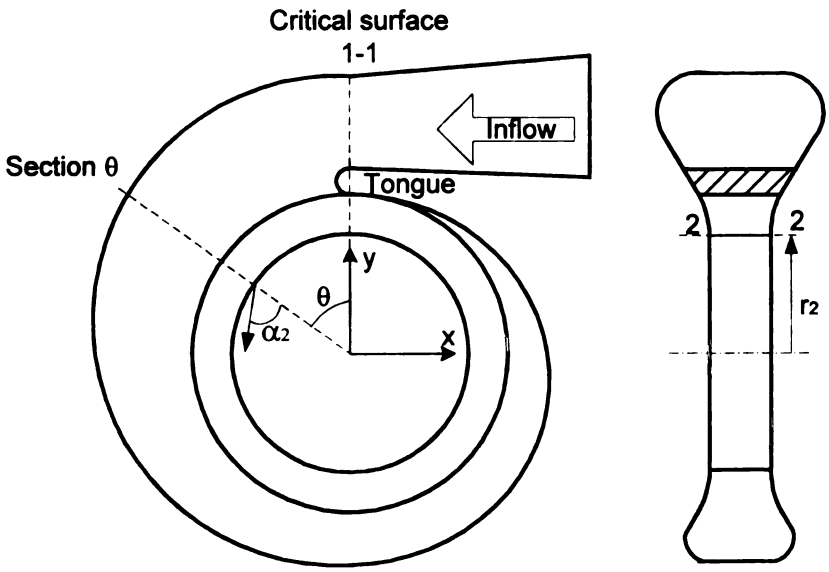

Figure 1.2 Configuration of a radial inflow turbine

1.4 Need for Vo

In the in

mainly applied

Because the imp

hemers, and it p

Extensive studies

understanding of t

ass for the impell

D. Liberti, 1968

mill particularly

The volute

fraction of vo

mechanism in the

reduction method

size performan

correlate the p

throid radius ra

ach the volute

nt of peak eff

appropriate co

ditions, the co

accelerated or d

ssfactions will

1.4 Need for Volute Study

In the interests of size, cost and response, the radial flow turbomachines are widely applied into the areas of petroleum pipelines and automotive turbochargers. Because the impeller or wheel is the component where the energy transformation happens, and it plays a dominant role in determining the performance of a turbomachine. Extensive studies have been carried out on its design, performance prediction and the understanding of the flow structure. At present stage, the ratio of benefit to the research cost for the impeller study is virtually close to zero, except for some special applications (Di Liberti, 1998). In contrast, the study on the stationary components is showing more profit, particularly, the volute study.

The volute study can be subdivided into the study of the volute itself and the interaction of volute with other components. The first study is to understand the flow mechanism in the volute, to obtain high efficiency designs, and to develop more accurate prediction methods. It focuses on the effect of the variation of the volute geometry on the volute performance. Traditionally, a systematic experimental parametrical study is made to correlate the performance with different geometrical parameters, such as area ratio, centroid radius ratio and their variations with the azimuth angles. The second study is to match the volute with other components. It is well known that the machine's operation point of peak efficiency can be different from the design point of the impeller due to inappropriate component combinations. Studies have shown that at the off-design conditions, the compressor volute does not sever as a collector any more; the flow can be accelerated or decelerated in the volute passage; circumferentially distorted pressure distributions will be created in diffusers and impellers. The performance of the machine

an therefore be

nal of both axes

flow condition.

wheel. The existi

he volute and the

15 Objectives and

An automo

he shaft and a cen

ciliary compress

mpressors will be

- **One-dimen**

both turbine

one-dimensi

is accelerate

on the turb

design meth

flow.

- **Three-dime**

dimensional

preliminary

design, aimi

can therefore be significantly reduced. In the radial flow turbines, the volute serves the role of both accelerating the fluid and distributing it over the periphery of the wheel. The flow condition over the wheel periphery directly determines the performance of the wheel. The existence of a recirculation region under the tongue, where the flow re-enters the volute and high mixing occurs, makes the volute/wheel interaction complicated.

1.5 Objectives and Structure of The Thesis.

An automotive turbocharger assembly consists of a radial turbine on one end of the shaft and a centrifugal compressor on the other end. In this thesis, the flow in the stationary components, that is, in the volutes of both radial turbines and centrifugal compressors will be studied. The objectives of the study are:

- **One-dimensional design method** In general, the design method is identical for both turbine and compressor volutes except for the loss models. However, the one-dimensional design of the turbine volute is of more interest because the flow is accelerated at design point. Therefore, the one-dimensional study is conducted on the turbine volute. It is to assess the earlier work on the one-dimensional design methods to determine which one can more accurately predict the volute flow.
- **Three-dimensional flow structure** The flow in volutes is of complicated three-dimensional nature. The one-dimensional design only gives a guideline at the preliminary design phase. The study of the volute flow structure is to improve the design, aiming at higher efficiency and wider work range.

- Volute m
  discharg
  decelera
  reducing
  study is t
  model for
  to dist
  CFD anal

is study. Some
perimental inve
odel to simulate
ssible. Some d
me theoretical a
better underst
e CFD analysis
perty of the
nomena; no fi

As shown
e research to
sional desig
amazing volut

- **Volute modeling and optimization** Because the mass flow is gradually discharged or accumulated over the volute periphery, an inappropriate deceleration or acceleration in the passage causes flow distortion in other parts, reducing the performance of the entire machine at off design conditions. This study is to obtain better match of the volute with other components. An analysis model for the entire machine will be proposed to simulate the impeller responses to distorted exit pressure, so as to optimize the volute geometry and matching.

CFD analysis is the main research tool, assisted with limited experimental data, in this study. Some of the conclusions from this study need to be backed up by more experimental investigations. It is fully understood that CFD analysis is a mathematical model to simulate such a complicated flow phenomena that no analytical solution is available. Some deviation of CFD results is inevitable from experimental data. Therefore, some theoretical analyses are performed to justify the simulation, and more important, to get better understanding of the flow. On the other hand, no one can deny the accuracy of the CFD analysis for the main stream which is less affected by the intrinsic turbulent property of the flow. Therefore, this study pays its major attention to the macro-phenomena; no fine flow structures on the walls are investigated.

As shown in figure 1.3, this dissertation starts with a literature survey on the volute research to appreciate the progress in this field. The main body begins from one dimensional design methods, goes over the complicated three dimensional flow field and the amazing volute/impeller interaction, then ends at a one dimensional analysis model.

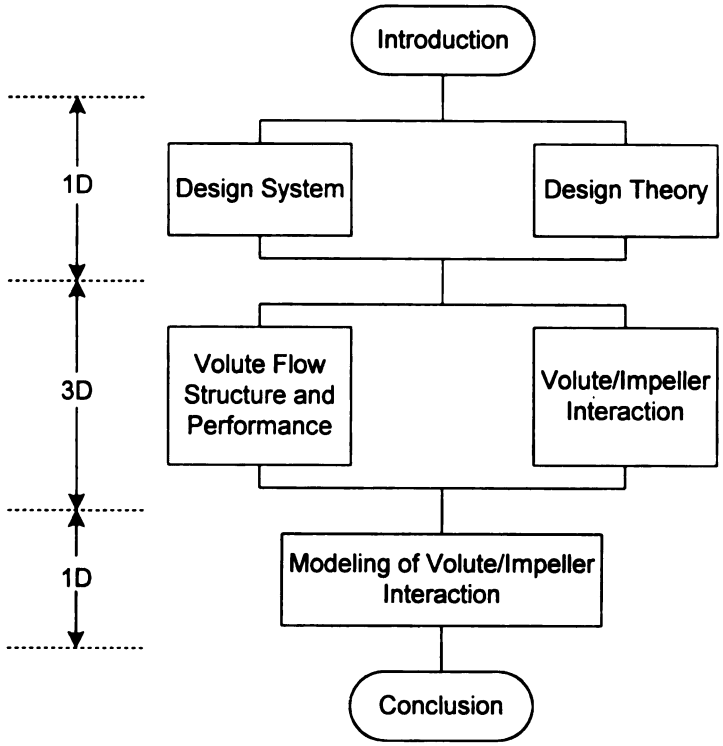

Figure 1.3 Thesis structure

Chapter 3 describes a volute design system. Because of its complicated geometry, it is difficult to design a volute and to generate structured grids for the volute. This system has been developed in the Turbomachinery Lab at Michigan State University for more than five years. Some design examples will be illustrated on both turbine and compressor volutes.

Chapter 4 presents an assessment of the turbine volute design approaches. Theoretical and numerical analysis are employed to investigate the effect of different approaches on the volute geometry and flow. The numerical analysis is compared with experimental data and theoretical analysis. A detailed investigation is conduct to understand the exit flow distortion of this volute. The flow structure inside the volute is also revealed.

Chapter

ompressor A

found that the

epending on the

n design and off-

Chapter

downstream pre

ecided at desig

hardly depends o

when the impeller

ach passage of th

Chapter

ased on the ob

passages under d

for this model

teraction. It is

ptimize volute g

The last c

Chapter 5 deals with the flow structure inside a single stage centrifugal compressor. Attention is paid to the volute/impeller interaction in axial direction. It is found that the volute swirling flow can be of forced vortex or free vortex patterns, depending on the axial distortion. A flow model is proposed to describe the flow structure at design and off-design conditions.

Chapter 6 investigates the impeller response to the circumferentially distorted downstream pressure due to the volute at off-design conditions. The entire compressor is modeled at design and off-design conditions. It is found that the impeller efficiency heavily depends on the slope of the exit pressure. The frozen rotor model also reveals that when the impeller exit pressure is distorted, the mass flow is non-uniformly distributed in each passage of the impeller.

Chapter 7 develops a one dimensional analysis model for the entire compressor based on the observation that the mass flow is non-uniformed distributed in impeller passages under distorted impeller exit pressure. A comparison with CFD results shows that this model has captured most of the flow characters due to the volute/impeller interaction. It is therefore a potential tool to optimize volute/impeller matching and to optimize volute geometry design.

The last chapter summarizes the research and lists some main conclusions.

Chapter 2

LITERATURE SURVEY

2.1 Introduction

The volute is the most neglected component of centrifugal compressors and radial inflow turbines. The number of publications existing in the literature is very small compared to the large number of papers about the other components of the radial machines. Experimental and theoretical volute investigations existing in the literature can be classified in three main groups. The first one deals with the influence of global volute geometrical parameters on the overall characteristics of compressors and turbines. Its main purpose is to predict the performance of volute. The second group is oriented towards mechanical problems and investigates the radial force on the impeller shaft caused by the volute. The study focuses on the interaction of the volute with other components. The third group gives an insight into the basic flow mechanisms in the volute and the sources of losses by providing detailed information about the volute flow field.

The literature survey presented in this chapter is divided into two parts, one for the compressor volutes and the other for the turbine volutes. Each part will describe the above three groups of study in terms of experimental and numerical observations and theoretical models.

2.2 Influence of

Paramet

major roles in d

pressure ratio, e

- Circumfe
- Circumfe
- Shapes o
- Position
- Tongue g

The first

the area and the

ection.

2.2.1 Circumfe

Hawth

ilures under

ectropic anal

f the azimuth

e the critical

ellipsis, beca

merical stud

Stiefe

ith the same

2.2 Influence of Volute Geometrical Parameters on Compressor Performance

Parametrical studies have shown that following geometrical parameters play major roles in determining the volute flow structures, and therefore in determining the pressure ratio, efficiency and operating range of a centrifugal compressor:

- Circumferential variations of the cross sectional areas
- Circumferential variations of the centroid radius of sections
- Shapes of the cross sections
- Positions of the volute inlet
- Tongue geometry

The first three parameters are related together to a certain degree, because when the area and the shape of the cross section are fixed, so is the centroid radius of a cross section.

2.2.1 Circumferential variation of the cross sectional area

Hawthorne (1964) summarized the design of the area circumferential variation of volutes under the assumption of incompressible and isentropic flows. One-dimensional isentropic analysis shows that the ratio of area to radius of the section is a linear function of the azimuth angle, and ends up with a value inversely proportional to the inflow angle at the critical surface. However, the real flow inside the volute is deflected from this analysis, because the flow is three-dimensional and viscous, therefore, experimental and numerical studies have to be carried out to study the deflection.

Stiefel (1972) presented a comparison of the performances of two compressors with the same impeller and vaneless diffuser but different volutes of varying cross section

figure 2.1c. Th

of figure 2.1b

smaller volute

pressure ratios

the flow becom

slope of the cur

However, the p

compressors has

Lopez Per

fitted with differe

s the standard v

slope and a circ

ave a rectang

istribution. The

(figure 2.1). The volute of figure 2.1a is optimized for a pressure ratio of 3.8. The volute of figure 2.1b is optimized for a pressure ratio of 6 and therefore 30% smaller. The smaller volute results in a more narrow operating range, but the flow is stable at all pressure ratios. The large volute has a large operating range at lower pressure ratios, but the flow becomes unsteady for higher pressure ratios. This can be found from the wavy shape of the curves and attributed to the flow separation in the compressor stage (stall). However, the problem of the volute influence on the stall onset in centrifugal compressors has not been investigated systematically up to now.

Lopez Pena (1987) compared the global performance of the compressor when fitted with different volutes and collectors as shown in figure 2.2 and 2.3. The first volute is the standard volute of a turbocharger compressor. It has a cross section of elliptical shape and a circumferentially increasing area. The other volutes, or exactly, collector, have a rectangular cross sectional shape and a circumferentially constant area distribution. These collectors differ only by the cross section area.

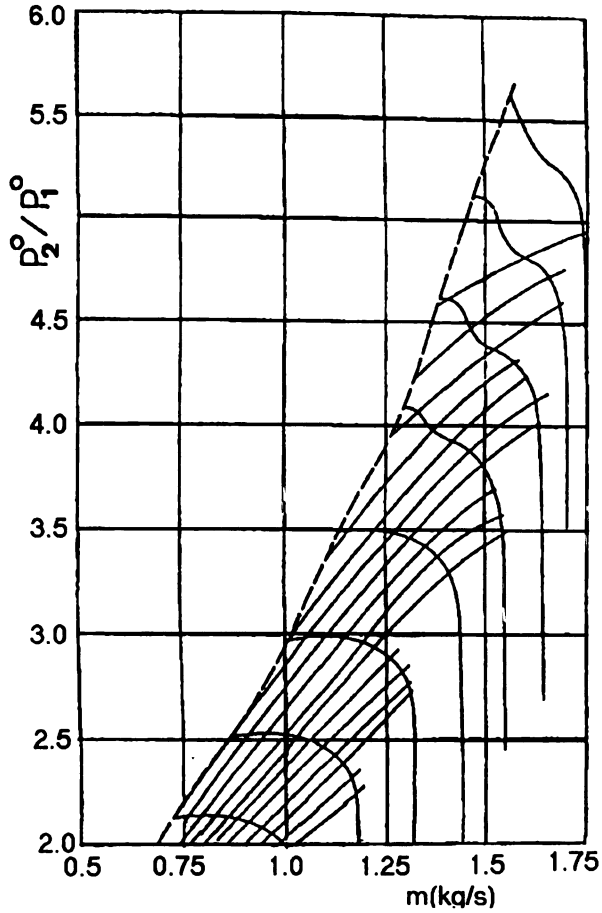

(a) Design pressure ratio 3.8

Figure 2.1 Compressor performance map (after Stiefel, 1972)

Figure 2.1 icon

Figure 2.1 (cont'd)

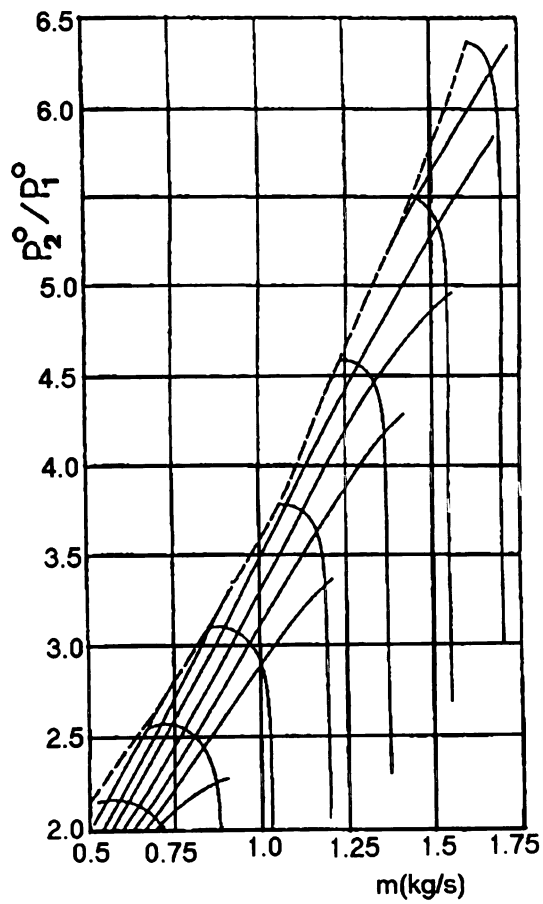

(b) Design pressure ratio 6

(a) Inc

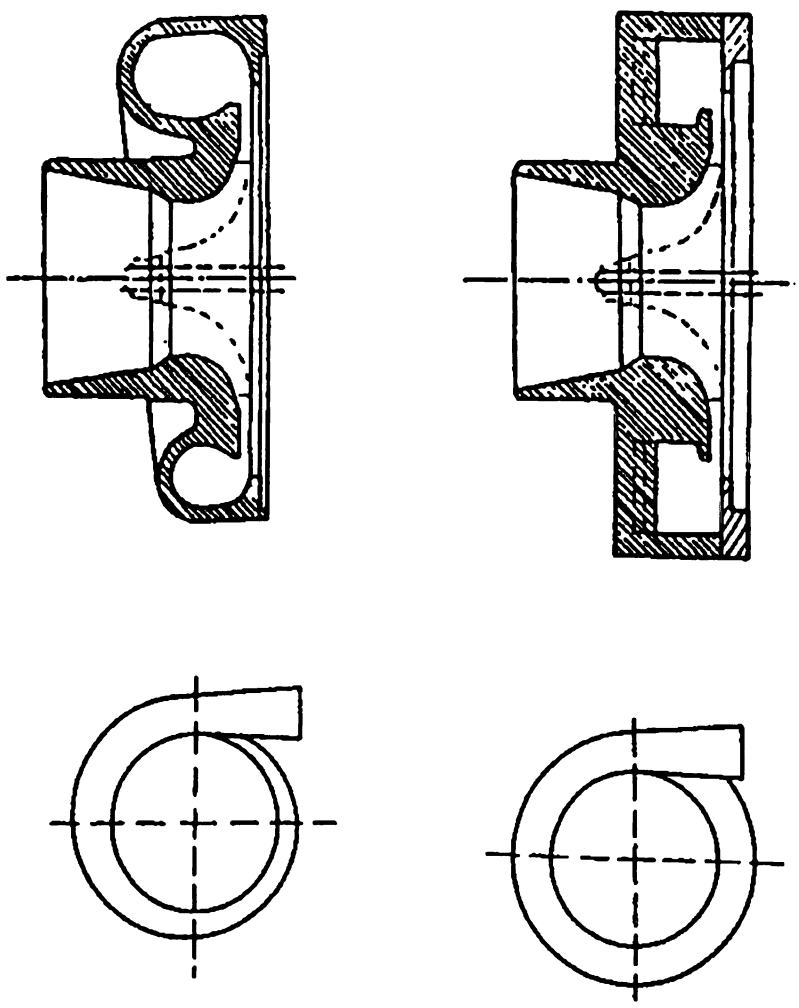

(a) Increasing cross sectional area (b) Constant cross sectional area

Figure 2.2 Types of volutes (after Lopez Pena, 1987)

Figure 2.4 sh

minimum cross sectio

2% smaller than the

surge occurs, moved

ollector is less d

ixation as show

hrough the diffuse

However, due to t

ollector causes

aximum mass f

dicates a separa

ith a large decr

rge pressure re

Figure 2.

f medium cross

he operating r

andard volute.

e the same as

olute is smalle

ritical diffuser

ressure leads to

Figure 2.4 shows the global performance of the standard volute and the volute of minimum cross section area at four different rpms. The minimum cross sectional area is 23% smaller than the exit area of the standard compressor volute. The mass flow at which surge occurs, moved to a smaller mass flow. This is due to the fact that the flow in the collector is less diffused than in the volute, therefore less circumferential pressure distortion as shown in figure 2.3. This circumferential pressure distortion propagated through the diffuser to the impeller exit where it induces instabilities and initiates surge. However, due to the separation of the flow over a large part of the collector channel, the collector causes a lower pressure ratio and efficiency than the standard volute. At maximum mass flow, a constant pressure region at the beginning of the volute channel indicates a separation zone. After this zone the air accelerates until the end of the volute with a large decrease of the static pressure, and the exit conical diffuser has to make a large pressure recovery and cause the decrease of efficiency and pressure ratio.

Figure 2.5 shows the global performance of the standard volute and the collector of medium cross section area, which is 3% smaller than the exit area of standard volute. The operating range is extended to both lower and higher mass flows relative to the standard volute. At maximum mass flow, the efficiency and pressure ratio of the collector are the same as of the standard volute. Since acceleration in the last part of the standard volute is smaller than in the collector, less kinetic energy has to be recovered in the exit conical diffuser, resulting in a better efficiency. The circumferential nearly uniform static pressure leads to the shifting of the surge mass flow to smaller values.

Figure 2.3 Stati pre

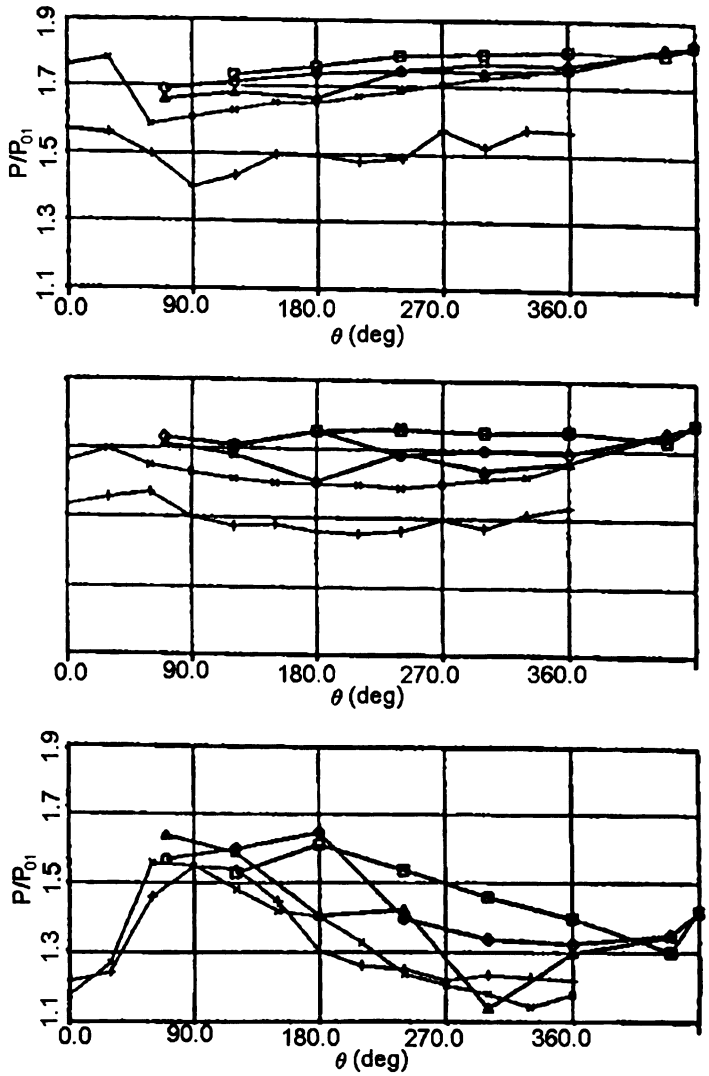

Figure 2.3 Static pressure distribution along the volute and diffuser of the standard compressor (after Lopez Pena, 1987)

Figure 2

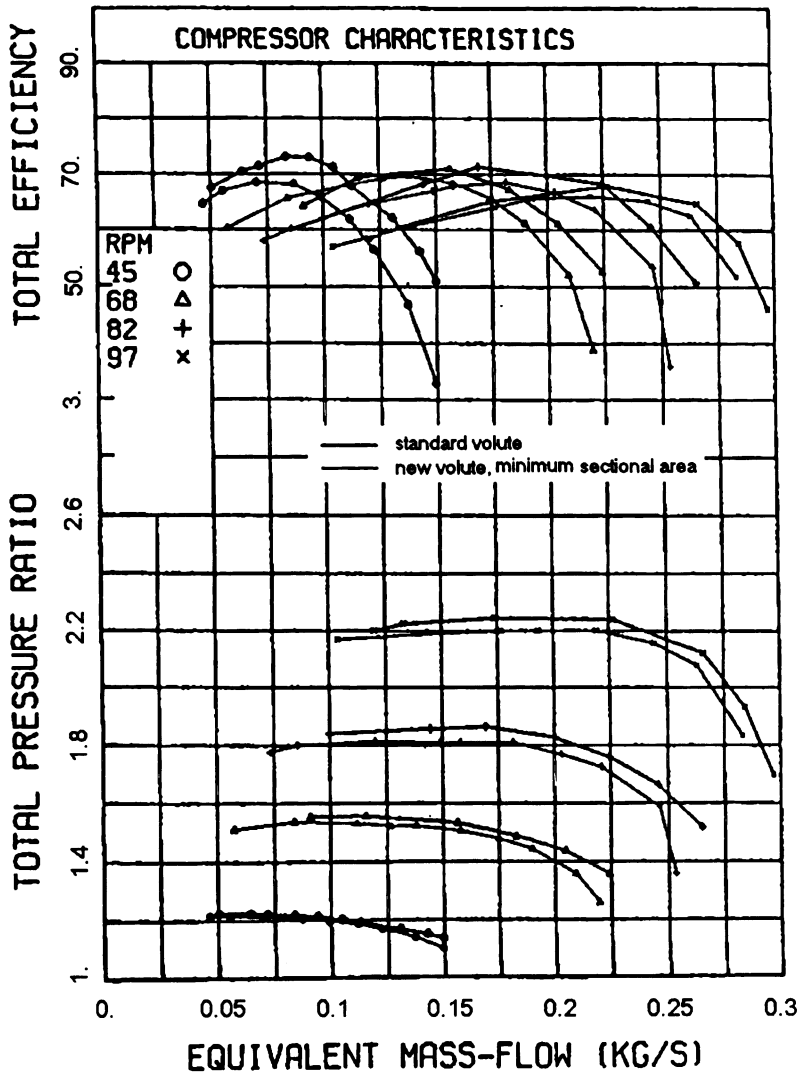

(a) Compressor performance

Figure 2.4 Performance with minimum area (after Lopez Pena, 1987)

Figure 2.4 (cont'd)

Figure 2.4 (cont'd)

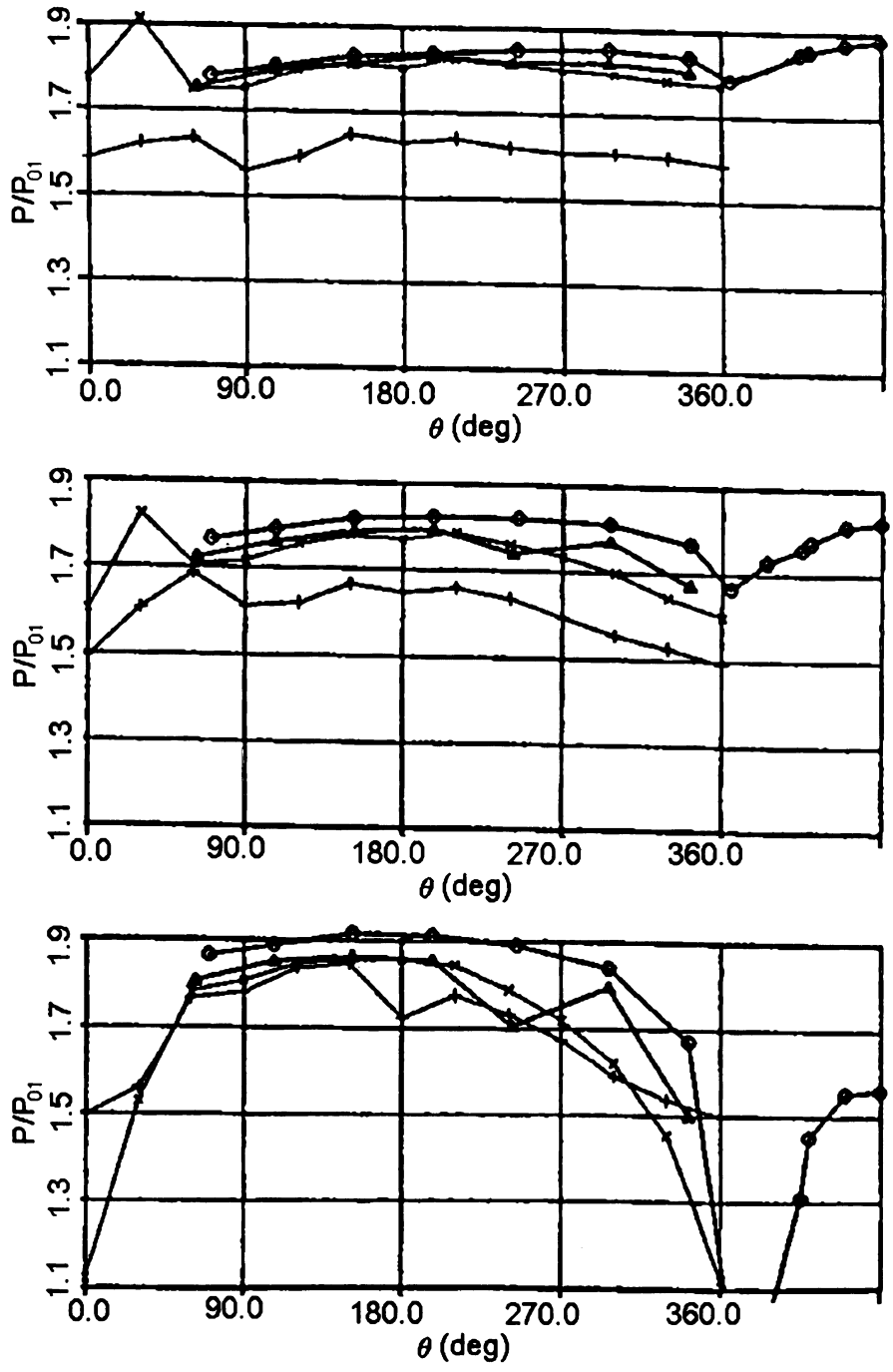

(b) Static pressure along volute and diffuser

Figur

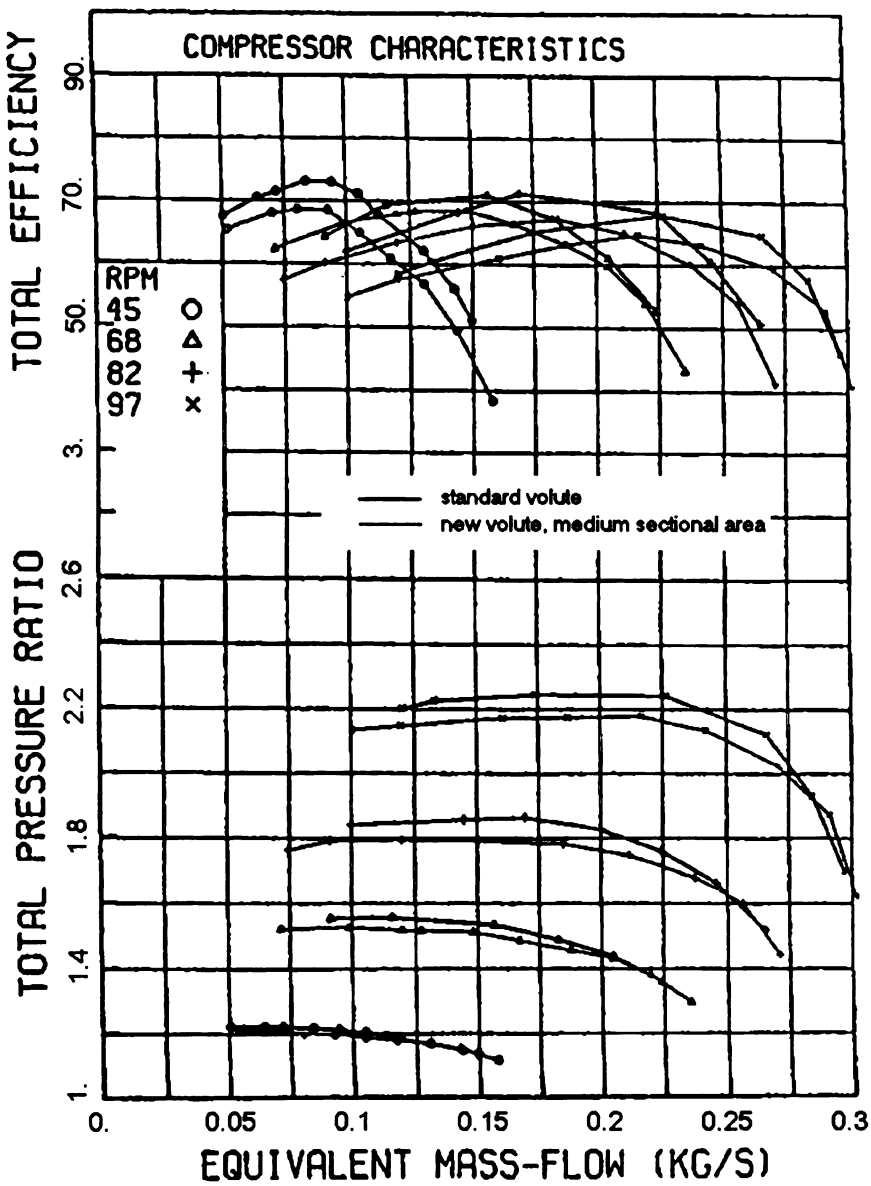

(a) Compressor performance

Figure 2.5 Performance with medium area (after Lopez Pena, 1987)

Figure 2.5 (cont'd)

Figure 2.5 (cont'd)

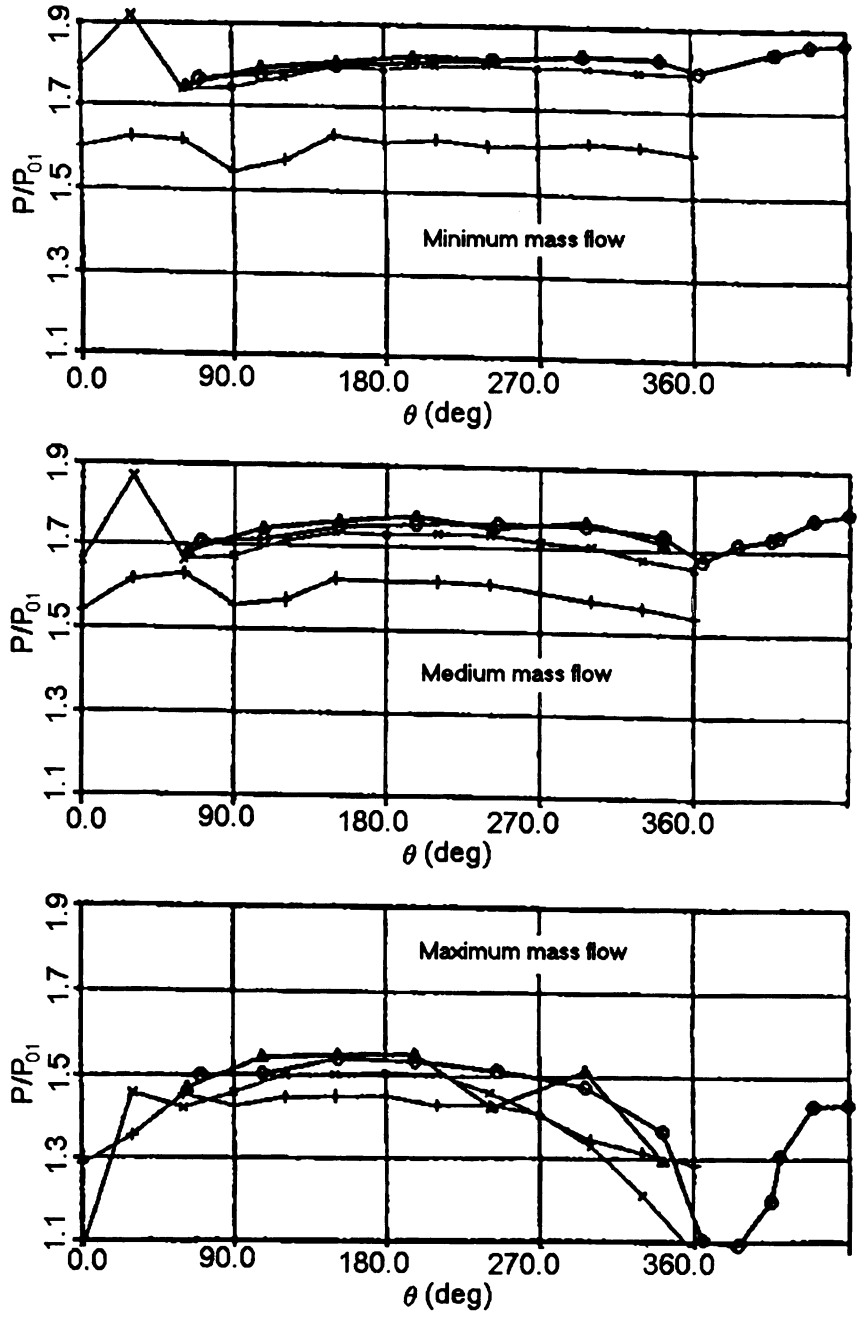

(b) Static pressure along volute and diffuser

Figur

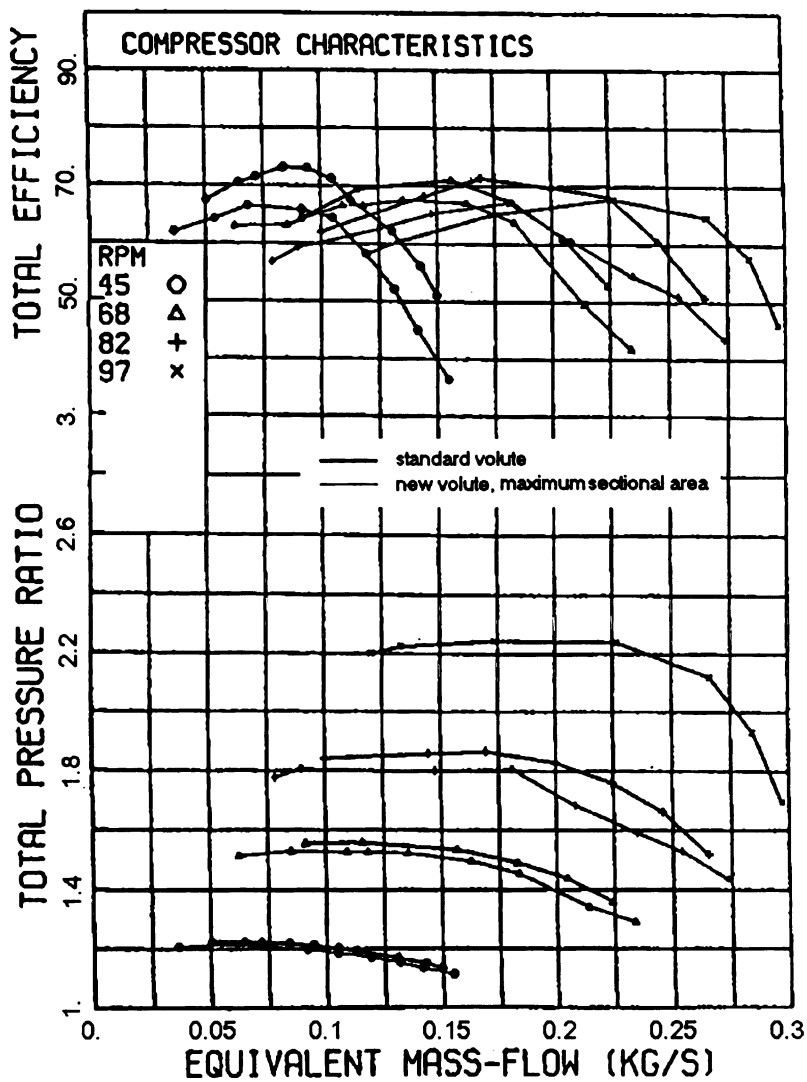

(a) Compressor performance

Figure 2.6 Performance with maximum area (after Lopez Pena, 1987)

Figure 2.6 (cont'd

Figure 2.6 (cont'd)

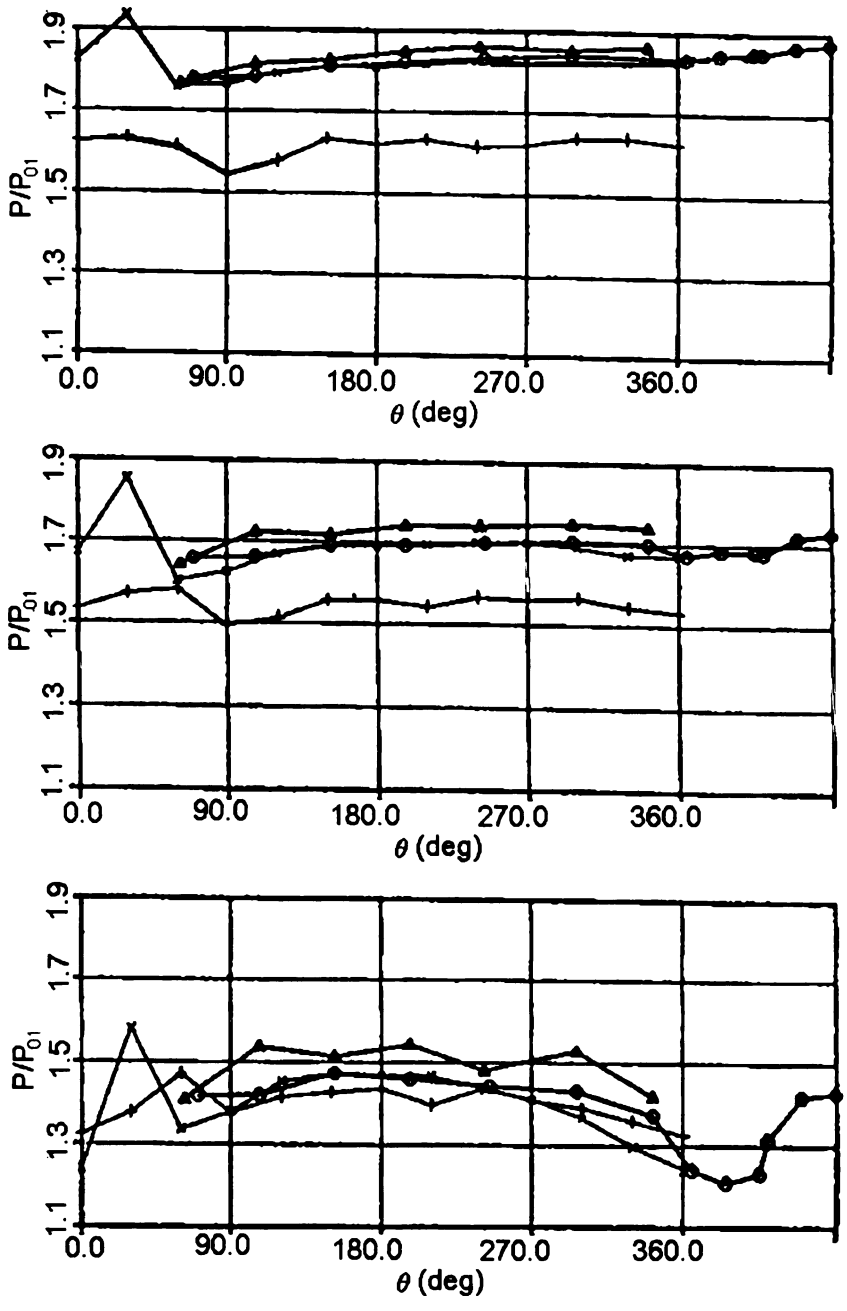

(b) Static pressure along volute and diffuser

Figure 2.6

which is 1"% larger

between medium

compared to the re

author was willing

2.2.2 Shape of the

At the disc

the use of either a

periphery, while

overhung or symm

in centrifugal con

The earli

section, to the k

and one overhu

(1996). The data

explained later.

(1978). Figure 2

volute appear to

circular cross se

small centroid d

Figure 2.6 shows the global characteristics of the volute with maximum area, which is 17% larger than the exit area of the standard volute. They show, at mass flows between medium and high, a relatively large drop in efficiency and pressure ratio compared to the results of the other collectors. The reason for this is unknown, and the author was willing to contribute it to the measurement errors.

2.2.2 Shape of the Cross Section

At the discharge from the stage, the flow is led to a tangential exit pipe through the use of either a collector or a scroll volute. The collector is of the same area over the periphery, while the volute section has a variable area. The volute may be of simple overhung or symmetric types. The simple overhung type is used almost exclusively today in centrifugal compressor design.

The earliest volute performance comparison in terms of the shape of the cross section, to the knowledge of the author, is found in mid 1950's. Two symmetric volutes and one overhung volute are compared in figure 2.7which is cited from Japikse's book (1996). The data of this figure show a preference for the overhung volute. This will be explained later. Similar experimental results were reported by Mishina and Gyobu (1978). Figure 2.8, also cited from Japikse (1996), shows that the losses in an asymmetric volute appear to be reasonably insensitive to the flow angle; the losses of a volute with a circular cross section are lower than those of a square or a rectangular cross section; a small centroid diameter appears to deteriorate the volute performance significantly.

Figure 2.7 Co

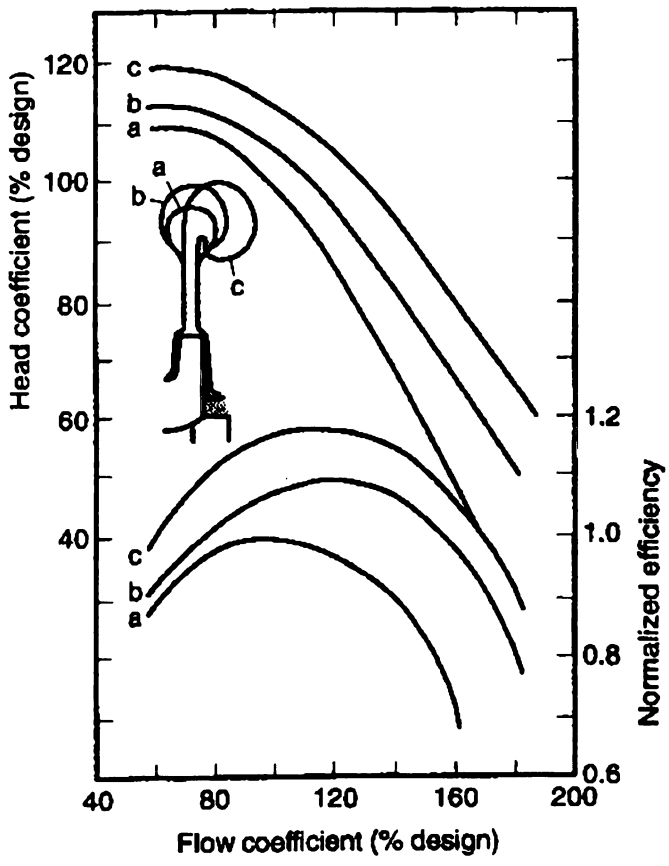

Figure 2.7 Comparison of performance for different volute geometries (Japikse, 1996)

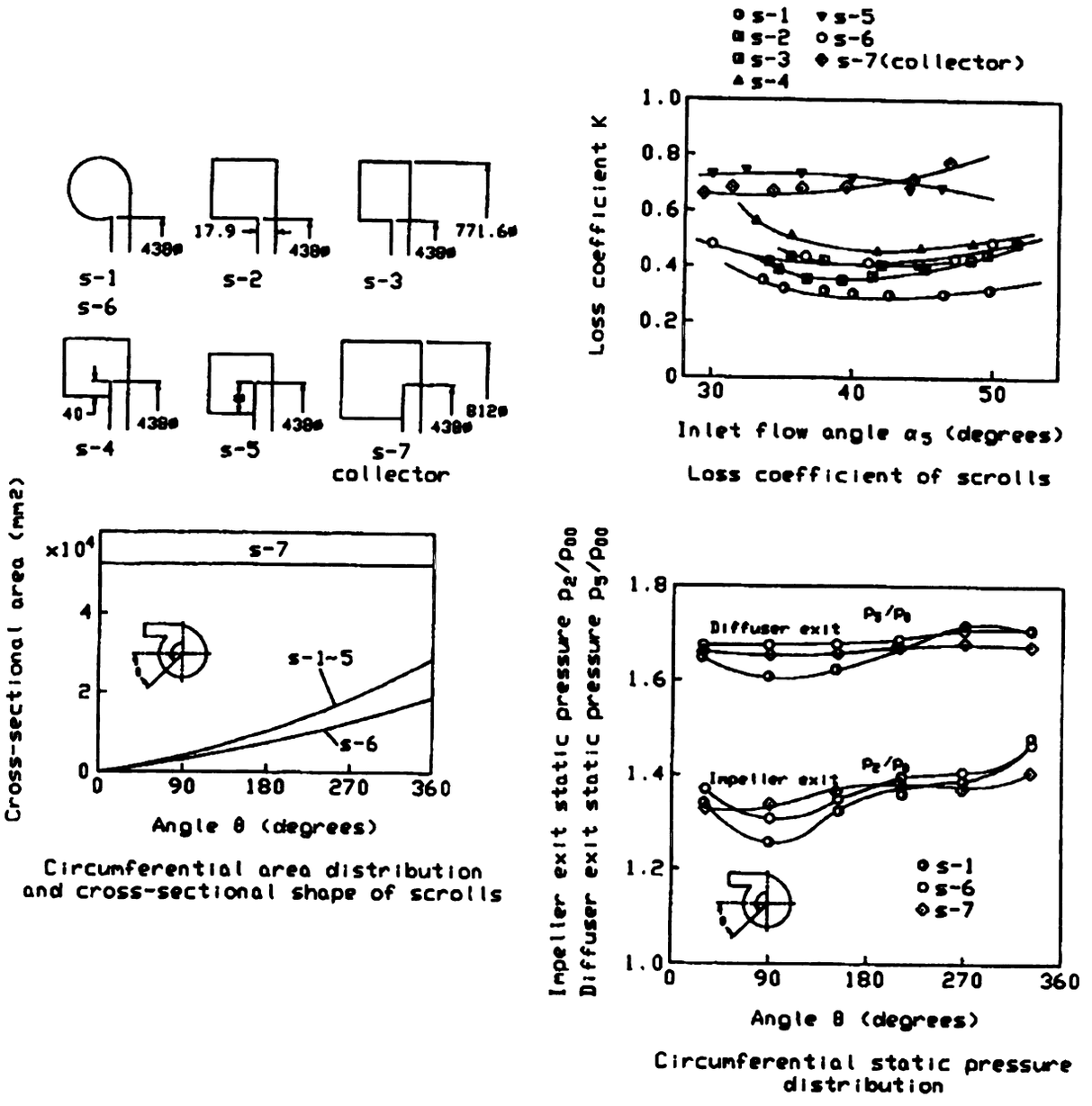

Figure 2.8 Effect of cross-sectional shapes on scroll preformance (after Mishina and Gyobu, 1978)

2.2.3 Radial Posit

Volutes ca

sectional area. An

cross-sections are

is shifted as far as

also possible. A v

volute can have a

internal volute, a

section. For the

cross-sections and

types comes fro

compressors, suc

or as stationary

considerations li

centrifugal comp

Taking into cons

as tightly wound

In the stu

volutes are loca

cross section sha

internal type vol

radius, has a ver

bad as the perfo

2.2.3 Radial Position of the Cross Section

Volutes can be subdivided according to the radial positions of their cross-sectional area. An external volute is what is mounted on the diffuser, i.e., the radii of all cross-sections are larger than the radius of the diffuser outlet. An internal volute is what is shifted as far as possible in the direction of small radii. Some other classifications are also possible. A volute can have a constant radius of the outer wall of each section; a volute can have a constant radius of each cross-section area, which can be an external or internal volute; a volute also can have a constant radius of inner wall of each cross-section. For the first and third types of volutes, they can be an external volute at some cross-sections and an internal volute at other cross-sections. The variation of the volute types comes from their application. In almost all areas of application of centrifugal compressors, such as exhaust-gas turbochargers in vehicles, in small gas turbine engines or as stationary industrial compressors, the available installation space and cost considerations limit the geometrical dimensions of the compressor. The dimensions of a centrifugal compressor are primarily dictated by the peripherally located collector casing. Taking into consideration the design size as well as material and manufacturing costs, the as tightly wound volute as possible is generally aimed at in practice.

In the study of Mishina and Gyobu (1978) show in figure 2.8, the s-2, s-4 and s-5 volutes are located at a decreasing radius. The other geometrical parameters, such as cross section shape and circumferential variation of sectional area, are kept constant. The internal type volute (s-5), which has a cross section radius smaller than the diffuser exit radius, has a very high loss coefficient for all operating points, and its performance is as bad as the performance of the collector (s-7). By locating the volute channel at a larger

radius (s-4), the l

the volute losses w

the conservation of

an extra diffusion o

The result

efficiency with the

Hagelstein

performance of

conclusions from

structures and ev

figure 2.9 that th

the internal volu

considerably red

towards the reg

11% smaller th

performance de

additional radia

component. Thi

swirling vortex

solid body regi

constant. It is c

between the fric

radius (s-4), the loss coefficient of the volute is decreased by 30%. Further decrease of the volute losses was obtained by increasing the volute radius (s-2). This is simply due the conservation of angular momentum. A larger center radius of the cross section gives an extra diffusion of the flow in the volute, so the friction loss is reduced.

The result of Stiefel (1972) confirmed that for all mass flows, a higher compressor efficiency with the volute located at the larger radius than the one located at small radius.

Hagelstein, *et al.* (2000) gave a systematic comparison of the flow field and performance of internal and external volutes of rectangular cross sections. The conclusions from their study are similar to others as mentioned above, but detailed flow structures and explanations can be found in this paper. From the study, it is shown in figure 2.9 that the total pressure ratio for the compressor stage is significantly worse for the internal volute. Moreover, the working range of the stage with an internal volute is considerably reduced as the choke margin for the internal volute is shifted appreciably towards the region of small mass flows. The efficiency of the internal volute is about 11% smaller than of the external volute at the optimum point. The explanation of this performance deterioration can be found in figure 2.10. The external volute has an additional radial space, which leads to further deceleration of the meridional velocity component. This is the reason for the weaker secondary vortex in the external volute. The swirling vortex is of forced vortex type, and the authors divided the swirling vortex into solid body region and an outer region where the swirling velocity is more or less constant. It is concluded that the vortex losses mainly occur in the transition region between the frictionless solid body core and the outer shell.

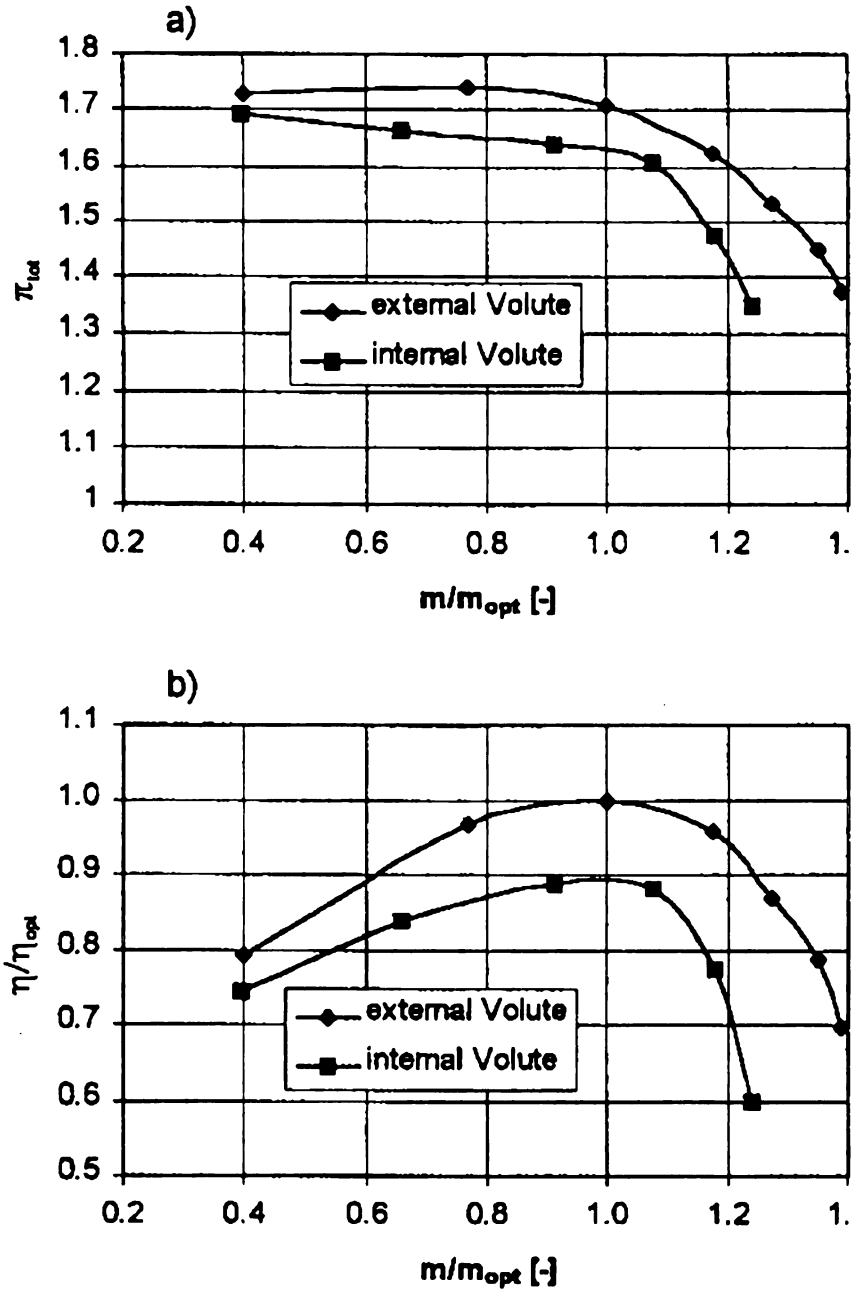

Figure 2.9 Comparison of Stage total pressure rise (a) and isentripic stage efficiency (b) (after Hagelstein, *et al.*, 2000)

Figure 2.10 Resu
for

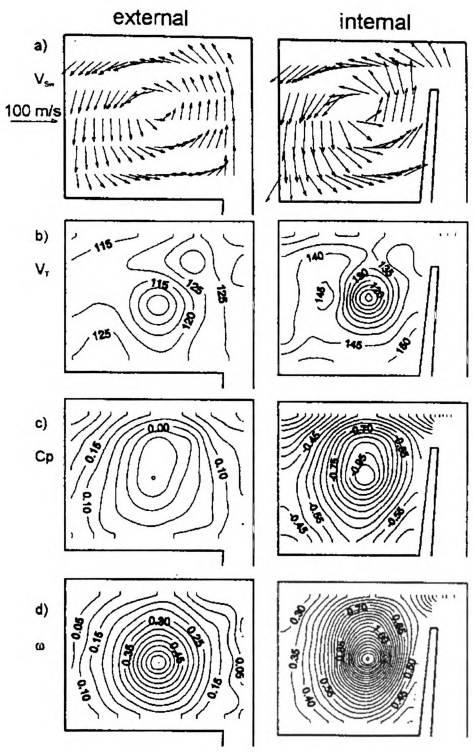

Figure 2.10 Results of probe traverse measurements in measurement plane 3 (180°) for norminal operating point (after Hagelstein, *et al.*, 2000)

2.2.4 Tongue Geo

The volute

of the location of

tongue shape relat

2.2.4 Tongue Geometry

The volute tongue can be radial or tangential for overhung volutes, but influence of the location of the tongue has not been investigated symmetrically. In the literature, tongue shape related study is almost exclusively conducted on pump volutes.

2.3 Theoretical P

The predic

Weber and Koroi

- Meridional ve
- Friction losses
- Some of the tan

It is comm

the volute inlet is

losses is expressed

The frictio

hydraulic diameter

within the volute

the through flow

considered for the

already accounted

depends on the R

from the standard

In order to

made. Firstly if th

2.3 Theoretical Prediction of Volute Performance

The prediction of volute performance was modeled by Japikse (1982 or 1996), Weber and Koronowski (1986). The assumptions adopted in these models are:

- Meridional velocity is lost, denoted by Δp^o_{MVDL};
- Friction losses are modeled as pipe flow, denoted by Δp^o_f;
- Some of the tangential velocity can be lost, denoted by Δp^o_{TVDL}.

It is commonly assumed that the head associated with the meridional velocity at the volute inlet is lost and it is called meridional velocity dump losses. The amount of losses is expressed by the following equation

$$\Delta p^o_{MVDL} = \frac{1}{2}\rho V^2_{mi} \tag{2.1}$$

The friction losses are calculated in function of the roughness of the wall, the hydraulic diameter of the volute channel (D_{hyd}), the path length of the fluid particles (L) within the volute (which is assumed to be equal to the length of the volute channel) and the through flow velocity (V_t) inside the volute. Only the through flow velocity is considered for the friction losses since complete dissipation of the meridional velocity is already accounted for in the meridional velocity dump losses. The friction coefficient depends on the Reynolds number and relative surface roughness and can be obtained from the standard friction charts for pipes

$$\Delta p^o_f = \omega_f \frac{L}{D_{hyd}} \frac{1}{2}\rho V^2_t \tag{2.2}$$

In order to calculate the tangential velocity dump losses, two assumptions are made. Firstly if the tangential velocity accelerates from the volute inlet to the volute

outlet ($V_2 \leq V_{2t}$).

However if the

flow diffuses an

pressure losses in

where $\omega_2 = 1$.

This theor

volute, specified

coefficient

n function of the

and the volute in

Flow is

following simp

velocity from

coefficient are

outlet ($V_{ti} \leq V_{te}$), then it is assumed that no tangential velocity dump loss occurs. However if the tangential velocity decreases from the volute inlet to the exit, then the flow diffuses and it is assumed that the total pressure loss is equivalent to the total pressure losses in a sudden expansion mixing process

$$\Delta p^{o}_{TVDL} = \omega_t \rho \frac{1}{2}(V_{ti} - V_{te})^2 \tag{2.3}$$

where $\omega_t = 1$.

This theory has been used by Japikse (1996) to calculate the performance of a volute, specified by means of the volute loss coefficient ω and static pressure recovery coefficient

$$C_p = \frac{p_e - p_i}{p_i^0 - p_i} \tag{2.4}$$

in function of the ratio of volute outlet area to volute inlet area

$$AR = A_e / A_i = \pi D_e^2 / 8\pi r_i b_i \tag{2.5}$$

and the volute inlet swirling parameter

$$\lambda = V_{ti} / V_{ri} \tag{2.6}$$

Flow is treated as incompressible and the friction losses are neglected. The following simple relations have been obtained in the case of accelerating tangential velocity from volute inlet to outlet. The loss coefficient and static pressure recovery coefficient are

$$\omega = \frac{1}{1+\lambda^2} \quad \lambda = V_{ti} / V_{ri} \tag{2.7}$$

$$C_p = \frac{\lambda^2 - 1/AR^2}{1+\lambda^2} \quad \lambda = V_{ti} / V_{ri} \tag{2.8}$$

In ca

Th

parameter

2.12. Mea

that this p

not for th

coefficie

n the ev

uniform

In case of decelerating through flow, they are given by

$$\omega = \frac{1}{1+\lambda^2} + \frac{(\lambda - 1/AR)^2}{1+\lambda^2} \quad \lambda = V_{ti}/V_{ri} \tag{2.9}$$

$$C_p = \frac{2(\lambda - 1/AR)}{AR(1+\lambda^2)} \quad \lambda = V_{ti}/V_{ri} \tag{2.10}$$

The calculated and measured variations of C_p and ω with volute inlet swirl parameter λ and the volute outlet to inlet area ratio AR are compared in figure 2.11 and 2.12. Measured and calculated static pressure rise coefficients agree well and it seems that this model provides a useful basis for the prediction of volute static pressure rise but not for the losses. The difference between the calculated and measured values of loss coefficient for high mass flows (smaller λ) can be due to neglecting the remaining swirl at the exit of the volute in the model but not in the measurements. The assumptions of uniform inlet and outlet flow conditions may not be satisfied.

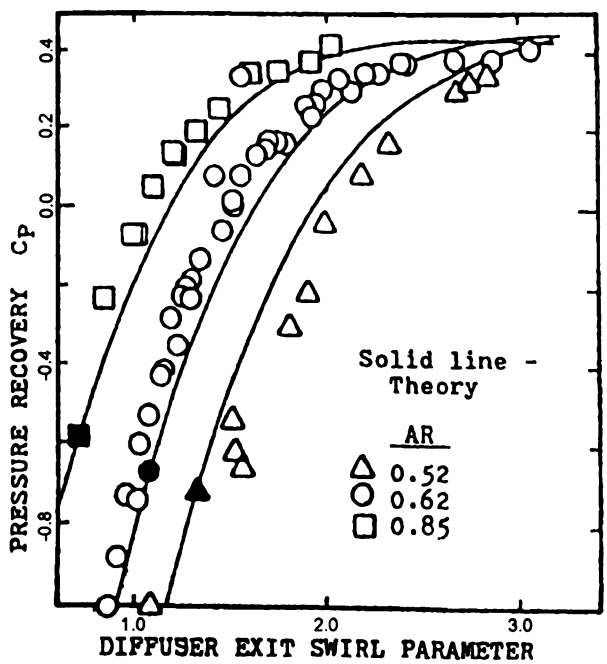

Figure 2.11 Volute pressure recovery coefficient comparison of theory and data (after Japikse, 1982)

Figure 2

Var

and analy

design con

takes into

includes th

•

Ro

an

di

•

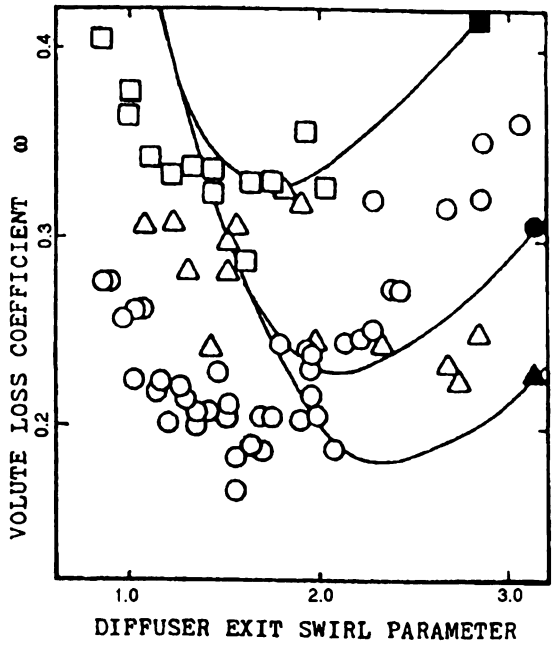

Figure 2.12 Volute pressure loss coefficient compason of theory and data (after Japikse, 1982)

Van den Braembussche *et al.* (1999) proposed an iterative model for the design and analysis of centrifugal compressor volutes. Because at off-design condition, even at design condition, the inlet flow of volute is not circumferentially uniform, this model takes into account the interaction of the volute with the impeller, therefore, this model includes the vaneless diffuser and the volute. The model performs following calculations,

- Rotor response calculation: to define the circumferential velocity distribution (V_{r2} and V_{t2}) resulting from a circumferential variation of the outlet static pressure distribution. At the first iteration, the static pressure is assumed to be constant and the diffuser inlet velocity is defined by the circumferentially averaged value.
- Diffuser flow calculation: to predict the diffuser outlet flow velocity components, total and static pressure distribution by calculating the diffuser static pressure rise

and loss

condit

- Volute f

Starting fr

static pres

diffuser ou

- Impeller

static pres

- Exit diffu

the exit d

With the

calculations, the

conditions at imp

when the new dif

model not only

volute impeller i

2.17 show that th

and losses at different circumferential positions as a function of the inlet conditions.

- Volute flow calculation: to approximate the three-dimensional flow in the volute. Starting from the nonuniform diffuser outlet flow, it defines the volute losses and static pressure rise, and updates the circumferential static pressure distortion at the diffuser outlet.
- Impeller outlet pressure calculation: to predict the rotor outlet circumferential static pressure variation as the function of the diffuser outlet pressure distortion.
- Exit diffuser flow calculation: to define the mixed-out conditions at the outlet of the exit diffuser downstream of the tongue.

With the exception of the last one, used only once for the overall performance calculations, these components are combined in an iterative procedure in which the flow conditions at impeller and diffuser outlet are adjusted. The iterative procedure is stopped when the new diffuser outlet pressure distribution equals the previous one. Therefore, this model not only predicts the performance of the volute, but also predicts the volute/impeller interaction, which results in the circumferential distortion. Figure 2.13 to 2.17 show that this model agrees with experimental very well.

Figure 2.1
fu

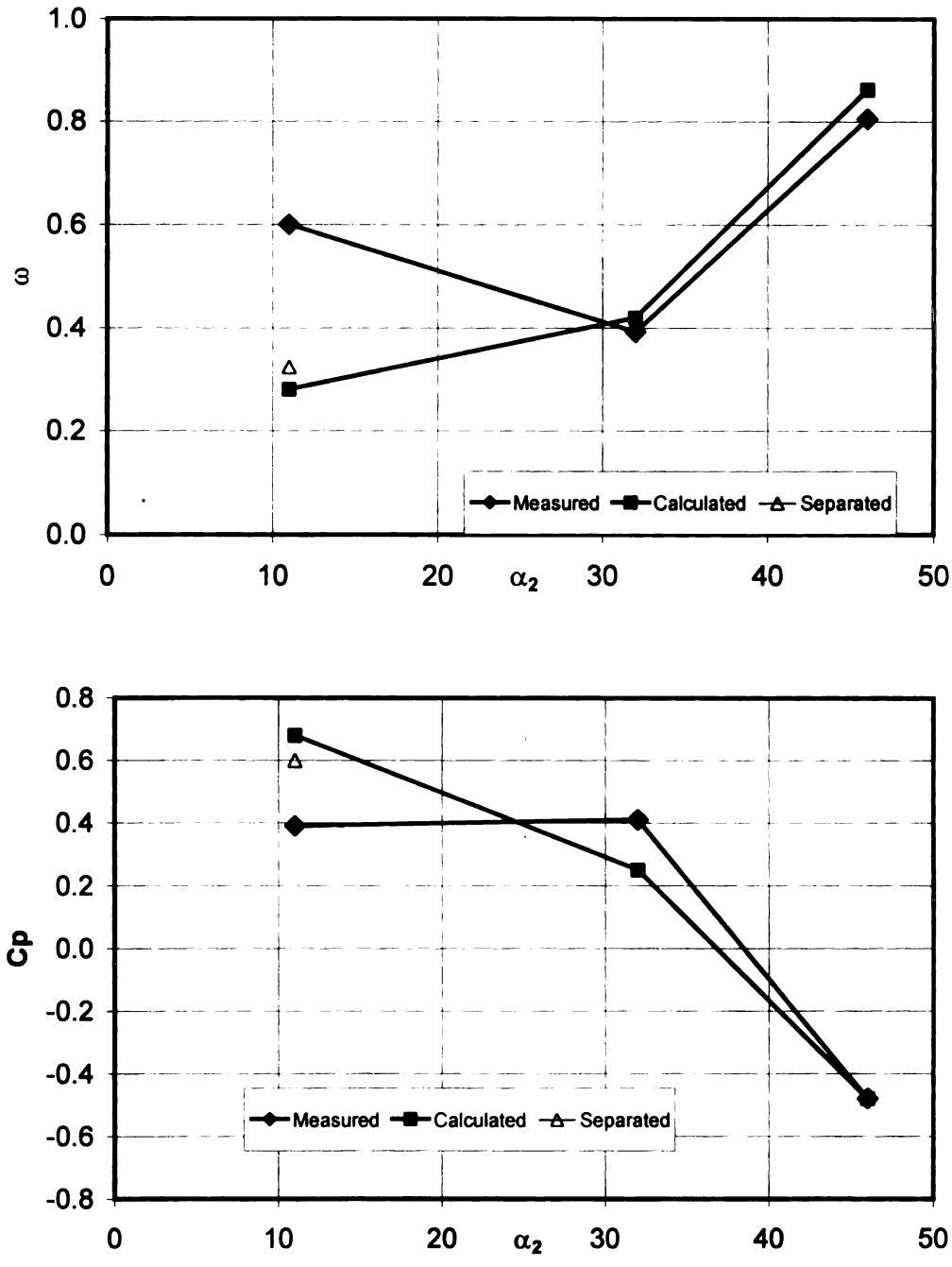

Figure 2.13 Loss and static pressure rise coefficient for the external volute as a function of the inlet angle (after Van den Braembussche, 1999)

P_3/P_{ref}

P_3/P_{ref}

P_3/P_{ref}

Figure 2.14

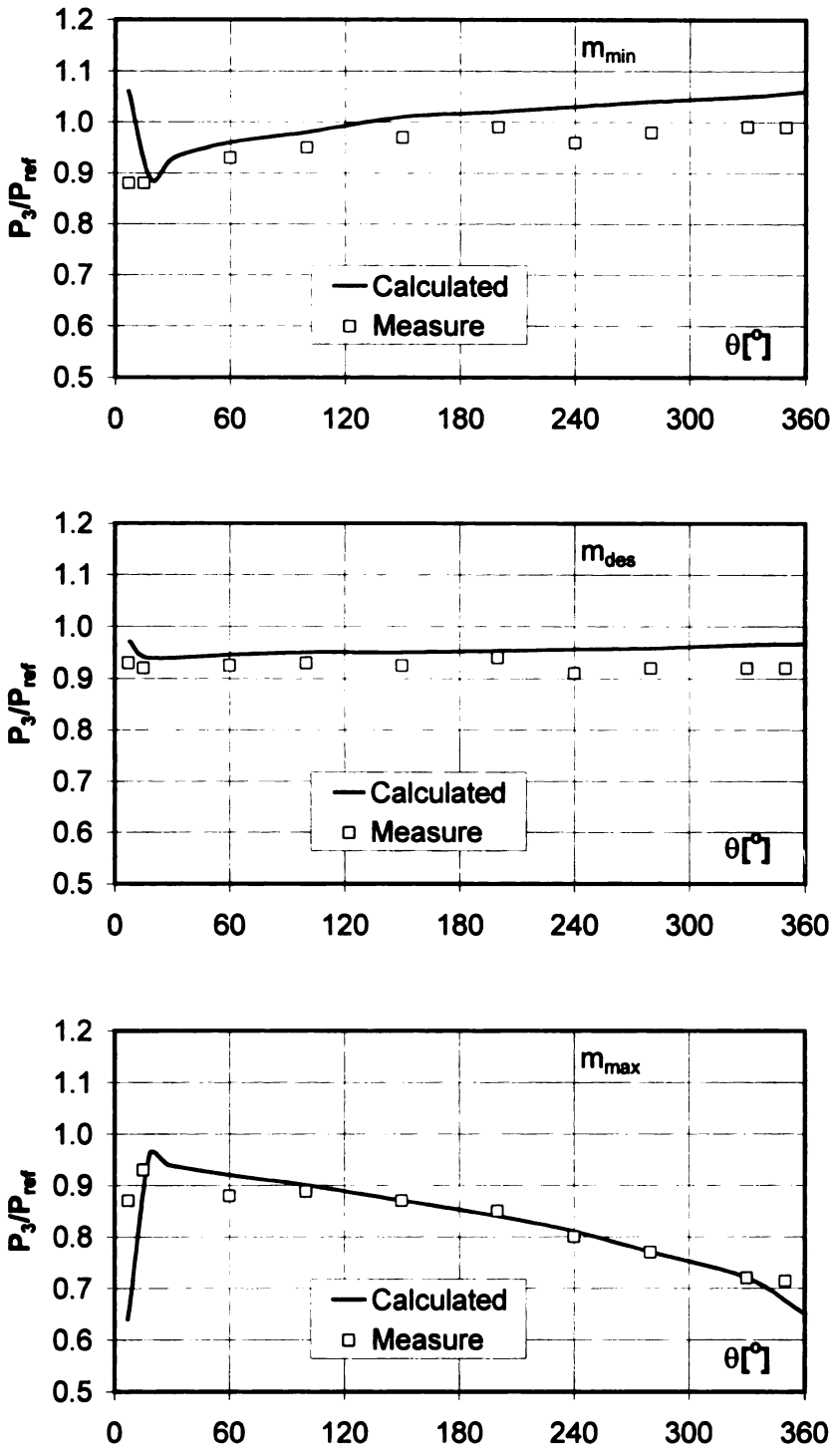

Figure 2.14 Circumferential static pressure distribution at three operating points (after Van den Braembussche, 1999)

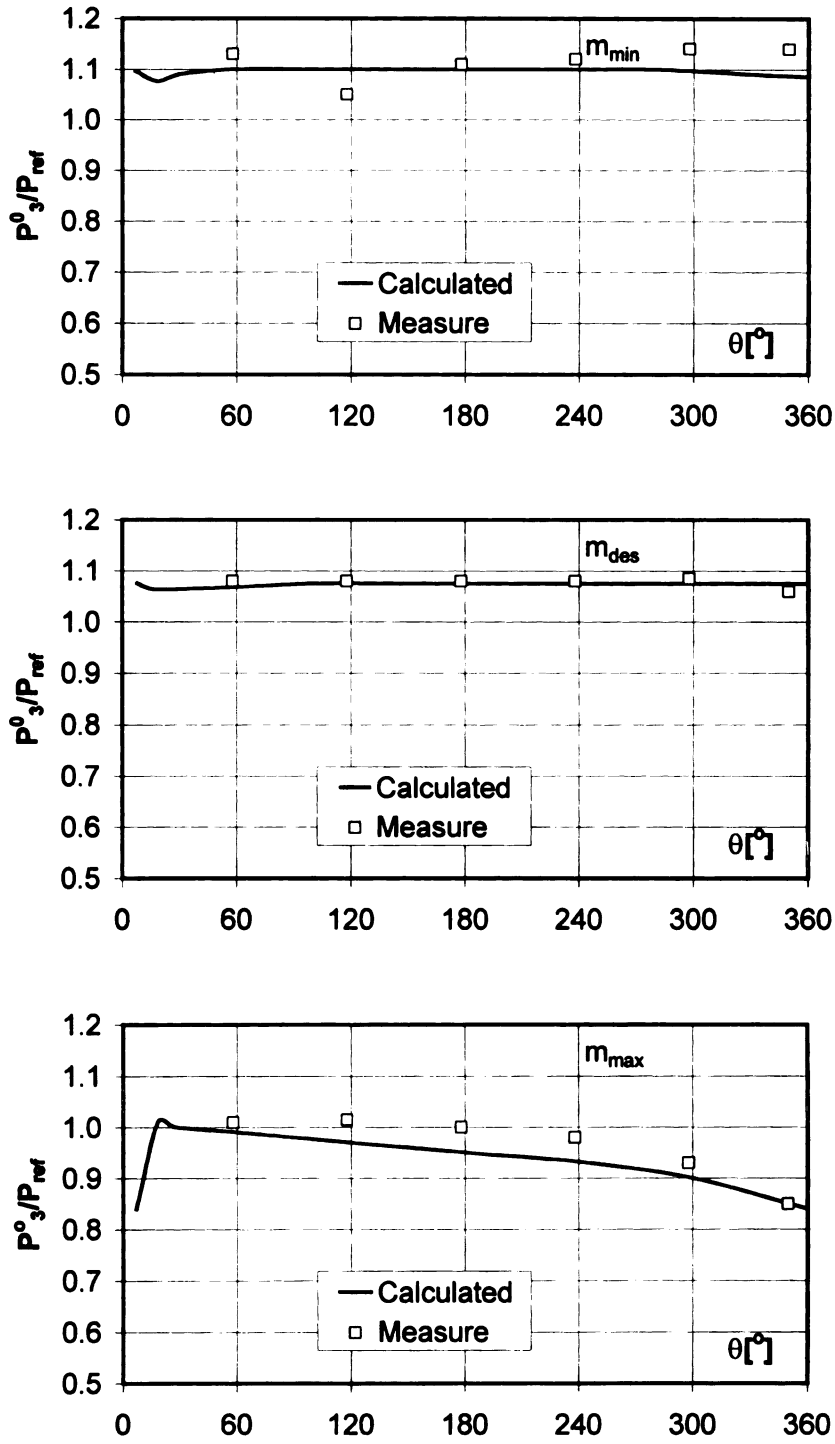

Figure 2.15 Circumferential total pressure distribution at three operating points (after Van den Braembussche, 1999)

Figure 2.16 C

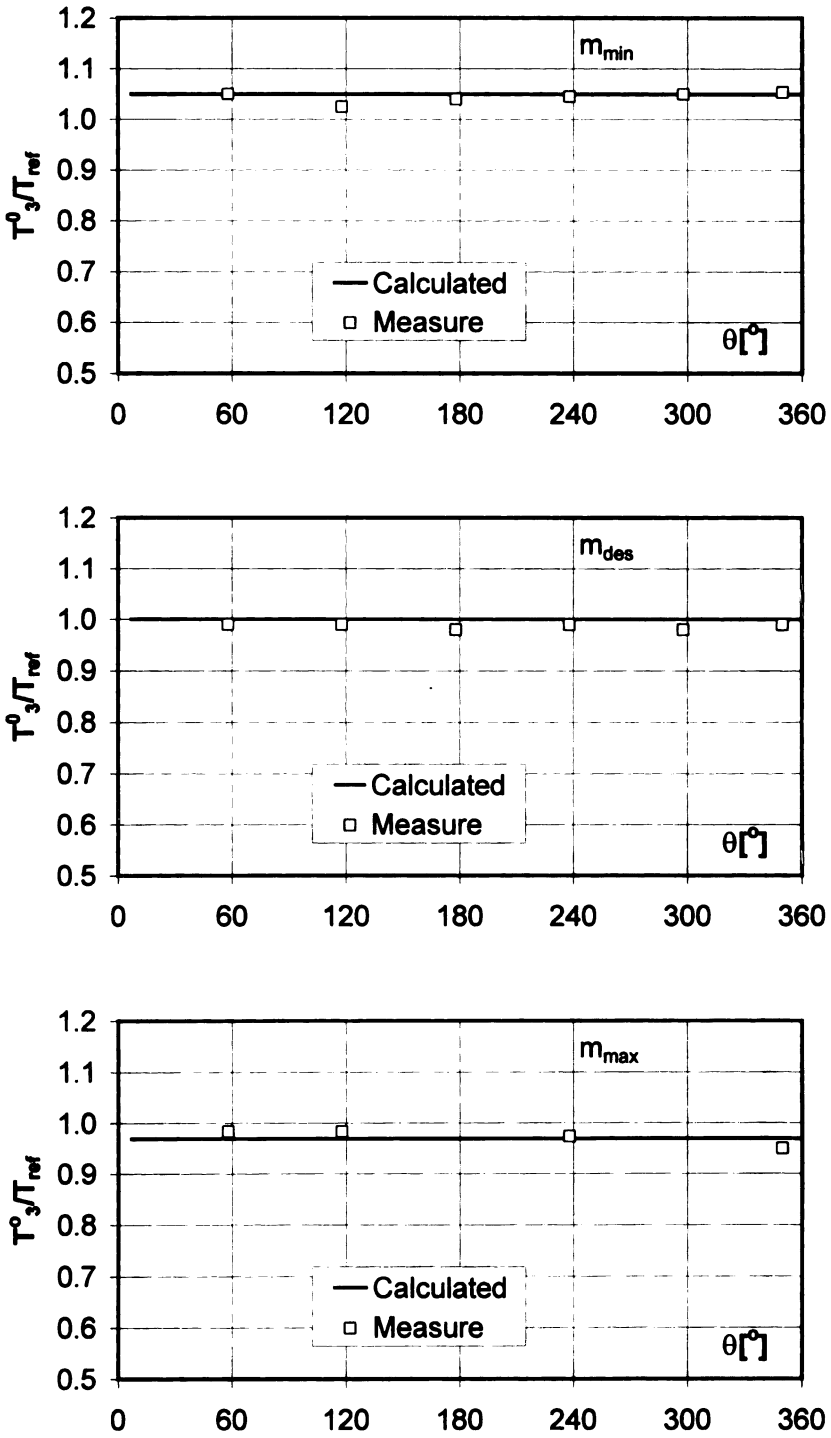

Figure 2.16 Circumferential total temperature distribution at three operating points (after Van den Braembussche, 1999)

Figure 2.17

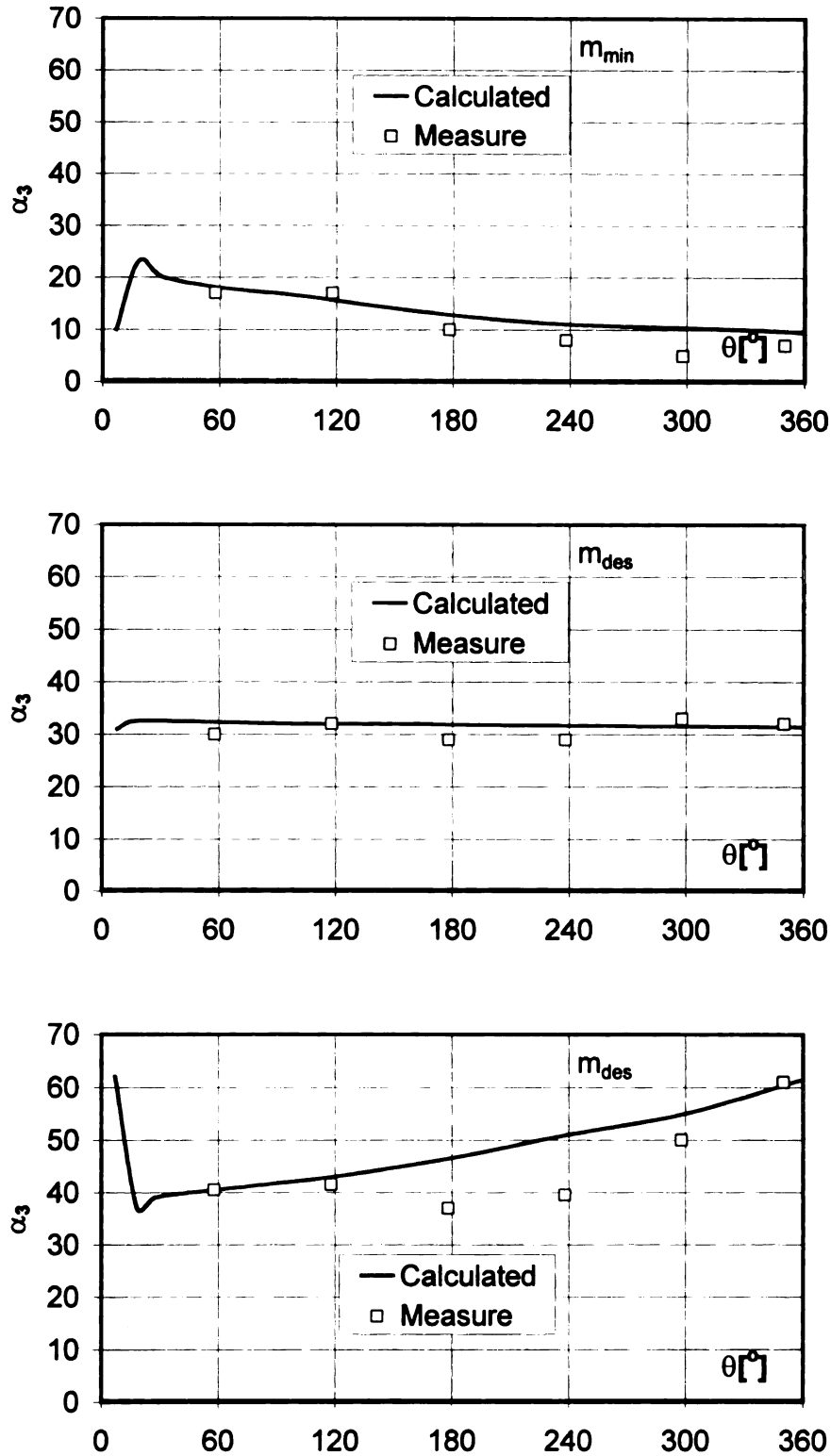

Figure 2.17 Circumferential absolute flow angle distribution at three operating points (after Van den Braembussche, 1999)

2.4 Radial Forc

The radi

variation along

the circumferen

of the papers c

cross sensors

Sikora (1986)

Gopalakrishna

element are no

value elemen

element. It is

the static pre

component o

action wh

velocity is th

at the direct

and the pres

Fat

response to

operations.

downstream

oscillation.

pressure

2.4 Radial Forces

The radial force on the impeller shaft is the result of a nonuniform static pressure variation along the circumference of the impeller outlet due to the volute. The origin of the circumferential static pressure variation has not been clearly justified up to now. Most of the papers concern the radial force in pumps because the higher density of the fluids causes serious radial loading. Only are these compressor related research reviewed here. Sideris (1986) tried to explain the radial force using continuity equation. Lorett and Gopalakrishnan (1986) claimed that if the velocities entering and leaving a volute element are not equal, the difference in momentum of the flows entering and leaving the volute element must cause a change in the static pressure within the length of the volute element. It is revealed that the outflow radial velocity from the impeller is higher where the static pressure is lower at the impeller periphery and vice versa. Since the radial component of the outcoming momentum from the impeller has the highest value at the location where the radial velocity is highest and the lowest value where the radial velocity is the lowest, one can expect that the radial component of momentum force acts in the direction opposite to the static pressure force. The balance of the momentum force and the pressure force will be the radial force acting on the impeller shaft.

Fatsis *et al.* (1997) conducted a numerical investigation of the centrifugal impeller response to downstream static pressure distortions imposed by volutes at off-design operations. An unsteady three-dimensional Euler solver with nonreflecting upstream and downstream boundary conditions and phase-lagged periodicity conditions is used for the simulation. The radial force is integrated by two different methods. One is the integration of pressure on the blade and hub surfaces for an unshrouded impeller, and the other uses

a control volume for the moment of momentum to take into account of the momentum in and out of the control volume. An interest conclusion, from the authors, is that the two methods give the same radial load on fine grids, which is equal to that from the first method on coarse grid. It is claimed that for a backswept impeller the largest contribution of the radial force is from the circumferentially nonuniform outlet static pressure distribution. The force component due to nonuniform outlet radial momentum is in the opposite direction and is much smaller. The contribution of the inlet tangential momentum, which is also small, is due to the nonzero absolute tangential velocity at leading edge, and is nearly perpendicular to the other ones. The remaining contributions are less significant. For the impeller of radial-ending blades of Eckardt, the pressure force is almost totally compensated by the force due to radial momentum at the outlet, so that the total force is much smaller than for the backswept impeller. The contribution of the nonuniform tangential momentum at the outlet is also (non)negligible. The authors explained this difference as that in the backswept impeller, the variation of the outlet static pressure causes larger tangential variation of momentum, thus larger variation of static pressure.

Flathers and Bache (1999) presented a computational investigation of a centrifugal gas compressor. It is claimed that it is the first time that a whole compressor with all the impeller passage and the volute is modeled by a viscous code. Except for the significant difference at small mass flow rates, the predicted magnitude and direction of the radial force are in agreement with the experimental investigation.

2.5 Flow Struc

To ultr

olute. flow st

design and ob

requires detail

The ex

emil Van den

of a centrifuge

has circular sl

egion close to

center. The zo

locations and

Figur

2.5 Flow Structure in Compressor Volutes

To ultimately understand the flow phenomena in a compressor, especially in the volute, flow structure study has to be conducted. It includes the flow field survey at design and off-design conditions, at steady and unsteady levels. Because this study requires detailed flow traverse measurement, it is very expensive and time consuming.

The experimental study of compressor volute flow structure has not been found until Van den Braembussche and Hande (1990) measured the flow inside a straight model of a centrifugal compressor volute in figure 2.18. The cross section of the straight volute has circular shape with a tangential inlet. A constant swirl velocity is measured in the region close to the walls and the swirl velocity has a forced vortex type distribution in the center. The zone of the forced vortex covers 30% of the cross section diameter at all axial locations and is almost independent of the mass flow as shown in figure 2.19—2.21.

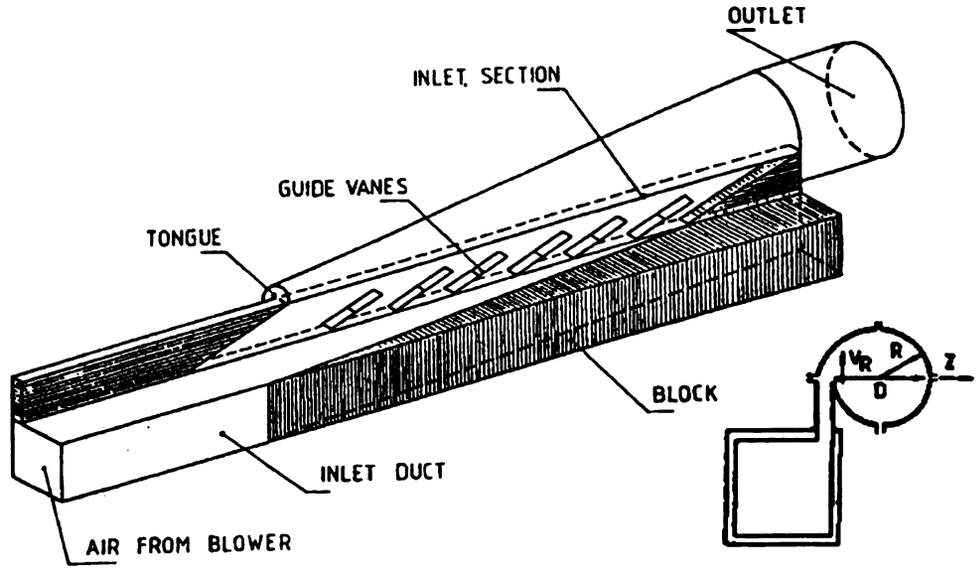

Figure 2.18 Straight volute 3D view (after Van den Braembussche, 1990)

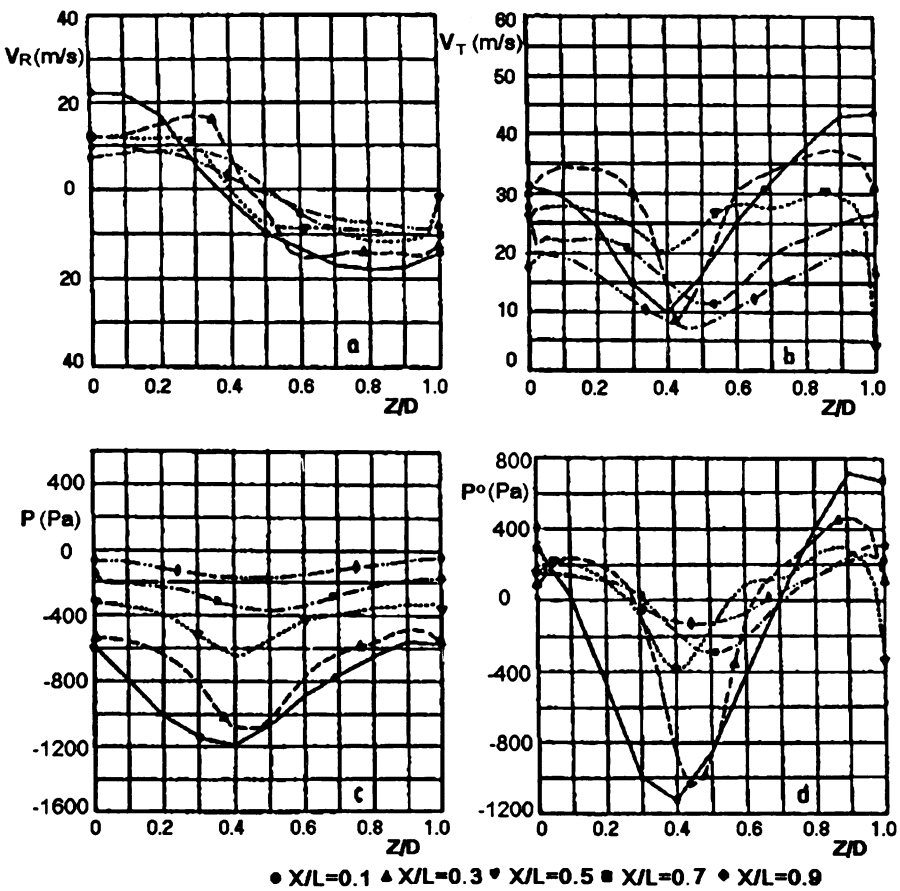

Figure 2.19 Measured velocity and pressure for small mass flow (after Van den Braembussche, 1990)

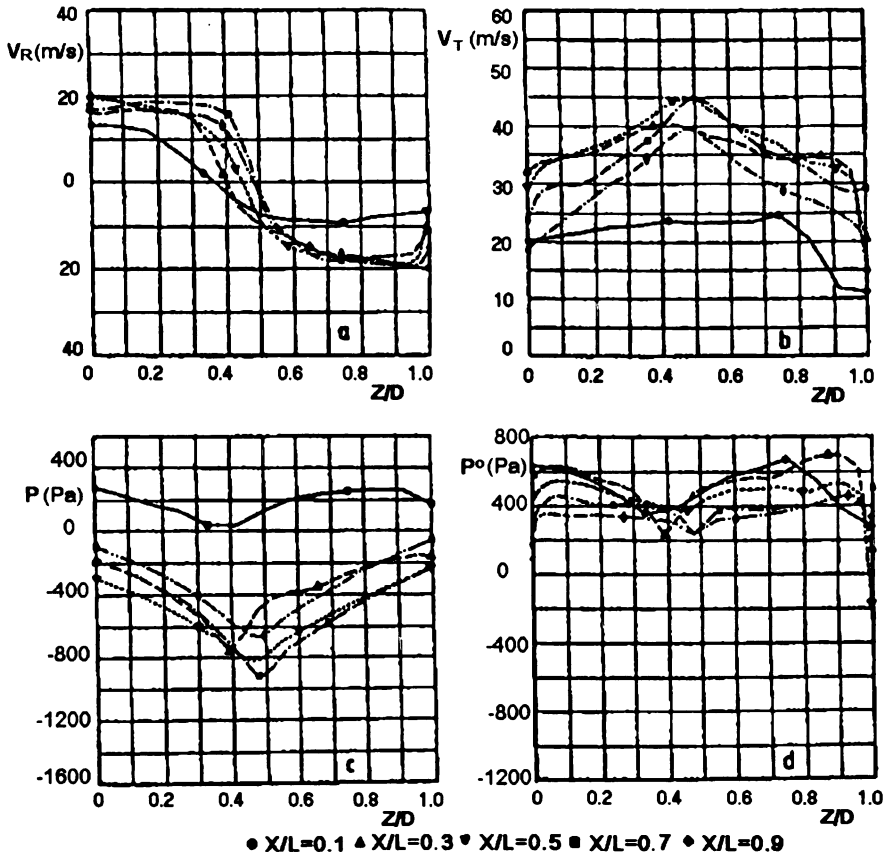

Figure 2.20 Measured velocity and pressure for optimum mass flow (after Van den Braembussche, 1990)

Figure

Figure 2.22

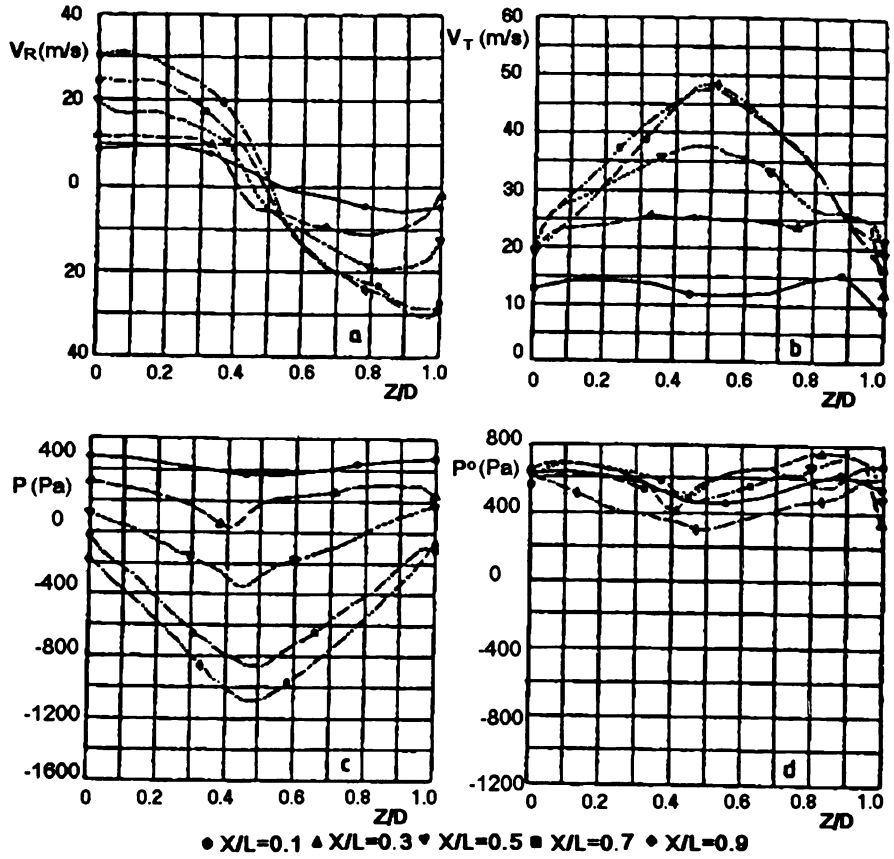

Figure 2.21 Mesured velocity and pressure for large mass flow (after Van den Braembussche, 1990)

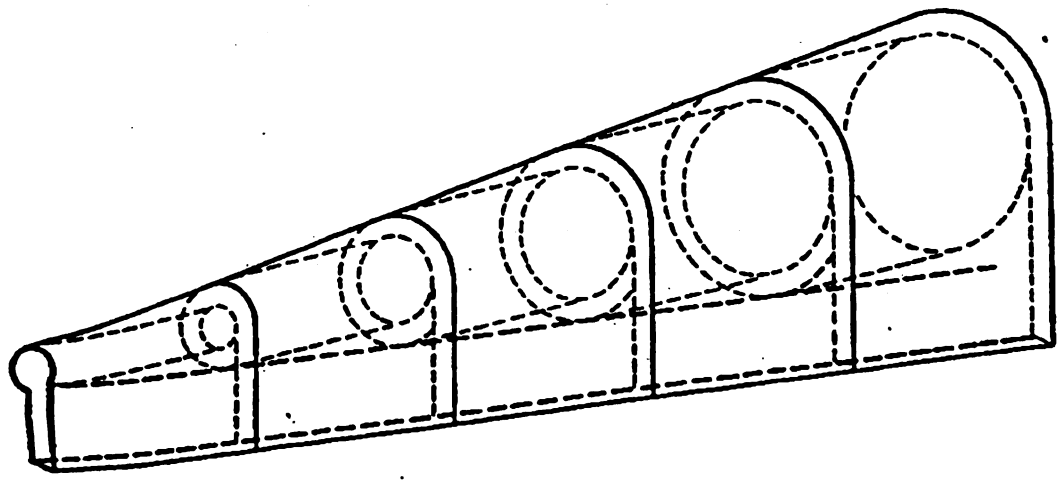

Figure 2.22 Superposition of vortex tubes in a volute (after Van den Braembussche, 1990)

Based on the observations, Van den Braembussche and Hande (1990) proposed a volute flow model (figure 2.22). The fluid entering close to the tongue at small radius fills the center of the volute. New incoming fluid downstream at a larger radius starts rotating around the upstream fluid. Vortex tubes of increasing radius are wrapped around the other and the each part of the fluid remains at constant radius. This structure is very different from the flow in a classical vortex tube (Escudier, 1979) where the fluid enters at constant outer radius and migrates from the outer radius to the center resulting in an increase of swirl velocity due to the conservation of angular momentum. Vortex tubes therefore have a free vortex circulation near the walls and forced vortex in the center.

Ayder (1993) measured the swirling flow in a centrifugal compressor volute with elliptical cross section at seven circumferential locations. The result (figure 2.23 – 2.24) is in agreement with the model of Van den Braembussche and Hande (1990). The contribution of this work is that the distorted circumferential total pressure distribution at the inlet of the diffuser changed the total pressure distribution inside the volute passage. The total pressure distribution is no longer a consequence of the swirl shear losses but results also from the way the volute is filled with fluid.

Hagelstein *et al.* (1999) presented an experimental and numerical investigation of the flow in a centrifugal compressor volute with rectangular cross section at seven circumferential locations. The flow field measurement at higher mass flow is presented in figure 2.25. The strong vortex flow pattern is clearly shown and its center coincides with the center of the cross-section. The rotational velocity of this vortex flow increases from near zero at the center to a higher value radially out. From the center to some radial distance the gradient is high, and thereafter it is moderate. In contrast to this, Ayder

(1993) observed a more or less linear distribution of the swirl velocity in a volute with elliptical cross section. In the case of a rectangular cross-section, the secondary corner flows, even though not measurable by the probe, are suspected to affect the flow mixing process in the volute.

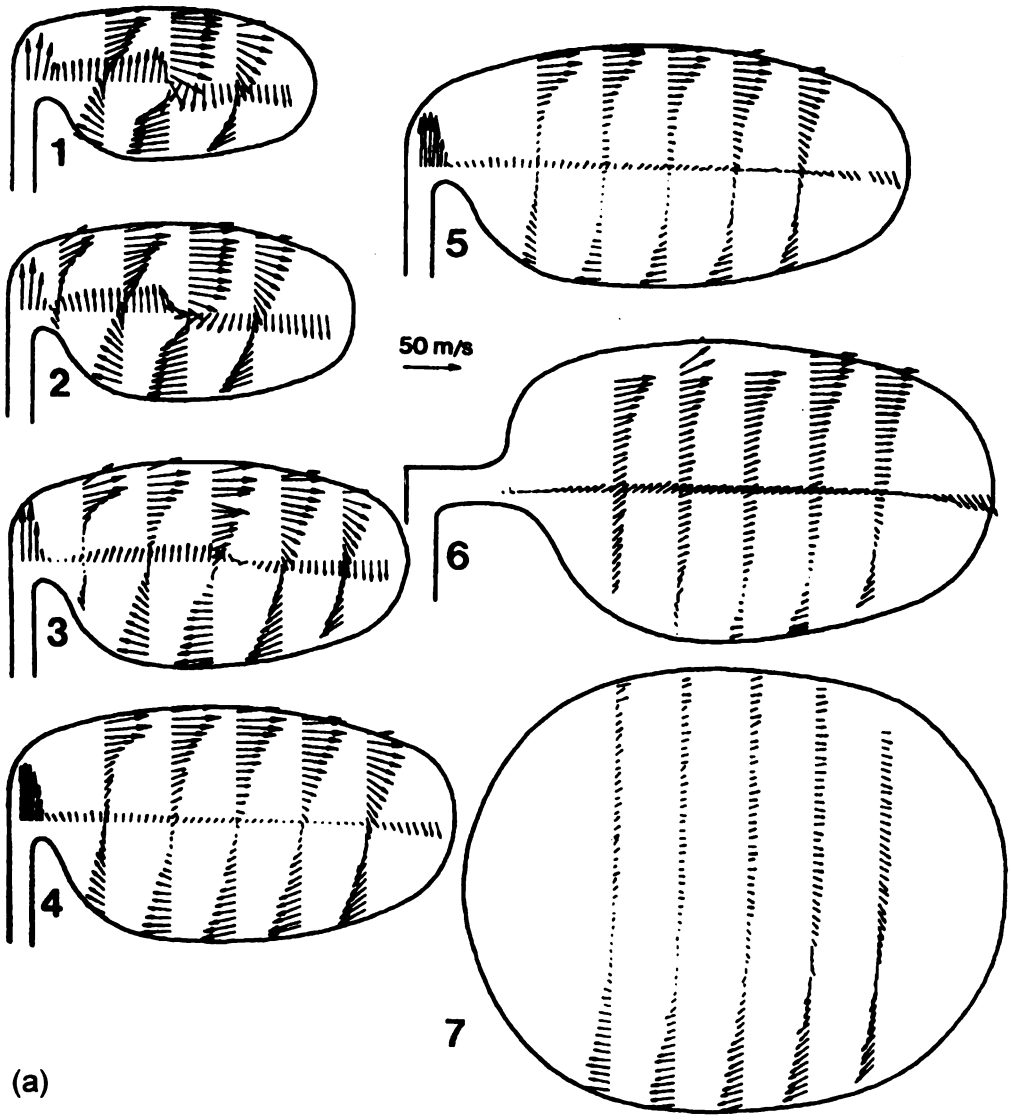

Figure 2.23 Swirl velocity (a) and total pressure (b) distribution at medium mass flow(after Ayder *et al.*, 1993)

Figure 2

(b)

Figure 2.23 (cont'd)

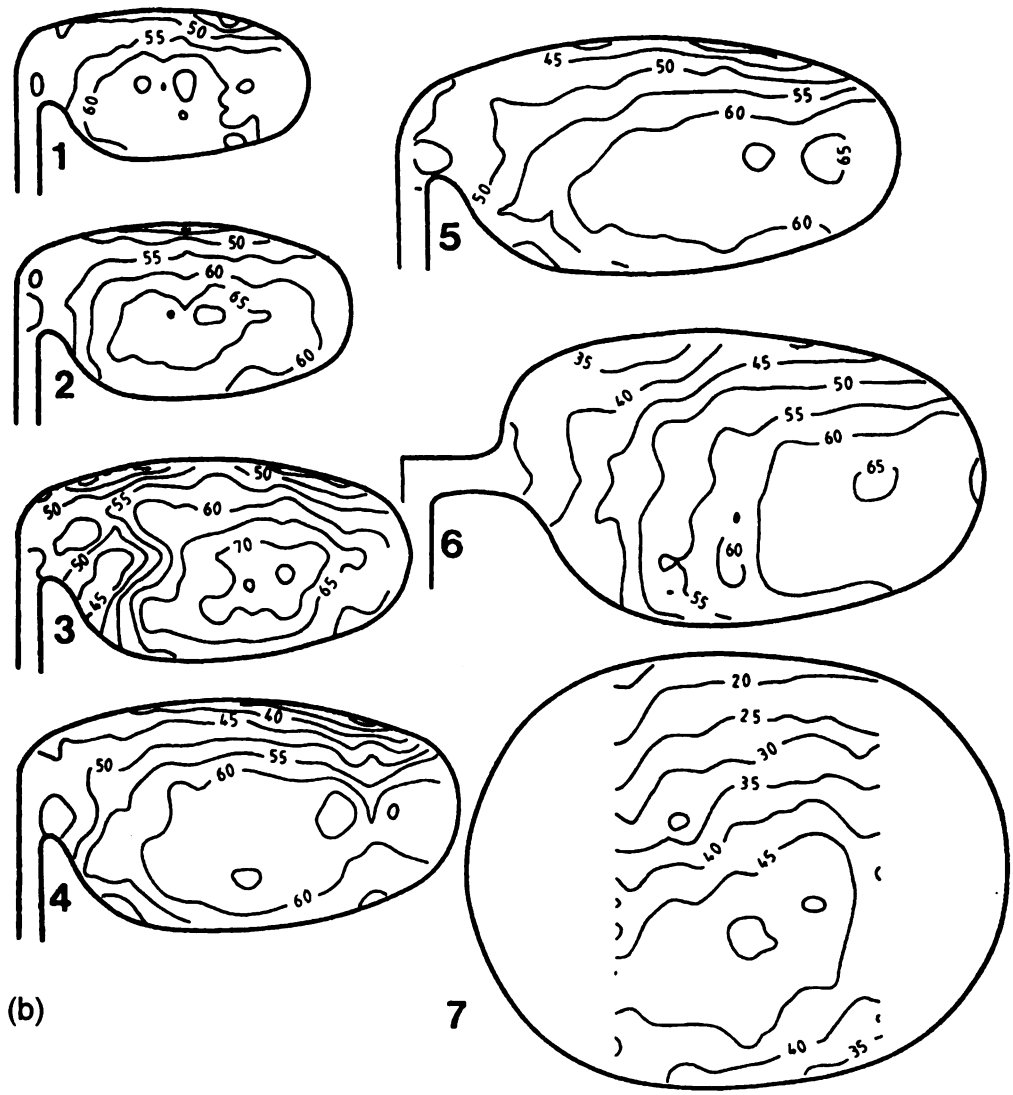

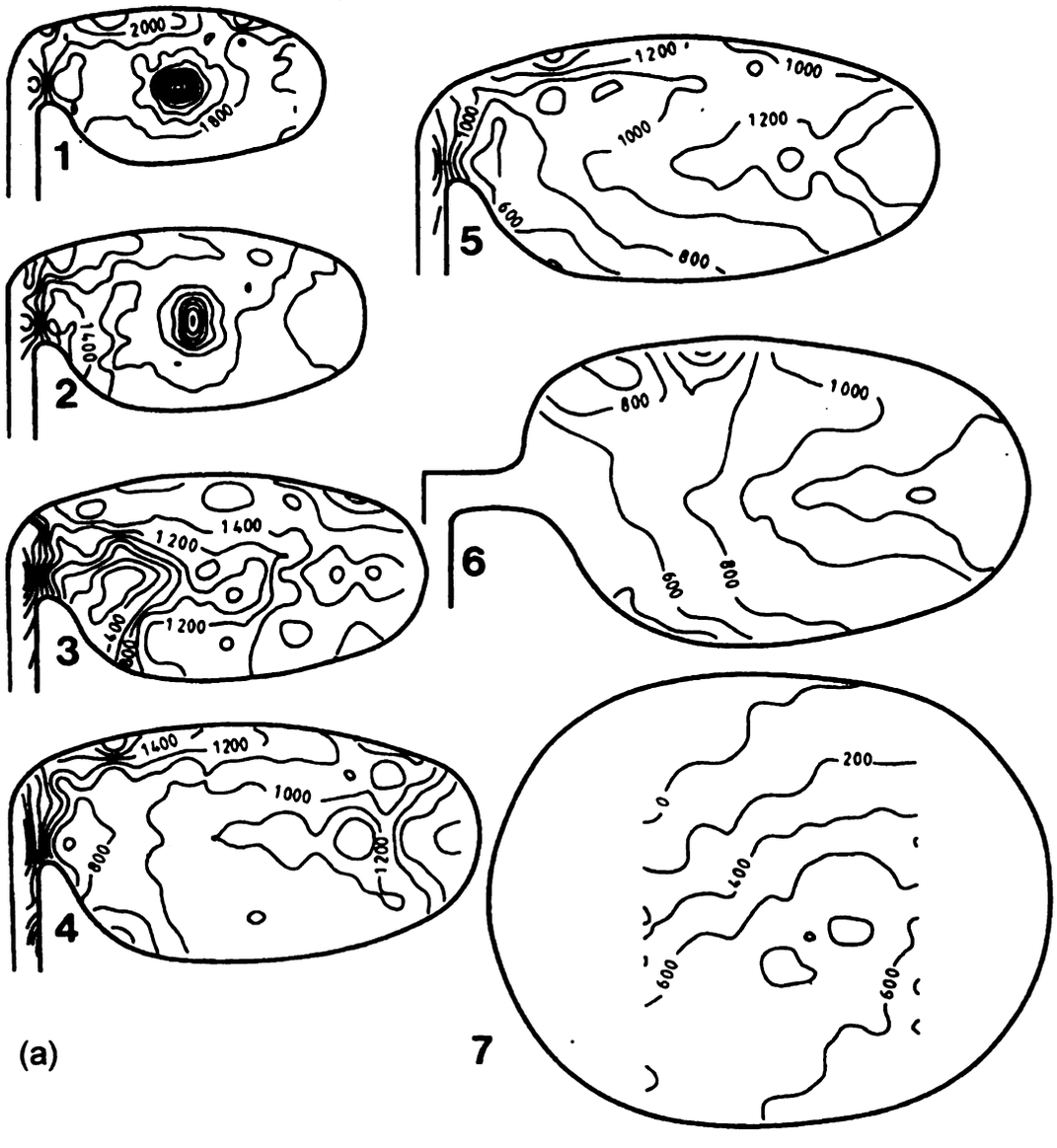

Figure 2.24 Through flow velocity (a) and static pressure (b) distribution at medium mass flow(after Ayder *et al.*, 1993)

Figure 2.24 (cont'd)

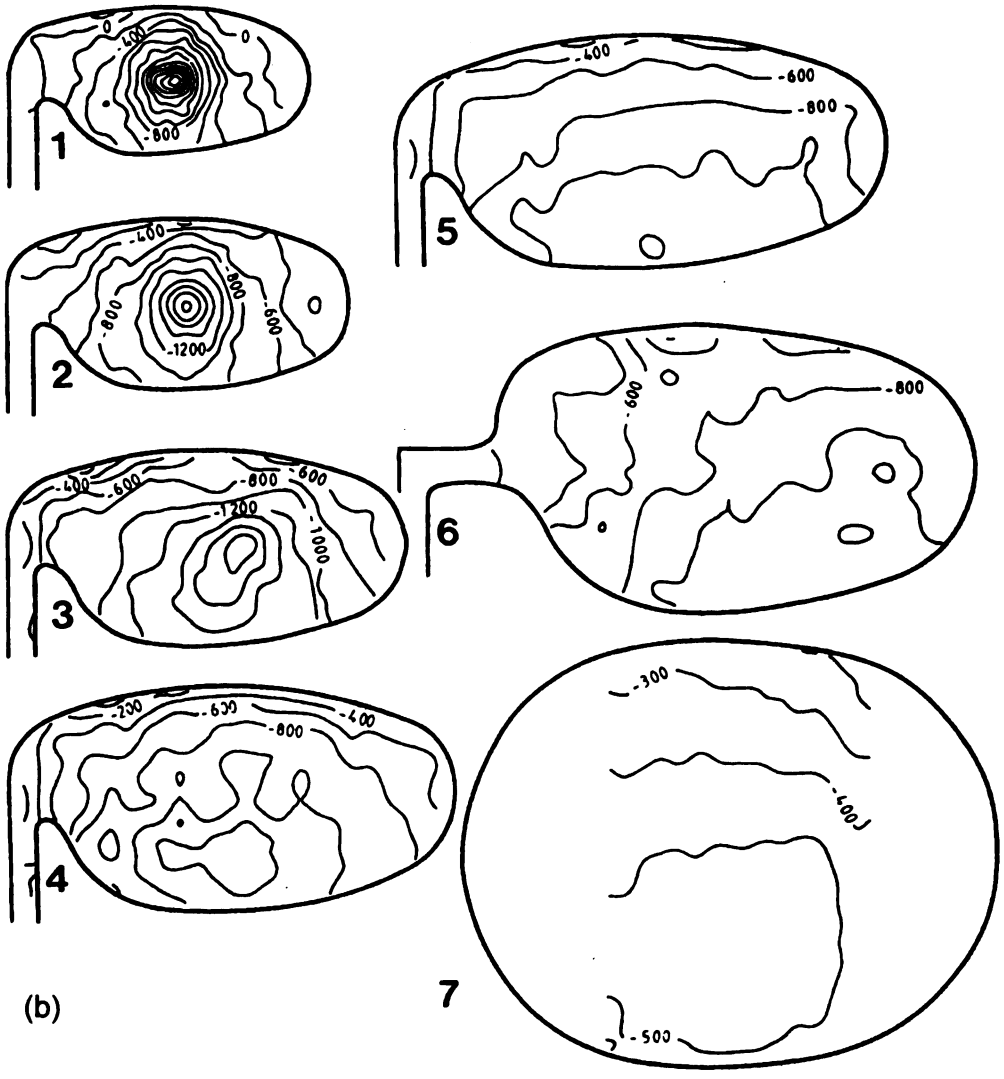

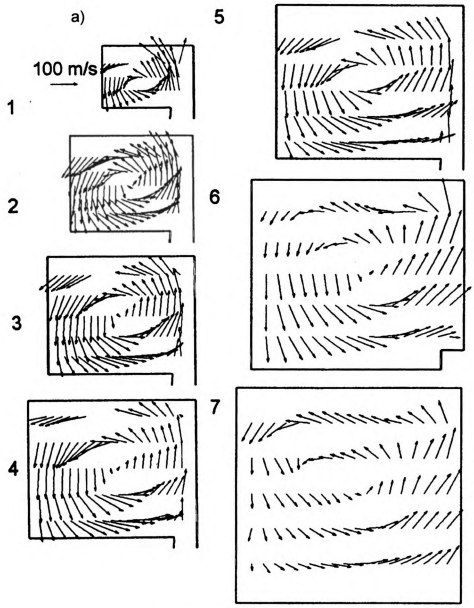

(a) Swirl velocity

Figure 2.25 Results of flow field measurements in planes 1 to 7 (m/m_{des}=1.35, Mu_2=0.86) (after Hagelstein *et al.*, 1999)

Figure 2.2

Figure 2.25 (cont'd)

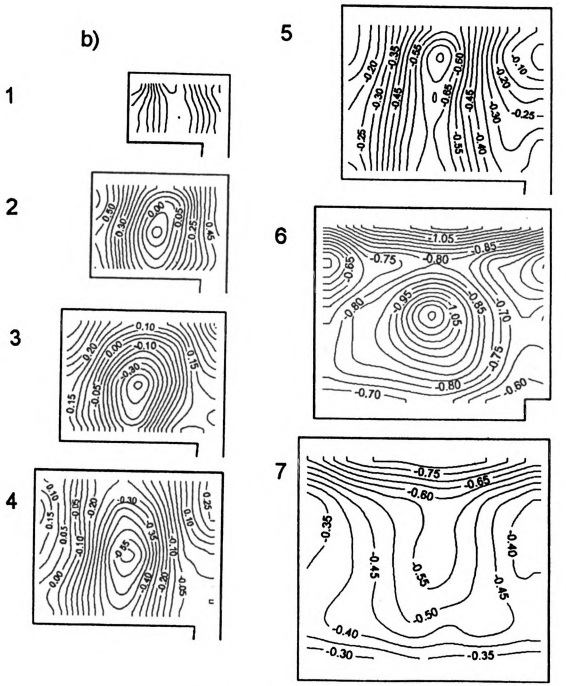

(b) Pressure recovery coefficient Cp

Figure

1

2

3

4

Figure 2.25 (cont'd)

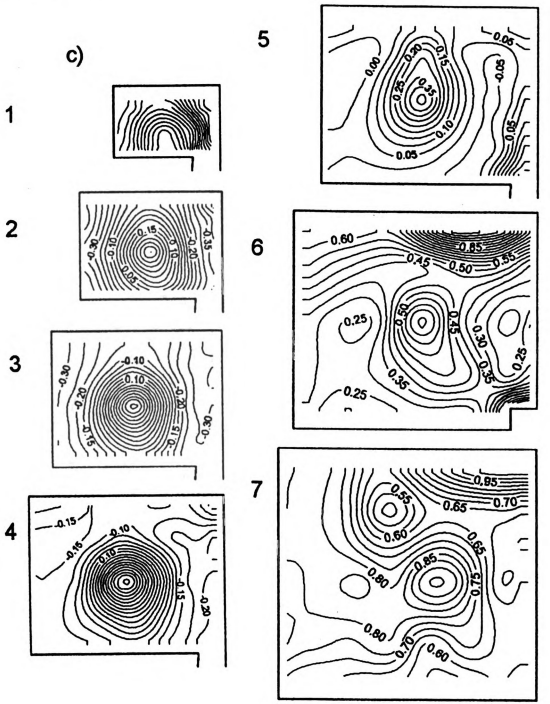

(c) Total pressure loss coefficient

Figure 2.25 (cont'd)

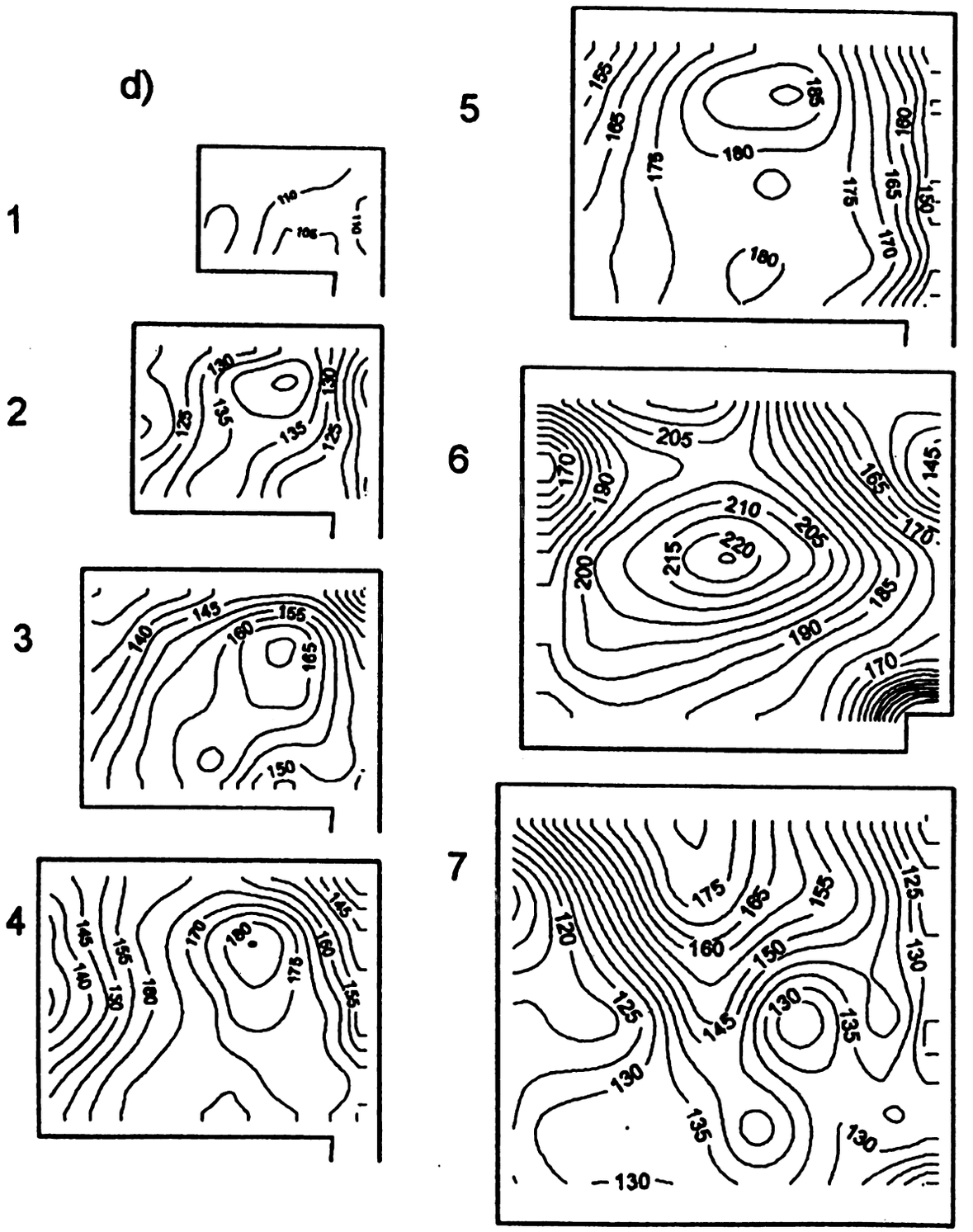

(d) Through flow velocity V_t

2.6 Studies in Radial Turbine Volutes

The study of turbine volutes is behind one of compressors due to the fact that the flow is accelerated in the machine, thus separation seldom happens. However, the importance of the turbine volute is highlighted by its effect on the overall performance of the machine. The flow Mach number varies from 0.3 to 0.7, even higher, resulting in the flow inside radial turbine volutes being no longer incompressible, which makes the turbine volute design much more complicated. In the literature, inconsistency can often be found. Therefore, this session will investigate the one-dimensional design and performance prediction methods, and then some three-dimensional flow field studies will be reviewed.

2.6.1 Preliminary Design

In many applications a volute, often vaneless, is employed to deliver the working fluid to the turbine rotor periphery. The basic design requirements for the vaneless volute are that it should:

- Accelerate the working fluid to the leading edge of the rotor and generate the desired rotor inlet conditions in terms of the magnitude and direction of the absolute velocity vector;
- Distribute the working fluid uniformly around the rotor periphery;
- Achieve these requirements as efficiently as possible, that is, with a minimum loss in stagnation pressure.

The preliminary design of the volute is usually based on the assumptions of an adiabatic incompressible flow, together with a free vortex distribution about the rotor.

This design method is well documented in literature, e.g., Hawthorne (1964), Wislicenus (1965), Brown (1947) and Watson (1993). The passage design is often specified in the form of the variation, with azimuth angle, of cross-section area, casing width or ratio of area to radius *A/r*. The incompressible design method gives the ratio of area to radius inversely proportional to the inflow angle, and linear distribution over the periphery. There are two factors that make the discharge flow no longer uniform and free-vortex.

The volute tongue is the main factor distorting the discharge flow of the volute. The desired rotor inlet condition is one of a uniform distribution of angular momentum about the rotor periphery, while the volute inlet conditions at the tongue are those of a fully developed turbulent pipe flow with a radial variation of angular momentum. In order to make these inlet conditions compatible with the desired volute discharge conditions, Chapple *et al.* (1980) suggested that the volute inlet duct should have a bend that extended up to 85-120 degrees about the rotor axis. Hussian and Bhinder (1982) studied the flow in a constant area square duct and concluded that if the angle subtended by the bend about the rotor axis is too small then the desired vortex will not be developed fully. On the other hand, they observed that as the angle subtended by the bend was increased, then tangential velocity at the inner radius began to decrease and eventually became smaller than that at larger radii. They concluded that for a constant area square duct the optimum subtended angle for the bend was 23°.

The other factor causing the exit flow distortion is the variation of the passage area. The experimental investigation of Whitfield (1990) and MacGregor *et al.* (1994) showed that the free vortex distribution was not maintained over all the full 360° of azimuth angle. In particular, over the latter part of the flow path (azimuth angles greater

than 270°) where the passage is relatively narrow and friction loss is predominated, the fluid is guided by the outer wall of the volute, or the inside wall of the tongue, and the solidity presented by the rotor.

Because flow is accelerated in the volute passage, the compressibility should be taken into account. Chapple *et al.* (1980) proposed a compressible design method, and the exit flow uniformness is restricted by the inlet flow. If the inlet flow can follow free vortex pattern, the exit flow can be rather uniform. Whitfield *et al.* (1994) proposed a design method to take into account the angular momentum losses and flow distortion up and down stream of the tongue. However, too many assumptions made the method inconsistent. The authors introduced an exponent m ($C_\theta r^m = constant$) to force the one-dimensional design and prediction method to agree with the free vortex pattern, however, the authors did not mention how the volute was designed. It is not certain whether the deflection of flow from free vortex pattern is caused by the loss of angular momentum or by the design. Therefore, it can be concluded that these has not been a one-dimensional design method to obtain uniform and free-vortex discharge flow up to now.

2.6.2 Three Dimensional Flow in Turbine Volute

Studies of the flow structure in the volute passage have been limited. A few experimental investigations were made on asymmetry volutes, which are different from the volute dealt with in this thesis. Therefore, they are reviewed briefly. Khalil *et al.* (1976) considered the losses in radial inflow turbines. Phenomenological models were developed to account for losses, based on experimental data. The need to reduce the non-uniformity within the volute discharge flow was identified and guide vanes were used to

direct the flow. Tabakoff *et al.* (1980, 1884) investigated the flow in the volute passage using hot wire anemometry. The measurements were taken without a rotor. There was evidence of strong secondary flows. The generation of these secondary flows is considered to be a potential area for energy losses. Poor performance may also be attributed to the poor distribution of the mass flow around the rotor. Inoue *et al.* (1987) experimentally investigated a turbine volute to investigate the effect of volute tongue and the ratio of area to radius. A strong secondary flow is observed being dominated by two large passage vortices, which causes radially inward flows of low energy fluids on the wall. As the ratio of area to radius decreases, the secondary flow is enhanced. The effect of the tongue is observed that too large tongue angle causes larger losses due to the accumulation of low energy fluids on the upper wall of the tongue. Large weak losses are observed downstream of the larger tongue. Too small tongue angle causes the increase of mixing losses between the inlet flow and the vortex flow inside the scroll. In summary, the flow in asymmetry turbine volutes is "brutal" as described by Dean (1973), cited from Japikse (1996).

The experimental investigation of symmetry volute flow is very limited; only two papers were found, (Whitfield, *et al.* 1990) and (MacGregor, *et al.* 1994). It is suspected that these two papers were done on the same experimental facility. The measurements were taken at six angular positions around the volute shown in figure 2.26. The first position for measurements was at ϕ=-21°; this represents the inlet passage to the volute. The tangential and radial velocity components are shown in figure 2.27. It is evident that a secondary flow is developed at inlet passage station. At all the stations inside the volute (figure 2.28—2.32), the tangential velocity shows axially uniform distribution, increasing

towards the exit. In contrast, the radial component begins with axially almost uniform distribution, and from ϕ=-102° it developed a "U" type axial distribution. It can be explained by the stronger secondary flow on the wall as in curved pipes. It is also observed that 2-4% of turbulent energy (figure 2.33) exists all over the passage, but it does not have a significant influence on the turbine and volute performance.

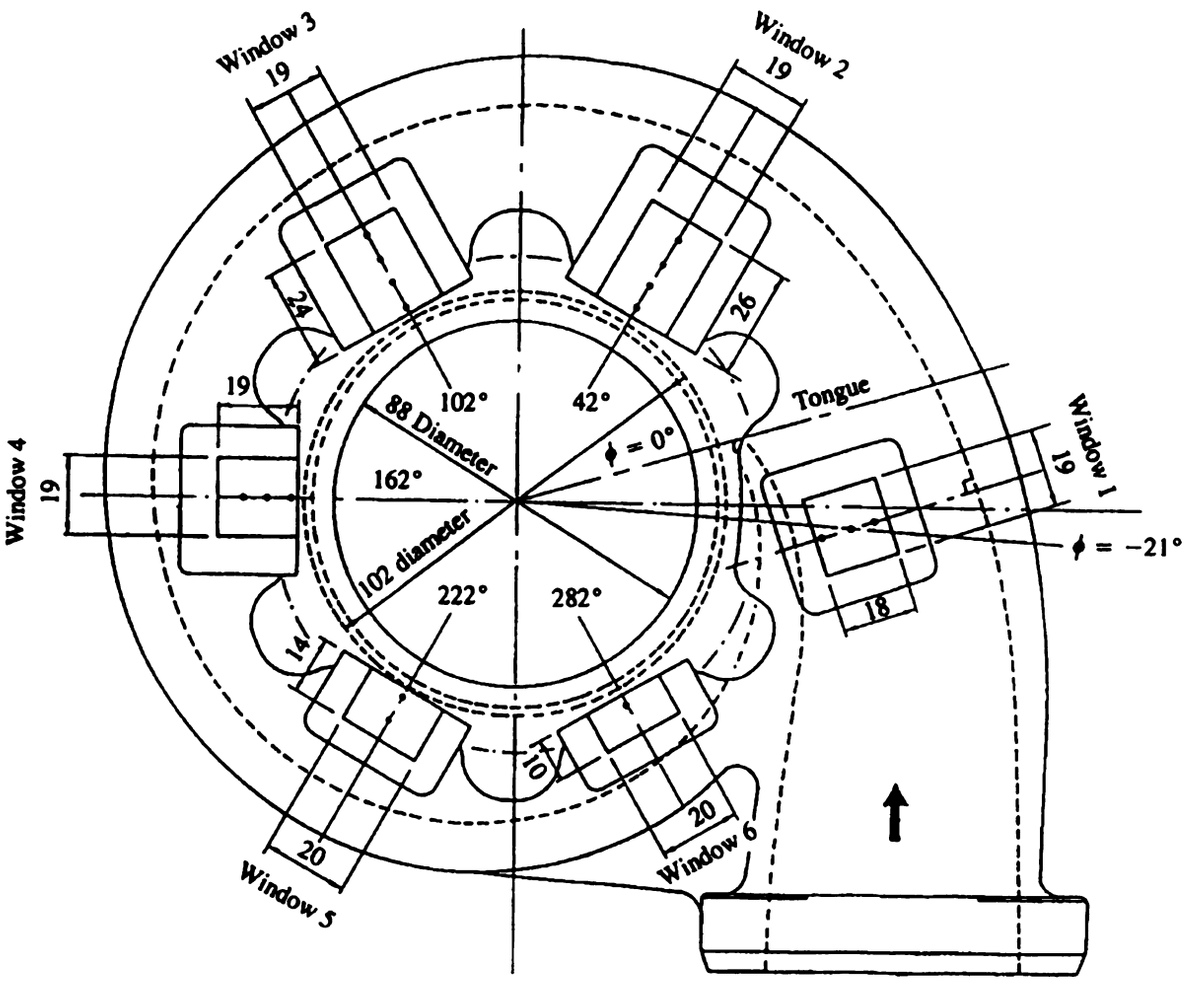

Figure 2.26 Position of measuring stations around the volute (after MacGregor, 1994)

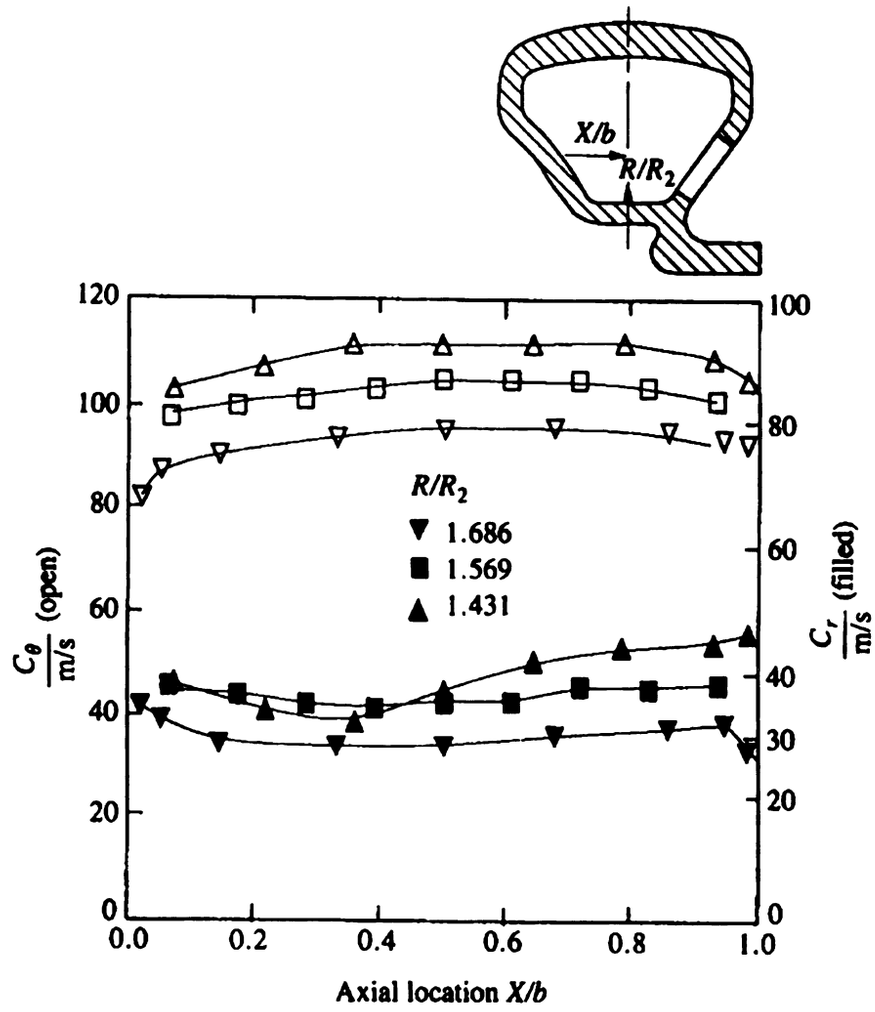

Figure 2.27 Passage velocity profile, ϕ=-21° (after MacGregor, 1994)

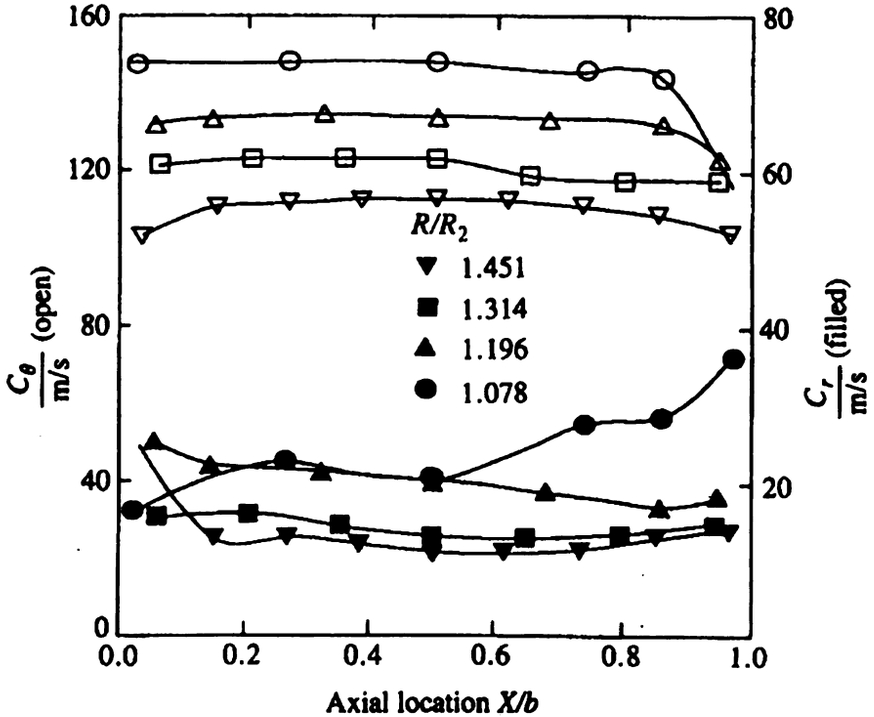

Figure 2.28 Passage velocity profile, ϕ=42° (after MacGregor, 1994)

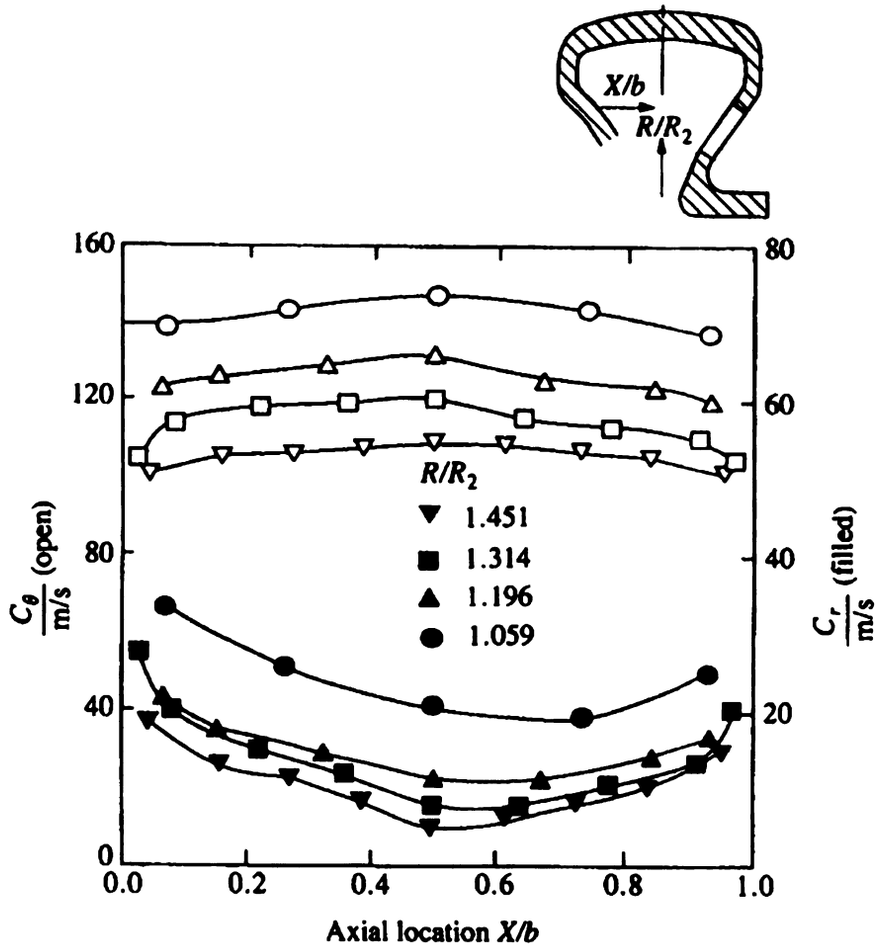

Figure 2.29 Passage velocity profile, ϕ=102° (after MacGregor, 1994)

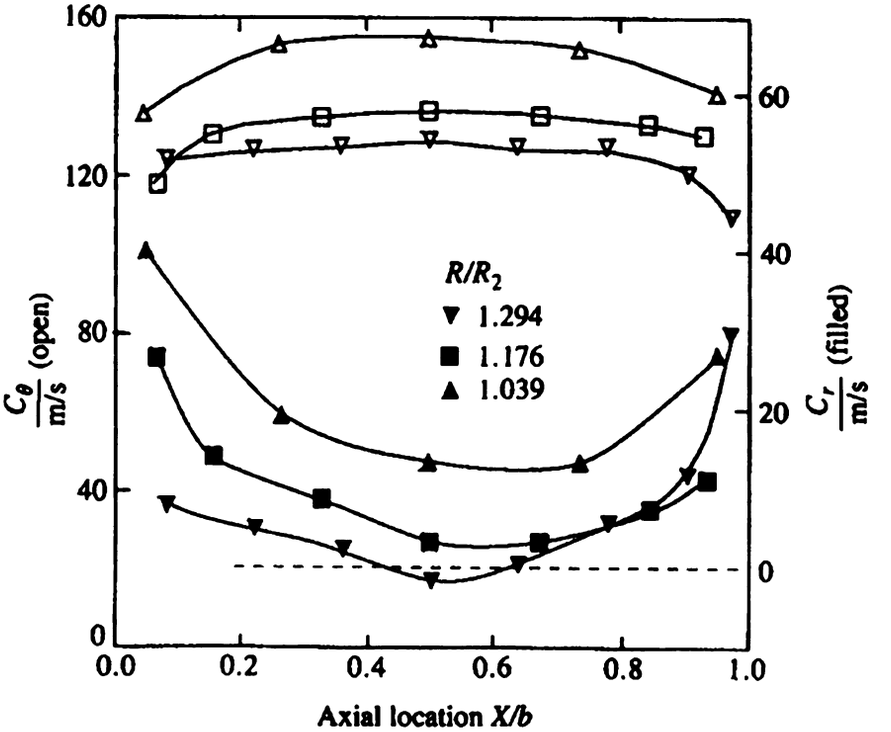

Figure 2.30 Passage velocity profile, ϕ=162° (after MacGregor, 1994)

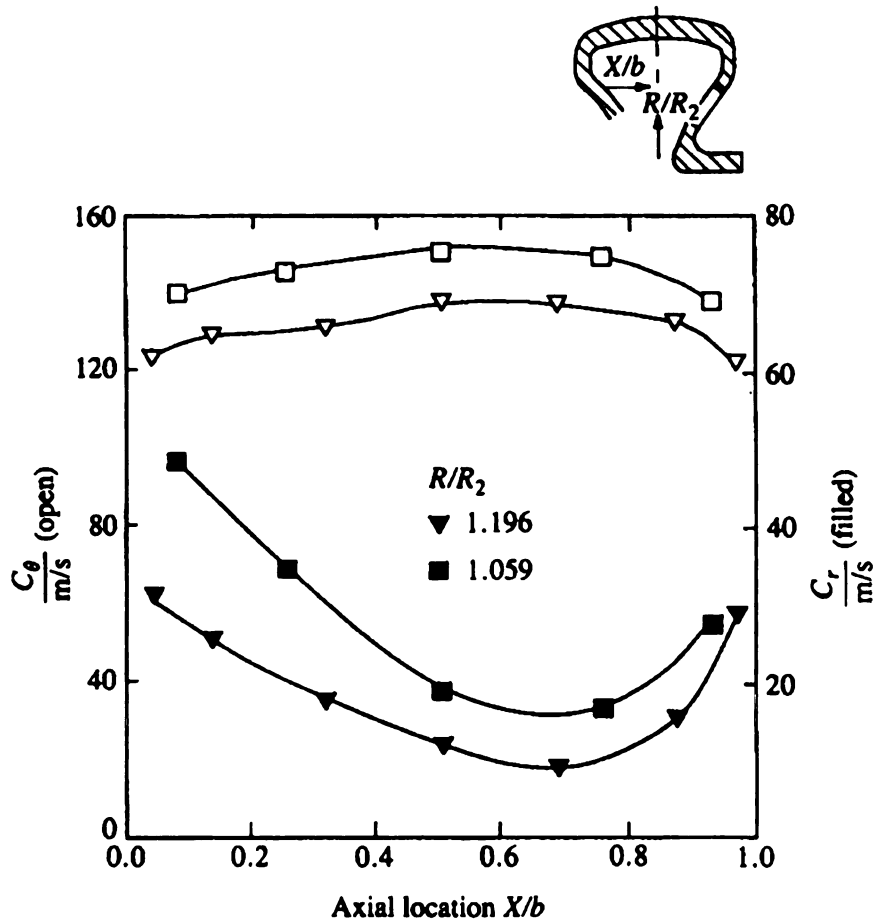

Figure 2.31 Passage velocity profile, ϕ=222° (after MacGregor, 1994)

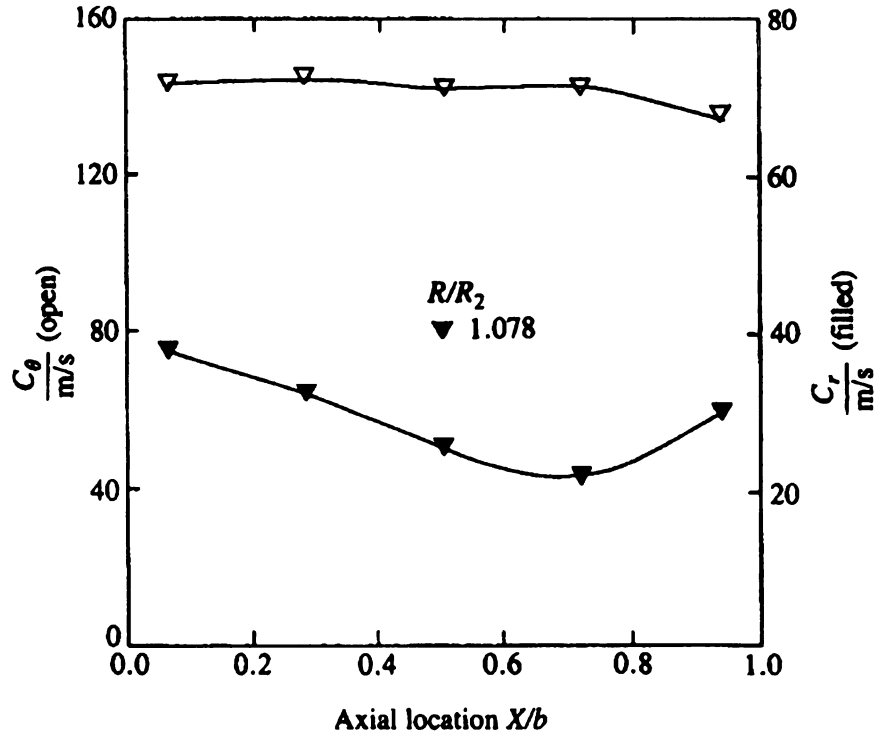

Figure 2.32 Passage velocity profile, ϕ=282° (after MacGregor, 1994)

Figure

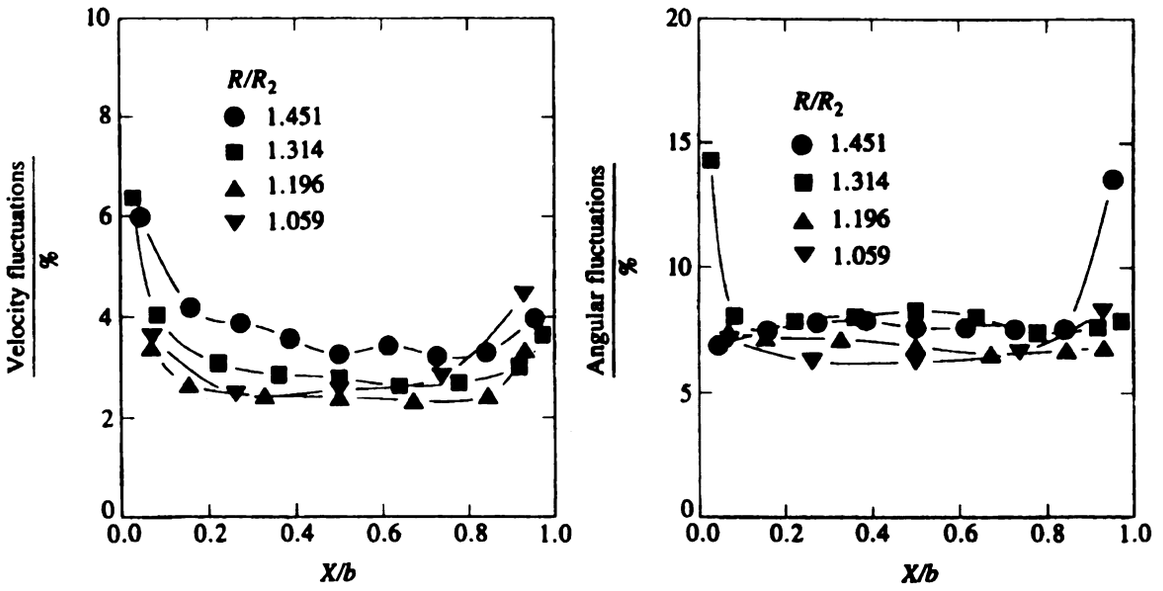

Figure 2.33 Fluctuating velocity and flow direction profiles at window 3 ϕ=102° (after MacGregor, 1994)

2.7 Conclusions

Experimental results of compressor volutes indicate that the shape and radial position of the volute channel have an important influence on the global performance of the volute. Very high global loss coefficients, as high as in collectors, have been reported for the internal type of volutes. The swirling flow has a forced vortex type of velocity distribution at the center of the rotation and a constant velocity close to the volute walls. However, more theoretical work is needed in order to explain the fine difference of the flow structure in different volutes and at different operating points.

The flow in the asymmetry turbine volute is brutal. Limited symmetry volute study shows that there is a need for volute design methods, and it can't be justified whether the deflection of volute flow from the free vortex pattern is caused by the angular momentum losses or by the design itself. The flow structure in turbine volute is depicted, but more theoretical work is needed to understand it. The circumferential variation of the radial velocity causes the non-uniform mass distribution over the volute periphery, but the reason is to be justified. The existence of the wheel causes the minimum radial velocity to move towards to the side of turbine wheel exit. This suggests that the symmetry volute can be tilted to get better match with the wheel.

Chapter 3

COMPRESSOR AND TURBINE VOLUTE DESIGN SYSTEM

3.1 Introduction

One of the most under analysed components in turbomachinery is the volute. This has been primarily due the to complex geometry, the high total cost of analysis, and uncertain gains in performance. The total analysis cost includes (1) geometry set up time (2) analysis time, and (3) time iterating on geometry and analysis until an acceptable design is achieved. As a result, the most widely practised method of designing volutes has been to use very simple, one dimensional inviscid flow (Watson *et al.*, 1993) techniques. While this is a convenient and straightforward design methodology, the flow within volutes is by no means one dimensional (Menter *et al.*, 1998) and (Sorokes *et al*, 1998) and (Whitfield *et al.*,1990). This chapter will discuss methodologies that focus on designing volutes with CFD analysis.

3.2 Design Methodologies

In general there are two different design methods for analysing turbomachinery components. One method uses a CAD system to generate geometry that is then exported to CFD analysis codes. The other method uses a self-contained program that generates the geometry and sets up the CFD parameters automatically.

CAD System Approach With current commercial CAD and CFD systems, volutes with complex geometry can be analysed. A typical CAD system approach is outline in Figure 3.1. The design process generally flows from a CAD generated solid

model that is exported via IGES or STEP to a mesh generation package. The mesh generation package can either be contained within a commercial CFD system or an independent program. Once inside the mesh generation system, the mesh spacing and topology must be defined. This work also involves fixing errors in the geometry that result from importing IGES or STEP files. Critical areas of the mesh are examined and refined before applying the boundary conditions and CFD processing commences. Upon successful convergence, the results are examined and appropriate modifications are made to the geometry and the entire process is repeated. However, this "CAD System Approach" has one major drawback; it has a high total cost of analysis. This results from the extensive time required to repeatedly iterate on geometry until an acceptable design is achieved. Typically, the time to generate a 3D solid model for CFD processing is in the order of 80 to 120 hours. This time is a function of part complexity and ease of use of the CAD system. In order to reduce the complete process time, often the aerodynamic designer must know how to use and manipulate a 3D CAD system. This can be difficult and time consuming considering the complex volute geometry. A designer fluent in 3D CAD systems may also be available, but at the expense of increased project resources for the increased interaction time between the aerodynamicist and the designer.

Design System Approach In the Design System Approach, geometry generation, mesh node spacing and boundary conditions are completely defined within an independent program that does not have a dependence upon CAD, shown in Figure 3.1. The volute system described in this chapter follows the "Design System Approach", where the aerodynamic designer can readily manipulate geometry and CFD programs. Thus, the time from generating volute geometry to performing CFD can be significantly

reduced, to the order of a few minutes. The time to complete CFD analysis depends upon the processor, mesh density, and convergence criteria. Iterations in geometry can be made within minutes prior to running CFD analysis. Thus, the Design System Approach allows the user to spend more time analysing the results rather than setting up the geometry and mesh. Additionally, the reduced design time allows for quicker time to market. Once an acceptable design has been achieved, the geometry is exported to the CAD system, where a drawing suitable for part procurement is produced. In this methodology, CAD is used as the final documentation tool, not an interactive design system. While this approach may significantly reduce iteration design time, it requires the development of a geometry generator. The geometry generator development is heavily dependent upon Cartesian mathematics and convergence schemes.

Future Considerations Based on future considerations, both design methods will benefit from increased computer power by reducing analysis time. However, the CAD System Approach to generating a solid model and exporting to CFD will still follow the same process. Although slight reductions in process time will occur, it is believed that no significant process time reductions will occur without some level of process automation. The Design System Approach incorporates process automation in the system development.

Currently, the output for CAD is simply a set of surface points defining each cross section. An experienced CAD user is still required to develop the necessary 2D drawings and/or 3D model before hardware can be procured. This activity can take a significant proportion of the total development program time. It is intended to develop a macro within the CAD environment to automatically generate the 3D model of the housing for

the purposes of procurement. It is also intended to generate automatically the traditional 2D drawings which are still required in some cases.

It is now possible to perform full stage analysis with several commercial 3D flow solvers. It is intended to link the current in-house rotor design system, RotorCad (Bruce, 1998), to VoluteCad in order to enable complete stage analysis.

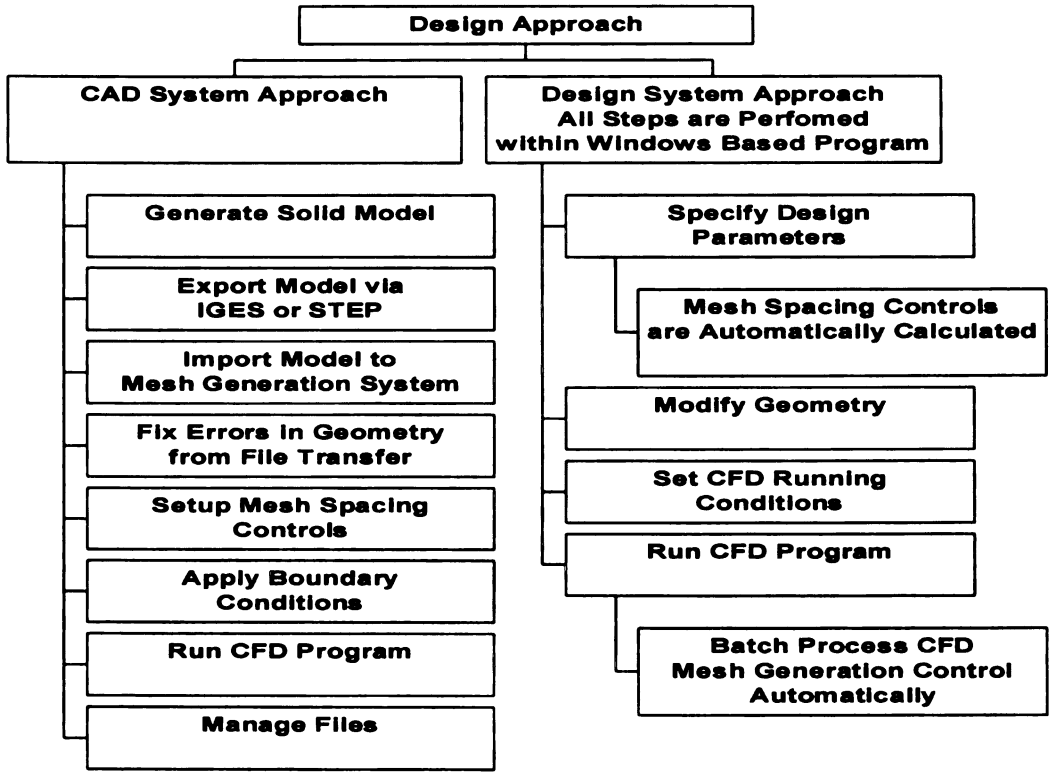

Figure 3.1: Comparison of CAD system approach and design system approach

3.3 Definitions

Figures 3.2 and 3.3 provide some background information on various stage components and volute types. The major stage components include the wheel and volute. The various volute types can be classified as circular, elliptical, rectangular, and overhung.

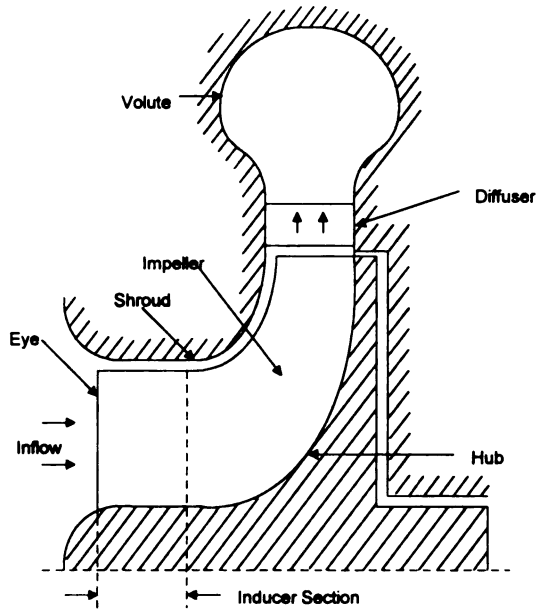

Figure 3.2 Cross section of centrifugal compressor

The geometry considered in this paper includes (1) twin-entry turbine volutes (2) single-entry turbine volutes and (3) compressor volutes. The twin-entry and single entry turbine volutes are shown in Figure 3.4. Figures 3.4 and 3.5 illustrate the design parameters including:

- Critical or Throat Area, A
- A/R Ratio
- Divider Wall Radius Ratio (divider wall radius / wheel radius)
- Tongue Radius Ratio (tongue radius / wheel radius)
- Foot Dimensions (length & height)

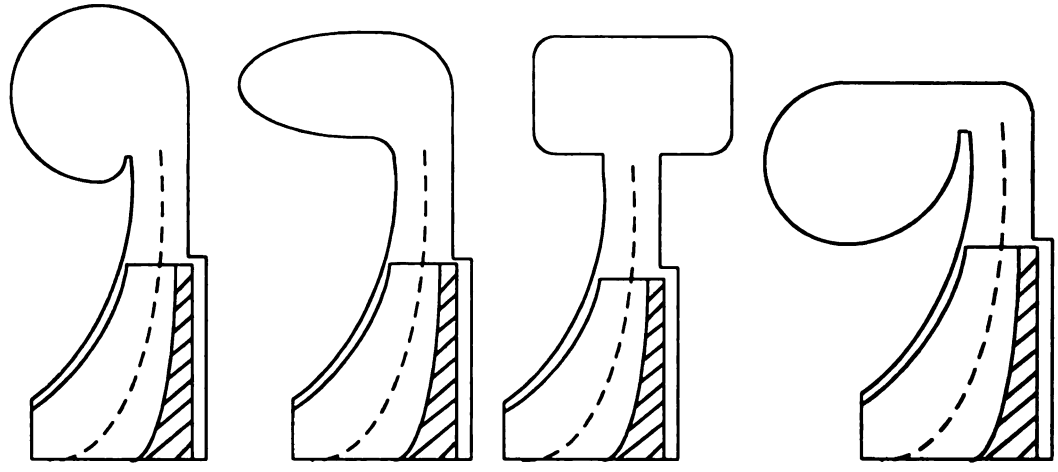

(a) Circular (b) Elliptical (c) Rectangular (d) Overhang

Figure 3.3 Types of volutes

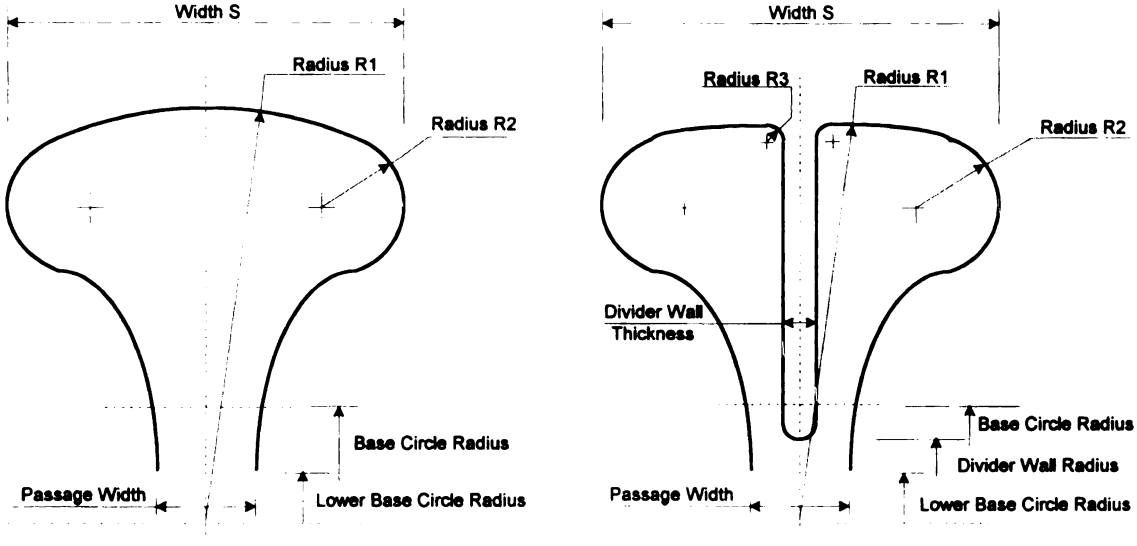

(a) Single-entry turbine volute (b) Twin-entry turbine volute

Figure 3.4 Design parameters

Compressor volutes can be developed using one of two-design types (1) constant inside diameter, CID (2) or constant centroid diameter, CC. These compressor volutes are shown in Figure 3.6. The CID volute is formulated by determining the cross-sectional shape such that the specified A/R ratio is maintained referenced to the base circle.

Similarly, the CC volute is formulated by determining the cross-sectional shape such that the centroid radius is constant for all angles.

Both turbine and compressor volutes are subjected to area and A/R distributions as functions of angle shown in Figure 3.7. Figure 3.7 shows these to be near linear, but this need not be the case.

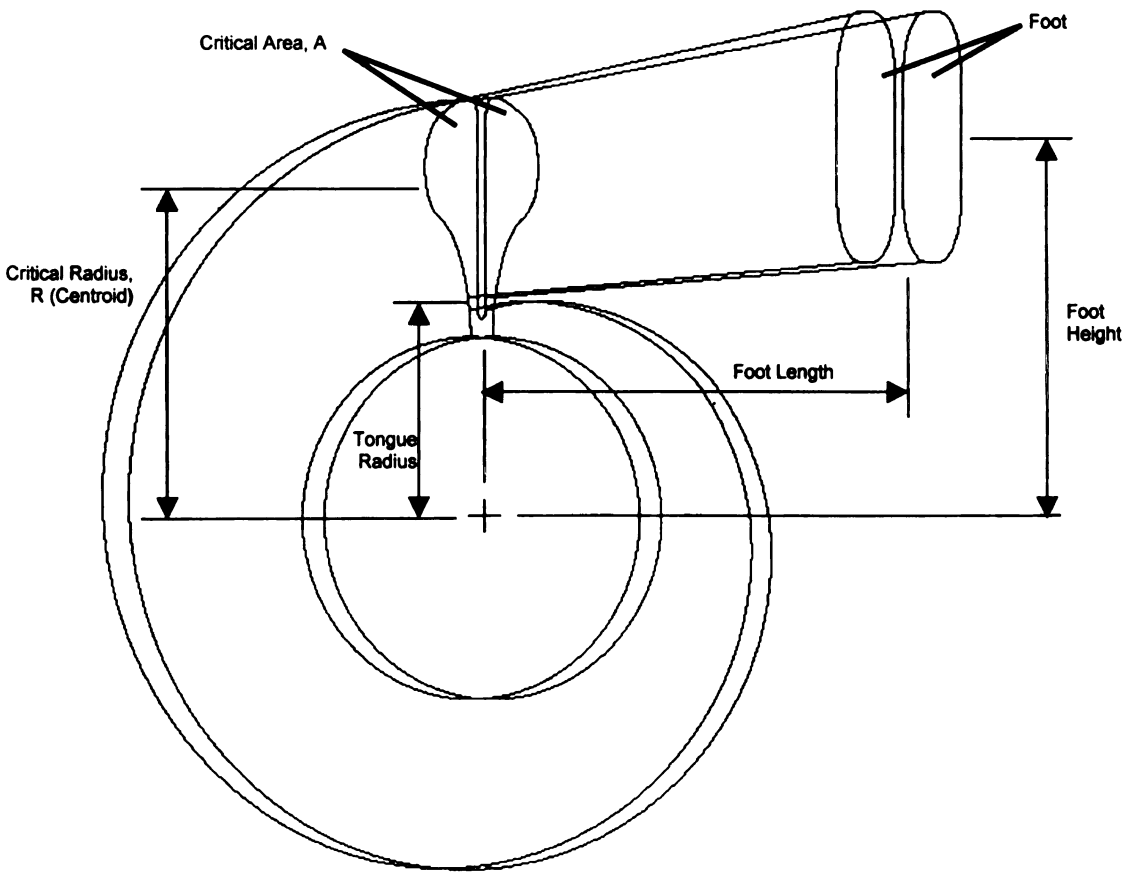

Figure 3.5 Convention of twin inflow volute

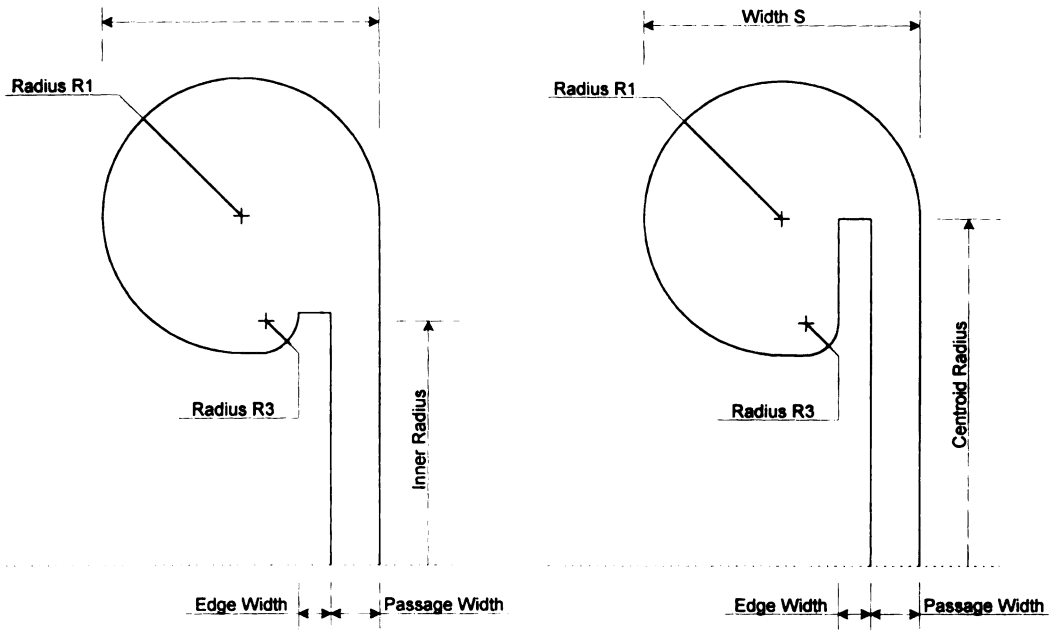

(a) Circular with constant inside diameter (b) Circular with constant centroid

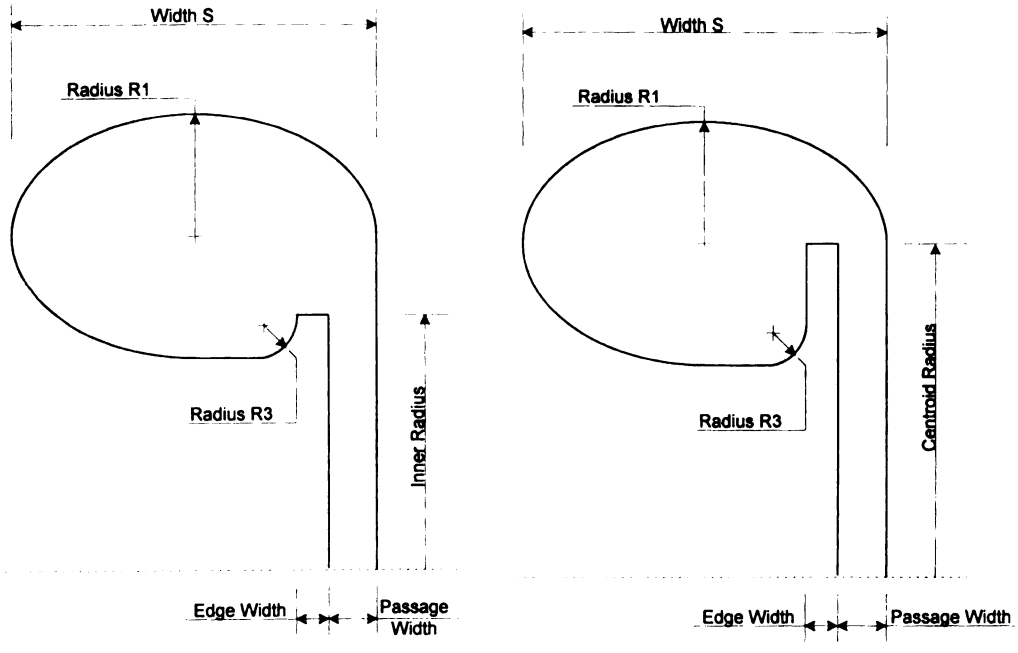

(c) Elliptical with constant inside diameter (d) Elliptical with constant centroid

Figure 3.6 Compressor volute design geometry

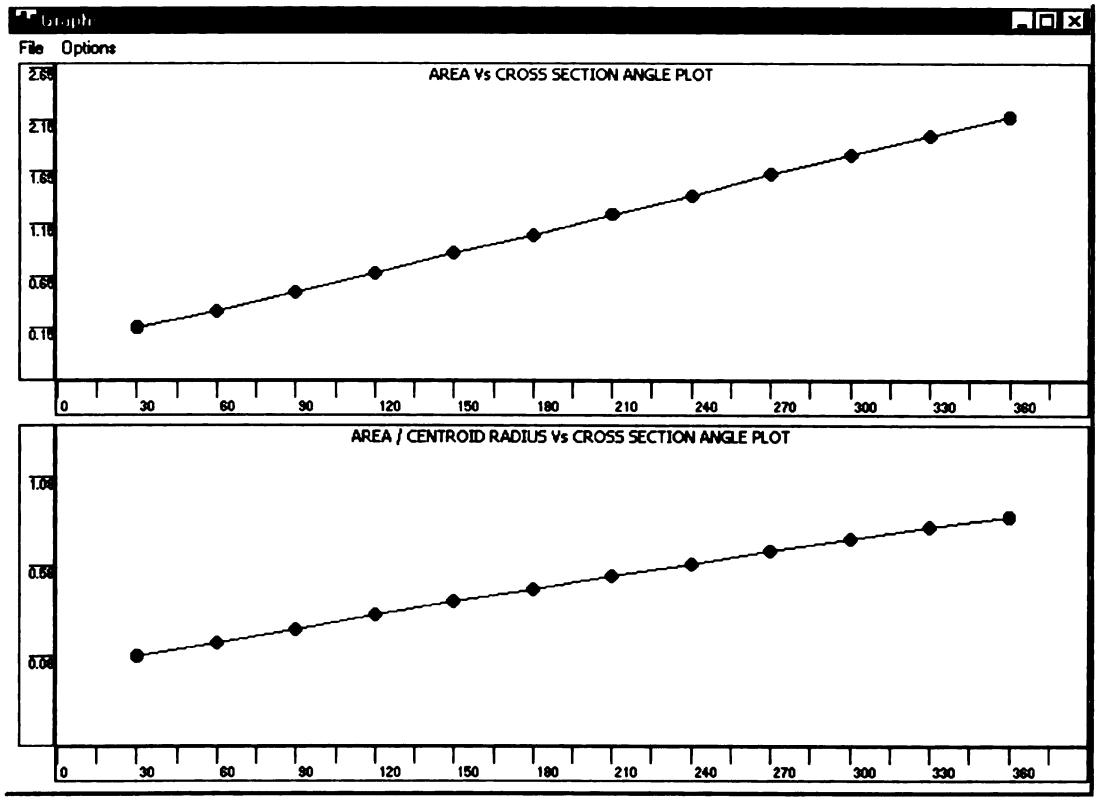

Figure 3.7 A/R and area distributions

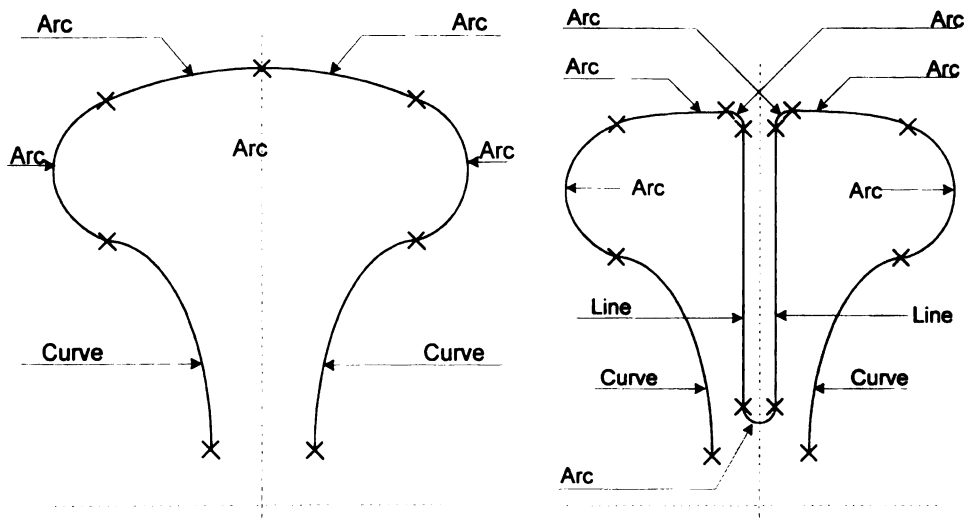

Figure 3.8 Turbine volute sections

3.4 Volute Sections

The volute cross-sectional shape can be defined by either (1) primitive drawing functions or (2) Bezier polynomials. The primitive drawing functions method is primarily used to analyse existing housings, while the Bezier polynomials are used for new designs.

Primitive Drawing Functions The primitive drawing functions include (1) lines (2) arcs (3) parabolas and (4) ellipses. These functions are used to define the cross-section geometry. Figure 3.8 & 9 shows the cross-sectional construction of each type of turbine and compressor volute respectively. The cross-sections are automatically calculated to maintain the specified area, A/R ratio, volute shape, and volute type using the primitives.

Bezier Polynomials The Bezier polynomials are used in a similar manner as the primitive drawing functions, except the shape of each section can be graphically changed. The Bezier polynomials are constrained to maintain tangency at the section end points as illustrated by Figure 3.10. The initial Bezier polynomials are automatically calculated to overlay the primitive drawing function volute representation. Thus, an existing volute can be easily changed using Bezier polynomials. An explanation of a single section Bezier polynomial formulation can be found in the appendix.

Cross-Section Distribution The cross-sections for each angle can be determined using a number of methods. First, the design cross-section shape can be scaled to the other angle locations based on an A/R distribution. The design cross-section is usually denoted at 360 degrees at the critical area. Thus, changes in the design cross-sectional shape such as height reduction are readily represented in other sections. This eliminates the need to repeat changes to each cross-section. Second, changes can occur

only at the specific cross-section and are blended to the adjoining cross-sections. Third, changes can occur for a range of cross-sections. The single section and multiple section changes are useful when the volute must be designed around permanent objects.

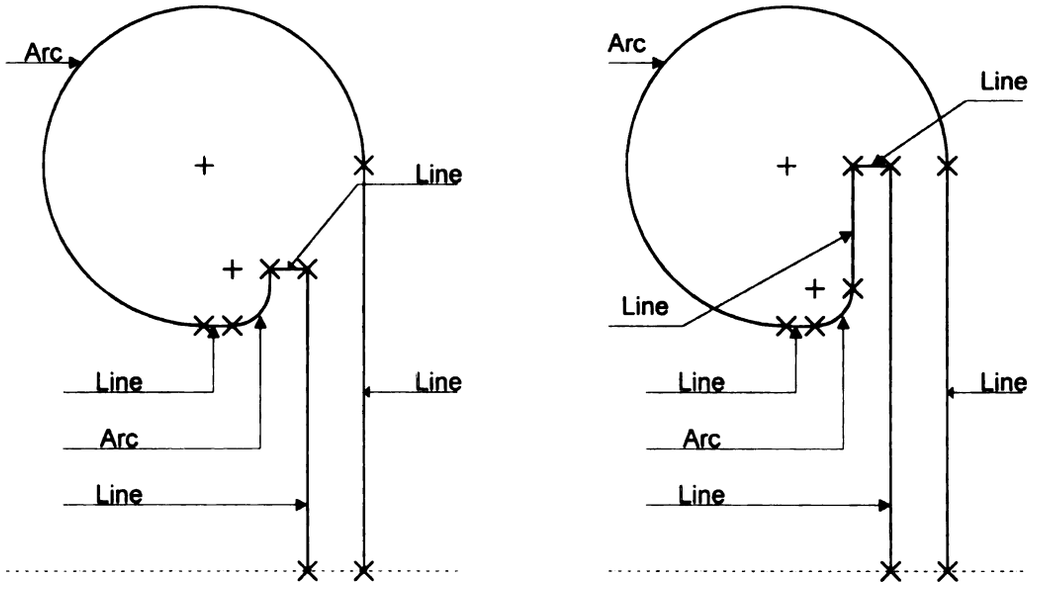

(a) Circular with constant inside diameter (b) Circular with constant centroid

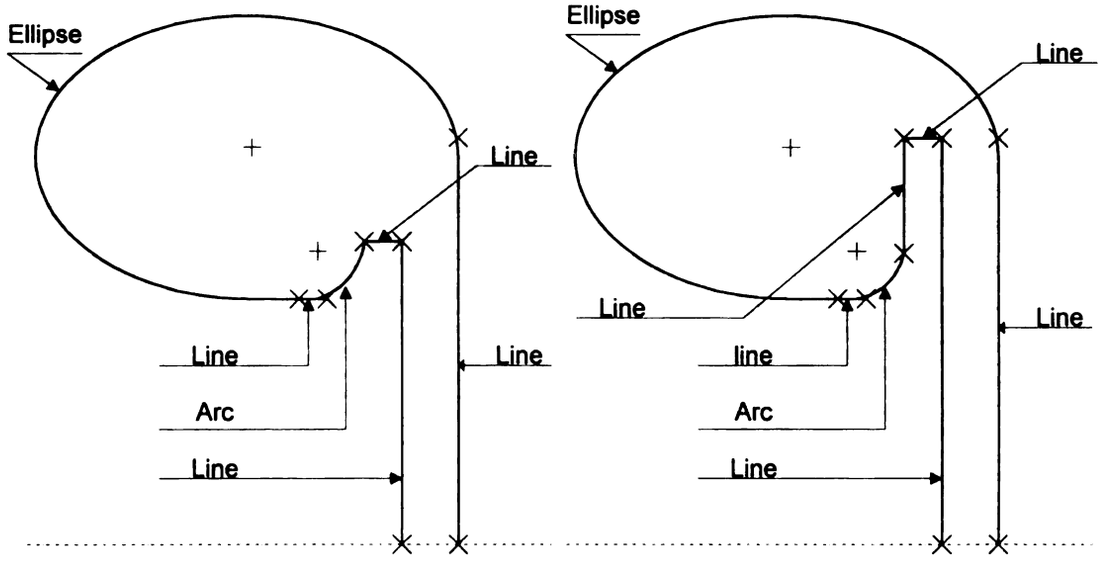

(c) Elliptical with constant inside diameter (d) Elliptical with constant centroid

Figure 3.9 Compressor volute sections

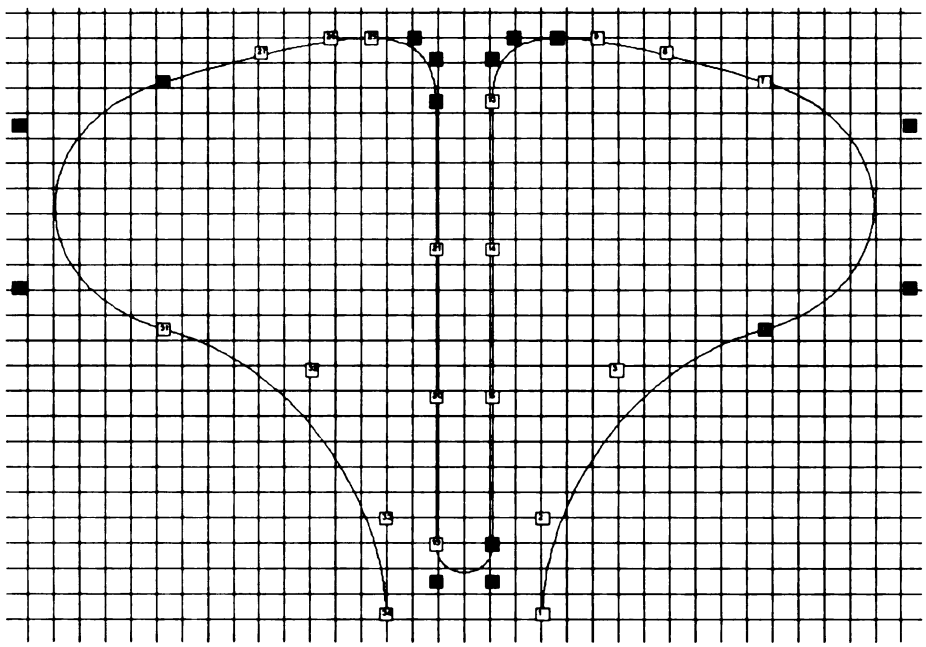

Figure 3.10 Bezier polynomial defined twin-entry volute

3.5 Viewing

There are several tools available during the geometry definition process to assist in the development of a satisfactory geometry:

- Overlay all cross sections in a 2D plane in order to visualise the change in cross-sectional shape around the volute. See Figure 3.11.
- Generate a 3D view of the entire volute. This view, as shown in Figure 3.12, can be rotated interactively so the user can determine whether the geometry is satisfactory.
- If a more detailed examination of the geometry is required, data files can be generated for a 3rd party 3D CFD post-processing package.

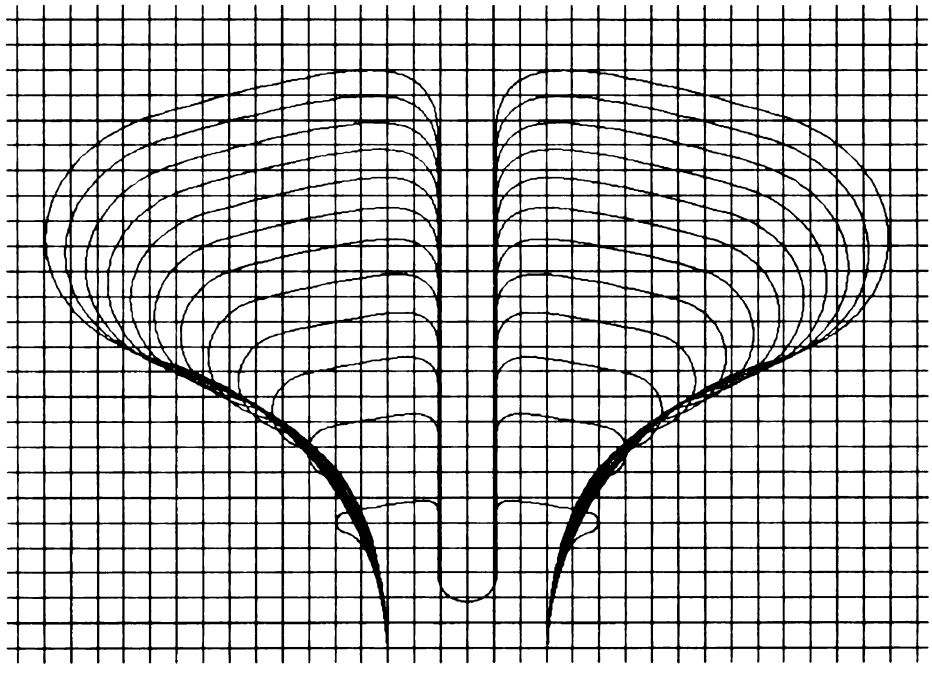

Figure 3.11 Overlay of 2D cross-sections for a twin-entry turbine volute

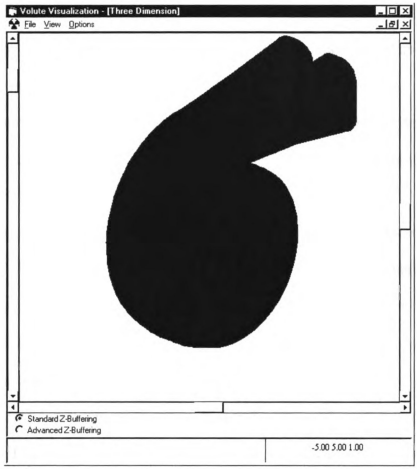

Figure 3.12 3D view of twin-entry volute core

3.6 Project management

The program organises each volute design into a project that manages all geometric iterations. The project file automatically maintains a sequential file naming system for storing all input and output data. This automatic file naming system frees the user from the mundane tasks associated with conventional Windows® based file saving dialogues.

3.7 Interface with CFD

One of the key elements to this "Design system approach" is the ability to move quickly from geometry specification to CFD analysis. Up to this point, the geometry generation process is completely independent of the CFD solver. The solver selected to perform the CFD analysis was CFX-TASCflow by AEA Technology. The mesh generator TASCgrid, is also a product of AEA Technology. The aim was to automate the grid generation process and the problem definition (i.e. boundary conditions and initial guess of the solution) as much as possible. This has been successfully achieved. The grid generation process is completely automatic and is controlled by a small set of parameters to specify the grid sizes of the various blocks. These values have default values but can be modified and saved if necessary.

A simple input screen shown in Figure 3.13 is used to define the boundary conditions and these conditions are also used as the basis for the initial guess. Once the boundary conditions have been specified, the necessary input files for the CFX-TASCflow pre-processors are generated and the pre-processing programs run in batch mode. On completion the CFX-TASCflow solver monitor dialogue form is displayed and the user simply clicks the 'Start' button to begin the flow solver. This entire process from completion of the geometry specification to the starting of the flow solver takes less than one minute.

Figure 3.14 shows a typical mesh for a compressor cover. The mesh is a multigrid mesh consisting of 4 blocks and uses "butterfly" meshes to ensure good grid quality. The total number of nodes in this particular example of a relatively coarse mesh is 150,000.

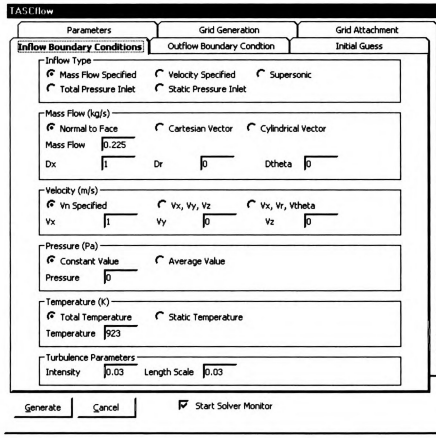

Figure 3.13 Input screen for CFD boundary conditions

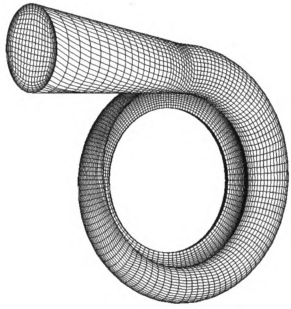

Figure 3.14 Typical compressor volute mesh with 150,000 nodes

3.8 Grid Generations

CFX-TASCflow uses structured grids. It requires grid to meet the following requirement to avoid the converging problem:

- The minimum grid angle is NOT less 20 degrees.
- The grid aspect ratio is less 100.
- Pinched meshes (figure 3.15) are acceptable, but they may cause converging problem.
- Grid attachment can be of the following types in the order of reduced preference: exact 1-to-1, many-to-1 and GGI. The first two types are of 2^{nd} order of accuracy and the GGI of 1^{st} order.

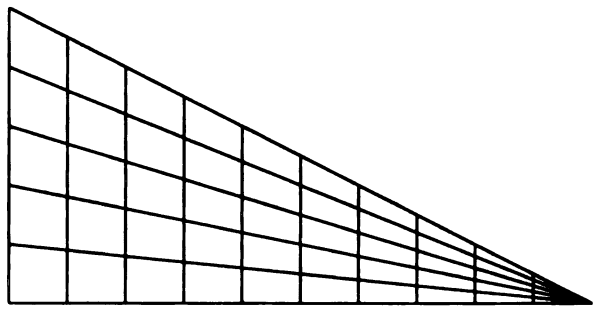

Figure 3.15 Pinched grid

The challenge for the volute grid generation is the tongue region, where the section θ=0°, section θ=360° and the beginning section of the cone overlap. Even though CFX-TASCflow provides a powerful grid attachment capability, GGI interface, careful treatments are still required to avoid the converging difficulty. The author's experience shows that the partial cell attachment as in figure 3.16a is likely to trigger converging problem, but the boundary curves of each grid are aligned as in figure 3.16b is guaranteed to lead to convergent results.

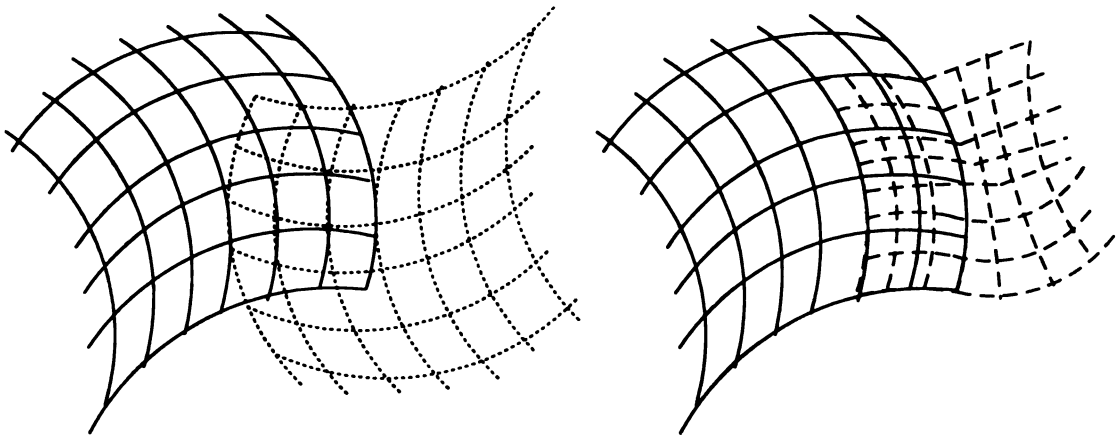

(a) Non-aligned boundaries (b) Aligned boundaries

Figure 3.16 Grid attachment

3.9 Design Examples

The program, VoluteCad, has been used in an attempt to improve the performance of a twin entry turbine housing currently in production on a 12 litre automotive diesel engine. While the detailed design of the housing cannot be published here, the housing had been designed using the traditional one-dimensional approach described earlier. The exercise was limited to modifying the A/R and Critical Area distributions of the housing to achieve a more uniform exit flow.

CFX-TASCflow was run with a uniform static pressure at the wheel inlet (the downstream boundary of the computational domain), although it is recognized that this is not an entirely satisfactory condition to impose at this position. Other possible approaches include:

- Uniform exit mass flow

- Extending the mesh further downstream to reduce the effect of the artificial constraint at the wheel inlet
- Full housing/rotor simulation

Figure 3.17 shows the predicted improvements on the distributions of velocity and flow angle at the wheel inlet. Experimental data is not available at this time.

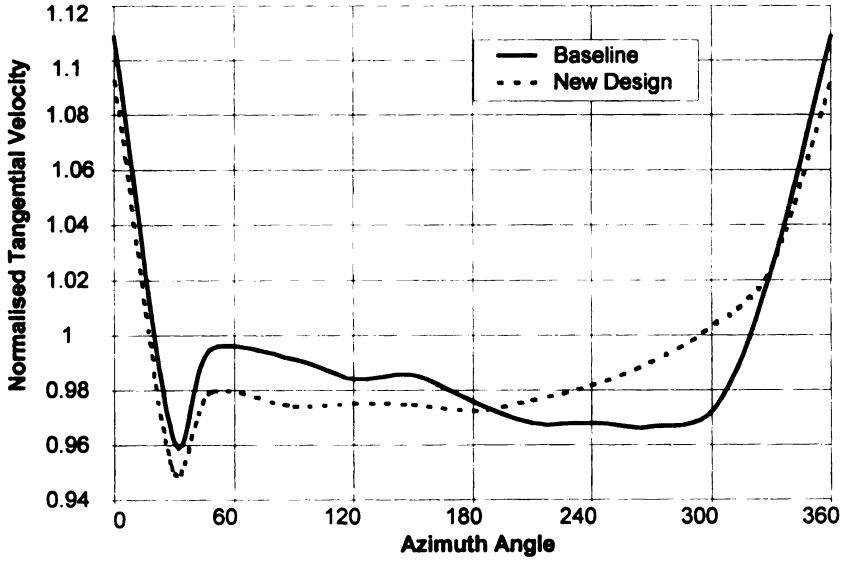

(a) Tangential velocity

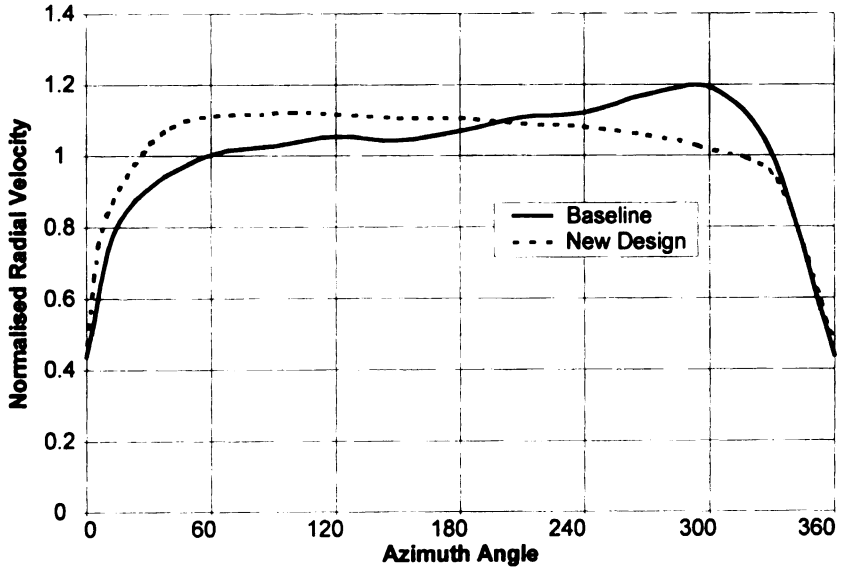

(b) Radial velocity

Figure 3.17 Design examples

Figure 3.17 (cont'd)

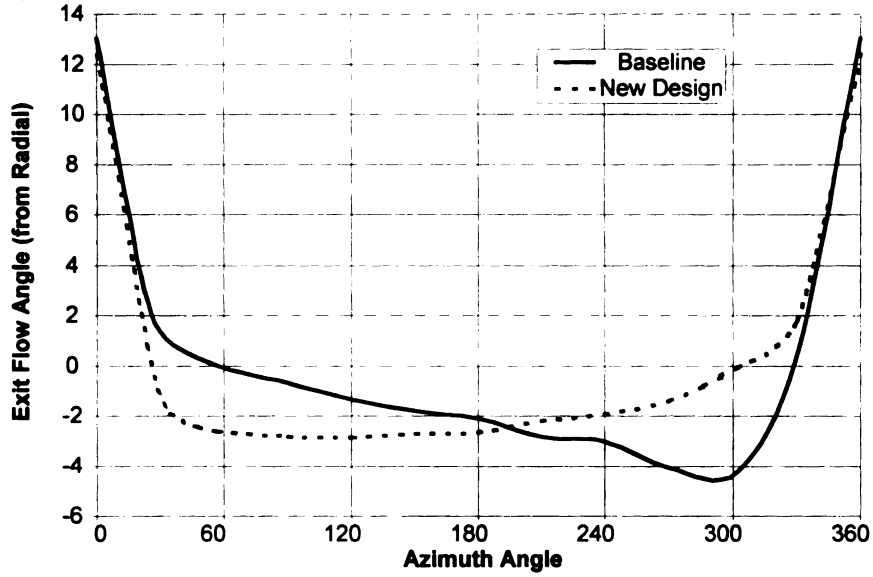

(c) Flow angle

3.10 Conclusions

This chapter presents a volute design system for both turbines and compressors. The flexibility of the geometry representation is implemented by Bezier polynomials. An interface with commercial CFD solver is built to generate grids and boundary conditions for the simulation. This system greatly reduces the cost of volute design by reducing the interaction between autoCAD systems and CFD solvers.

Chapter 4

COMPARATIVE STUDY OF VOLUTE DESIGN APPROACHES

4.1 Introduction

For reasons of design simplicity, compactness, reduced cost and reasonable performance, most internal combustion engine turbochargers are fitted with vaneless radial or mixed flow turbines. An object of the volute design is to prepare uniform free vortex inflows centered about the wheel centerline for the wheel while keep the energy losses minimum.

Based on the conservation of angular momentum, a variety of free vortex design approaches have been proposed to specify the geometrical configuration of volutes. The incompressible approach gives the ratio of area to radius A/r inversely proportional to the discharge flow angle at the critical surface, and linear distribution over the channel. When compressibility is concerned, design approaches based on the centroid flows suffer from the problem of closure because density is taken into account. Several assumptions are available, for example, Mach number linearly distributes over the channel (Whitfield, 1994), or the centroid path is assumed to be a streamline (Whitfield, 1994), and so on. However, as noted by Hussain (1982), the ignorance of the variation of volute width results in non-uniform volute exit flow, even though the area/radius ratio follows the free vortex design. An important progress in the compressible flow volute design was proposed by Chapple, et al. (1980). From the continuity, angular momentum conservation, and the assumption of isentropic flow, Chapple obtained a field of radial and tangential velocity components after giving an empirically specified variation of

width/radius ratio. Then the streamline that represents the desired mass flow rate is the outer wall of the volute. It was shown that this approach made the volute flow much uniform, therefore a high efficient centripetal turbine was designed, even though the flow on the critical surface does not follow the free vortex pattern. There are also some two dimensional design methods, for example, Chen (1996) and Owarish, et al. (1992). However, to what extent compressibility affects the volute design is still uncertain.

The flow structure of a turbine overhang volute with exit guide vanes was experimentally investigated by Tabakoff (1980), and a strong secondary flow was found inside the volute, causing the distortion of the scroll discharge flow. The flow structure in symmetry scrolls, which are widely used in turbochargers, has not been intensively investigated, thus the losses in this kind of volutes are commonly assumed to be caused by friction (Chapple, et al., 1980). Measurements on the discharge surface (Whitfield, 1994), (Miller, 1987) and (Benisek, 1987) show that the flow losses are relatively small due to the flow acceleration, and the distributions are rather uniform.

In this chapter, a theoretical comparison is carried out to assess the effect of incompressible and compressible design methods on the volute geometry and the flow. A numerical simulation is also performed to assess the difference of the volute flow with respect to the free vortex pattern.

4.2 Theoretical Assessment

A free vortex flow means that (1) the tangential velocity is inversely proportional to the radius; (2) the radial velocity is circumferentially constant. The first requirement is the result of conservation of angular momentum, while the second is an enhanced mass conservation. For the volute design, it is expected that at least the discharge flow should follow the free vortex pattern. In this investigation, both discharge and centroid flows are compared with this pattern.

4.2.1 Incompressible approach

The incompressible approach is well documented in literature; see references in (Chapple, et al., 1980). To make this paper self-completed, a brief description is given here. The continuity requires that the mass flow passing the section of azimuth angle θ be discharged from its down stream exit surface, therefore the conservation of mass gives:

$$\rho V_\theta A_\theta \sin\alpha_\theta = (2\pi - \theta) r_2 b_2 \rho V_2 \cos\alpha_2 + \dot{m}_0 \tag{4.1}$$

$\dot{m}_0$ is the re-circulation mass flow rate under the tongue. By assuming the geometrical center of the section is the center of the mass averaged angular momentum of the same section, the conservation of angular momentum gives the constant circulation:

$$r_\theta V_\theta \sin\alpha_\theta = r_2 V_2 \sin\alpha_2 \tag{4.2}$$

The ratio of area to radius is obtained by dividing (4.1) by (4.2)

$$A_\theta / r_\theta = (2\pi - \theta) b_2 / \tan\alpha_2 + A_0 / r_0 \tag{4.3}$$

A_0/r_0 is the ratio under the tongue. Therefore, for a specified discharge flow angle and width, the ratio of area to radius changes linearly over the volute channel. The area and

radius of each cross section are determined by solving equation (4.3) and a pre-determined shape of the volute cross section, $A = f(z,r,\theta)$. That is, in the incompressible design approach, the geometrical design is isolated from the aerodynamic design. At the critical surface, equation (4.3) becomes

$$A_1/r_1 = 2\pi b_2/\tan\alpha_2 + A_0/r_0 \tag{4.4}$$

Because the ratio of area to radius is a measure of the discharge flow angle, this parameter became a label of volutes in industry.

4.2.2 Compressible Approach

If the compressibility is concerned, one more flow parameter, density, is to be determined. Because the number of conservation laws does not increase, the number of unknowns is 1 bigger than that of the governing equations, resulting in the problem of closure. Several empirical assumptions, or correlations, were introduced to proceed with the centroid flow design. Besides, as in the incompressible design approach, the geometrical center and the mass averaged angular momentum center of a section are assumed to be identical. Because of these assumptions, the centroid flow design of compressible flows is no longer unique.

It is noticed that compressibility is not related with the conservation of angular momentum, that is, $r_\theta V_\theta \sin\alpha_\theta = r_2 V_2 \sin\alpha_2$ applies to both incompressible and compressible flows under the isentropic condition. In the compressible flow regime, the superposition of the flow of a constant circulation and the sink flow is very similar to turbine volute flows. In compressible flows, the outer wall has the possibility to be the

outmost streamline after the width of the passage and the variation of density are taken into account as shown in figure 4.1.

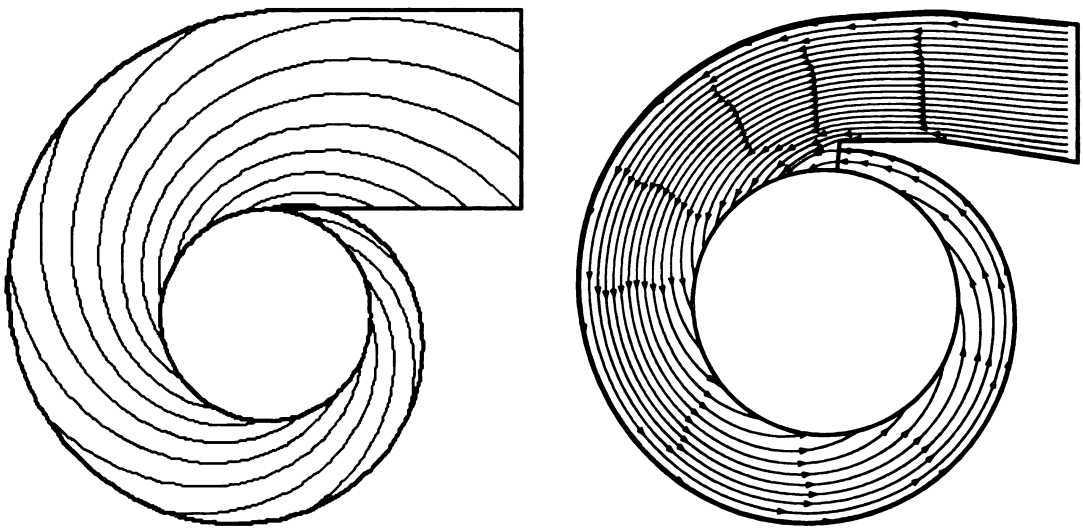

(a) Free vortex flow + sink flow (b) Volute flow

Figure 4.1 Streamlines of free vortex plus sink flow and volute flow

Based on this observation, an important design approach was proposed by Chapple, et al. (1980). For isentropic flows, this method can be revised in terms of Mach numbers:

$$\frac{\dot{m}}{2\pi p_0\sqrt{\gamma/RT_0}} = brM\left(1+\frac{\gamma-1}{2}M^2\right)^{-\frac{1}{2}\frac{\gamma+1}{\gamma-1}}\cos\alpha \tag{4.5}$$

$$\frac{r_2\sin\alpha_2}{r\sin\alpha} = \frac{M}{M_2}\left[\frac{1+\frac{\gamma-1}{2}M_2^2}{1+\frac{\gamma-1}{2}M^2}\right]^{1/2} \tag{4.6}$$

Here, the subscript θ is removed because all the geometrical and flow parameters are assumed to be circumferentially constant in Chapple's approach. Given the total parameters and mass flow rate at inlet, discharge Mach number and flow angle at the

wheel periphery, and if the width b of a volute at radius r is given, these two equations will give a flow field in terms of Mach numbers and flow angles, and the streamline represents the desired mass flow will be the outer wall of the volute. The geometrical parameters, such as area A, geometrical center r, as well as their ratio A/r, of each section can be obtained from this solution. Chapple et al. (1980) noticed that this design approach requires a free vortex flow on the critical surface, and usually it is not achievable. However, this requirement is not critical.

4.2.3 Theoretical Comparison

If a volute designed by an incompressible approach is applied into compressible flows, is the discharge flow uniform and free vortex? As in all the compressible centroid approaches, the identical center assumption is used in this comparison. That is, the geometrical center, the mass averaged center and the center of the mass averaged angular momentum of a cross section are identical. By this assumption, the conservation of mass in the compressible flow is interpreted as: the mass flow passing a cross section is equal to the exit mass flow from the discharge surface downstream of this cross section,

$$A_\theta \sin\alpha_\theta = b_2 r_2 \cos\alpha_2 \frac{M_2}{M_\theta}\left[\frac{1+\frac{\gamma-1}{2}M_2^2}{1+\frac{\gamma-1}{2}M_\theta{}^2}\right]^{-\frac{1}{2}\frac{\gamma+1}{\gamma-1}}(2\pi-\theta) \tag{4.7}$$

Multiplied by equation (4.6), after rearrangement, the ratio of area to radius is,

$$\frac{A_\theta}{r_\theta} = \frac{(2\pi-\theta)b_2}{\tan\alpha_2}\left[\frac{1+\frac{\gamma-1}{2}M_2^2}{1+\frac{\gamma-1}{2}M_\theta^2}\right]^{-\frac{\gamma}{\gamma-1}} \tag{4.8}$$

which is the counter part of equation (4.3) in compressible flows. If a volute designed by the incompressible approach, that is, A/r is a linear function of θ, then from equation (4.8), Mach number must be kept constant, which contradicts to the real flows. Therefore, the application of incompressible volutes to compressible flows cannot result in the free vortex flow, and the discharge flow is distorted. Table 4.1 lists the difference of A/r at the critical surface between the incompressible (equation 4.4) and compressible (equation 4.8) design approaches. The comparison is based on M_1=0.35. It can be seen that the difference becomes larger with the increase of discharge Mach numbers. For the volute to be discussed, the incompressible approach gives the A/r about 15% larger than the compressible approach. The effect of larger A/r on the averaged exit flow can be understood in this way: when the critical area is the same, the larger A/r, the smaller r, therefore, the smaller inflow angular momentum. Thus, it can be expected that the exit flow angle will be smaller than the desired value.

Table 4.1 Comparison of A/r between incompressible and compressible approaches

M_2	0.35	0.45	0.55	0.65	0.75	0.85	0.95
$(A/r)_{com}/(A/r)_{inc}$	1.0000	0.9472	0.8861	0.8194	0.7494	0.6786	0.6089

On the other hand, any compressible centroid design approach is vulnerable if it is based on the identical center assumption, because the ratio of area to radius is uniquely related with Mach numbers (Equation 4.8). Any introduction of empirical relations to close the equation system will cause a confliction of the equation systems.

4.3 Numerical Simulation

The theoretical analysis proved that the incompressible design approach results in distorted flows in compressible applications, because the ratio of area to radius is bigger. A numerical simulation is performed on a previously designed volute to answer another question: what happens to the flow if the ratio of area to radius follows the compressible design approach, but it is smaller?

4.3.1 Calibration Design

A previously designed volute has been tested and laser data were reported by Benisek (1987). This volute has a trapezoidal sectional shape as shown in figure 4.2. Its width b is a linear function of r except for the rounded corners to reduce secondary flows. The compressible design approach of Chapple is employed to calibrate the design of this volute. The equation (4.5) is modified to account for the total pressure losses

$$\frac{\dot{m}}{2\pi p_{0r}\sqrt{\gamma/RT_0}} = brM\left(1+\frac{\gamma-1}{2}M^2\right)^{-\frac{1}{2}\frac{\gamma+1}{\gamma-1}}\cos\alpha \tag{4.9}$$

The total pressure p_{0r} is assumed to be circumferentially constant in order to be consistent with Chapple's design approach, and is computed from a correlation of total pressure loss coefficient, defined by

$$\omega = \frac{p_{0r} - p_{01}}{p_{01}} \tag{4.10}$$

The adiabatic efficiency of the volute is defined by

$$\eta = \frac{1-T_2/T_1}{1-(p_2/p_1)^{\frac{\gamma-1}{\gamma}}} \tag{4.11}$$

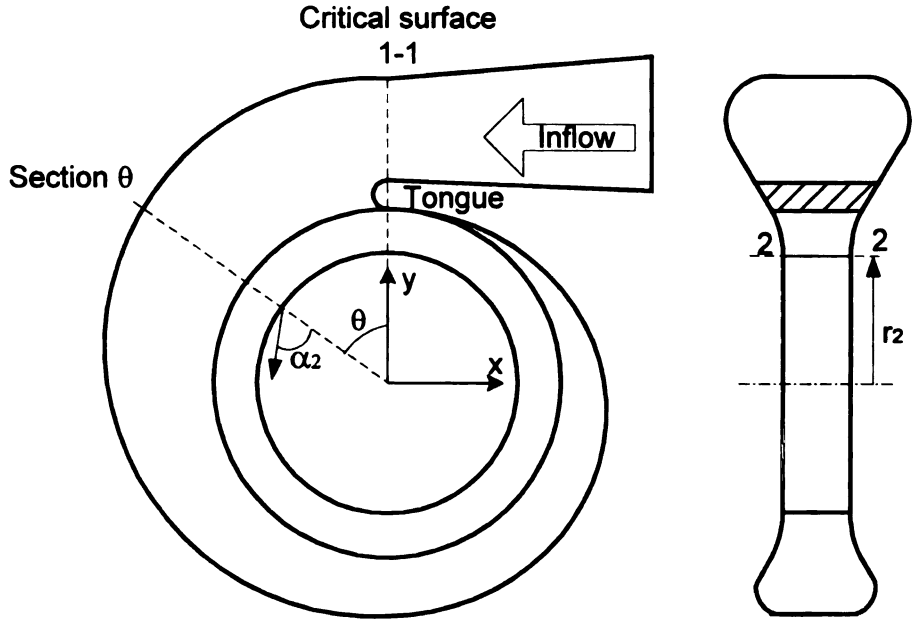

Figure 4.2 Volute convention

The efficiency is related with the total pressure loss coefficient by substituting (4.10) into (4.11)

$$\eta = \frac{1-\left(\frac{p_2}{p_1}\frac{1}{1-\omega}\right)^{\frac{\gamma-1}{\gamma}}}{1-(p_2/p_1)^{\frac{\gamma-1}{\gamma}}} \tag{4.12}$$

Figure 4.3 shows the *A/r* distributions from different approaches. The curve of the free vortex compressible design is from equation (4.6), equation (4.9—4.12), and the pre-given section shape that is the same as the previous design. The total pressure loss is assumed to be a linear function of *r*, and its value at the exit surface is given such that the efficiency from this calibration design is identical to that of the previous design. It can be seen that the previous design is similar to the free vortex compressible design, but it is

smaller, due to the different calculations of the ratio A_0/r_0 under the tongue. Figure 4.3 also shows that the incompressible approach gives bigger *A/r*.

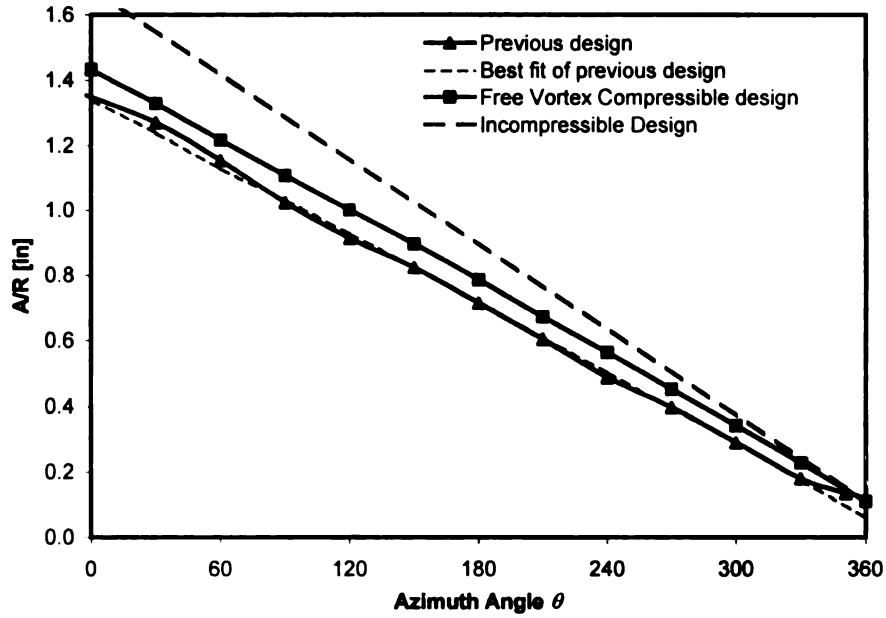

Figure 4.3 Comparison of *A/r*

4.3.2 CFD Model

The commercial CFD software, AEA TASCflow, was run for this volute. The validation of TASCflow can be found, for example, in (Flathers, 1994) which dealt with a geometrically complicated inlet volute. The grid, generated by a self-written code, is shown in figure 4.4. The use of butterfly grids is to reduce the grid distortion in the corners. The inflow conditions include the inlet total pressure, total temperature, and flow direction. Because the inlet turbulent parameters were not measured at the time of the experiment, they are given empirically. The outflow flow condition is assumed a constant pressure over the discharge surface also due to the lack of experimental data. The pressure is iterated until the desired mass flow rate is obtained. Because a turbine wheel

was assembled in the experimental facility, it is expected that the rotating of the wheel should smooth the pressure on the volute discharge surface.

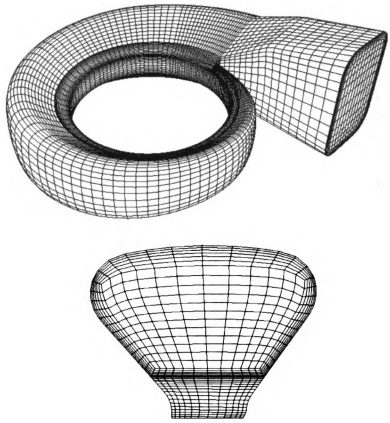

Figure 4.4 Grid

Figure 4.5 shows the comparison of the discharge flow angles between CFD and experiment. The experimental data showed a smoother circumferential variation of the flow angle over the discharge surface while the velocity distribution is slightly more distorted. However, the agreement of CFD with experimental data indicates that the model can be used to analyze the volute flow. Because of the lack of traverse data on the volute cross-section, the CFD analysis became the only way to get insight into the flow mechanism. To compensate for this weakness, the CFD results will be decomposed to compare with the free vortex design.

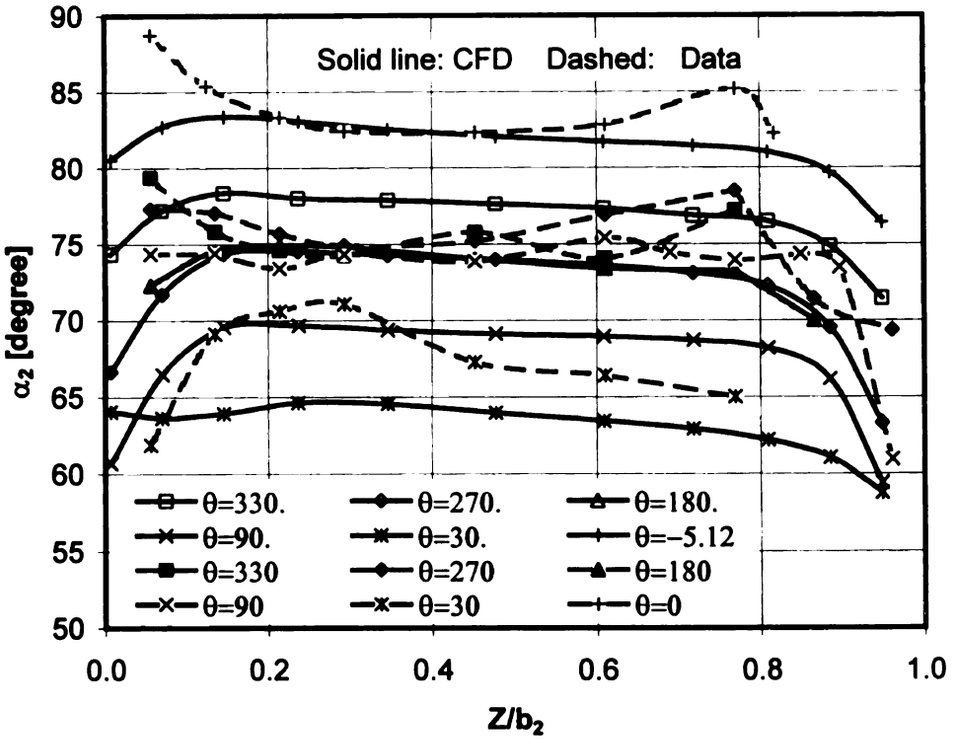

(a) Flow angle

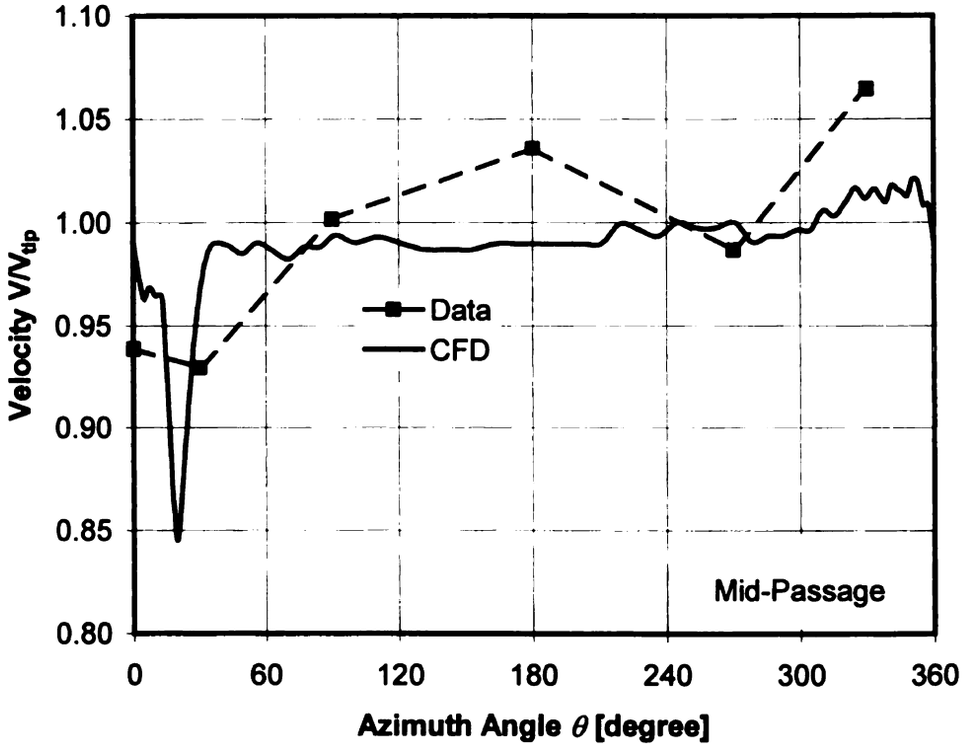

(b) Velocity

Figure 4.5 Comparison of exit flow

The flow in the volute channel is similar to the flow in a curved pipe, but the discharge from the inner surface makes the volute flow structure significantly different from that of the curved pipe. There are two counter-rotating vortices in the curved pipe flow (Schlichting, 1979), resulting in stronger swirling velocity on the sidewalls and reduced radial velocity on the symmetry surface. The swirling vector plot from CFD in Figure 4.6, however, shows that the radial velocity is almost radially uniform on the symmetry surface except for the near wall region and no noticeable vortex flow exists in the central passage. Therefore, it is reasonable to investigate the degree to which the volute flow agrees to the free vortex design on the centroid line and the symmetry surface.

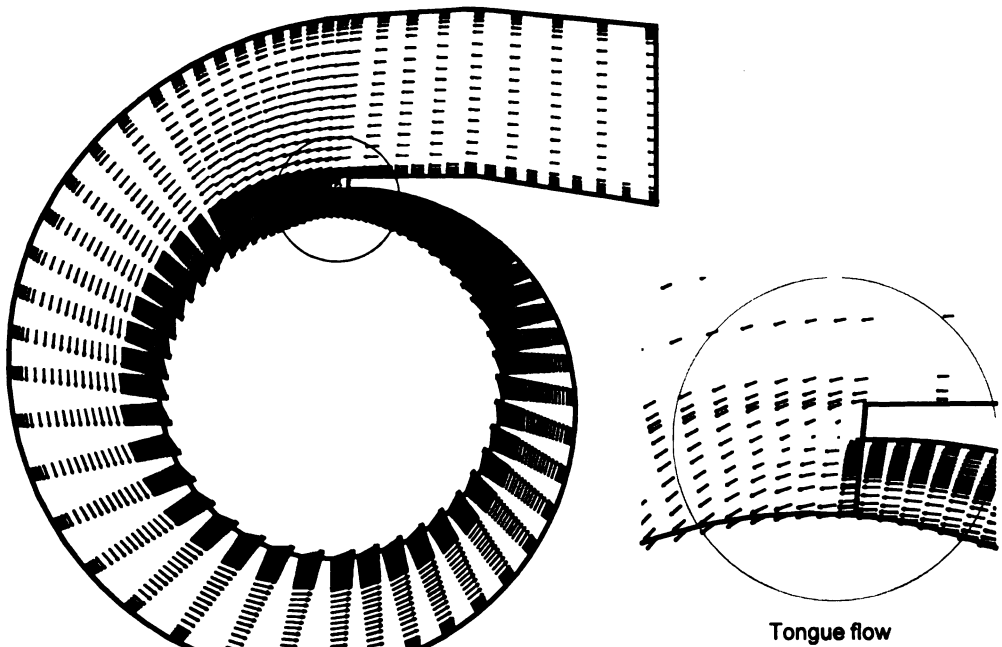

(a) Through flow

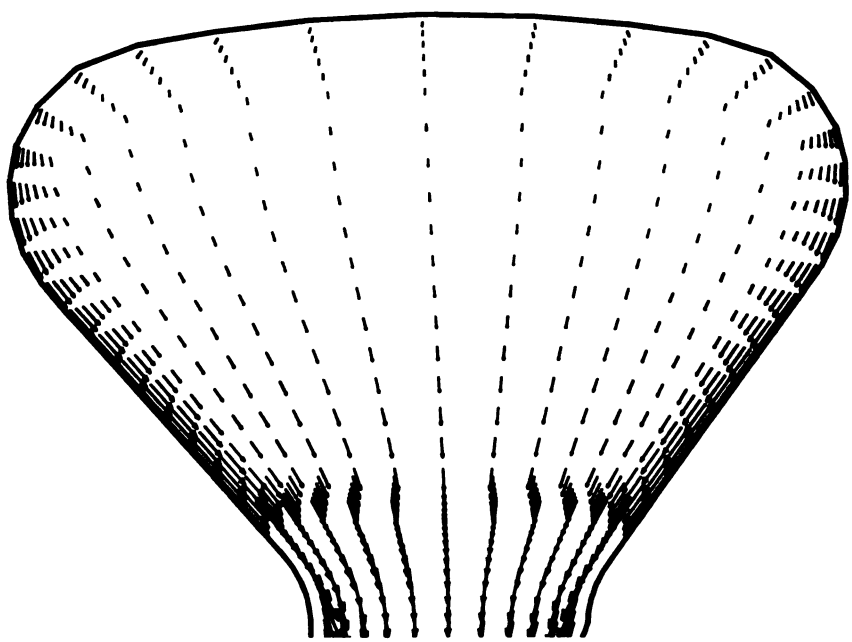

(b) Swirling flow

Figure 4.6 Through flow and swirling flow vectors

4.3.3 Comparison of CFD with Free Vortex Design

From here on, the free vortex design refers to the calibration design, which incorporates the total pressure losses, so that the efficiencies from CFD and the free vortex design are identical. It should be noted that the flow is no longer free vortex after the losses are taken into account. The use of the terminology free vortex is an approximation.

Centroid Flow Figure 4.7 compares the centroid Mach number and flow angle variations between CFD and the free vortex approach. A good agreement of the Mach number variation is observed from figure7 (a). The higher Mach numbers from CFD indicate that the centroid flow is more accelerated due to the smaller *A/r*. The centroid flow angle is compared in figure 7(b). Of interest is the radical change of the Mach numbers upstream of the tongue ($\theta = 360^o$) and the significant deviation of the centroid flow angle up and down stream of the tongue. These phenomena are caused by the radical acceleration around the tongue, the weak flow from the tongue and their interaction as shown in figure8. The weak flow produces the high losses (figure9), resulting in the small constant pressure zone downstream of the tongue. The creation of this constant pressure zone makes a stronger pressure gradient immediately below the constant pressure zone. Whether this phenomenon is caused by the outflow boundary condition of the CFD model is needed to investigate later. The irregular oscillation of the Mach numbers from CFD may be due to the distortion of *A/r* shown in figure3. In general, the centroid flow follows the tendency of the free vortex design, even though this volute is slightly smaller than the free vortex design.

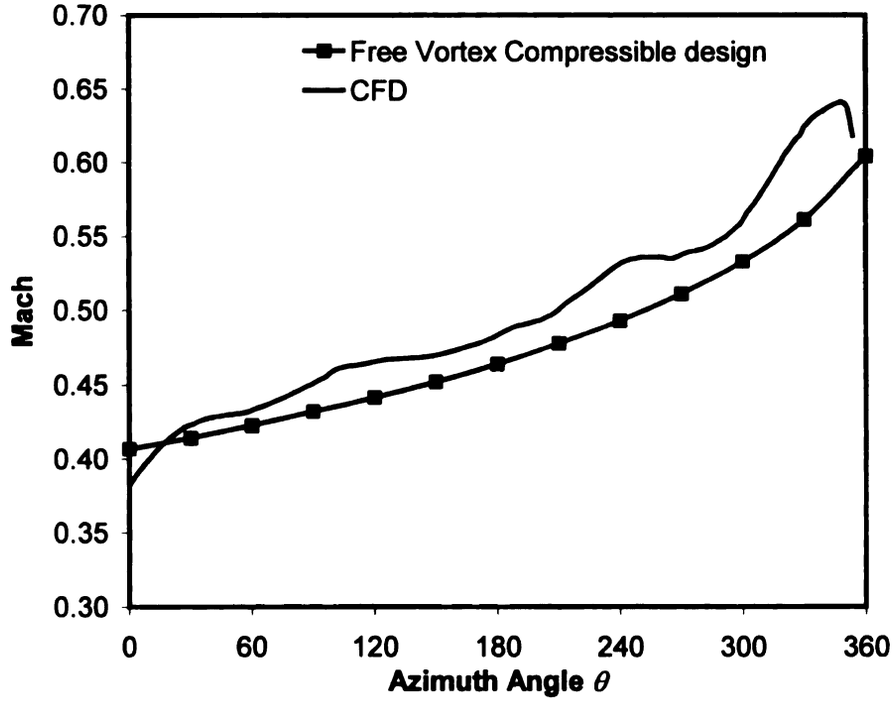

(a) Mach Numbers

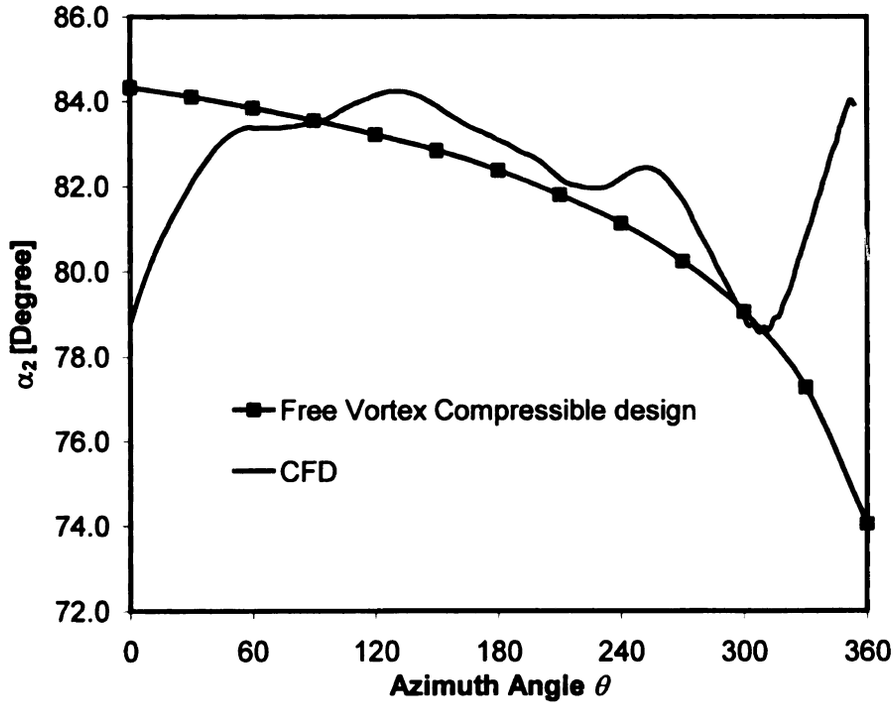

(b) Flow angle

Figure 4.7 Comparison of centroid flow

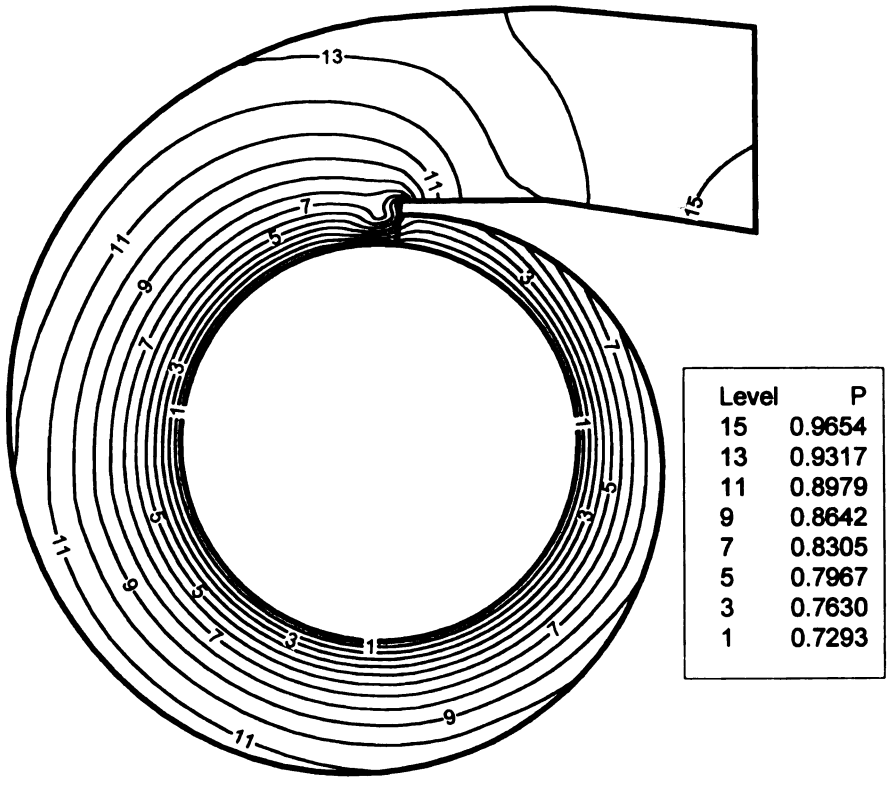

Figure 4.8 Pressure contours on symmetry surface

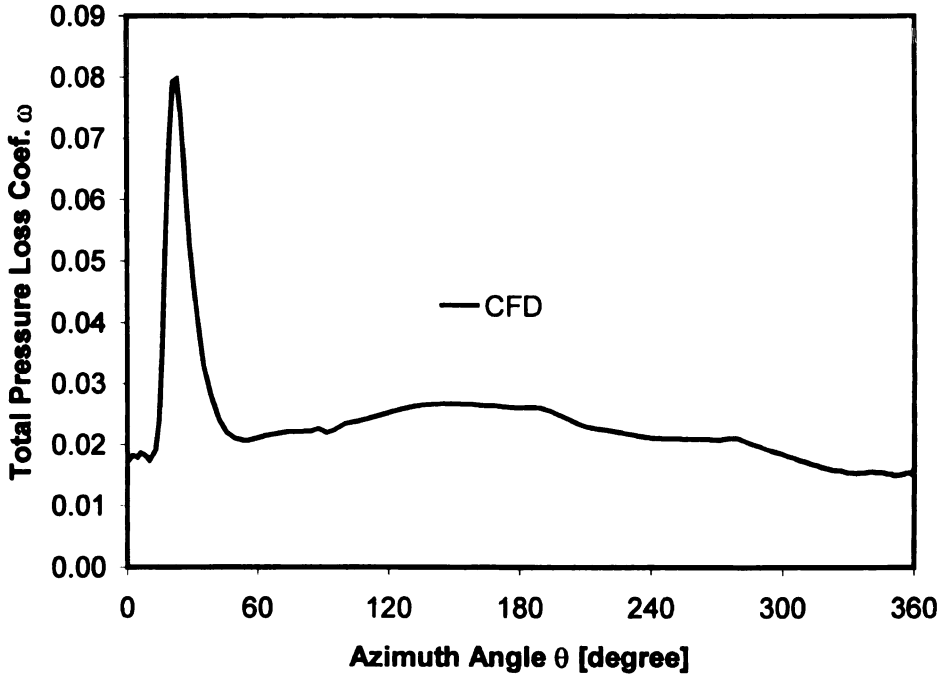

Figure 4.9 Total pressure loss coefficient

Flow on Symmetry Surface The tangential velocity on the symmetry surface is plotted against the free vortex design in figure10. The overall agreement of CFD results with the free vortex design is satisfactory. The CFD results are located above the free vortex design, due to the fact that the volute is of smaller *A/r*. On the surface of $\theta = 30^o$, the CFD curve goes close to the free vortex curve, ending up with an apparent distortion on the lower radius end, indicating the growth of the angular momentum losses from the outwall to the exit due to the weak flow of the tongue. As the flow moves downstream, the effect of the tongue gradually disappears, indicated by the better agreement of CFD results with the free vortex design on surface $\theta = 90^o$ and $\theta = 180^o$. After surface $\theta = 180^o$, the difference between the CFD result and free vortex design shows an opposite tendency to the upstream. The smaller tangential velocity on the higher radius end shows the effect of the wall; the boundary layer on the wall becomes thicker, resulting in the velocity deficit in the near wall region. On the surface $\theta = 330^o$, the difference becomes larger, suggesting that the flow is speeded up due to the deflection of *A/r* from the free vortex design in this region.

In summary, the smaller *A/r* of the volute causes the tangential velocity component bigger than the free vortex design over all the passage downstream of the tongue. The weak flow of the tongue causes the deficit of tangential velocity near the discharge surface downstream of the tongue, while the boundary layer on the wall causes the deficit near the wall upstream of the tongue. This analysis suggests that a good one-dimensional design approach should be able to distinguish these two different losses.

The comparison of the radial velocity components (figure11) shows that the radial velocity component lies above the free vortex curve at first, then moves gradually close

to the free vortex curve, and at last it lies under the free vortex curve at the surface $\theta = 330^o$. The radial pressure gradient is responsible for this deviation. Figure8 shows that the radial pressure gradient near the discharge surface is gradually reduced from the surface $\theta = 0^o$ to $\theta = 360^o$. The distortion of the pressure gradient could be due to the fact that the volute has a smaller ratio of area to radius, but a detailed study is needed to relate this phenomenon with the change of the ratio.

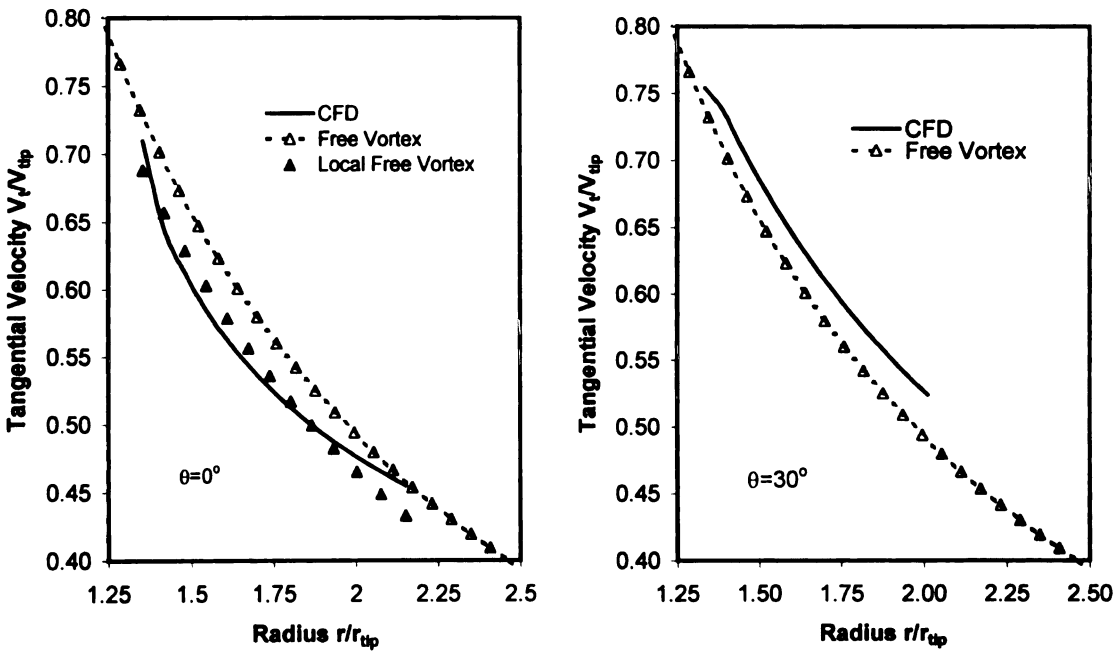

Figure 4.10 Comparison of tangential velocity with free vortex

Figure 4.10 (cont'd)

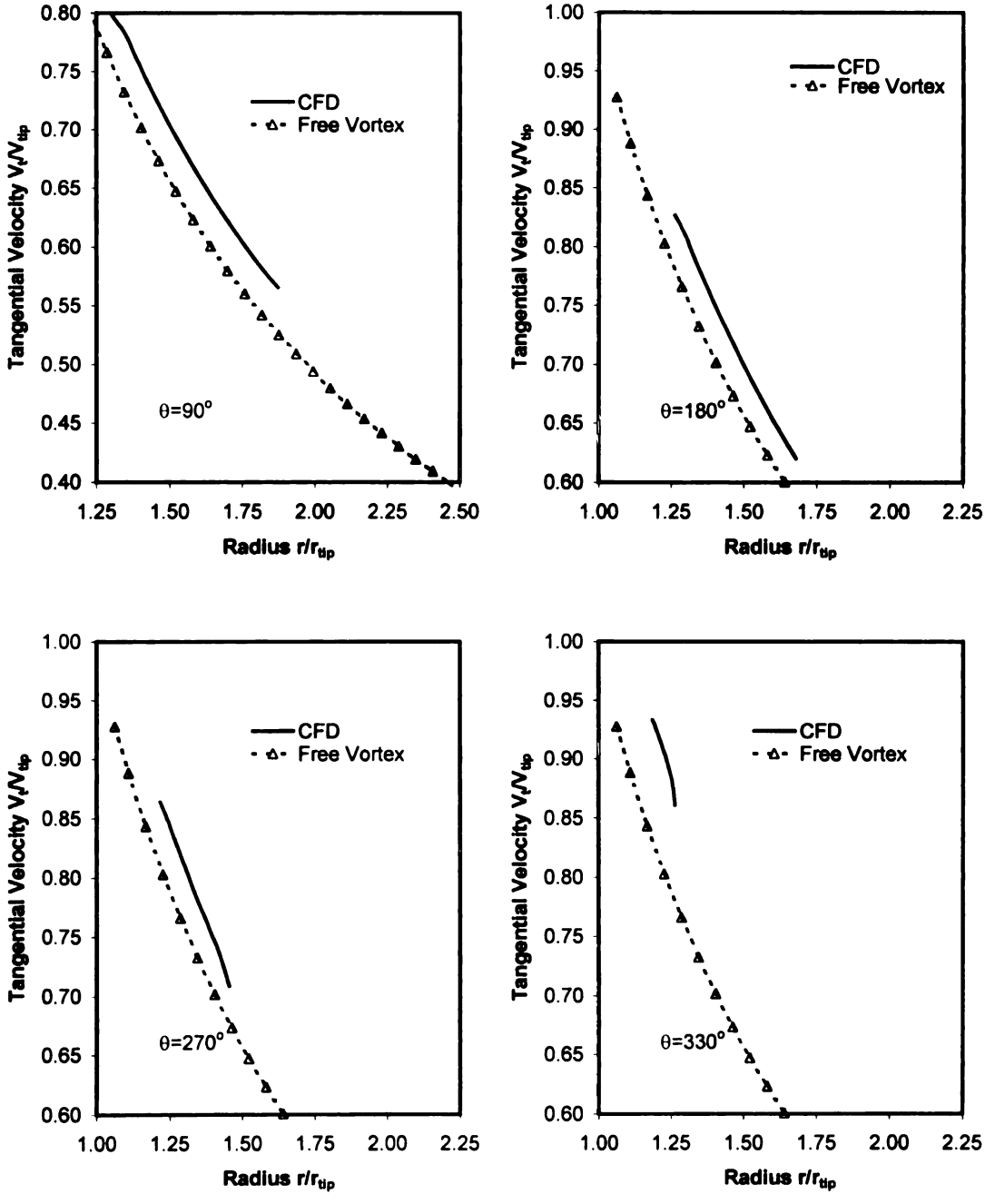

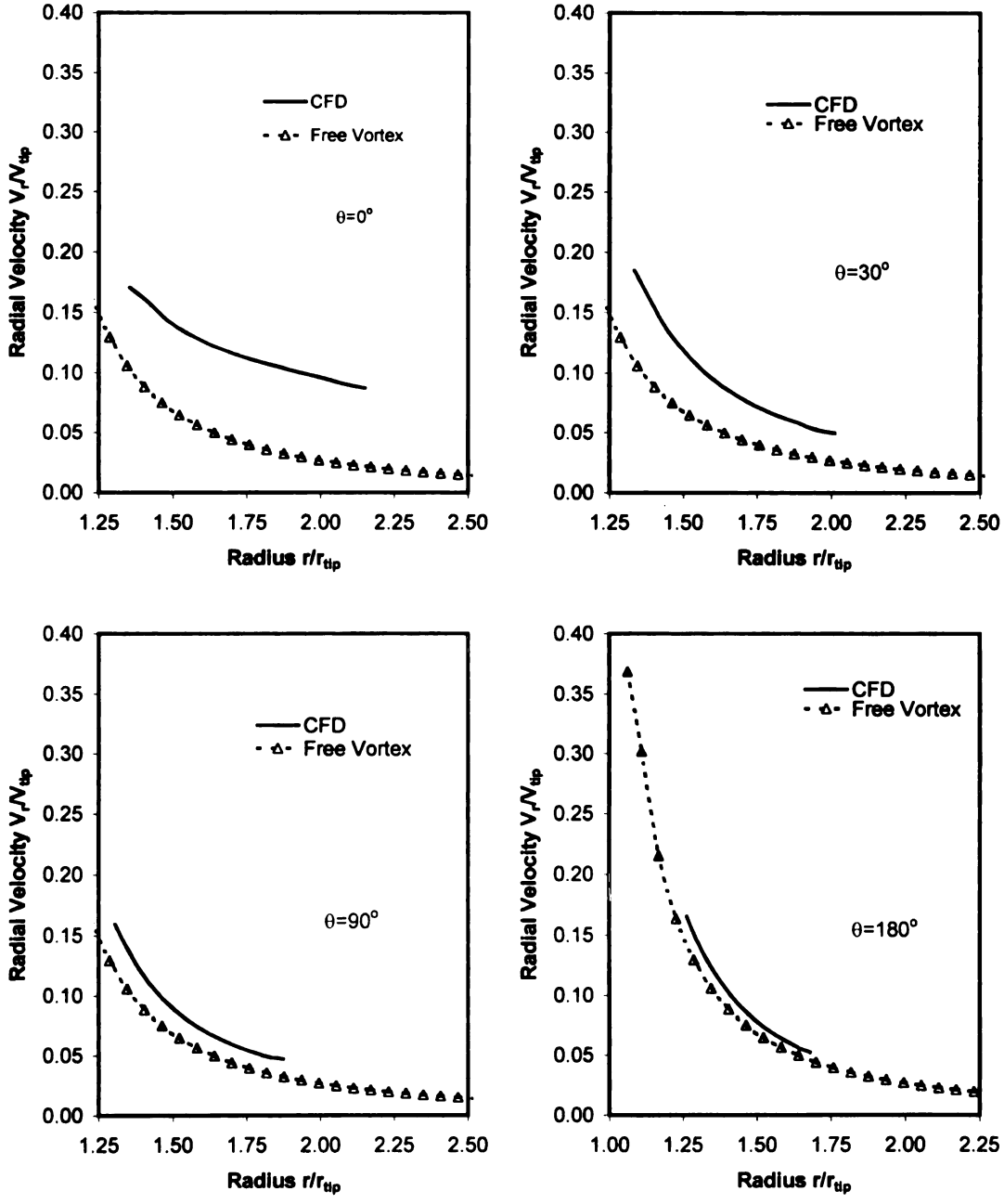

Figure 4.11 Comparison of radial velocity with free vortex

Figure 4.11 (cont'd)

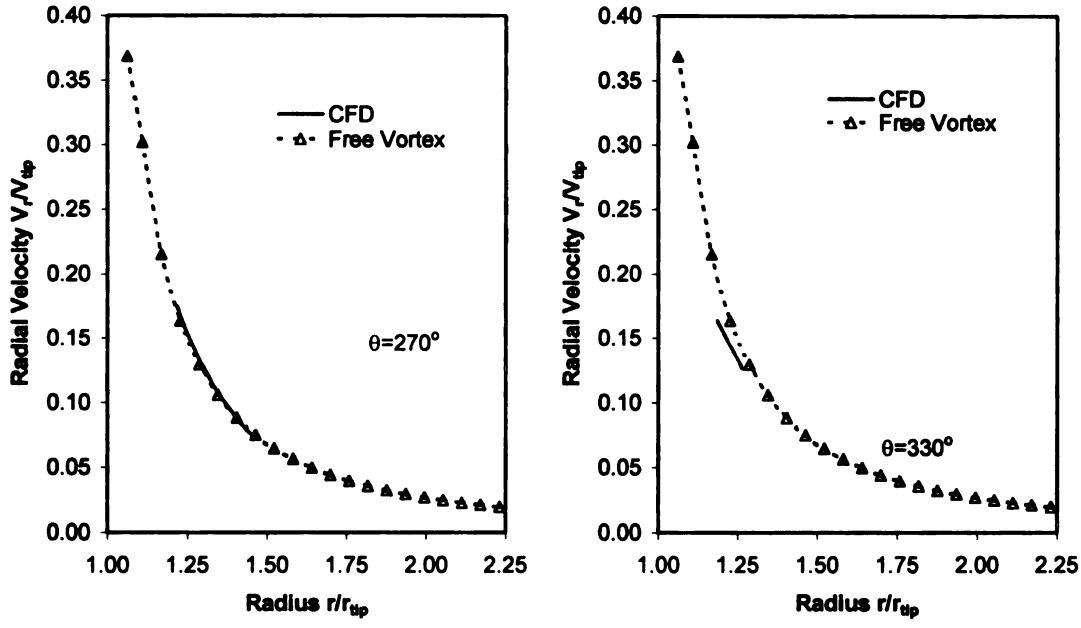

4.4 Conclusion

One-dimensional conceptual design of the inflow turbine volute is assessed by the means of theoretical analysis and numerical simulation. It is proved that the incompressible approach gives a volute with bigger *A/r*, resulting in a smaller average exit flow angle for compressible flows. Chapple's compressible design approach is extended to take into account of the total pressure losses. A numerical simulation is conducted on a previously designed volute to investigate the deviation of the flow from the free vortex design. It is shown that when the ratio of area to radius of the volute is smaller that the free vortex design, the Mach numbers of the centroid flow are higher and the centroid flow angle is distorted at both ends. The weak flow of the tongue and the recirculation flow under the tongue are among the factors contributed to the angle distortion. It is also observed that the weak flow of the tongue causes the deficit of the tangential velocity component near the discharge surface downstream of the tongue; the thicker boundary layer causes the deficit of the tangential velocity component near the outwall upstream of the tongue. The radial velocity component at first lies above the free vortex design, then constantly goes below the free vortex design. A possible reason is that the ratio of area to radius of the volute is slightly smaller than the free vortex design.

Chapter 5

VOLUTE FLOW STRUCTURES

5.1 Introduction

A single-stage centrifugal compressor consists of impeller, diffuser (vaned or vaneless), and volute. Impeller and diffuser flows have been studied extensively, and volute flow study has appeared as an interesting research field for further improving the compressor performance. Van den Braembussche and Hande (1990) measured a straight model of a centrifugal compressor volute. Based on their measurement, they described the volute flow as:

- The fluid entering close to the tongue at small radius fills the center of the volute.
- New fluid entering further downstream at a larger radius starts rotating around the upstream fluid.
- Vortex tubes of increasing radius are wrapped around each other and each vortex tube remains at constant radius.

Ayder et al. (1993, 1994) gave a detailed measurement and numerical simulation of the flow structure of the volute at design and off-design conditions. Hagelstein et al. (1999) presented a detailed flow measurement of a rectangular volute at an off-design condition of higher mass flow rate.

The interaction between volute and impeller was studied experimentally by Hagelstein, Van den Braembussche, Keiper, and Rautenberg (1997). At off-design conditions, the volute produces a peripheral pressure distortion, leading to a periodic

throttling of the impeller flow and oscillating of the radial force on the impeller shaft. Flathers et al. (1999) satisfactorily predicted the variation of radial force magnitudes and directions with the mass flow rates using CFX-TASCflow. Sorokes, Borer, and Koch (1998) experimentally investigated the circumferential static pressure non-uniformity on a multi-stage compressor. The numerical study of Hillewaert (1999) showed that the pressure variation at the vaneless diffuser inlet could be up to 10% for near surge flow.

Except for the use of some models (Hillewaert and Van Den Braembussche 1999), the numerical investigation of the pressure circumferential distortion at the impeller exit is very expensive because all the impeller passages have to be simulated together, and the unsteady flow has to be resolved at tiny time steps. However, since the upstream effect of the volute has previously been studied and found to be ½ that at the diffuser exit, as shown by Hagelstein et al. (1997) and Sorokes et al. (1998), it is therefore deemed reasonable to simply circumferentially average the impeller exit fluxes as a starting flow for the diffuser/volute analysis.

This Chapter numerically investigates the flow structure inside the compressor by circumferential averaging at the exit of the impeller. Based on the CFD results, a flow model is proposed to describe the flow inside the diffuser and volute of the compressor.

5.2 CFD Model

The commercially available CFD software, CFX- TASCflow, is employed for this study. The validation of this code for the configuration of centrifugal compressors can be found, for example, in the work of Flathers (1994, 1999). The code solves the Reynolds averaged Navier-Stokes equations in primitive variable form. The effects of turbulence

were modeled using the standard κ–ε turbulent model. To make the simulation timely economical, wall function is used to resolve the wall flows. The simulation is believed converged when maximum residuals are reduced to 1.E-4.

The code allows for connecting simple blocks into a multi-block assembly. A convenient feature of TASCflow is that the grids are not required to match at the connect interface. This makes it easy to connect volute grids at the critical surface, where one side is of the smallest area and the other side of the largest one. A self-coded volute grid generator was used to generate the volute and vaneless diffuser grid. The grid of the volute is of butterfly section to reduce the grid skewness (figure 5.1). The commercial impeller grid generator, TASCgen, is employed to generate the impeller grid. In this study the grid is relatively coarse with $87 \times 16 \times 13 = 18{,}096$ points for one passage of the impeller and 145,535 for the volute. The impeller is shrouded and the volute is designed of constant centroid radius.

In this assembly as shown in figure 5.1, there are two distinct components: impeller that is rotating and volute and vaneless diffuser, which are stationary. A sliding grid interface between these two components is defined as "stage interface" using TASCflow grid attachment facility. It tangentially averages the exit fluxes of impeller for the inflow of the diffuser, but pressure distortion is allowed, because it is detrimental to the prediction in many situations, especially when there are significant elliptic effects at the sliding interface (e.g. upstream of a leading edge). To avoid this problem the local interface pressure, p_{ip} is determined from the local nodal pressure plus a perturbation,

$$p_{ip}^{s} = p_{nodal} + \delta p_{stator} \text{ (stationary side)} \qquad (5.1)$$

$$p_{ip}^{t} = p_{nodal} + \delta p_{rotor} \text{ (rotation side)} \tag{5.2}$$

The values of δp are constant over each side of the interface. It is convenient to relate each δp to the single interface pressure, $p_{\text{int }erface}$, such that the area weighted average nodal pressure on each side of the interface are equal to each other, and to $p_{\text{int }erface}$

$$p_{\text{int }erface} = \frac{\sum_{stator} A_{ip} p_{ip}^{s}}{\sum_{stator} A_{ip}} \tag{5.3}$$

$$p_{\text{int }erface} = \frac{\sum_{rotor} A_{ip} p_{ip}^{r}}{\sum_{rotor} A_{ip}} \tag{5.4}$$

The above equations are rearranged to give the following

$$p_{ip}^{s} = p_{nodal} + \left(p_{\text{int }erface} - \overline{p}_{nodal}^{s}\right) \tag{5.5}$$

$$p_{ip}^{r} = p_{nodal} + \left(p_{\text{int }erface} - \overline{p}_{nodal}^{r}\right) \tag{5.6}$$

where

$$\overline{p}_{nodal}^{s} = \frac{\sum_{stator} A_{ip} p_{nodal}}{\sum_{stator} A_{ip}} \tag{5.7}$$

$$\overline{p}_{nodal}^{r} = \frac{\sum_{rotor} A_{ip} p_{nodal}}{\sum_{rotor} A_{ip}} \tag{5.8}$$

Therefore, the stage model does not remove the static pressure distortion from the interface. The resulted pressure distribution on the interface is a combination of physics and numerical algorithm. However, because of the averaging of other fluxes, it is more

economical to model one passage of the impeller. Periodic boundary condition is assigned to the blade grid tangential surfaces. This model is believed to be good for compressor performance prediction, see TASCflow user's manual. This Chapter limits the discussion to the flow axial distortion at the averaging station and the axial and circumferential interaction of diffuser/volute in the 90 degree bend between diffuser exit and volute inlet.

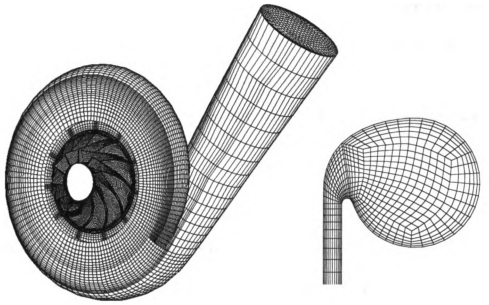

Figure 5.1 Compressor grid

The inflow boundary condition was assigned upstream of the impeller at station 1-1 as total temperature, total pressure, and flow angles. Mass flow rate was imposed on the exit of the cone as the outflow boundary condition. Because CFX-TASCflow does not require a uniform exit, the cone was not artificially extended.

5.3 Results

The compressor was designed for pipeline applications. The tip Mach number at design point is 0.65, and the diffuser ratio D_5/D_2 is 1.9. The compressor was tested at Solar Turbines Incorporated closed loop facility before the CFD study was performed, but the experiment result was not released to the CFD group until the CFD study was done. The purpose of the experiment was to obtain the performance of the compressor; therefore, only the parameters at the compressor inlet and exit flanges were measured. The purpose of CFD study is to get insight into the volute/diffuser interaction in order to find some design rules for the volute. The code was run at design and two off-design conditions: 75% and 125% of design mass flow. The CFD results are reported here.

5.3.1 Compressor performance

The experiment was run at 10901 rpm, while the CFD study was conducted at 10530 rpm; therefore, the overall performance is compared in terms of non-dimensional parameters as shown in figure 5.2.

The inlet flow coefficient and isentropic head coefficient are defined as

$$\Phi = \frac{Q_1}{\frac{\pi}{4} \times D_{tip}^2 \times U_{tip}} \tag{5.9}$$

$$\Psi = \frac{2C_p \times (T_{08} - T_{01}) \times \eta_{isen,t-t}}{U_{tip}^2} \tag{5.10}$$

It can be seen that the three points from CFD are in good agreement with experiment data. The CFD points are above the experimental curve due to the fact that the CFD

model did not incorporate the leakage flow in the labyrinth between the shroud outer wall and the case. The performance of the impeller is also compared in figure 5.2. It can be seen that the performance of the impeller can be rather different from that of the compressor, even in the tendency. The difference between the curves of the impeller discharge and cone discharge shows the effect of the stationary components on the compressor performance.

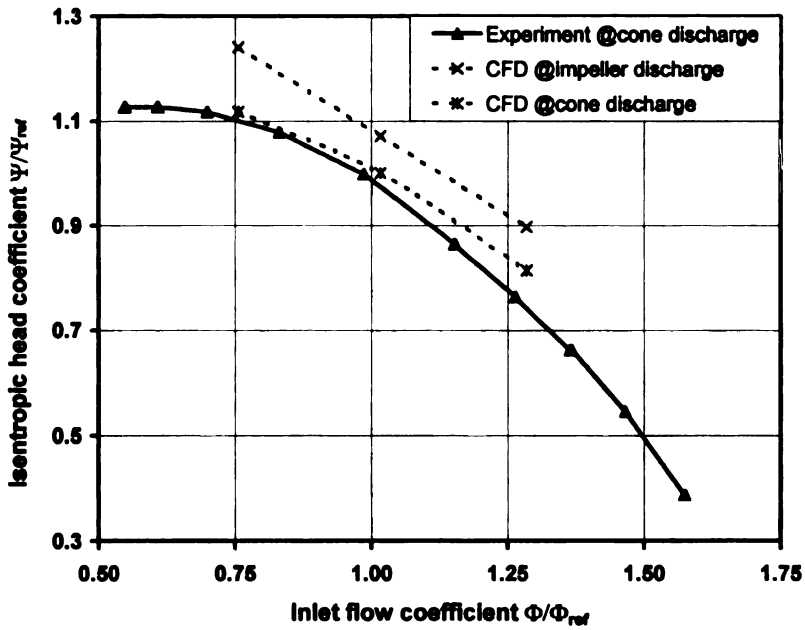

Figure 5.2 Compressor performance

The performance of each stationary component is presented in figure 5.3 in terms of pressure recovery and total pressure loss coefficient. They are defined with respect to station 4-4, which is the grid interface between the impeller and diffuser.

$$c_p = \frac{p - p_4}{p_{04} - p_4} \tag{5.11}$$

$$\omega = \frac{p_{04} - p_0}{p_{04} - p_4} \tag{5.12}$$

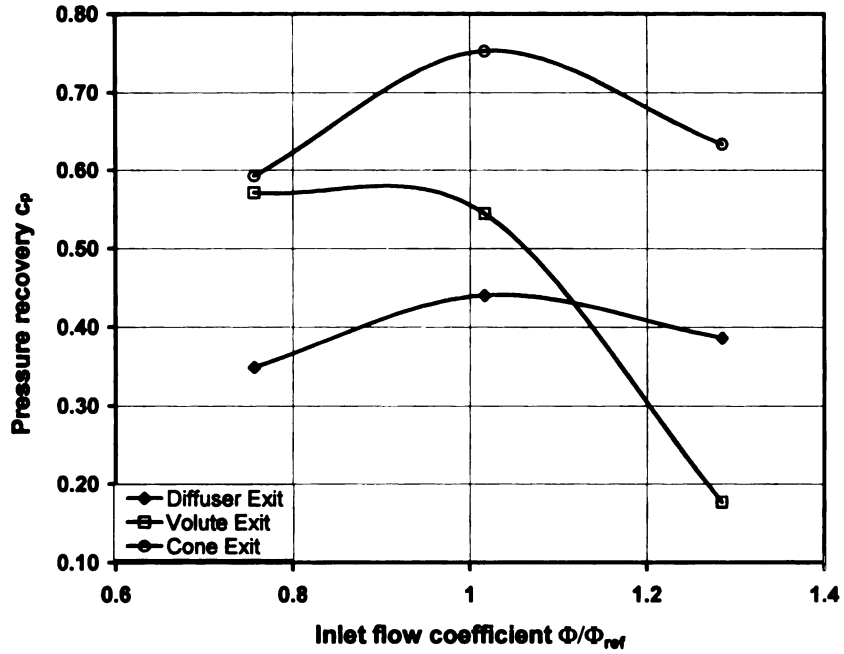

(a) Pressure recovery

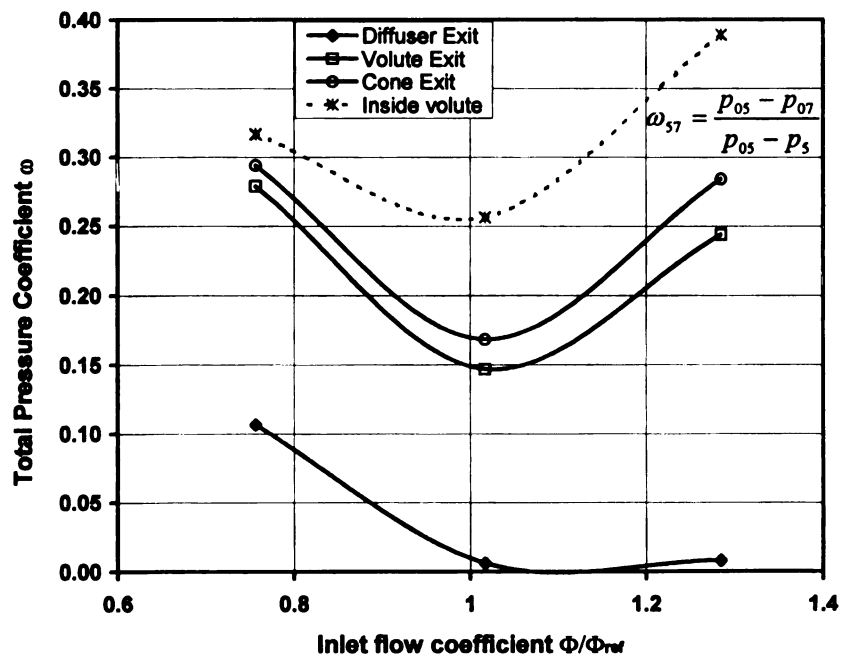

(b) Total pressure loss coefficient

Figure 5.3 Component performance

At the design mass flow rate, the pressure is converted from kinetic energy consistently in both volute and exit cone. At the off-design of smaller mass flow, the flow is decelerated in the volute, resulting in a considerably high pressure rise in the volute and a relatively small rise in the cone. At the high mass flow point, the flow is accelerated in the volute and then heavily compressed in the exit cone. These observations are in agreement with that of Van den Braembussche (1990). The total pressure loss in the stationary components increases as the operation point goes away from the design point in both directions. The losses occurred in the diffuser decrease as the mass flow increases due to the increased ability to overcome the adverse pressure gradient. The shorter path of a particle inside the vaneless diffuser also reduces the losses as the mass flow increases. Losses that occur in the volute comprise the largest percentage of the losses occurring in the stationary components. The loss in the volute increases slightly as the mass flow decreases from the design point to the lower mass flow and it increases significantly as the mass flow rate goes higher from the design points. This Chapter focus on the mechanism of how the losses increase as the operation point goes away from the design one. The change of flow structures will be investigated.

Figure 5.4 shows the mass-averaged static and total pressure variation in the circumferential direction at diffuser exit. The static pressure (figure 5.4a) varies smoothly except for the tongue region. A strong circumferential favorite pressure gradient is built around the tongue at lower mass flow, and a relatively weaker adverse pressure gradient exists at higher mass flow. This significant pressure distortion around tongue results in the change in flow structure over this region. At design mass flow the static pressure increases circumferentially, indicating that the volute is oversized for the design flow.

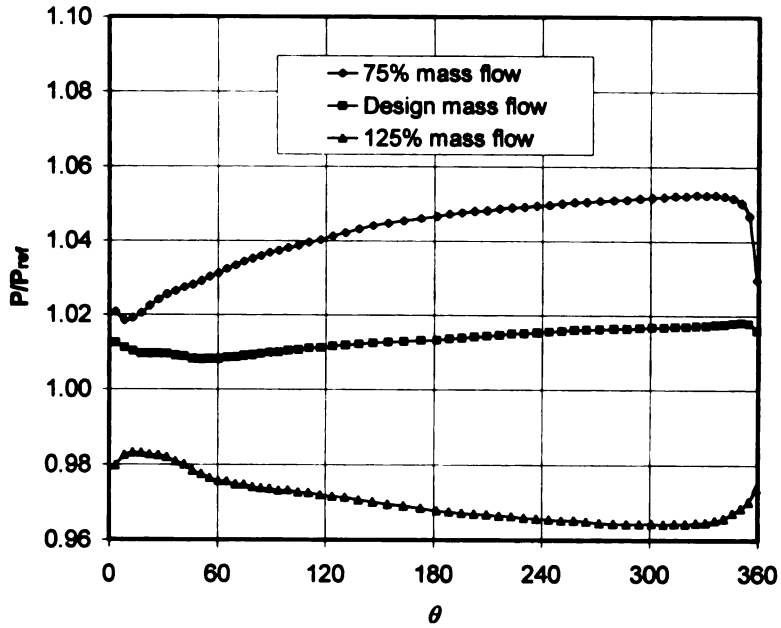

(a) Static pressure

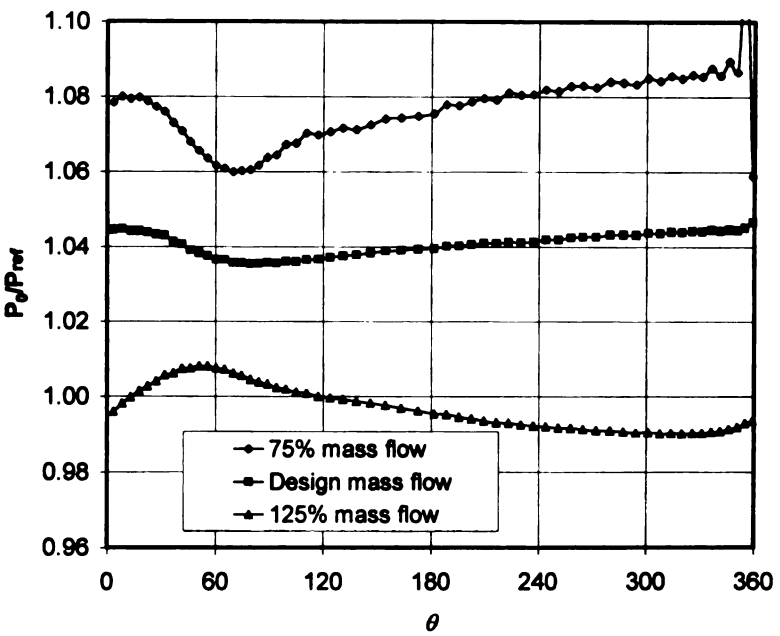

(b) Total pressure

Figure 5.4 Mass-averaged static and total pressure variations in circumferential direction at diffuser exit

The total pressure (figure 5.4b) circumferentially increases at lower mass flow and decreases at higher mass flow. The main reason for this total pressure distortion is the stage interface on which the static pressure distortion is not total removed; it is therefore a phenomenon of the numerical model. However, At all mass flows, the region downstream of the tongue shows more rapid static and total pressure variations; therefore, the flow structure around the tongue deserves further investigation.

5.3.2 Flow at diffuser inlet and exit

The comparison of the flows at the diffuser inlet and exit is presented in figure 5.5, which shows the flow variation in the axial direction. The inlet flow of the diffuser comes from the stage model of the grid interface. Even though the circumferential distortion is not completely removed, the comparison is only carried out on section which is far away from the tongue, for example, θ=180°. The flow at the diffuser exit varies tangentially, but only section θ=180° is presented here. Many studies on the vaneless diffuser flow can be found in (Japikse 1996), but few studies have been done on the effect of volutes on the diffuser flow. The purpose of the current analysis is to distinguish the volute upstream effect.

At the inlet of the diffuser, the static pressure is almost constant over the diffuser width because the flow is almost parallel to the wall. The tangential velocity component increases from hub to shroud because more work is added to the fluid in shroud region by the impeller. At the lower mass flow rate, the energy per mass added by the impeller is highest, thus it exhibits highest tangential velocity. Also largest kinetic energy was

converted, resulting in the highest static pressure rise in the impeller. The opposite case occurs at the higher mass flow rate. Thicker boundary layers can be found on both hub and shroud walls at the lower mass flow rate, which indicates that the boundary layer grows faster in the impeller. The radial velocity exhibits different axial tendency. At lower mass flow rates, more flow exits from the impeller from the shroud side, while more flow exits from the hub side at higher mass flow. The impeller exit flow pattern depends on the secondary flows inside the impeller (see Krain 1988).

By comparing the upper with the lower plots in figure 5.5, it can be seen that all the axial distortion found at the diffuser inlet is consistently amplified at the exit. The total pressure loss (figure 5.5e) and the static pressure recovery (figure 5.5a) increases from hub to shroud at all mass flows. At lower mass flow, even though the exit pressure axial distribution is more uniform, the pressure recovery, therefore the velocity components and flow angles, is still non-uniform. The exit flow angle (figure 5.5d) near the hub is close to 90°, which is an indication of the flow separation. It also can be seen that the flow becomes more tangential from inlet to exit on the hub side and more radial on the shroud side. It means that there is a mass migration from hub to shroud inside the vaneless diffuser. At the higher mass flow, the pressure recovery significantly increases from hub to shroud. Both velocity components are reduced significantly near the shroud wall (figure 5.5b, c). Contrary to the lower mass flow, the flow inside the vaneless diffuser at higher mass flow becomes more tangential on the shroud side and more radial on the hub side, indicating a mass migration from shroud to hub. These different exit flow patterns from the diffuser will influence the flow structure in the volute as will be discussed.

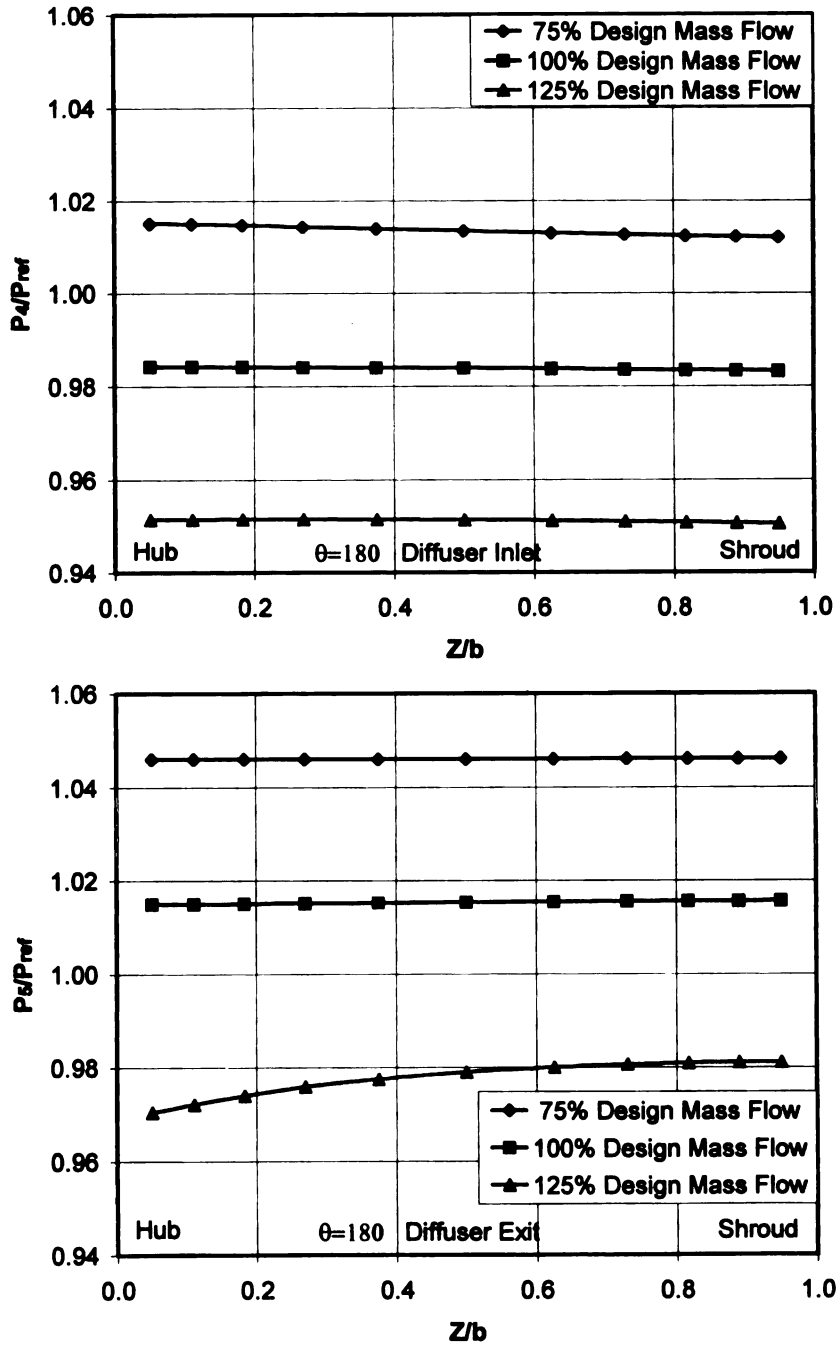

(a) Pressure variation in axial direction

Figure 5.5 Diffuser Flows (upper: inlet, lower: exit)

Figure 5.5 (cont'd)

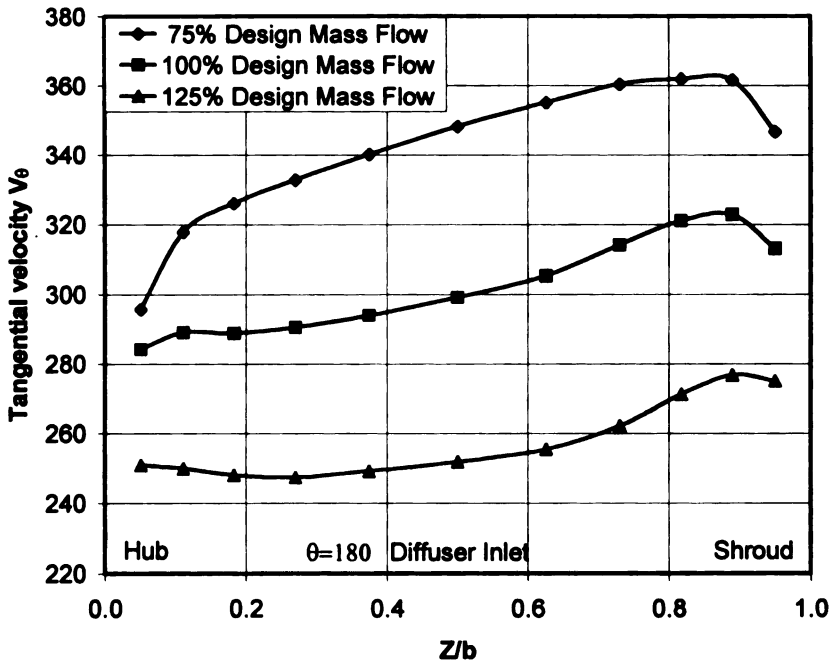

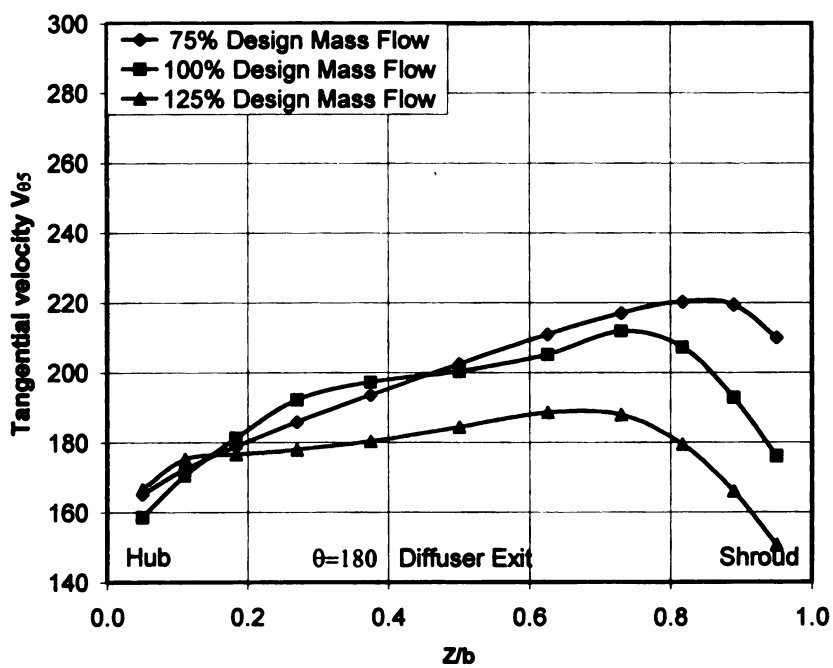

(b) Tangential velocity variation in axial direction

Figure 5.5 (cont'd)

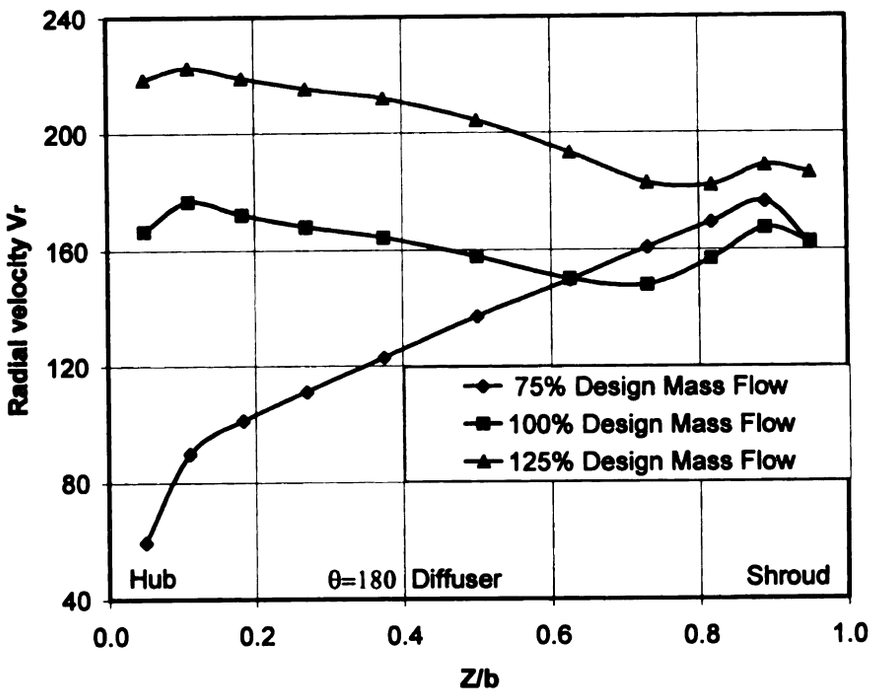

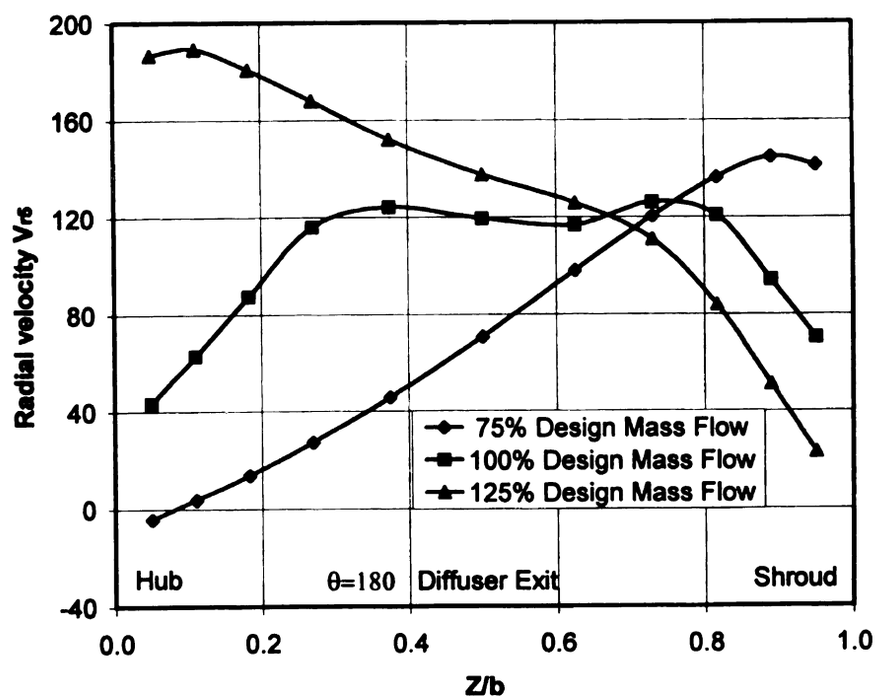

(c) Radial velocity variation in axial direction

Figure 5.5 (cont'd)

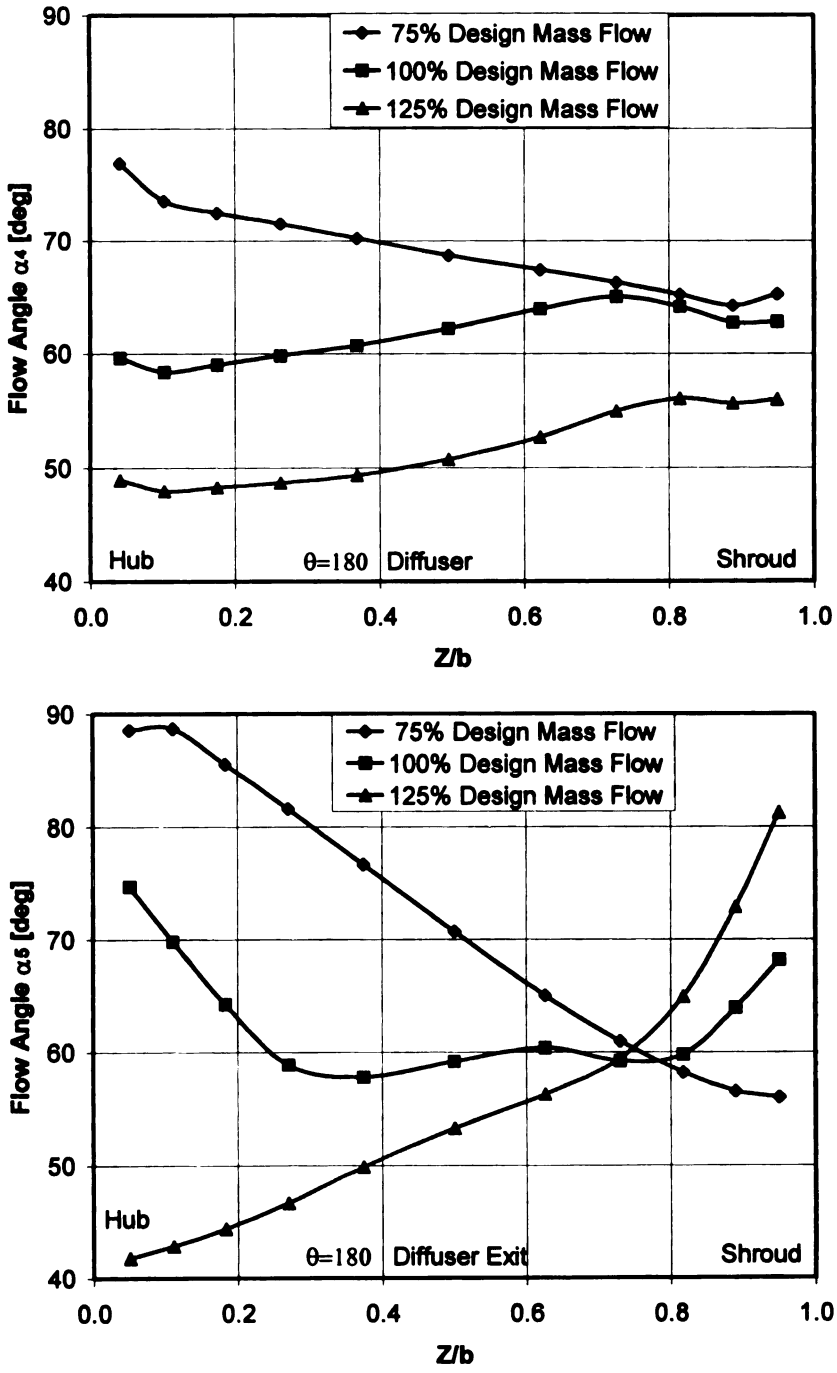

(d) Flow angle variation in axial direction

Figure 5.5 (cont'd)

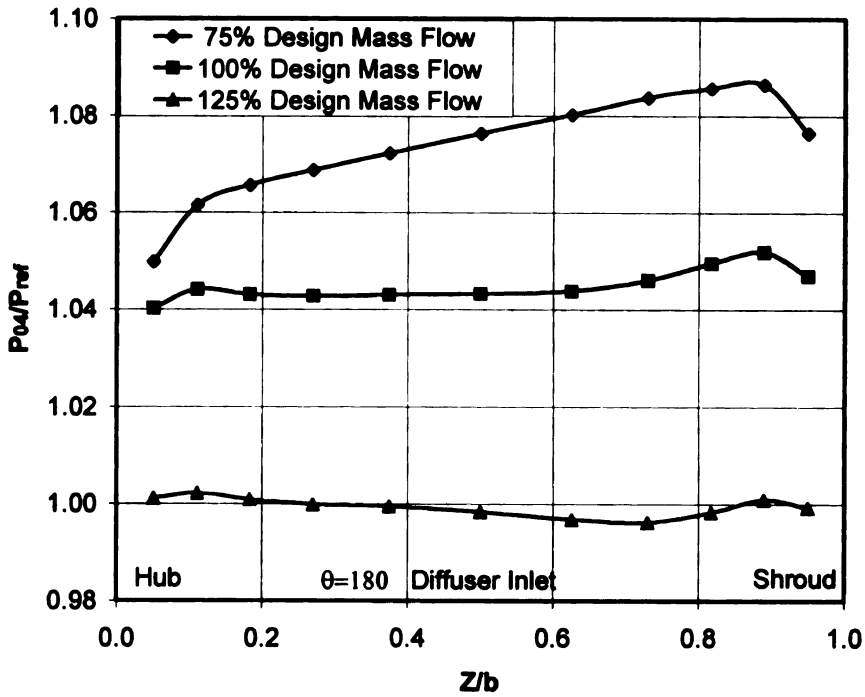

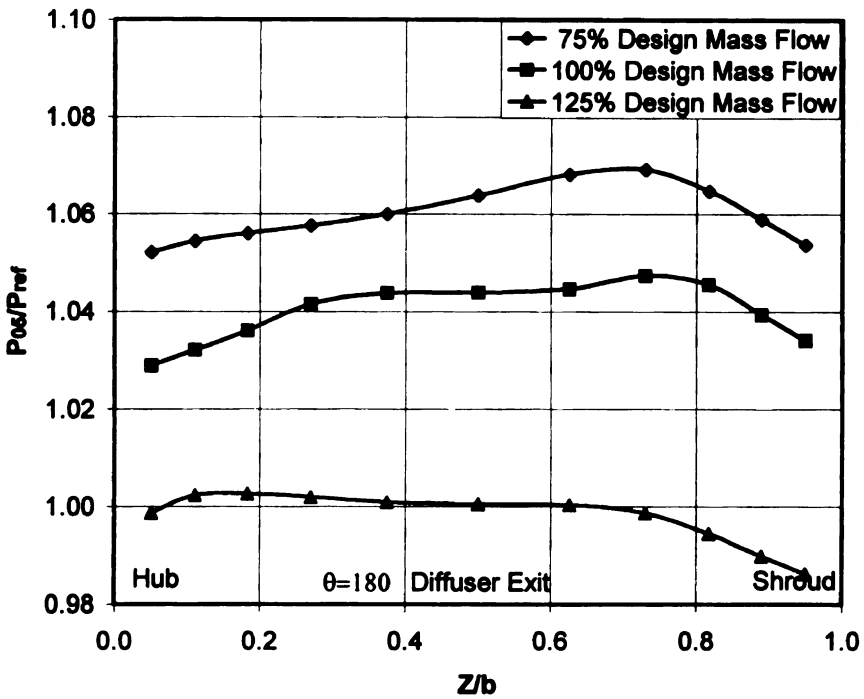

(e) Total pressure variation in axial direction

It seems that the mass migration inside the vaneless diffuser is not the volute upstream effect. However, the axial variations of static pressure recovery shown in figure 5.5a and total pressure losses shown in figure 5.5e are definitely the indications of the volute upstream effect because they are independent of the mass flow rate and the inflow pattern of the vaneless diffuser. The static pressure gradient at the vaneless diffuser is produced by the curvature of the section profile, hence the curvature of streamlines, in the 90 degree bend between the vaneless diffuser and the inlet of the volute. The high loss happened on the shroud side can be due to the higher diffusion. This is especially true for the lower mass flow rate because the inflow on the shroud side is more radial than on the hub side (figure 5.5d).

5.3.3 Flow in volute

The different inflow patterns result in different flow structures in the volute, even though the variation of the inlet patterns is influenced by the volute itself. The flow field from the CFD analysis is presented in terms of surface vectors (figure 5.6), through flow velocity contours (figure 5.7), static pressure contours (figure 5.8), and total pressure contours (figure 5.9) on selected sections. The flows in the vaneless diffuser are also shown together.

At all mass flows, the flow from the diffuser is turned from radial direction to horizontal in the 90 degree bend between the diffuser and the volute. At the design point from section θ=90° to θ=360° the flow shows a typical forced vortex flow pattern of clockwise rotation in the core. A narrow shell of free vortex flow also can be seen on the wall on section θ=90° and θ=180°. A mechanism will be proposed later to explain the

pattern differences of the swirling flow. Of interest is that the center of the forced vortex does not move in one consistent radial direction as the flow travels from θ=90° to θ=360°, which results from the design of the volute. As will be shown in Chapter 7, the volute centroid radius increases up to θ=95°, then it keeps going down. The flow pattern at the lower mass flow rate is similar to that at the design mass flow, but no free vortex region can be spotted on the wall.

The higher mass flow pattern differs from the others in the twin opposite rotating vortices on the first two sections. The clockwise rotating vortex initially occupies a small region; then as it goes downstream, its size grows. The counter-clockwise rotating vortex initially takes almost half the area at section θ=90°, then it gradually disappears. Instead, a free vortex zone appears on the periphery of the forced vortex. The production and diffusion of the counter clockwise vortex is believed to be an important source that causes the volute loss to increase significantly at higher mass flow. Because of the existence of the counter clockwise vortex, the forced vortex takes a smaller area, hence has stronger radial velocity gradient, resulting in higher friction losses. In terms of the free vortex flow pattern, the swirling flow at design mass flow is much more similar to that at higher mass flow. It means that this volute is still undersized for the design mass flow, even though it was designed to be oversized.

The common feature of the through flow velocity distribution at all the mass flow rates is that the contour curves align in axial direction and change to radial direction at the section of θ=360°. The curvature of the volute channel produces a radial pressure gradient, which is much stronger than the pressure gradient caused by the swirling on the section surface as shown in figure 5.8. As the flow approaches the exit, volute channel

curvature becomes smaller. Therefore the pressure gradient by this curvature is weakened; and the pressure gradient from the sectional swirling exhibits more power in shaping the contours, resulting in the change of the contour orientation. As the mass flow increases, the change of the contour orientation is reduced. It means that pressure gradient from the volute passage curvature is still strong enough to shape the through flow contours on section θ=360° at higher mass flows.

The total pressure contours (figure 5.9) shows that strong total pressure gradient zone occurs in the sections of small azimuth angles (θ=90°), indicating that the total pressure loss mostly happens in the small area sections immediately downstream of the tongue. For the higher mass flow, the strong total pressure gradient zone remains at section θ=180°, and concentrates at the center of the swirling flow vortex. The high loss fluids come from the twin vortex. Yong and Japikse (1982) proposed that at higher mass flow, the volute losses come from the loss of the meridional velocity of the inflow. The higher the mass flow rate is, the higher the meridional velocity is, the higher the losses are. At lower mass flow, the losses come from the loss of the meridional velocity and the pressure dumping loss, which is estimated as the one in a sudden mixing process. As the mass flow decreases, the velocity dumping losses are reduced, but the pressure dumping losses are increased. The balance grows as the mass flow reduces. The simulation result (figure 5.3b) supports this assumption, but it reveals a new loss mechanism: at higher mass flow, the loss increase comes from the twin vortex flow and the free vortex shell, which result from the inlet distortion. The reason for the increase of loss at lower mass flow will be investigated.

75% design flow

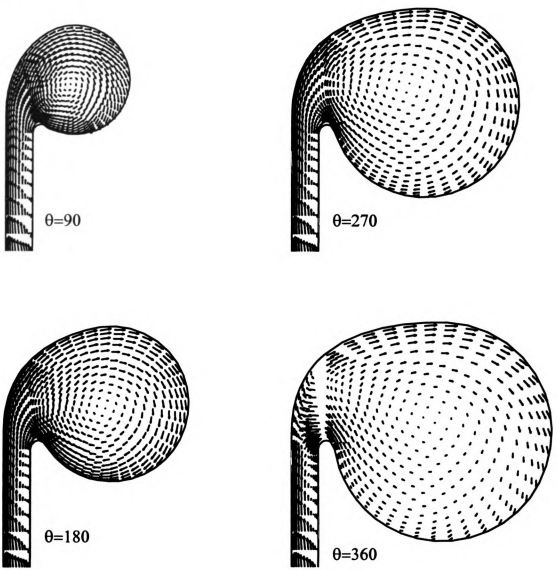

(a) 75% design mass flow

Figure 5.6 Surface vectors of swirling flows

Figure 5.6 (cont'd)

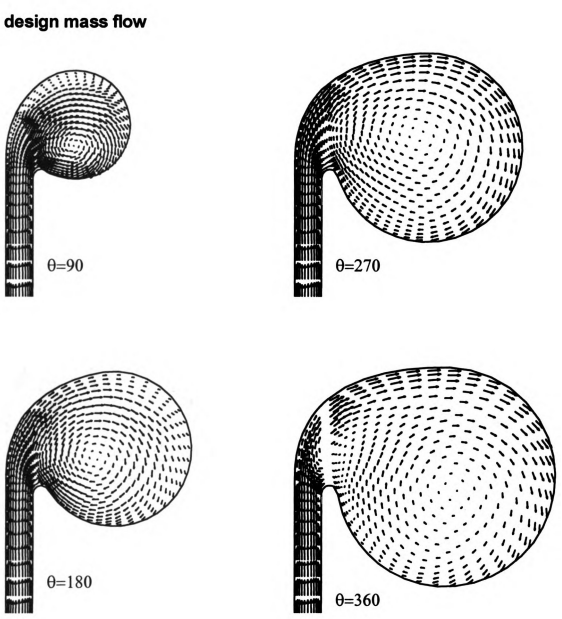

(b) design mass flow

Figure 5.6 (cont'd)

125% design flow

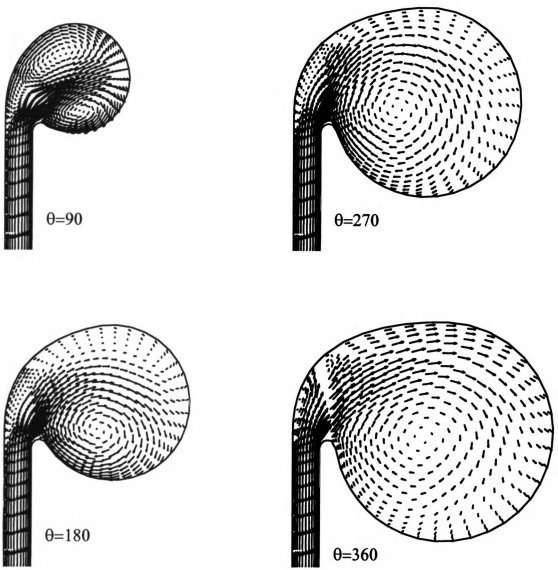

(c) 125% design mass flow

75% design flow

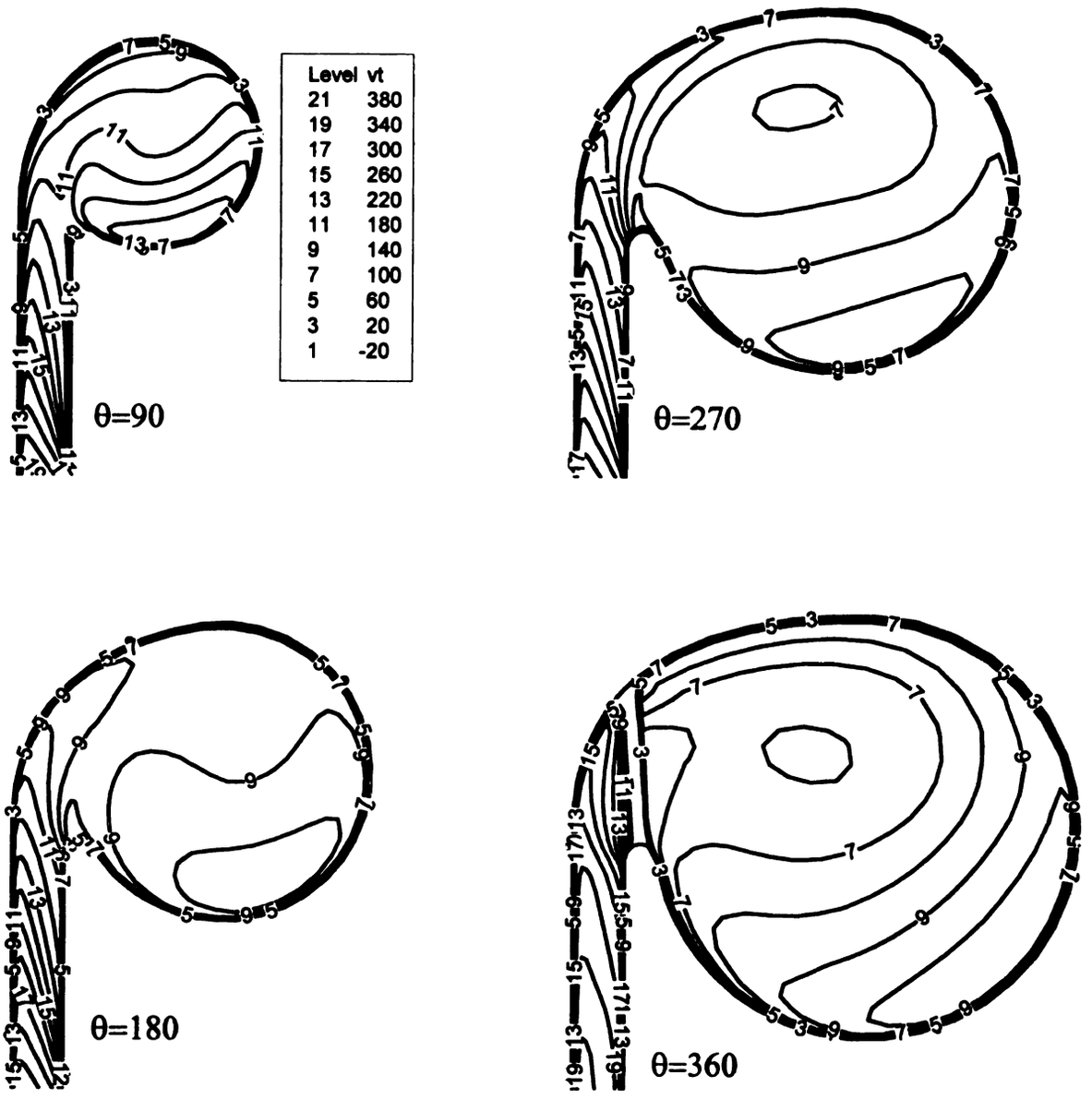

(a) 75% design mass flow

Figure 5.7 Contours of through flow velocity

Figure 5.7 (cont'd)

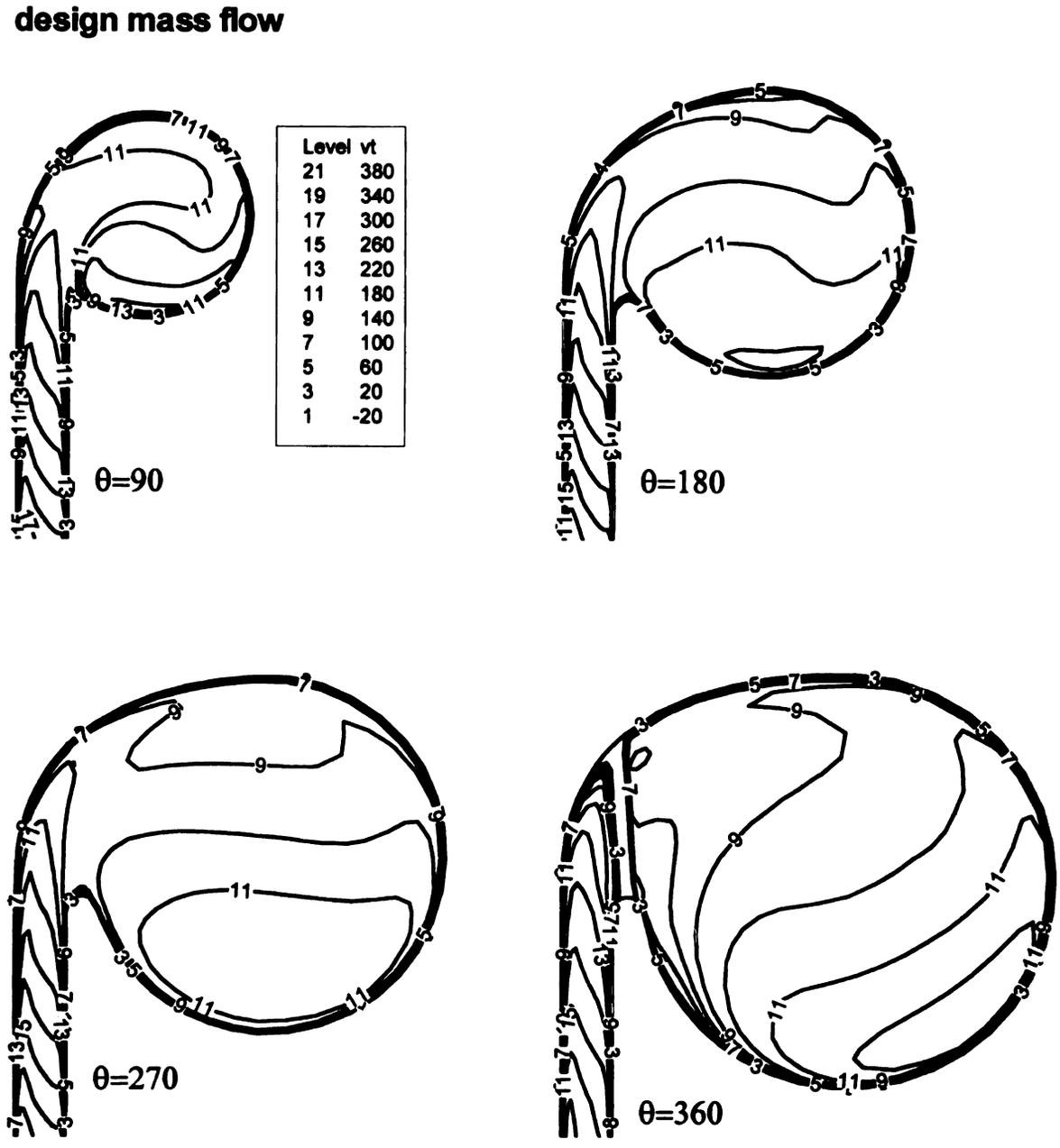

(b) design mass flow

Figure 5.7 (cont'd)

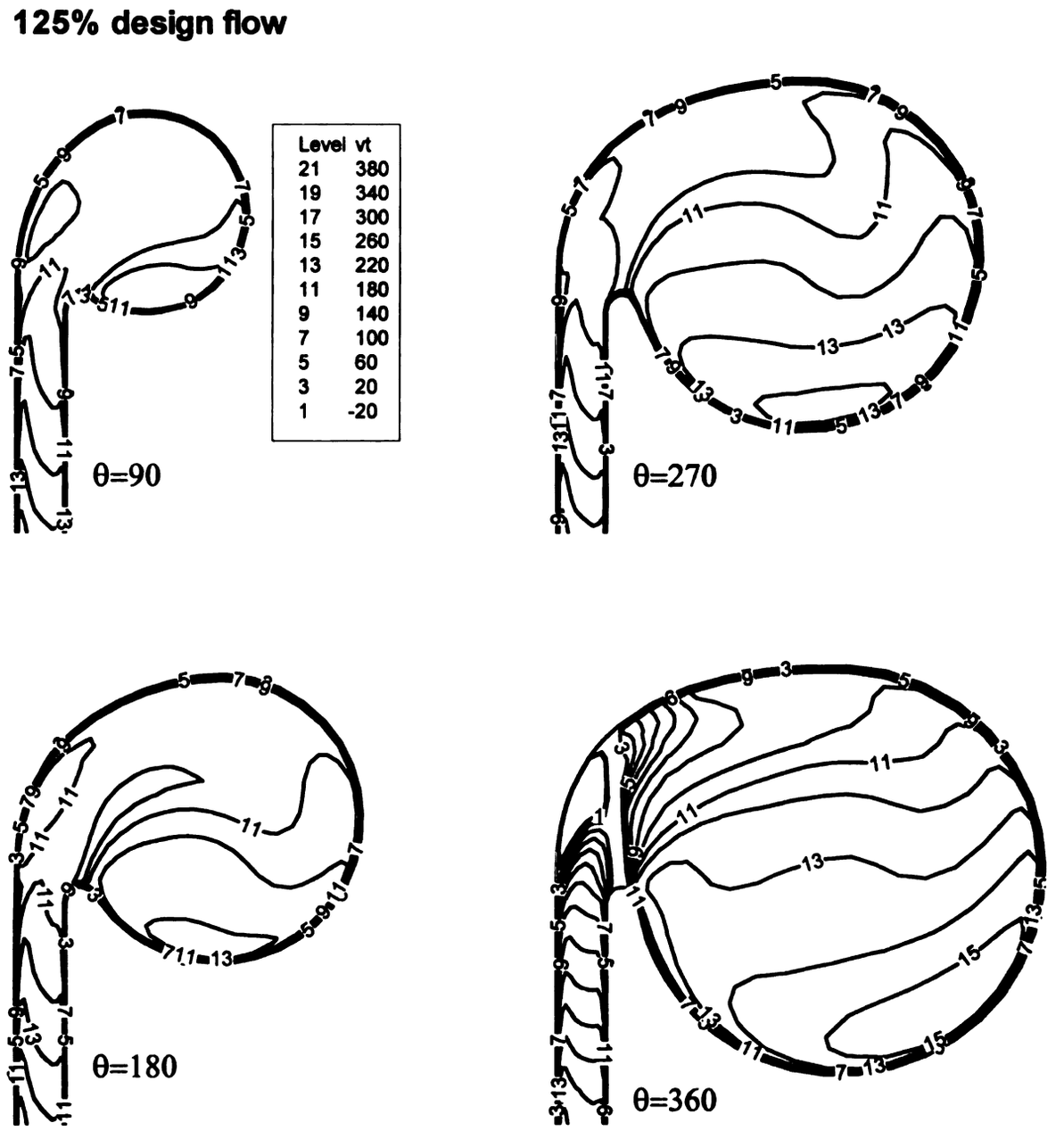

(c) 125% design mass flow

75% design flow

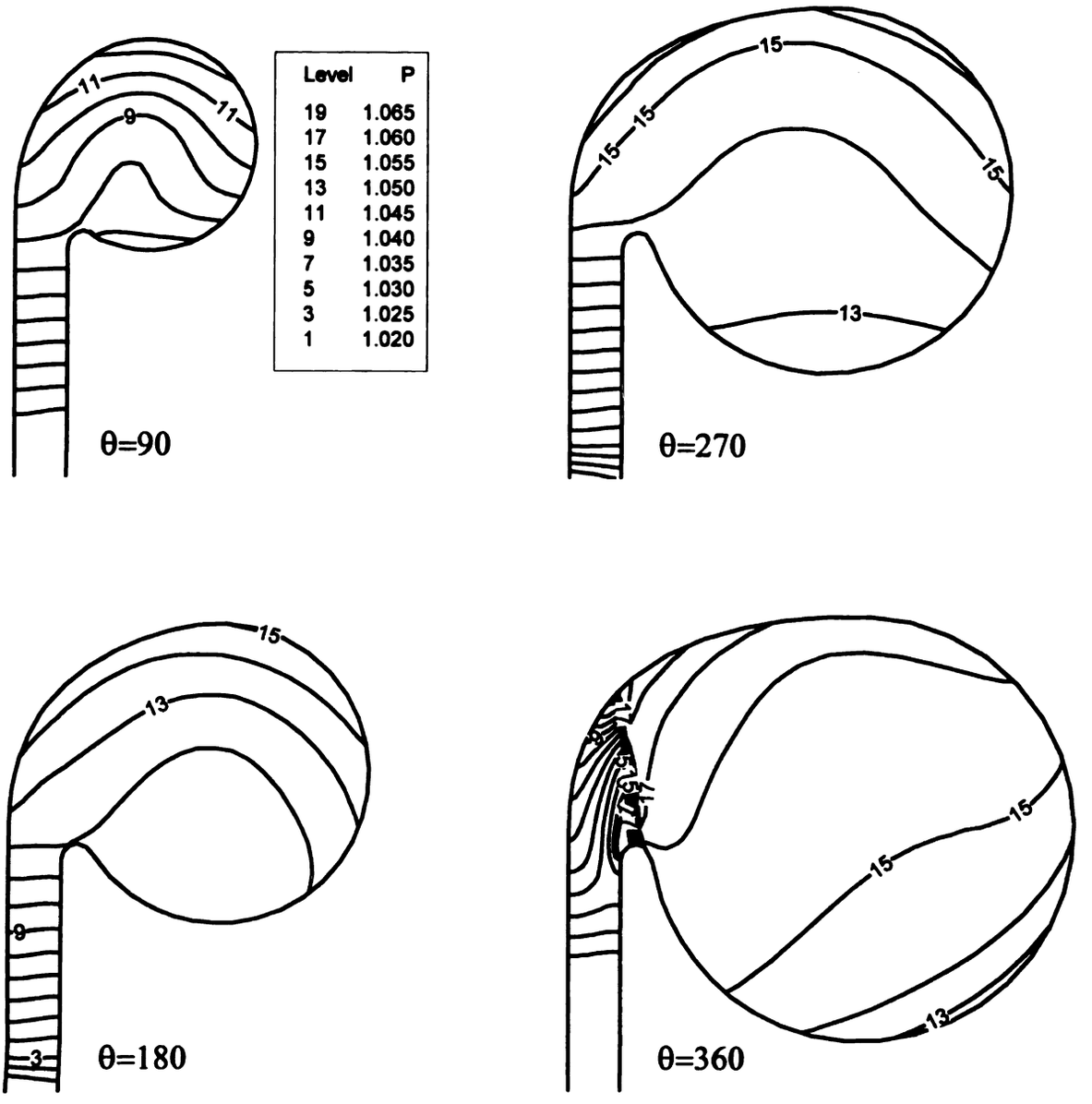

(a) 75% design mass flow

Figure 5.8 Contours of static pressure

Figure 5.8 (cont'd)

design flow

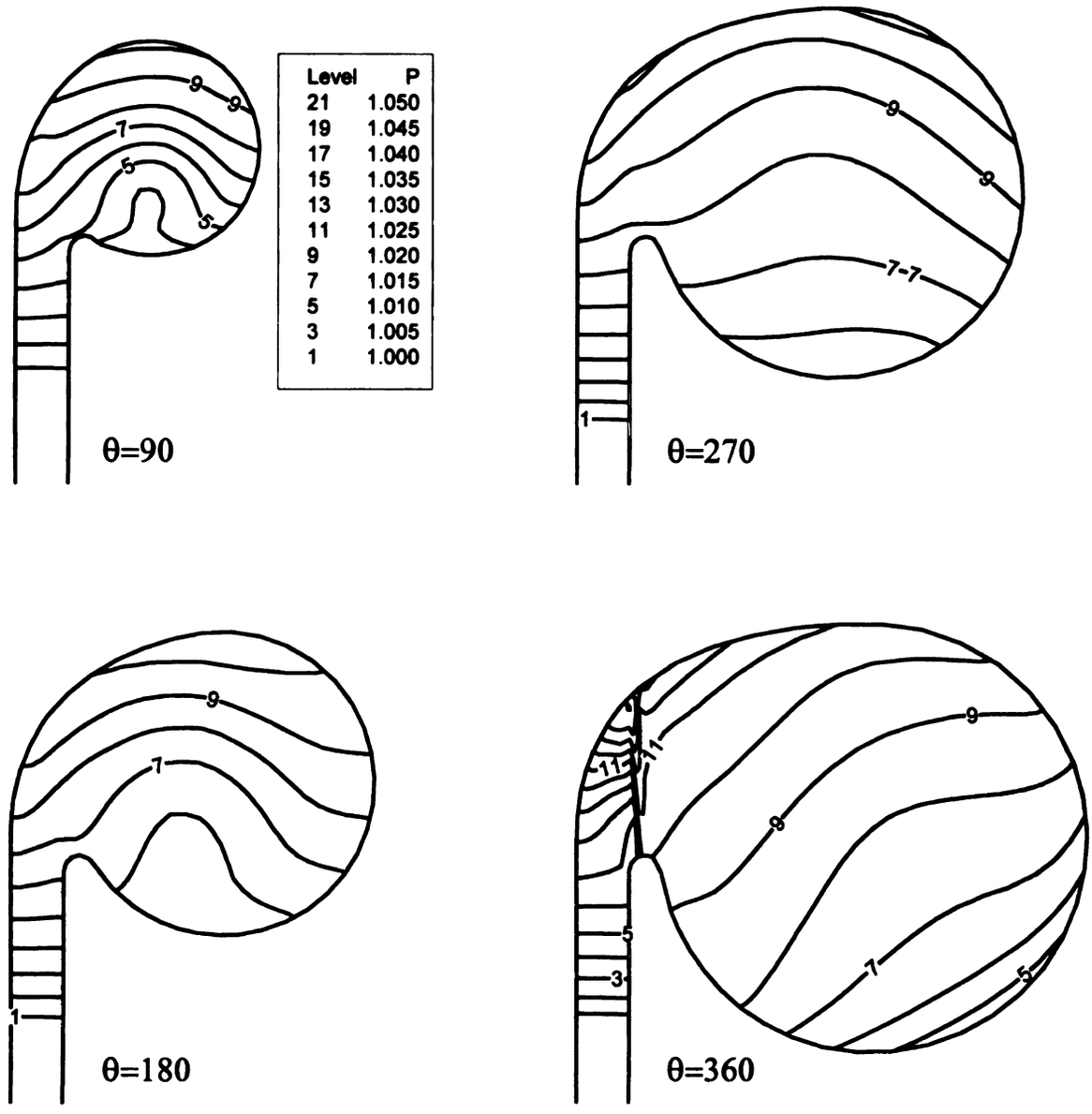

(b) design mass flow

Figure 5.8 (cont'd)

125% design flow

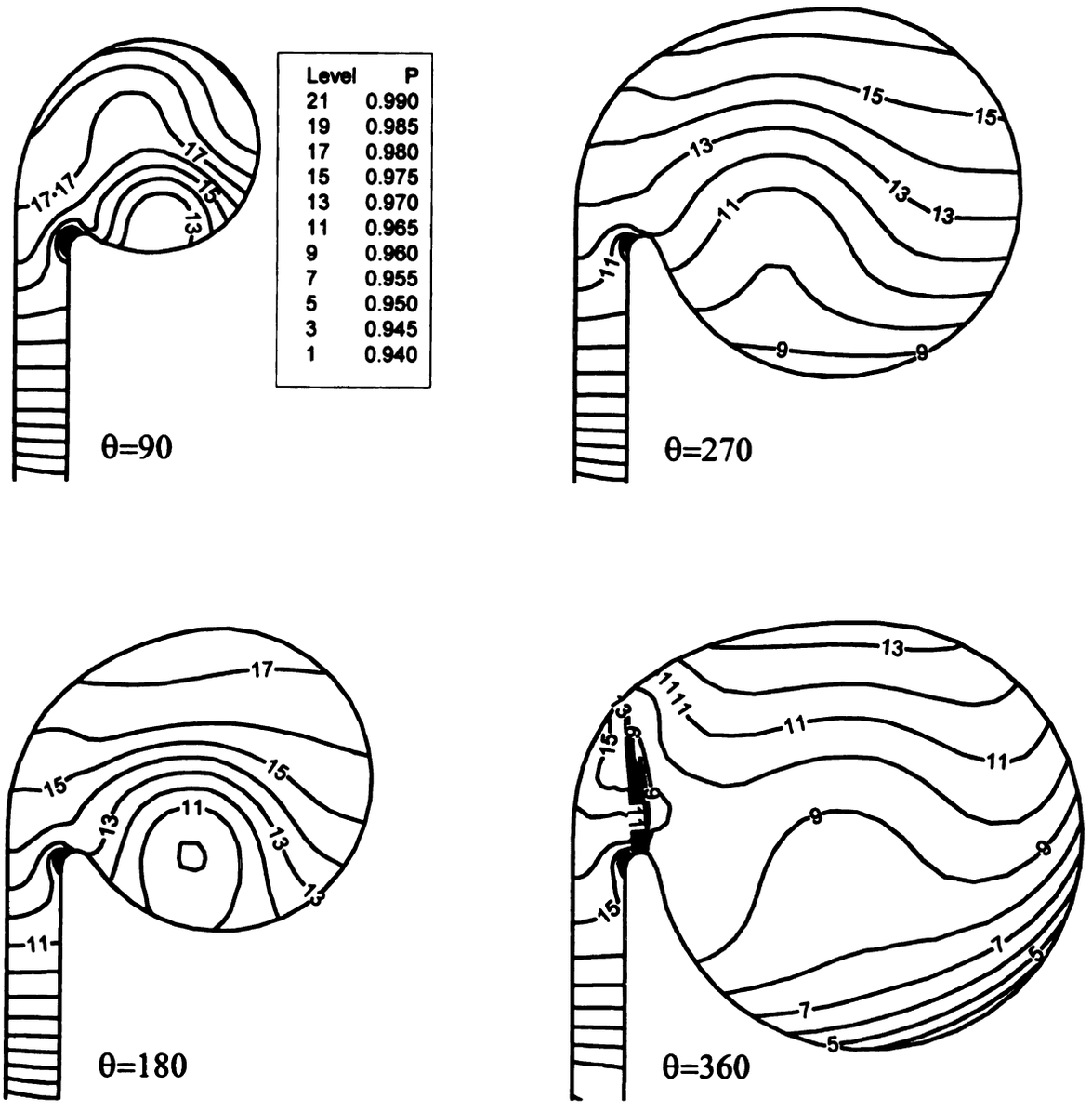

(c) 125% design mass flow

75% design flow

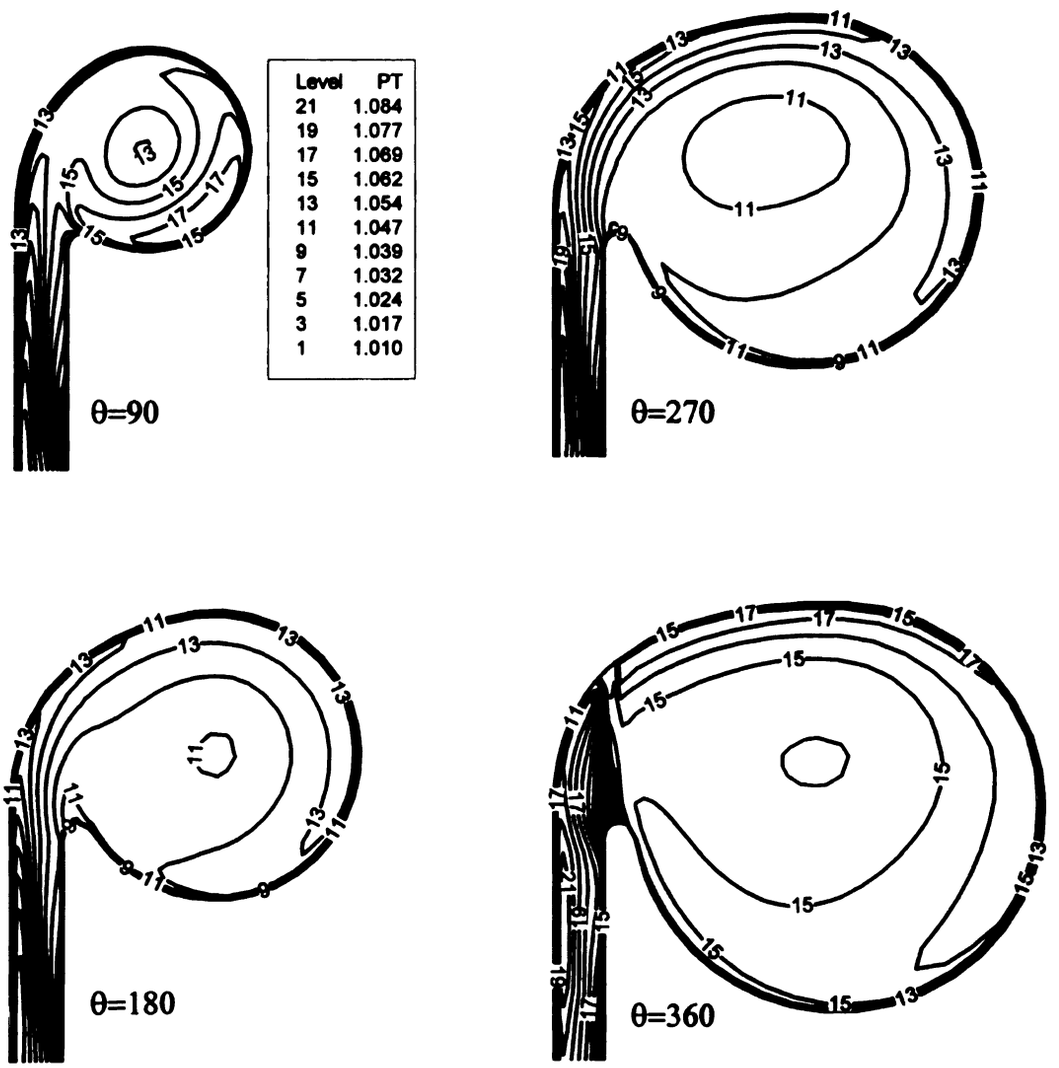

(a) 75% design mass flow

Figure 5.9 Contours of total pressure

Figure 5.9 (cont'd)

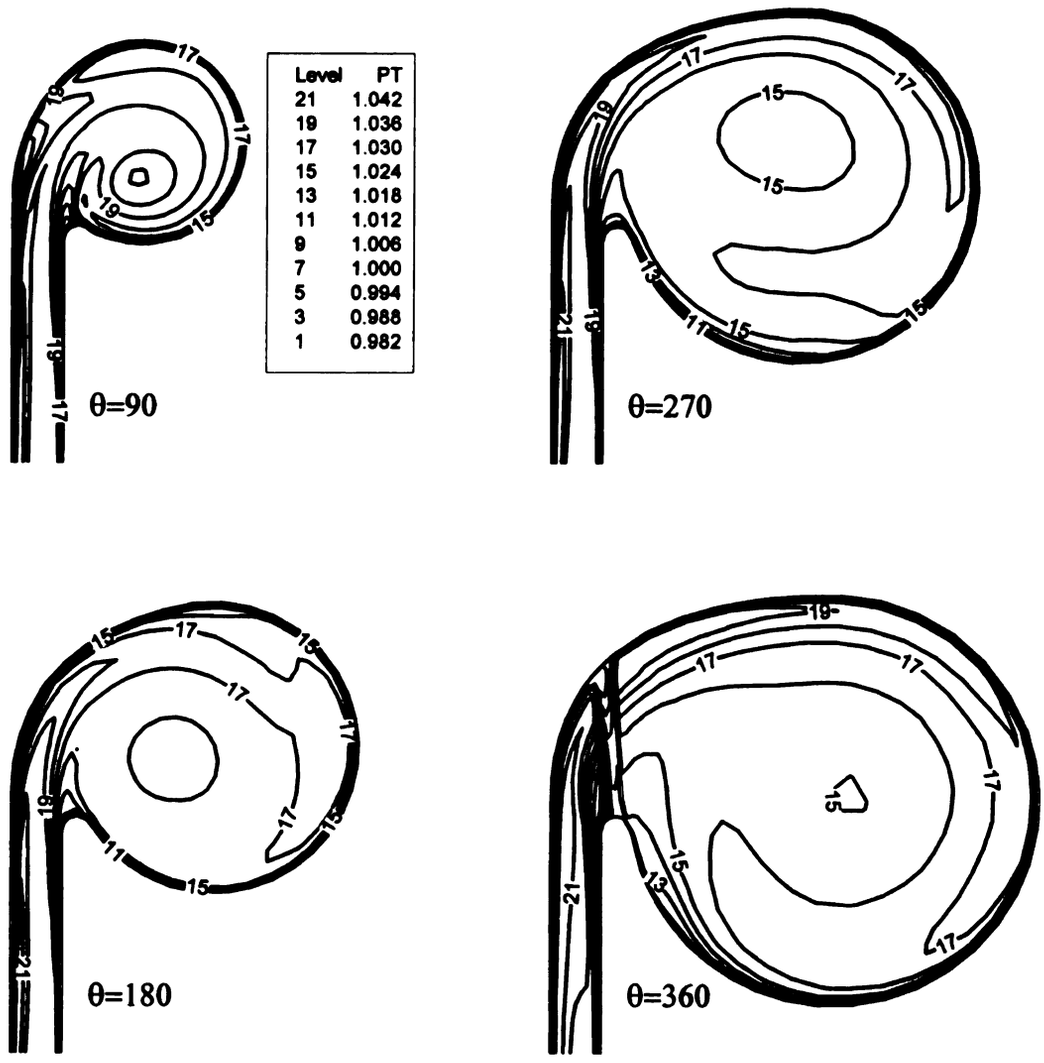

(b) design mass flow

Figure 5.9 (cont'd)

125% design flow

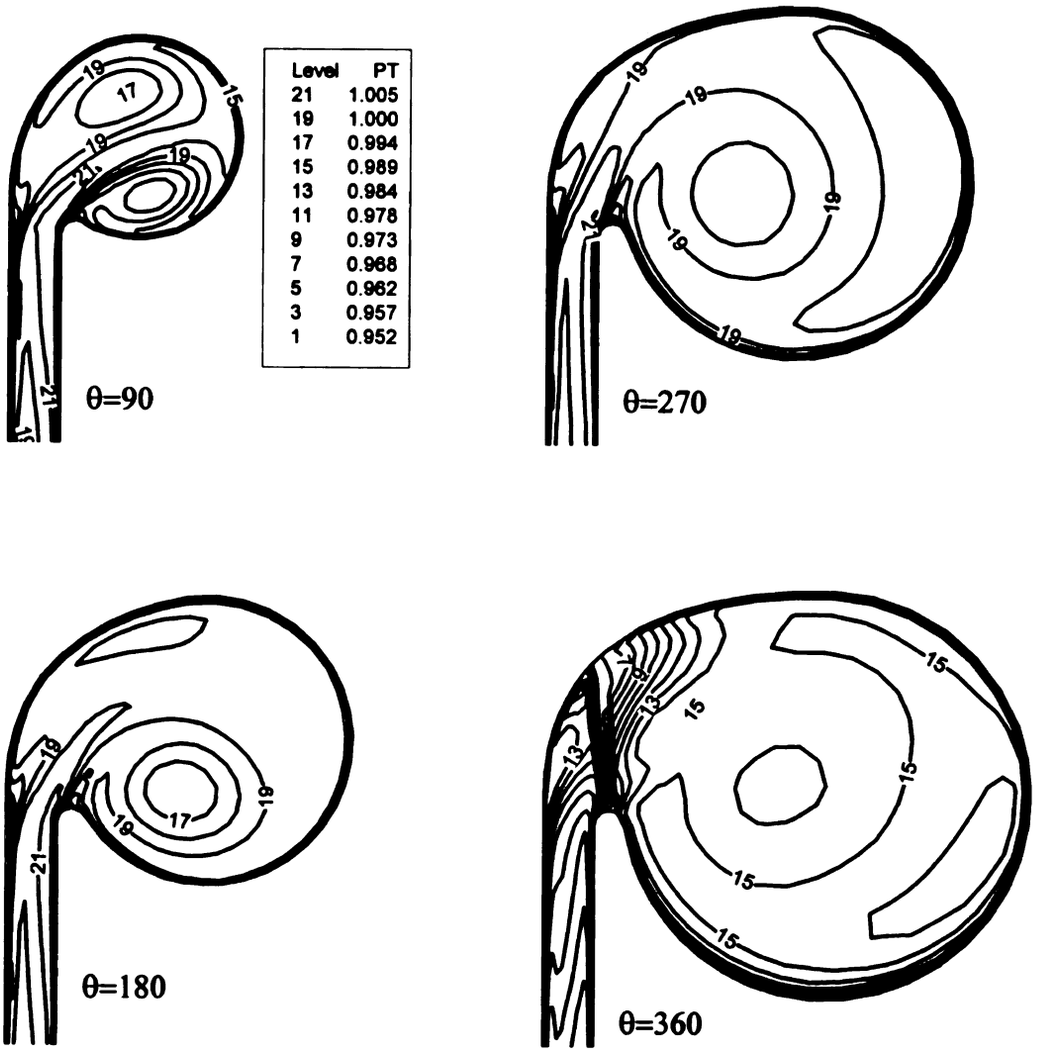

(c) 125% design mass flow

5.3.4 Swirling flow models

The different swirling flow patterns (single vs. twin vortices, free vortex vs. forced vortex) are now being further investigated using streamlines. Figure 5.10 shows the streamlines starting from section θ=250° and θ=335° (section D) at the three mass flow rates. Because the streamlines from section θ=335° will go through the critical surface (tongue section), they will experience the sudden pressure variation at off design conditions as shown in figure 5.4 Thereafter, streamlines refer to these from section θ=335°, unless indicated otherwise.

At design mass flow, the streamline pattern (figure 5.10a) can be summarized as:

- Streamlines on the hub side (blue) go into the volute first and fill the center region of section A while rotating at high frequency. They compose the forced vortex.
- Streamlines on the shroud side (red) go into the volute later, and rotate at larger radii and at lower rotate frequencies. They compose the free vortex.
- After they travel 360°, the streamlines from the hub side go closer to the forced vortex center; these from the shroud side have been entrained into the forced vortex. The streamlines from θ=250° (yellow) rotate around these from θ=335°.
- By comparing the relative positions of streamlines from shroud side on section B and C, it can be seen that some of the streamlines rotate counter-clockwisely (From section B to C, they are supposed to go farther away from the shroud wall in the axial direction if they rotate clockwisely).

The streamlines at lower flow (figure 5.10b) are described as:

- Since the inflow is axially distorted, the streamlines are twisted in the vaneless diffuser, resulting in the streamlines on the shroud side going into volute first. But all the streamlines (from both hub and shroud sides) rotate at an identical frequency, indicating that the flow is of solid body motion (forced vortex). The only difference between the streamlines is the phase lag.

- The fluids on the shroud side have higher total pressure, which prevents their streamlines from counter-clockwise rotation (this will be explained).

- The streamlines from θ=250° separate into two groups. The shroud side group rotates around the streamlines already in the volute and exits from the volute. The hub side group is of lower total pressure (figure 5.4e) therefore cannot reach the volute under the radial pressure gradient before it arrives at the tongue section. It simply degenerates into recirculation mass, and moves in the center of the forced vortex.

The streamlines at higher mass flow (figure 5.10c) show a rather different pattern (for clearness, the streamlines from θ=250° are not plotted), and are described as:

- Streamlines on the hub side go directly into the cone diffuser, resulting in a reduction in mass flow inside the volute. Streamlines on the shroud side go into the volute, rotating in counter-clockwise direction.

- Streamlines from the mid passage follow different paths: the streamline close to the hub exits to the cone; the one close to the shroud side goes into volute; the one at mid goes into volute first, then turns back, goes over the tongue, and exits from the volute.

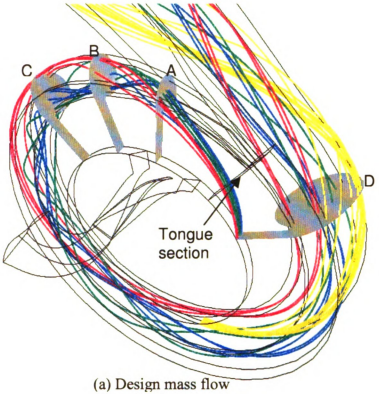

(a) Design mass flow

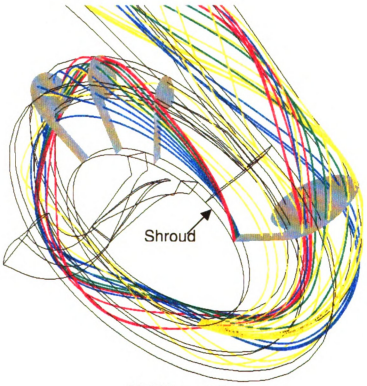

(b) 75% mass flow

Figure 5.10 Streamlines (Images are presented in color)

Figure 5.10 (cont'd)

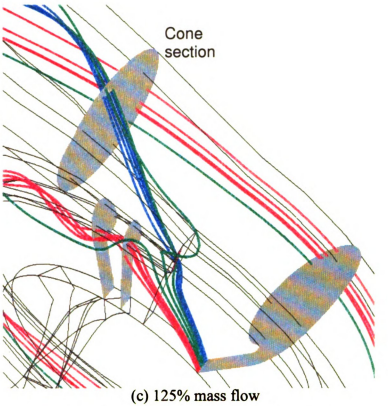

(c) 125% mass flow

- After 360°, the streamlines going inside the volute are found at larger radius with respect to the forced vortex center. The fluids on these streamlines compose the free vortex flow.

At all operation points, the streamlines that originate from other circumferential positions and are not exposed to the tongue pressure distortion exhibit similar flow patterns to their peers in figure 5.10, but they do not show the twin vortex structure. The essence of the observed flow patterns at different mass flow rates is the same as Van den Braembussche's model: new coming fluids rotate around the old ones. However, the new models take into account the axial distortion of vaneless diffuser inflow and the circumferential static pressure distortion due to the tongue. At design and higher mass flows, the hub side streamlines from section θ=335° start the opposite rotation

downstream of the tongue, then develop into free vortex flow, and at last are entrained into the forced vortex. Because of the opposite rotation, the counter-clockwise rotating streamline suffers more energy losses. The stronger the opposite rotation, the higher is the loss. This explains why the loss is significantly increased at higher mass flow. The recirculation is found at the lower mass flow; the flow in the volute does not exit from volute, instead, it turns into the volute again. This explains why the loss is slightly increased at lower mass flow.

Figure 5.11 explains the generation of the opposite rotation vortex using force analysis on the section A downstream of the tongue. The fluid particle is balanced under the act of centrifugal forces and pressure gradient forces

$$\vec{F}_p + \vec{F}'_p + \vec{F}_t + \vec{F}_s = 0 \tag{5.13}$$

Here, $\vec{F}_t, \vec{F}_s$ are the centrifugal forces due to the through flow and the swirling flow. $\vec{F}_p, \vec{F}'_p$ are the force due to the pressure gradients caused by the through flow and swirling flow, respectively. Because of the pressure gradient from the through flow, which is guided by the volute channel, a particle moves from A to B to C will be decelerated, and from C to D to A will be accelerated. If the particle does not possess enough through flow velocity or if its path is of high radius of curvature than that of the volute passage, its centrifugal force is reduced; thus, it can be retarded or turned back when is moving along the path A-B-C. Therefore, for the fluid particles, the left side of the volute is an unstable region, the upper left region being the most unstable.

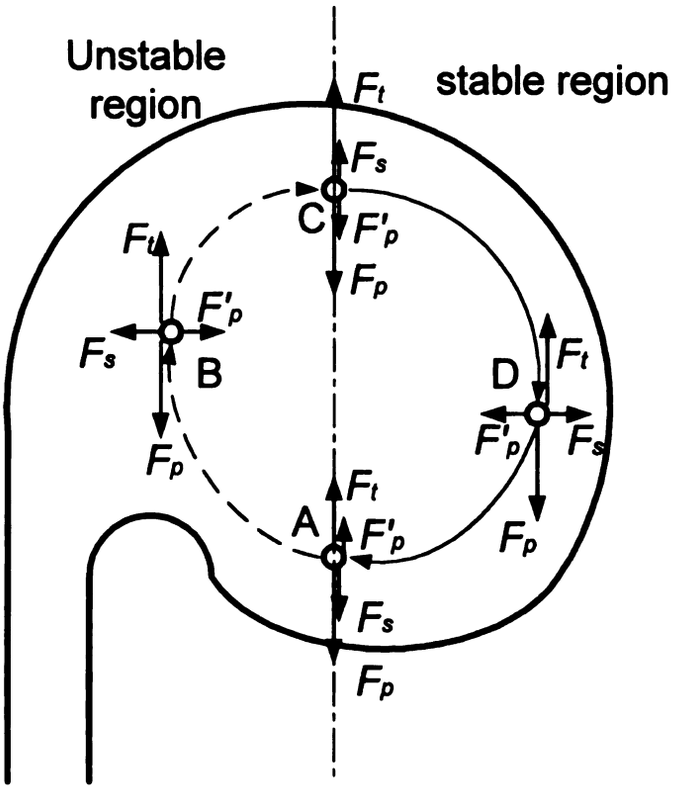

Figure 5.11 Force analysis

At lower mass flow, the particle passing through the tongue section will be accelerated because of the circumferential pressure gradient (figure.5.4). Therefore, it is strong enough to go through the adverse pressure gradient region. This is why no opposite rotation happens at this flow rate.

At higher mass flow, the adverse circumferential pressure gradient will decelerate any particle going through the tongue section. Therefore, the particles in the unstable zone will not have enough kinetic energy to resist the adverse radial pressure gradient. The heavily retarded particle will be pulled tangentially by the inner particle of forced vortex flow, resulting in the free vortex flow on the wall or will be entrained by the free vortex flow. The particles that are turned back by the adverse radial pressure gradient compose the opposite rotation flow.

5.4 Conclusions

A numerical investigation of the flow structure inside the stationary components of a centrifugal compressor is performed in this Chapter. The following conclusions have been reached:

- At all mass flow rates, the losses occurred in the volute accounts for a large portion of the total losses in the stationary components. As the mass flow rate increases up to the design point, the loss in the vaneless diffuser is reduced; after that the loss stays constant. On the contrary, the loss in the volute decreases before the mass flow rate reaches the design point; then it consistently increases faster as the mass flow increases.
- The upstream effect of volute is indicated by the higher static pressure rise and higher total pressure loss on the shroud side of the vaneless diffuser.
- In the vaneless diffuser, the inlet distortion is always exaggerated at all mass flows.
- In the volute, the flow basically follows Van den Braembussche's model. A new model is proposed to take into account the axial distortion at the vaneless diffuser inlet and the circumferential pressure distortion at off-design conditions. At lower mass flow, the lower total pressure fluids from the hub side upstream of the tongue cannot exit the volute. Instead, they move into the force vortex center, resulting in recirculation. At higher mass flow, a twin vortex structure is found at downstream of the tongue. The recirculation and the twin vortex structure are attributed to the increase of total pressure losses at off-design conditions.

Chapter 6

STEADY-STATE VOLUTE/IMPELLER INTERACTION

6.1 Introduction

The study of volute flows in centrifugal compressors is highlighted by the fact that the circumferential distortion occurs inside the volutes and vaneless/vaned diffusers at off-design conditions. This distortion propagates upstream and causes flow fluctuation in impellers. The efficiency drop of a centrifugal compressor at off-design conditions can be attributed to many factors, but the flow distortion caused by volute is definitely among them.

The circumferential pressure distortion in the volute has attracted much attention recently. Van den Braembussche and Hande (1990) reported and explained the pressure distortion at the vaneless diffuser exit of a straight model at off-design conditions. At lower/higher mass flow, the flow inside the volute is decelerated/accelerated according to continuity, resulting in pressure increasing/decreasing according to the conservation of momentum. Ayder et al. (1993) confirmed that the vaneless diffuser exit flow was distorted in a centrifugal compressor with a volute of elliptic cross sections.

The interaction between volute and vaneless diffuser can be in both axial and circumferential directions. The axial interaction is indicated by the dependence of the volute flow structure on the diffuser inflow (Gu, et al., 2000). The circumferential interaction is suggested by the static and total pressure distortion at the diffuser exit. The phase lag between the static and total pressure distortions has been observed by Ayder et al. (1993) and Hagelstein et al. (1999), respectively. At high mass flow, Ayder observed a

maximum total pressure region around 70° downstream the tongue, which is about 30° lag of the maximum static pressure. It was explained as the variation of the impeller efficiency. Due to the mass flow variation along the circumference of the impeller, blades are operating at different conditions. At lower mass flow, Hagelstein noted that the total pressure is seen to increase due to the increase in the throttling effect circumferentially, and the minimum value of the total temperature and (total) pressure is found at about θ=120°, which corresponds to a position behind the tongue. It is explained that the phase shift is due to the impeller response to the perturbation of the tongue, which is transmitted along a streamline to the diffuser exit.

The volute/impeller interaction essentially is an unsteady phenomenon. Fatsis et al. (1997) suggested using the acoustic Strouhal number to quantify the relative effects of the rotation and pressure wave propagation. The acoustic Strouhal number was defined as

$$St = \frac{fL}{c} \tag{6.1}$$

Here, L is normally defined as the length of a blade passage, whereas f is the number of rotations per second times the number of perturbation waves around the circumference. For the impeller discussed in this Chapter, the Strouhal number is around 0.133 when f is replaced by rotation frequency. It indicates that the pressure wave propagation is much faster than the rotation of the impeller. That is, the pressure perturbation finishes traveling over the passage at almost the same time as when the impeller moves to a new position. Therefore, the "frozen rotor model" provided by CFX-TASCflow (1999) can be used to study the pressure distortion due to the volute.

In this Chapter, the flow fields of a centrifugal compressor stage are simulated at three mass flow points using the *frozen rotor model*. Tongue flow field is investigated to

explain the circumferential pressure distortion at the vaneless diffuser exit. The effect of pressure distortion due to the volute is observed in the impeller passages as each passage working at different exit pressure at off-design conditions.

6.2 CFD Models

A single stage pipeline centrifugal compressor, manufactured by Solar Turbines Incorporated, is studied to investigate the circumferential pressure distortion due to the volute. It has a small total-to-total pressure ratio of 1.4 but allows higher mass flow. The impeller has 11 backward swept blades of 53.5°. The tip Mach number at the design point is 0.65 and the diffuser ratio D_5/D_2 is 1.9. The impeller grid of a single passage was generated by the commercial code, Bladegen. A self-written code then read in the single passage grid and sweeps to 360° in such a way that the impeller has a uniform pitch. The volute grid is generated by a self-written code. A butterfly section is used to reduce the grid skewness. The size of the model is $87 \times 16 \times 13 = 18{,}096$ points for one passage of the impeller and 145,535 for the volutes, and the number of total points is 344,591. Figure 6.1 shows the grid for this study. The convention of the compressor is shown in figure 6.2 which is the same as figure 1.1.

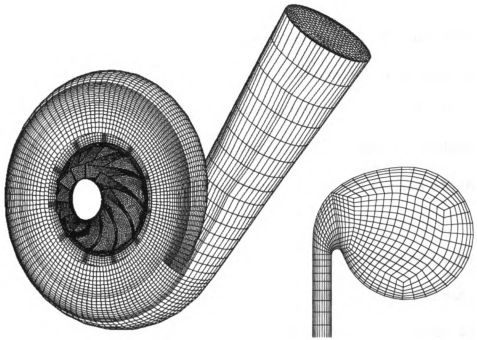

Figure 6.1 Compressor grid

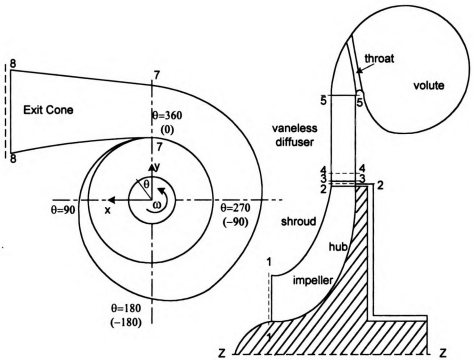

Figure 6.2 Compressor convention

The commercially available CFD software, CFX-TASCflow, is employed for this study. The validation of this code for the configuration of centrifugal compressors can be found, for example, in the work of Flathers (1994, 1999). The code solves the Reynolds averaged Navier-Stokes equations in the primitive variable form. The effects of turbulence are modeled using the standard k-ε turbulent model. To make the simulation timely economical, wall function is used to resolve the wall flows. This explains why the grid in this study is relatively coarse.

To investigate the pressure distortion due to the volute, the impeller and volute must be solved as a coupled system. TASCflow provides a simulation model, referred to as Steady-State Multiple Frame of Reference (MFR) analysis. A sliding interface was established between the two components. Numerical details of this methodology were outlined in Galpin et al. (1995). The frozen rotor model achieves a frame change across the interface without a relative position change over time and without any interface averaging. Therefore, all the impeller passages have to be modeled. Local flow features are allowed to transport across the interface; thus, pressure nonuniformities in the volute are allowed to propagate upstream to the impeller, which results in different exit flow conditions for each impeller passage. This model is an exact representation of the case Sr=0 in which either the sound speed is infinite or the rotation speed is zero and is an approximation when the Strouhal number is small enough as in this case. Flathers and Bache (1999) used this model to predict the radial force of impeller.

The inflow boundary condition was assigned upstream of the impeller at station 1-1, which is about one chord upstream of the impeller, in order to capture the flow distortion at the impeller leading edge. Uniform total temperature, total pressure and flow

angles are assigned on this station. Mass flow rate was imposed on the exit of the cone as the outflow boundary condition. At off-design points, only the assigned exit mass flow rate was changed. On the sliding interface between the volute and impeller, the frozen rotor model is employed as discussed above.

The code was run at three mass flow rates: one being design mass flow, one being 75% design mass flow, and one being 125% design mass flow. It took about 48 hours to iterate 400 steps to reduce the maximum residual to 1e-4 at design point on Sun Workstation 450 using one of its processors. At lower mass flow, it took much longer time.

6.3 Results and discussion

As will be shown, the predicted performance of the compressor is too close to the experimental one at lower mass flow. The fact is that the CFD model didn't incorporate the leakage loss in the cavity; the predicted performance should be better than the experimental one. This motivated the authors to investigate the steady-state interaction to understand 1) the propagation mechanism of the perturbation with lower acoustic Strouhal numbers and 2) the characteristic of the numerical model. The performance of the compressor is therefore presented first. Contributions to the performance variation are then explored, which include the flow in the diffuser, tongue flow, and the flow in the impeller passages.

6.3.1 Compressor performance

The experiment was run at 10901 rpm, while the CFD study was conducted at 10530 rpm. The overall performance is therefore compared in terms of non-dimensional parameters as shown in figure 6. 3. The inlet flow coefficient and isentropic head coefficient are defined as

$$\Phi = \frac{Q_1}{\frac{\pi}{4} \times D_{tip}^2 \times U_{tip}} \tag{6.1}$$

$$\Psi = \frac{2C_p \times (T_{08} - T_{01}) \times \eta_{isen,t-t}}{U_{tip}^2} \tag{6.2}$$

It can be seen that the predicted compressor performance from the frozen rotor model shows a different tendency; the isentropic head drops faster as the operation points shift left. The comparison of the impeller performance between stage model (Gu, et al.,

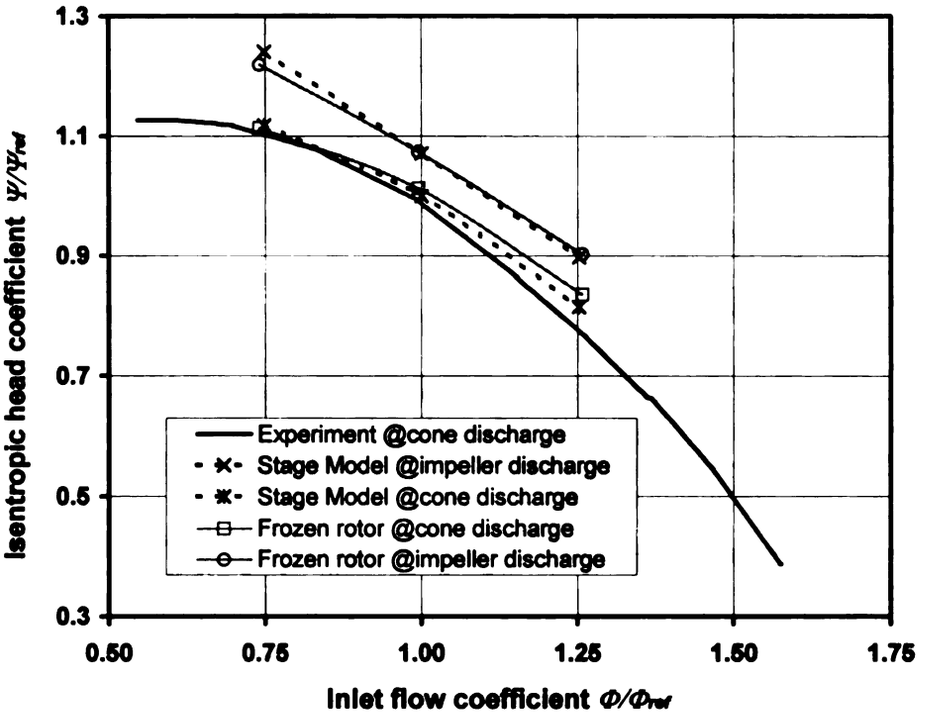

Figure 6.3 Compressor performance

2000) and frozen rotor one indicates that the frozen rotor model predicted less isentropic head at lower mass flow and higher head at higher mass flow. The difference between the curves at impeller discharge and the cone discharge represents the losses in the vaneless diffuser and volute. It can be seen that the losses in the volute and vaneless diffuser are predicted higher at lower mass and lower at higher mass flow, compared to the stage model. The essential difference between stage model and frozen rotor one is their responses to the pressure perturbations of different Strouhal numbers. In the stage model, the pressure perturbation from the tongue dies out at the grid interface, preventing the impeller from any disturbance. The frozen rotor model assumes that the perturbation propagates into the impeller at an infinite speed, which is a good approximation for low frequency perturbations. Therefore, the generation and propagation of the pressure perturbations will be investigated.

6.3.2 Perturbation generation

The generation of the pressure perturbation has been clearly stated by Van den Braembussche and Hande (1990). At off-design conditions, the pressure begins a gently circumferential increase or decrease downstream of the tongue and ends up with a maximum or minimum around the tongue. The tongue region therefore is the location where the radical pressure distortion occurs. The circumferential position of the extreme varies with the flow rate. Figure 6.4 shows the pressure distortion on the surface in the mid of the vaneless diffuser at lower mass flow. The impeller passage is numbered from 0 to 10 for later use.

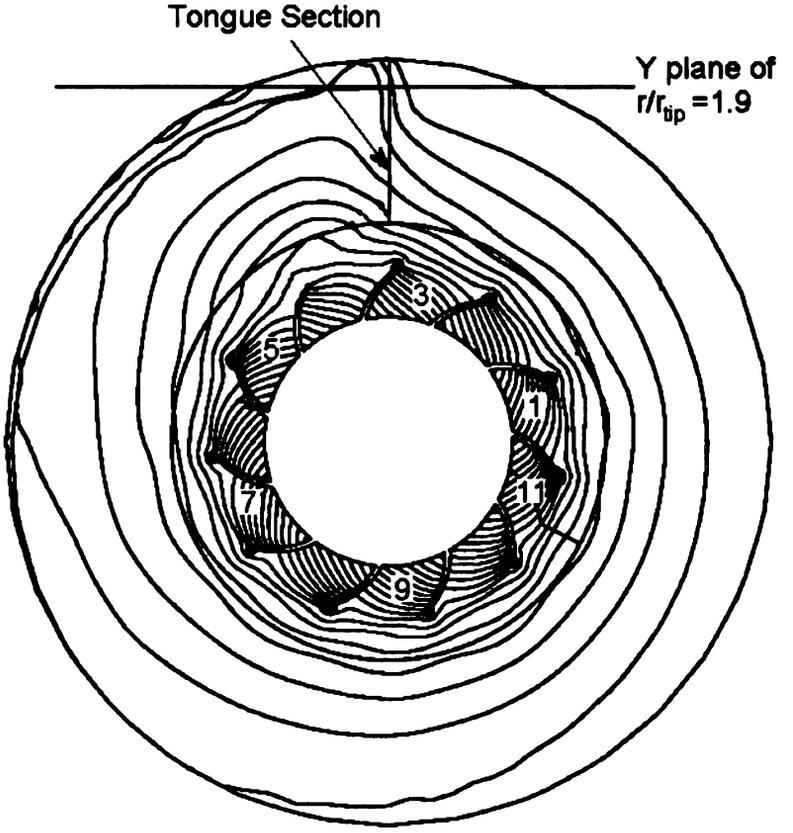

Figure 6.4 Pressure distortion on a z-surface at 75% mass flow

The pressure contours are plotted in figure 6.5a on a y-plane surface of 1.9 r_{tip} to the z-axis. This plane cuts the tongue. It can be seen that at lower mass flow, the pressure distribution is rather uniform at the beginning of the conical diffuser. Radical flow expansion happens around the tongue in the volute passage of smaller area. Flow is strongly accelerated due to this pressure gradient, resulting in flow deflection from the conical diffuser passage to the volute passage of smaller area as shown in figure 6.6a. The beneficial effect of the mass immigration to the volute passage is that the deflected mass increases the total mass flow rate inside the volute; the circumferential pressure distortion is therefore smoothed. The detrimental effect is that additional losses will be generated due to the friction associated with the longer path of the fluid particles and the thickened boundary layers on the volute wall due to the incidence to the tongue.

At higher mass flow (figure 6.5b), a maximum pressure zone is seen at the beginning of the conical diffuser passage, indicating that the acceleration process in the volute passage stops before the flow reaches the tongue. This is in agreement with the observation of Hagelstein et al. (1999) that the minimum pressure at higher mass flow is located upstream of the tongue. One surprising observation is that an acceleration process begins in the conical diffuser inlet! The tongue separates the upstream flow passage into the exit cone passage and the volute passage of small area. The tongue and the small volute passage seem to be a forward step for the upstream flow. The velocity vector shown in figure 6.6b confirms that the flow pattern has the character of a forward step flow. This explains why flow acceleration happens at the beginning of the conical diffuser. Contrary to the small mass flow, the upstream flow deflects into the diffuser

passage, reducing the total mass flow rate in the volute. The flow deflection also causes a tongue incidence, resulting in thickened boundary layers on the other side of the volute wall. The vector plot also shows that the twin vortex structure at higher mass flow (Gu, et al., 2000) happens downstream away from the tongue. It indicates that the twin vortex structure is mainly created by the non-uniformness in the axial direction. One conclusion from this analysis is that a vertical tongue (as in this Chapter) has an advantage over the horizontal one in that the vertical tongue is capable of adjusting the total mass flow in the volute such that the operation point of the volute is closer to the design point than the operation point of the impeller.

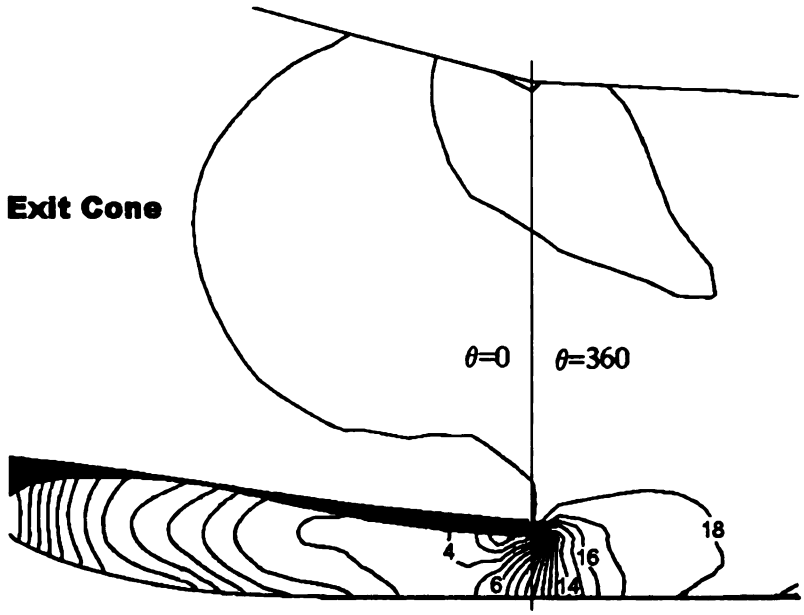

(a) 75% mass flow

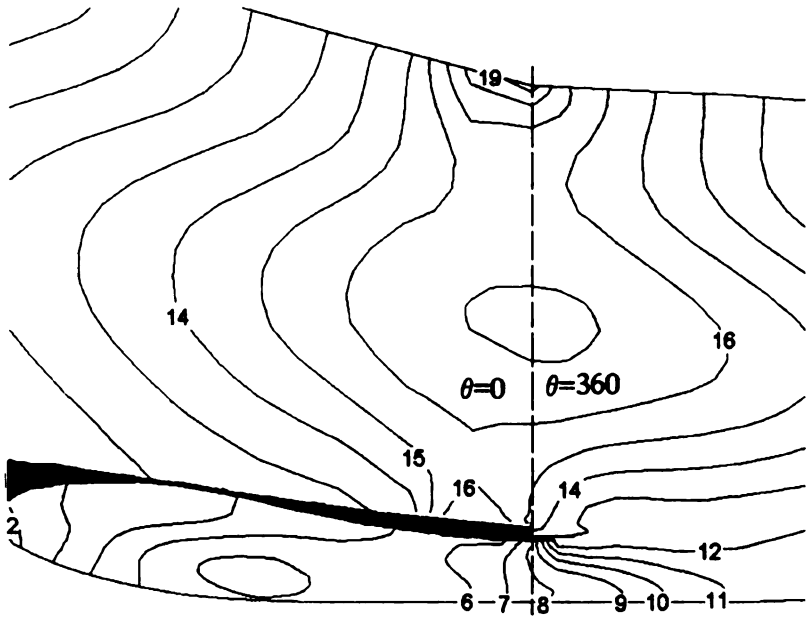

(b) 125% mass flow

Figure 6.5 Pressure contours on the y-plane

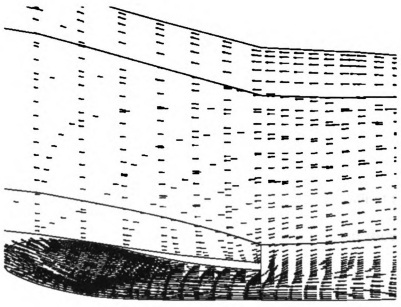

(a) 75% mass flow

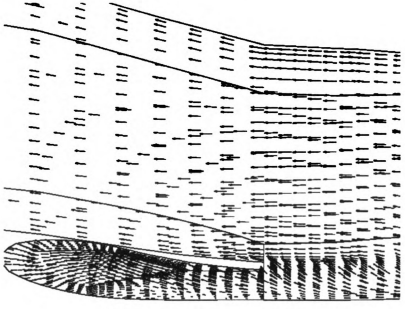

(b) 125% mass flow

Figure 6.6 Vectors on the y-plane

6.3.3 Propagation in the vaneless diffuser

It is commonly assumed that the circumferential distortion is transmitted in the vaneless diffuser passage, even through the interactions among streamlines can exist. Therefore, Stanitz's equations (1952) were employed to transmit the distortion (Van den Braembussche, et al., 1999). However, the phase lag between total pressure and static pressure circumferential distortion indicates that the streamline interaction is not negligible. The distortion propagation in the vaneless diffuser is a result of the streamline interaction, which is tracked by the mass averaged static and total pressures distribution at the three surfaces as shown in figure 6.7. The surfaces of $r/r_{tip} = 1.85$ and $r/r_{tip} = 1.06$ are the end and beginning of the vaneless diffuser, respectively. The surface of $r/r_{tip} = 1.25$ lies in between.

The static pressure (figure 6.7a) at the lower mass flow increases downstream of the tongue and reaches the maximum upstream of the tongue, resulting in an abrupt favorite circumferential pressure gradient around the tongue. This favorite pressure gradient prevents the generation of the twin vortices. The same tendency of pressure distortion is observed inside the vaneless diffuser and at the exit of the impeller. An opposite case occurs at the higher mass flow rate where the maximum pressure occurs downstream of the tongue. A weaker adverse circumferential pressure gradient is built around the tongue. In both cases, the radical pressure distortion occurs and propagates inwards to the axis in the region between -30° and 60° around the tongue at all the three radial locations.

Figure 6.7b shows that the total pressure circumferential variation is similar to that of the static pressure at the beginning of the vaneless diffuser; the locations of the total pressure extremes are identical to these of the static pressure. It means that the passage with higher exit pressure added more work to the fluid inside the passage. The lowest total pressure point at lower mass flow and the highest total pressure point at higher mass flow are convected downstream as the flow goes through the vaneless diffuser. This explains why there is a phase lag between static and total pressure distortion at the diffuser exit.

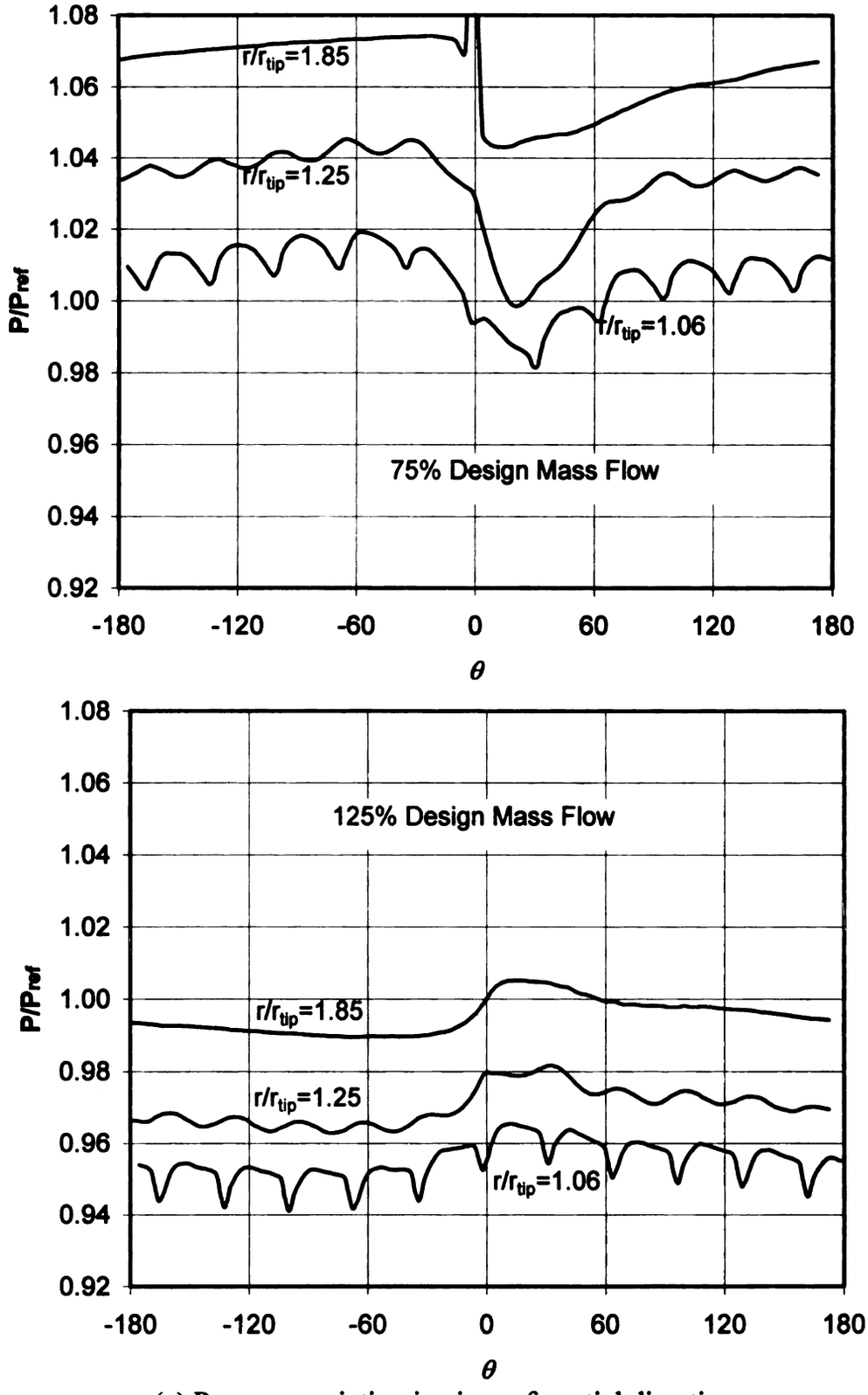

(a) Pressure variation in circumferential direction

Figure 6.7 Perturbation in the vaneless diffuser

Figure 6.7 (cont'd)

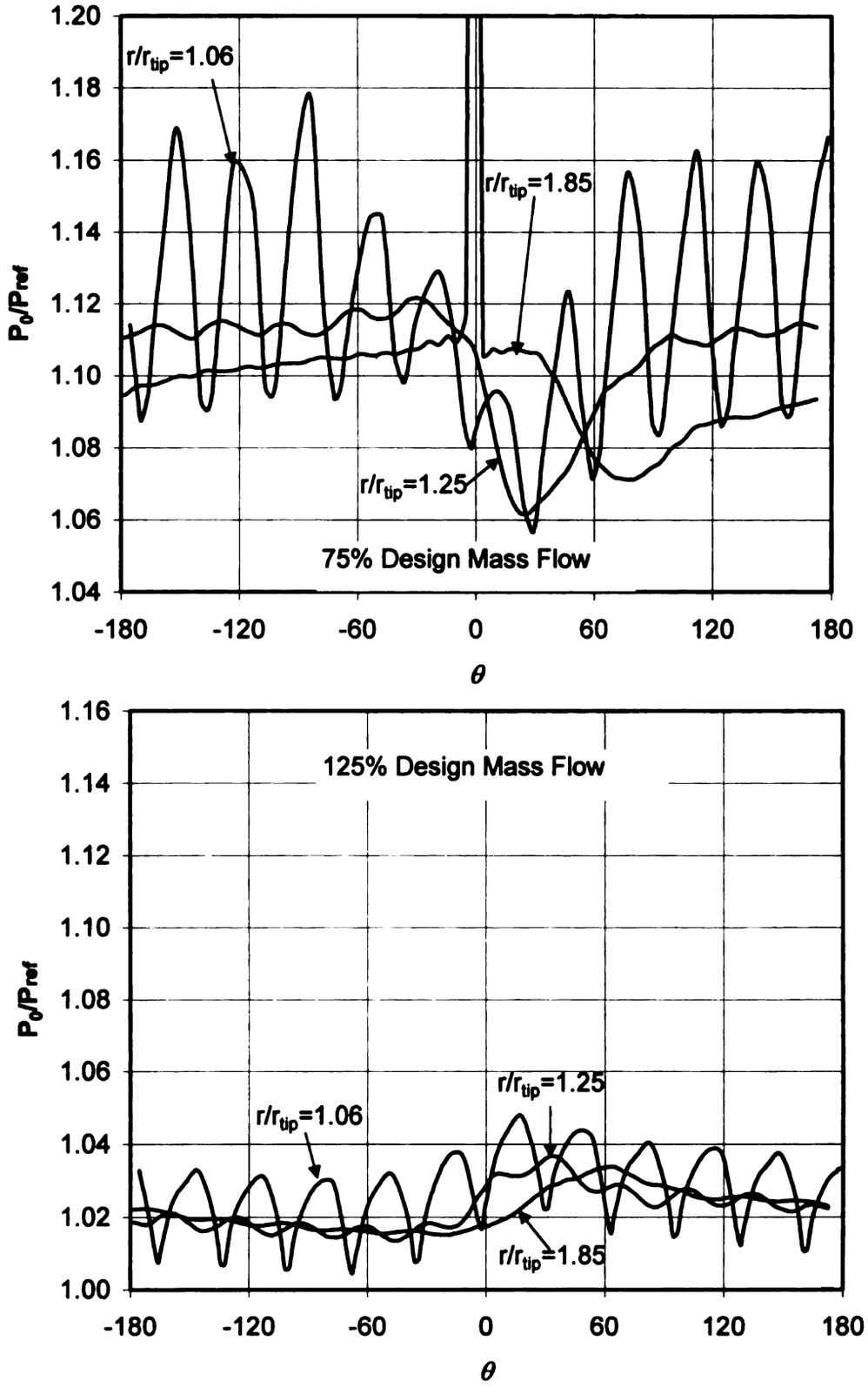

(b) Total pressure variation in circumferential direction

It is of interest to notice the phase difference between the distortions of static pressure and that of total pressure, which can be described as 1) at the impeller exit there are no significant phase differences between static pressure and total pressure; 2) at the diffuser exit, the radical distortions in total pressure happen downstream of the static pressure distortion; 3) the radical static pressure distortion happens at the same circumferential position, which is around the tongue section, regardless of the radial positions. Therefore, it is necessary to take into account the streamline interactions when modeling the distortion propagation in the vaneless diffuser.

The phenomenon reported by Hagelstein et al. (1997) and Sorokes et al. (1998) was not observed that the pressure distortion at diffuser inlet is ½ of that at the diffuser exit. This discrepancy could result from the frozen rotor model because this model lacks the capability to simulate the response of the impeller to the higher frequency perturbations where the acoustic Strouhal number is above zero.

6.3.4 Exit flow of the impeller

Impeller exit flow can be either of jet/wake two-zone or of a single zone. Johnson and Moore (1980) pointed out that the size and location of the wake are mainly determined by the Rossby number, $Ro = W/\omega R_n$. Krain's (1988) experimental study revealed that the classical jet/wake exit flow was replaced by a single zone flow in his impeller with backward swept blades, even through swirling flow happened inside the impeller passage. However, it is not fully understood how the impeller responds to the distorted exit pressure.

The impeller in this Chapter has 53.5° degree backward swept blades. Figure 8 shows the rotary pressure contour at the impeller exit. As shown in figure 6.4, passage 3 and 4 are located upstream and downstream of the tongue, respectively. Passages 7 and 8 are located further downstream of the tongue. At all mass flow rates, the periodicity between passage 7 and 8 indicates that the effect of the pressure distortion away from the tongue can be neglected. At design (figure 6.8c, d) and high mass flow rates (figure 6.8e, f), the fluids with low rotary pressure concentrate in the suction/shroud corner, showing the classical jet/wake pattern. No significant difference can be seen between the passages around tongue and these away from tongue. It indicates that at design and higher mass flow rates, the circumferential pressure distortion has very limited impact on the impeller flow. It could be due to the fact that at higher mass flow, the pressure distortion is relatively weak compared with that at lower mass flow as shown in figure 6.7a. The other reason is that the pressure circumferential variation has different slopes at higher mass and lower mass flows.

At lower mass flow, however, the flow pattern around the tongue is obviously different from that away from the tongue (figure 6.8a,b). In passages 7 and 8, the pitch-wise rotary pressure gradient dominants the exit flows. A higher loss region (label less than 10) occupying almost half of the passage indicates higher losses happened in these passages. On the contrary, the flow around the tongue shows a similar pattern as in design and higher mass flows. It suggests that the flow in the passage around the tongue is closer to the design flow than the flows in other passages.

In summary, the pressure distortion makes each passage of the impeller work at different operation conditions. However, the exit flow pattern does not depend on the

level of the exit pressure exclusively. Instead, it is determined to some degree by the slope of the pressure variation. This is especially true at lower mass flow. Passages 3 and 4 have different exit pressure levels but have same tendency of slopes. The exit flow patterns therefore are the same. At higher mass flow, the pressure slightly increases around the tongue, so no significant flow pattern changes can be observed.

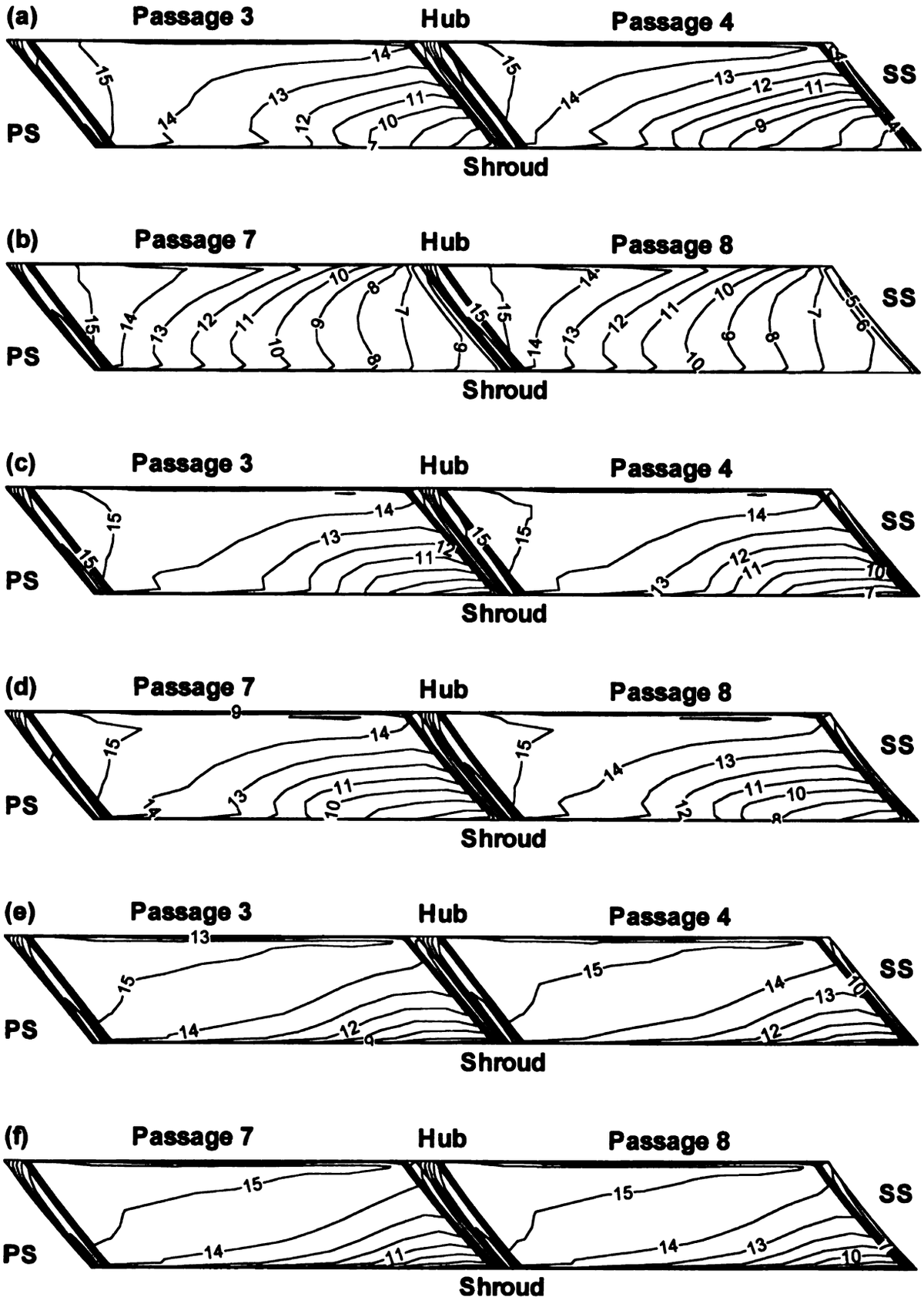

Figure 6.8 Rotary pressure contours at impeller exit

6.3.5 Flow in the Impeller

Because of the circumferential pressure distortion at the impeller exit, each passage of the impeller runs at different operation points as predicted by the frozen rotor model. The numerical results are presented in terms of mass-averaged parameters over each passage. The first circumferential surface of the impeller grid overlaps the last one in the passage 0 over which the averaging is not conducted.

Figure 6.9a shows the pressure variation in each passage at the inlet (station 1-1) and outlet (station 2-2) of the impeller. It is clearly shown that the pressure variation at the inlet is identical to that at the outlet at all mass flows. The inlet static pressure changes through two mechanisms: flow rate and inlet blockage. Higher flow rates and higher blockage lead to lower inlet static pressure.

It seems plausible to analog the flow in each passage predicted by the frozen rotor model to the flow in an impeller at different operation points. For example, as the total mass flow increases, the average exit pressure (figure 6.9a) and isentropic head coefficient (figure 6.9b) are reduced. This analogy also holds true for passage 4, which is closest to the tongue downstream. At low mass flow, the exit (also inlet) static pressure of passage 4 is the lowest, so the mass flow in this passage (figure 6.9c) is the highest. However, the variations of mass flow in passage 2 and 3 contradict this analogy at lower mass flow. In these two passages, the exit pressure is above the average; so is the mass flow! The only explanation for this phenomenon is that flow in these two passages must be of different structures. Figure 6.9d shows that negative incident angles exist at passage 2-4, while positive ones exist at all other passages. The positive incidence causes the flow to separate earlier on the suction-side/shroud corner in passage 2 and 5 as shown in figure

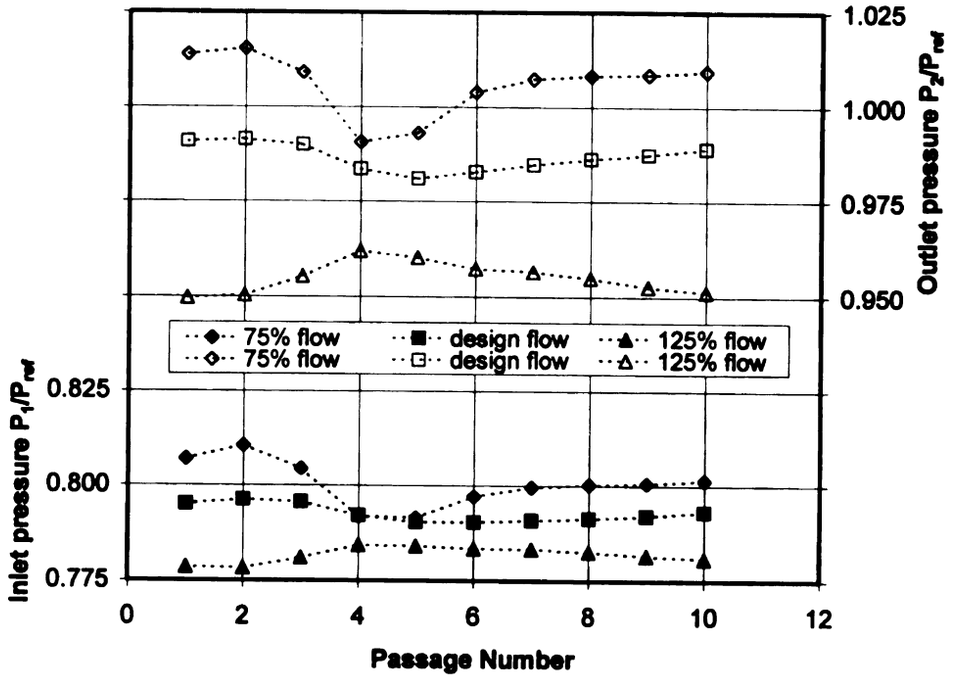

(a) Pressure distortion

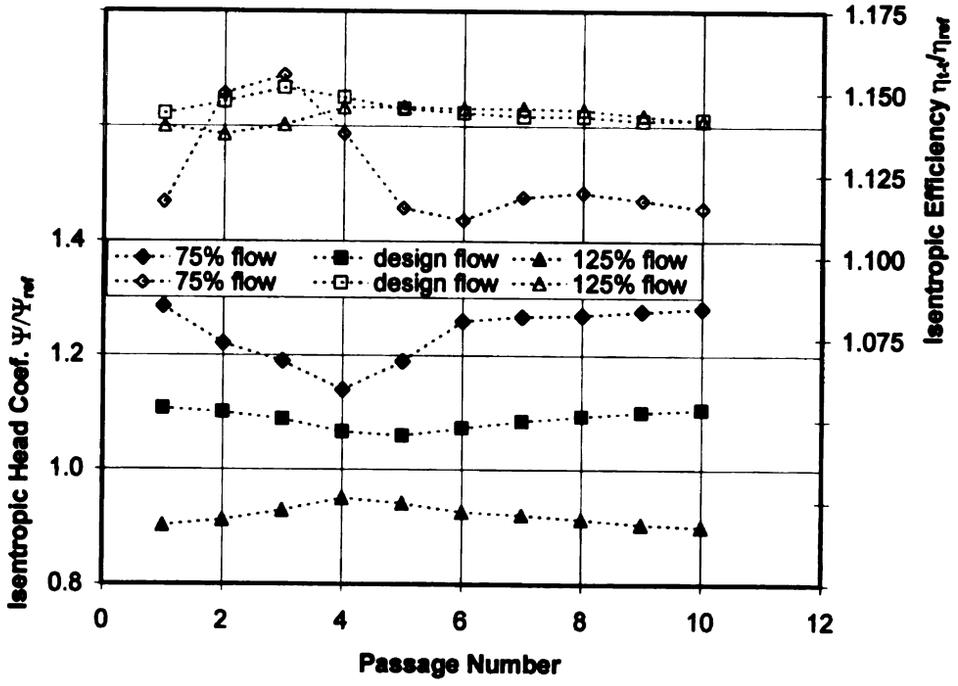

(b) Performance of each passage

Figure 6.9 Flow in impeller passages

Figure 6.9 (cont'd)

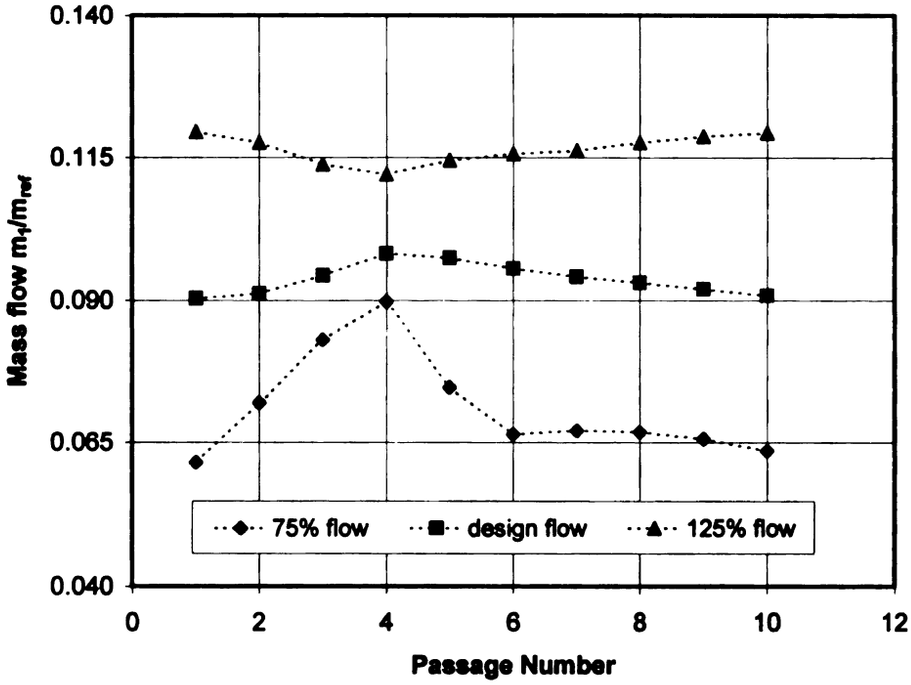

(c) Mass flow in each passage

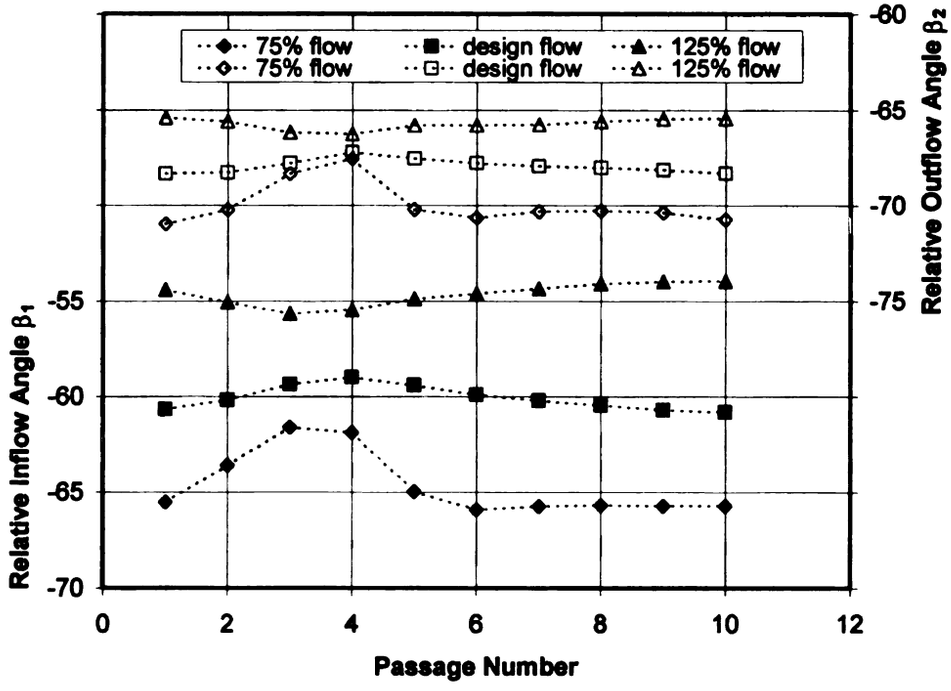

(d) Relative flow angle of each passage

6.10, resulting in higher blockage. However, the separation in passage 2 is much less than in passage 5, which is typical for the passages away from the tongue. This explains why more mass flow goes through passage 2 and 3, but the inlet pressure of these passages is still higher. The flow structure change also can be observed at the exit of the impeller. In fact, Figure 6.8 has shown that at lower mass flow, the rotary pressure contours at the exit of passages 3 and 4 are similar to that at design and higher mass flows, but passages 7 and 8, as well as other passages, are different.

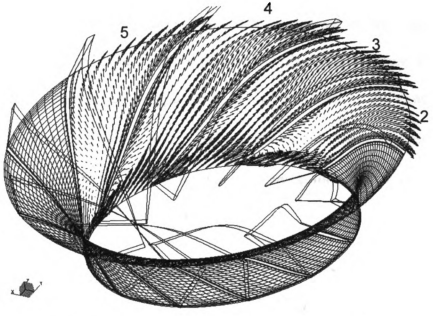

Figure 6.10 Surface vectors near shroud surface

By comparing the circumferential pressure variation at the impeller exit (figure 6.7a), it can be seen that at low mass flow, the flow pattern changes in the passages 2-4 upstream of the tongue are caused by the pressure slope at the impeller exit. The pressure is seen decreasing in passages 2-4 as the impeller rotates, while the pressure is seen increasing in the other passages. The effect of pressure variation on the flow structure can be studied by force analysis on a balanced flow particle, as shown in figure 6.11. The

equation of motion for the relative flow, assuming an inviscid flow without body force, is given by (Di Liberti 1998)

$$\frac{D\vec{W}}{Dt} + 2\vec{\omega} \times \vec{W} - \omega \times \vec{U} = -\frac{\nabla p}{\rho} \tag{6.3}$$

In this equation, the first term represents the relative acceleration, and the second and third the forces due to Coriolis and centrifugal acceleration, respectively. In a streamline coordinate system, the projection of the equation of the motion in the normal direction is

$$\frac{W^2}{R_n} - 2\omega W + \omega U \sin\beta = \frac{1}{\rho}\frac{\partial p}{\partial n} \tag{6.4}$$

The forces are plotted in figure 6.11. Their sum is balanced by the force due to the pressure gradient. It can be seen that the purpose of blade back sweeping is to introduce the normal component of centrifugal force $\omega U \sin\beta$, as well as the centrifugal force W^2/R_n due to streamline curvature, to counteract the Coriolis force. The circumferential pressure gradient is therefore reduced, resulting in more uniform exit flows.

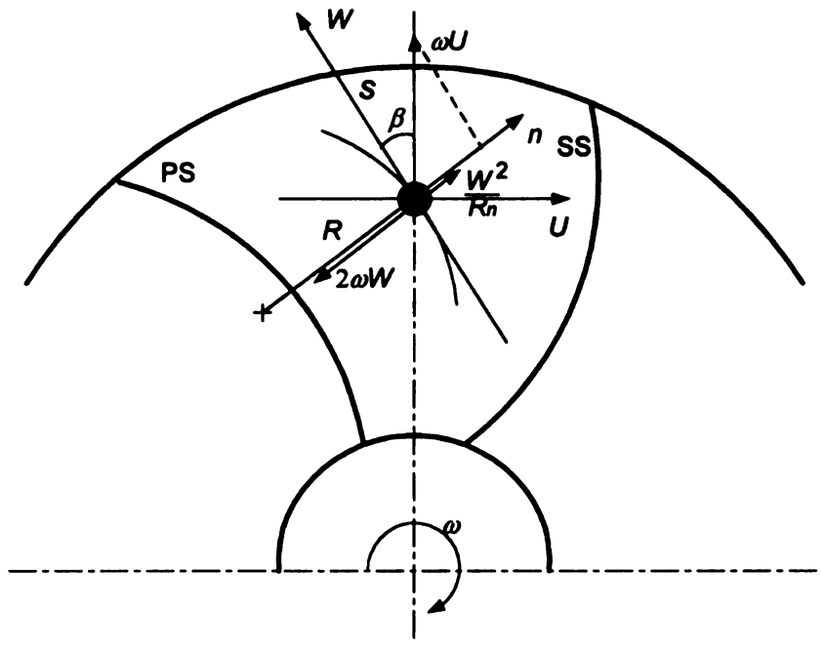

Figure 6.11 Forces acting on a fluid particle inside an impeller passage

At the design point, the blade was back swept in such a way that the balance of the force in the normal direction is zero, so the pressure is tangentially uniform. At lower mass flow, the pressure on the pressure side is higher than on the suction side for passage 3 and 4. It indicates that the flows in these two passages are more radial, as if the back sweeping angle is reduced. However, the pressure gradients in the other passages are reversed; higher pressure exists on the suction side, which totally violates the basic design philosophy. It requires that the streamline be more tangential to generate a strong enough normal component of the centrifugal force, which severely deteriorates the flow on the suction side. Therefore, these passages with higher exit pressure on the suction side show lower efficiency (figure 6.9b)

In summery, the deterioration of the impeller performance at lower mass flow is not caused by the radical pressure variation around the tongue but by the gently increased pressure in the circumferential direction. At higher mass flow, the impeller performance is not reduced significantly because only a few passages downstream of the tongue face the circumferentially increased pressure. It should be noted that the frozen rotor model failed to predict the decay of the pressure distortion. The actual pressure distortion at the impeller exit therefore is less severe, resulting in smoother flow variation in a passage over one rotation period. This explains why the frozen rotor model did not accurately predict the compressor performance at off-design conditions.

6.4 Conclusions

The steady-state volute/impeller interaction is numerically studied using the frozen rotor model provided by the commercially available CFD software, CFX-TASCflow. The pressure distortion due to the volute at off-design conditions is traced from the tongue to the impeller inlet. The following conclusions have been reached:

- The frozen rotor model is applicable to the compressor flow where the acoustic Strouhal number is close to zero. It cannot predict the response of the impeller to pressure perturbation of higher frequency.
- The pressure gently increases circumferentially at lower mass flow, and gently decreases at high mass flow. The radical pressure variation around the tongue is caused by the incidence to the tongue at off-design conditions.
- The frozen rotor model failed to predict the decay of the pressure perturbation when it propagates upstream from the vaneless diffuser exit to the inlet. It indicates that the decay of the perturbation is a response of the impeller to the perturbation of higher frequency.
- The performance drop of the compressor at off-design conditions is mainly due to the performance drop of the impeller. The circumferentially increased pressure at the impeller exit is detrimental to the impeller flow. Therefore, at higher mass flow, the impeller efficiency deterioration comes from these passages upstream of the tongue in the range of about 150°. At lower mass flow, all the passages but the two around tongue are responsible for the lower impeller efficiency.
- A design idea is that the undersized volute is beneficial to the impeller due to the fact that the impeller is experiencing the exit pressure of negative slopes.

Chapter 7

ONE DIMENSIONAL MODELING OF COMPRESSOR FLOW

7.1 Introduction

Considerable efforts have been made for the flow modeling of compressor components individually. The modeling of the entire compressor is very helpful in matching components. It is well known that the peak efficiency point of a compressor can be different from the peak efficiency point of its impeller, resulting from the mismatching of components.

A comprehensive review on the research of impellers was given by Japikse (1996). He catalogued the impeller design into three levels. At the first level, one simply employs the principles of similitude to achieve a geometrically and fluid dynamically precise scaling from one application to another. At the second level, one attempts to use correlations of basic component performance to mix and match components for new applications. The well-known one-zone impeller design method falls into this level. At the third level, one proposes comprehensive models and utilizes them systematically in the design and development process to find new optimum configurations, for example, the two-zone philosophy.

A mixing process occurs after the fluid exits from the impeller; however, the modeling of this mixing is extremely difficult. The flow in the vaneless diffuser can be modeled by mass and angular momentum conservations. Stanitz (1952) introduced a comprehensive treatment of the vaneless diffuser and published a set of one-dimensional

equations that take into account the friction losses. Japikse (1982) showed that results from these equations are in good agreement with experimental data.

A modeling technique for the simple overhung volute was created by Young and reported by Japikse (1982). The losses are estimated by assuming that the meridional component of kinetic energy entering the volute is totally lost, and the pressure loss is equivalent to the total pressure loss in a sudden expansion mixing process when the flow is decelerated in the volute passage. Japikse showed that the pressure recovery in absolute value was over-predicted for accelerated flows and under-predicted for decelerated ones but in a reasonable narrow range, and the pressure loss coefficient was significantly over-predicted for accelerated flows and slightly under-predicted for decelerated ones. This suggests that when the flow is distorted at the inlet of the volute, the sum of pressure recovery and pressure loss coefficient depends on the average algorithm used to calculate the inlet and outlet parameters. Because this approach can be derived from mass and energy conservations, it is called energy approach here.

Van den Braembussche and Hande (1990) proposed another analytical method to predict the flow in the volute. They assumed that the swirling velocity component and the total pressure follow pre-specified non-dimensional radial distributions, respectively. The meridional component (swirling one) is not totally lost; instead, the friction loss caused by the swirling velocity is calculated as the loss in the pipe flow. However, the comparison showed a significant difference from the experimental data. A more delicate model was proposed by Van den Braembussche et al. (1999) to predict the flow in the entire compressor from impeller to vaneless diffuser and to the volute. A significant enhancement is to use angular momentum conservation to calculate the pressure in the

volute passage. This approach therefore is called the momentum approach. There is a significant printing-error in the integrated equation of angular momentum that the item for the angular momentum entering the volute from the volute inlet was missed (Van den Braembussche 2000). It is also not justified if the torque caused by the pressure force on the volute wall can be calculated in the way reported by that paper.

In this chapter, theoretical modeling of the entire compressor will be described; it simulates the response of the compressor to the pressure distortion at the vaneless diffuser exit. It is assumed that each passage of the impeller will have different mass flow when the exit pressure is distorted. The machine is divided into several circumferential segments. Each segments is treated as a stream tube, therefore, calculated separately. The level 2 model is used to simulate the impeller flow, and the Stanitz equations are employed for the vaneless diffuser flow. The volute flow is calculated by both momentum and energy approaches. A comparison is thus conducted between these two approaches. The model is compared with a CFD analysis (Gu, 2001), and good agreement is found.

7.2 Model

The flow inside a centrifugal compressor is modeled from each component. The machine is divided into segments circumferentially. All the equations in the model apply to the segments. Each segment will pass different mass flow when the impeller exit flow is circumferentially distorted due to volute at off-design conditions. Therefore, this model can justify the design point.

7.2.1 Impeller Inlet Calculation

The inlet total temperature, total pressure and mass flow of each segment are given to begin the calculation. The flow is assumed to be axial. The inlet static pressure, temperature, density and velocity are calculated by the following equation set

$$T_{01} = T_1 + \frac{C_1^2}{2C_p} \tag{7.1}$$

$$p_{01} = p_1\left(\frac{T_{01}}{T_1}\right)^{\frac{k}{k-1}} \tag{7.2}$$

$$\dot{m} = \left(\pi\left(r_{1s}^2 - r_{1h}^2\right) - Z_R t_1 \left(r_{1s} - r_{1h}\right)\right) C_1 \rho_1 \tag{7.3}$$

$$p = \rho RT \tag{7.4}$$

7.2.2 Impeller Response – Level 2 Model

Many analysis models for impeller flow can be found in (Japikse 1996). Here, the second level model, as named by Dr. Japikse, is used to calculate the impeller exit flow for the sake of simplicity. Therefore, the impeller efficiency of each segment has to be pre-specified. The following equations are used and the inflow is assumed to be axial.

$$\Delta W = C_p(T_{02} - T_{01}) = C_{\theta 2}U_2 - C_{\theta 1}U_1 \approx C_{\theta 2}U_2 \tag{7.5}$$

Or

$$I_0 = C_p T_1 + \frac{C_1^2}{2} = C_p T_2 + \frac{W_2^2}{2} - \frac{U_2^2}{2}$$

$$\Delta \dot{m} = \left(\Delta \theta r_2 - \frac{\Delta \theta}{2\pi} Z_R t_2 \right) b_2 \rho_2 C_{m2} \tag{7.6}$$

$$p = \rho RT \tag{7.7}$$

$$C^2 = C_\theta^2 + C_m^2 \tag{7.8}$$

The efficiency of the impeller is defined as

$$\eta = \frac{T_{02}' - T_{01}}{T_{02} - T_{01}} = \frac{\left(\frac{p_{02}}{p_{01}} \right)^{\frac{k-1}{k}} - 1}{\frac{T_{02}}{T_{01}} - 1} \tag{7.9}$$

which leads to the equation for the exit total pressure calculation

$$p_{02} = p_{01} \left[1 + \eta \left(\frac{T_{02}}{T_{01}} - 1 \right) \right]^{\frac{k}{k-1}} \tag{7.10}$$

The exit tangential velocity component $C_{\theta 2}$ is calculated from correlations of slip factor (See figure 71 for the definitions of velocity components)

$$C_{\theta 2} = U_2 + C_{m2} \tan \beta_{2b} - C_{slip} \tag{7.11}$$

$$C_{slip} = U_2(1 - \sigma) \tag{7.12}$$

Therefore

$$C_{\theta 2} = U_2 \sigma + C_{m2} \tan \beta_{2b}, \quad \frac{C_{m2}}{U_2} = \frac{C_{\theta 2}/U_2 - \sigma}{\tan \beta_{2b}} \tag{7.13}$$

The model integrates different correlations of slip factors, for example, *Wiesner* correlation

$$\sigma = 1 - \sqrt{\cos\beta_{2b}} / Z_R^{0.7} \tag{7.14}$$

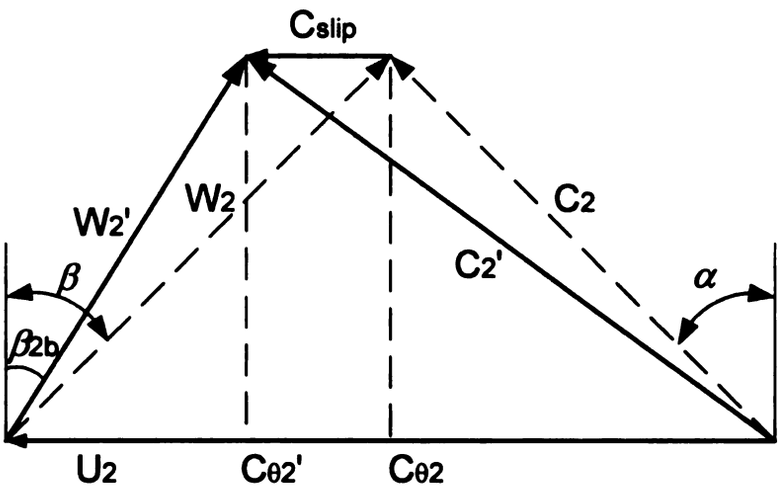

Figure 7.1 Impeller exit velocity triangle

If the slip factor is expressed in $\sigma' = \frac{C_{\theta 2}}{C_{\theta 2}'}$, which is related with σ by

$$1 - \sigma = \frac{C_{\theta 2}}{U_2}\left(\frac{1}{\sigma'} - 1\right) \tag{7.15}$$

The velocity components can then be expressed as,

$$\frac{C_{\theta 2}}{\sigma'} = U_2 + C_{m2}\tan\beta_{2b}, \quad \frac{C_{m2}}{U_2} = \frac{\frac{C_{\theta 2}}{U_2}\frac{1}{\sigma'} - 1}{\tan\beta_{2b}} \tag{7.16}$$

Examples are *Stanitz*, and *Balje* correlations,

$$\sigma' = 1 - 0.315\left(\frac{2\pi}{Z_R}\right) \quad \text{(Stanitz)} \tag{7.17}$$

$$\sigma' = \frac{Z_R}{Z_R + 6.2\left(\frac{r_1}{r_2}\right)^{2/3}} \quad \text{(Balje)} \tag{7.18}$$

If the slip factor correlation contains the radial velocity component, as in Yadav and Misra's model

$$\sigma' = 1 - \frac{0.855\pi^2}{Z_R}\frac{C_{m2}}{U_2} \quad \text{(Yadav and Misra 1973)} \tag{7.19}$$

The meridional velocity component is calculated by solving the equation

$$\frac{C_{\theta 2}}{U_2} = \left(1 - \frac{0.855\pi^2}{Z_R}\frac{C_{m2}}{U_2}\right)\left(1 + \tan\beta_{2b}\frac{C_{m2}}{U_2}\right) \tag{7.20}$$

7.2.3 Vaneless Diffuser Calculation

Stanitz equations for the vaneless diffuser simulation are adopted in the model, even though these are strong interactions among streamlines when the inlet of the vaneless diffuser is distorted. The drawback of this model will be discussed later. The equations are:

$$C_m\frac{dC_m}{dr} - \frac{C_\theta^2}{r} + c_f\frac{C^2\cos\alpha}{b} + \frac{1}{\rho}\frac{dp}{dr} = 0 \tag{7.21}$$

$$C_m\frac{dC_\theta}{dr} + \frac{C_m C_\theta}{r} + c_f\frac{C^2\sin\alpha}{b} = 0 \tag{7.22}$$

$$\frac{1}{\rho}\frac{d\rho}{dr} + \frac{1}{C_m}\frac{dC_m}{dr} + \frac{1}{r} = 0 \tag{7.23}$$

$$p = \rho RT \Rightarrow \frac{1}{\rho}\frac{dp}{dr} = R\left(\frac{dT}{dr} + T\frac{1}{\rho}\frac{d\rho}{dr}\right) \tag{7.24}$$

$$T_0 = T + \frac{C^2}{2C_p} \Rightarrow \frac{dT}{dr} = -\frac{1}{C_p}\left(C_m\frac{dC_m}{dr} + C_\theta\frac{dC_\theta}{dr}\right) \tag{7.25}$$

The skin friction coefficient c_f is calculated by the equation suggested by Japikse (1996, p3-4)

$$c_f = k\left(\frac{1.8\times10^5}{\mathrm{Re}}\right)^{0.2} \tag{7.26}$$

Here, the Reynolds number is based on the inlet diameter and velocity. The constant k is given a value of 0.01 also suggested by Japikse (1996). The equations are reorganized in a form suitable for the Runge-Kutta integration

$$\frac{dC_\theta}{dr} = -\frac{C_\theta}{r} - c_f\frac{C^2\sin\alpha}{C_m b} \tag{7.27}$$

$$\frac{dC_m}{dr} = \frac{\frac{k-1}{k}C_\theta\frac{dC_\theta}{dr} + \frac{p}{r\rho} + \frac{C_\theta^2}{r} - c_f\frac{C^2\cos\alpha}{b}}{\frac{C_m}{k} - \frac{p}{C_m\rho}} \tag{7.28}$$

$$\frac{dT}{dr} = -\frac{1}{C_p}\left(C_m\frac{dC_m}{dr} + C_\theta\frac{dC_\theta}{dr}\right) \tag{7.29}$$

$$\frac{1}{\rho}\frac{d\rho}{dr} = -\frac{1}{C_m}\frac{dC_m}{dr} - \frac{1}{r} \tag{7.30}$$

$$\frac{1}{\rho}\frac{dp}{dr} = \left(-\frac{k-1}{k}C_m - \frac{p}{C_m\rho}\right)\frac{dC_m}{dr} - \frac{k-1}{k}C_\theta\frac{dC_\theta}{dr} - \frac{p}{r\rho} \tag{7.31}$$

The streamline is tracked by

$$\frac{d\theta}{dr} = \frac{C_\theta}{C_m}\frac{1}{r} \tag{7.32}$$

7.2.4 Volute Modeling

The flow in the volute is assumed to be incompressible. Van den Braembussche et al. (1999) applied integrated mass conservation and angular momentum equation to the segment of volutes. Japikse (1982) applied the mass and energy equations to the entire

volute passage. In the current model, both approaches are adopted with some minor modifications.

The angular momentum approach is described first. The mass and angular momentum conservations are applied to the segment (figure 7.2),

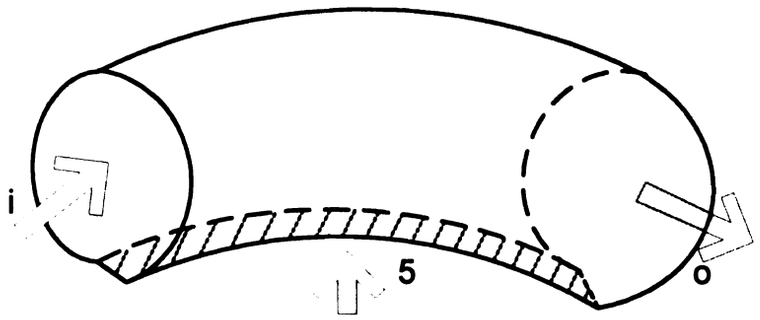

Figure 7.2 Control volume for a volute segment

$$\rho_i C_{ti} A_i + \rho_5 C_{m5} A_5 = \rho_o C_{to} A_o \tag{7.33}$$

$$R_i A_i \left(p_i + \rho_i C_{ti}^2\right) + R_5 A_5 \rho_5 C_{m5} C_{t5} + R_i \bar{p}\left(A_o - A_i\right) = R_o A_o \left(p_o + \rho_o C_{to}^2\right) + M_{loss} \tag{7.34}$$

Equation (7.34) differs from Van den Braembussche's equation in that the inflow angular momentum (second item on left hand side) is taken into account, and the torque caused by the pressure on the volute wall is estimated in a different way by the third item on the left hand side. The torque caused by viscous forces on the wall can be estimated similarly for the pipe flow. To simplify the problem, this viscous loss is neglected. The pressure loss caused by the flow mixing between the new coming flow with the one already in the volute passage is estimated as in a sudden mixing process

$$M_{loss} = p_{DUMP}\left(A_o - A_i\right) R_i \tag{7.35}$$

$$p_{DUMP} = \varepsilon_1 \frac{\rho}{2}\left|C_5^2 - C_i^2\right| \tag{7.36}$$

Here, ε_1 is an empirical parameter. The average pressure over the segment on the volute wall is estimated as

$$\bar{p} = \frac{1}{2}(p_i + p_o) \tag{7.37}$$

By substitution, the exit velocity and pressure are calculated as

$$C_{to} = C_{ti}\frac{A_i}{A_o} + C_{m5}\frac{A_5}{A_o} \tag{7.38}$$

$$\begin{aligned}\left[1 - \frac{1}{2}\frac{R_i(A_o - A_i)}{R_o A_o}\right]p_o = {} & \frac{R_i A_i}{R_o A_o}\left(p_i + \rho C_{ti}^2\right) + \frac{R_5 A_5}{R_o A_o}\rho C_{m5} C_{\theta 5} \\ & + \frac{1}{2}\frac{R_i(A_o - A_i)}{R_o A_o}\left(p_i - \varepsilon_1 \rho\left|C_5^2 - C_i^2\right|\right) - \rho_o C_{to}^2\end{aligned} \tag{7.39}$$

By introducing the swirl factor $\lambda = C_{\theta 5}/C_{m5}$, the angular momentum equation becomes

$$\begin{aligned}\left[1 - \frac{1}{2}\frac{R_i(A_o - A_i)}{R_o A_o}\right]p_o = {} & \frac{R_i A_i}{R_o A_o}\left(p_i + \rho C_{ti}^2\right) + \frac{\lambda}{1+\lambda^2}\frac{R_5 A_5}{R_o A_o}\rho C_5^2 \\ & + \frac{1}{2}\frac{R_i(A_o - A_i)}{R_o A_o}\left(p_i - \varepsilon_1 \rho\left|C_5^2 - C_i^2\right|\right) - \rho_o C_{to}^2\end{aligned} \tag{7.40}$$

One advantage of this approach is that it uncouples the swirling flow velocity component from the model. However, this approach does not give satisfactory results when ε_1 is arbitrarily chosen as 0.

The energy equation approach is to apply energy conservation to the segment

$$\left(\frac{p_i}{\rho} + \frac{C_i^2}{2}\right)A_i C_{ti} + \left(\frac{p_5}{\rho} + \frac{C_5^2}{2}\right)A_5 C_{m5} = \left(\frac{p_o}{\rho} + \frac{C_o^2}{2}\right)A_o C_{to} + W_{loss} \tag{7.41}$$

Here, the energy loss consists exclusively of the viscous work on the volute wall, which is equal to zero under the assumption of adiabatic wall. The total pressure loss caused by the mixing of the flow in the volute passage and the inflow cannot be represented in the energy equation.

Following Japikse's assumption, the swirling velocity inside the volute is neglected. A mixing loss model is introduced to account for the effect of the swirling velocity, which is correlated to the through flow by

$$W_{loss} = \varepsilon_2 \frac{1}{2}\left|C_5^2 - C_i^2\right| A_5 C_{m5} \tag{7.42}$$

Here, ε_2 is another empirical coefficient. The energy equation is reduced to

$$\left(\frac{p_i}{\rho} + \frac{C_i^2}{2}\right)\frac{A_i C_i}{A_o C_o} + \left(\frac{p_5}{\rho} + \frac{C_5^2}{2}\right)\frac{A_5 C_{m5}}{A_o C_o} = \left(\frac{p_o}{\rho} + \frac{C_o^2}{2}\right) + \frac{\varepsilon_1}{2}\left|C_5^2 - C_i^2\right|\frac{A_5 C_{m5}}{A_o C_o} \tag{7.43}$$

The volume flow ratios can be related with the volute inlet swirling factor by

$$\frac{A_i C_i}{A_o C_o} = \frac{A_i C_i}{A_i C_i + A_5 C_{5m}} = \frac{1}{1 + \frac{A_5}{A_i}\frac{C_{m5}}{C_{\theta 5}}\frac{C_{\theta 5}}{C_i}} = \frac{1}{1 + \frac{A_5}{A_i \lambda'}}, \quad \lambda' = \lambda \frac{C_i}{C_{\theta 5}} \tag{7.44}$$

$$\frac{A_5 C_{m5}}{A_o C_o} = \frac{A_5 C_{m5}}{A_i C_i + A_5 C_{m5}} = \frac{1}{1 + \frac{A_i}{A_5}\frac{C_{\theta 5}}{C_{m5}}\frac{C_i}{C_{\theta 5}}} = \frac{1}{1 + \frac{A_i \lambda'}{A_5}} \tag{7.45}$$

By substitution, the pressure on the outlet surface of the segment is calculated by

$$\begin{aligned} p_o &= \frac{A_i C_i}{A_o C_o}\left(p_i + \frac{\rho}{2}C_i^2\right) + \frac{A_5 C_{m5}}{A_o C_o}\left(p_5 + \frac{\rho}{2}\left(C_5^2 - \varepsilon_2\left|C_5^2 - C_i^2\right|\right)\right) - \frac{\rho}{2}C_o^2 \\ &= \frac{p_i + \frac{\rho}{2}C_i^2}{1 + \frac{A_5}{A_i \lambda'}} + \frac{p_5 + \frac{\rho}{2}\left(C_5^2 - \varepsilon_2\left|C_5^2 - C_i^2\right|\right)}{1 + \frac{A_i \lambda'}{A_5}} - \frac{\rho}{2}C_o^2 \end{aligned} \tag{7.46}$$

7.2.5 Iteration

This model can be run in an iterative way. After an initial guess of mass flow distribution for each segment, the pressures at vaneless exit p_5 and in the passage of the volute p_k are calculated. The difference of these two pressures can be estimated by

$$p_5 - p_k = \int_k^5 \frac{\rho C_\theta^2}{r} dr \tag{7.47}$$

The free vortex flow assumption can be used

$$C_\theta r = \Gamma \tag{7.48}$$

Here, Γ is a constant. So the pressure difference is calculated as

$$p_5 - p_k = 2\rho\Gamma\left(\frac{1}{r_k^2} - \frac{1}{r_5^2}\right) \tag{7.49}$$

If this equation is not satisfied, the mass flow of each impeller segment is adjusted by

$$m_i^{n+1} = m_i^n\left(1 + \varepsilon_3\left(\frac{p_k - p_5}{p_5}\right)\right) \tag{7.50}$$

Here, ε_3 is a relaxation coefficient. The impeller efficiency of each segment has to be adjusted empirically.

7.3 Comparison

The above theoretical model is compared with a numerical result from TASCflow. A single-stage centrifugal compressor produced by Solar Turbine Inc. is used as a platform. The sketch and convention of the compressor can be found in Chapter 6. The main design parameters of the compressor are: $r_2/r_{1s}=1.54$, $r_5/r_2=1.85$, $A_5/A_7=1.5$ $\beta_{2b}=53.5^{\circ}$ and machine Mach number $U_2/a_2=0.63$.

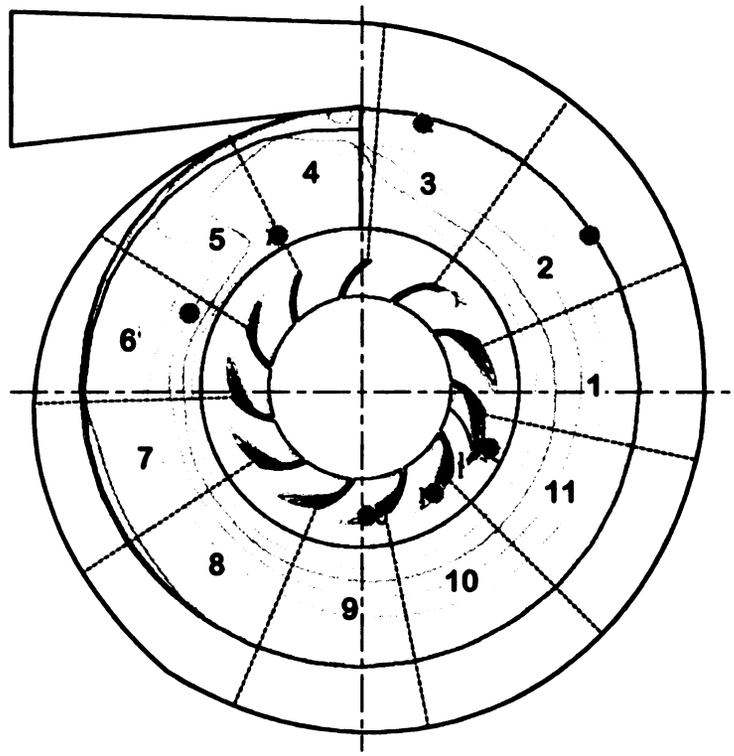

Figure 7.3 Compressor segments

The numerical results of three operation points (75%, 100% and 125% design mass flow rates) were obtained from the Frozen Rotor Model provided by TASCflow as reported in Chapter 6. In the CFD model, the circumferential distortion due to the volute can be transformed through the grid interface between the impeller and vaneless diffuser. The centrifugal compressor is divided into 11 segments circumferentially; each rotor

passage is a segment (figure 7.3). If more segments are used, the mass flow rates of some segments are too small due to the blockage of the blade and the resulting weak flow. Because the losses cannot be precisely predicted, the theoretical model is not iterated to obtain the mass flow distribution in each segment. Instead, the mass flow rate and efficiency of each segment from TASCflow are used to begin the theoretical model calculation.

7.3.1 Impeller Inlet

The theoretical model begins the impeller calculation from the mass flow rate and total-to-total efficiency of each segment obtained from the CFD simulation as shown in Figure 7.4. The inflow is assumed to be absolutely axial. Passage 4 has the highest mass flow at design and lower mass flows because this passage is under the lowest exit pressure (see Chapter 6). The efficiency of each passage is rather uniform at design and higher mass flows, but it varies dramatically at the lower mass flow with the highest efficiency in the passages 2 and 3 upstream of the tongue. This is due to the mass flow rate and the slop of pressure at the impeller exit (see Chapter 6).

The inlet static pressure and relative inflow angle are compared in figure 7.5 and 7.6, respectively. The inlet static pressures are in very good agreement with the CFD results with the maximum difference less than 1% at the lower mass flow. The model results in more uniform inlet static pressure distribution. In the CFD calculation, the mass flow varies continuously, whereas in the model, the mass flow is a step function and one passage is isolated from other passages. This explains why the pressure is more uniform from the one-dimensional model. For the design and lower mass flow rates, the model

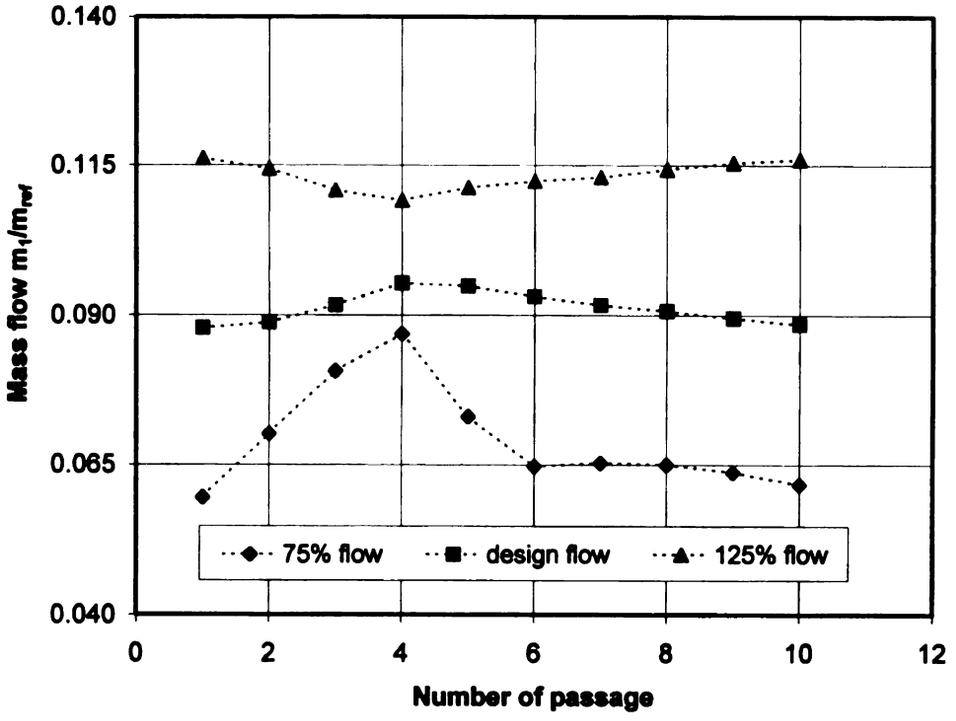

(a) Mass flow in each passage

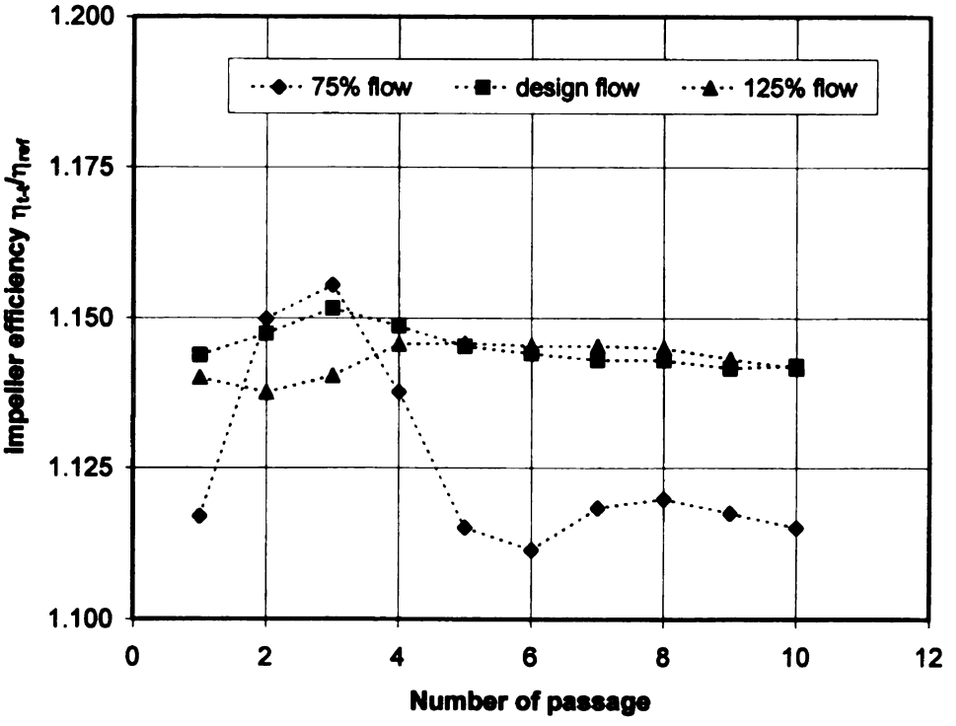

(b) Total-to-total efficiency

Figure 7.4 Input for the theoretical model

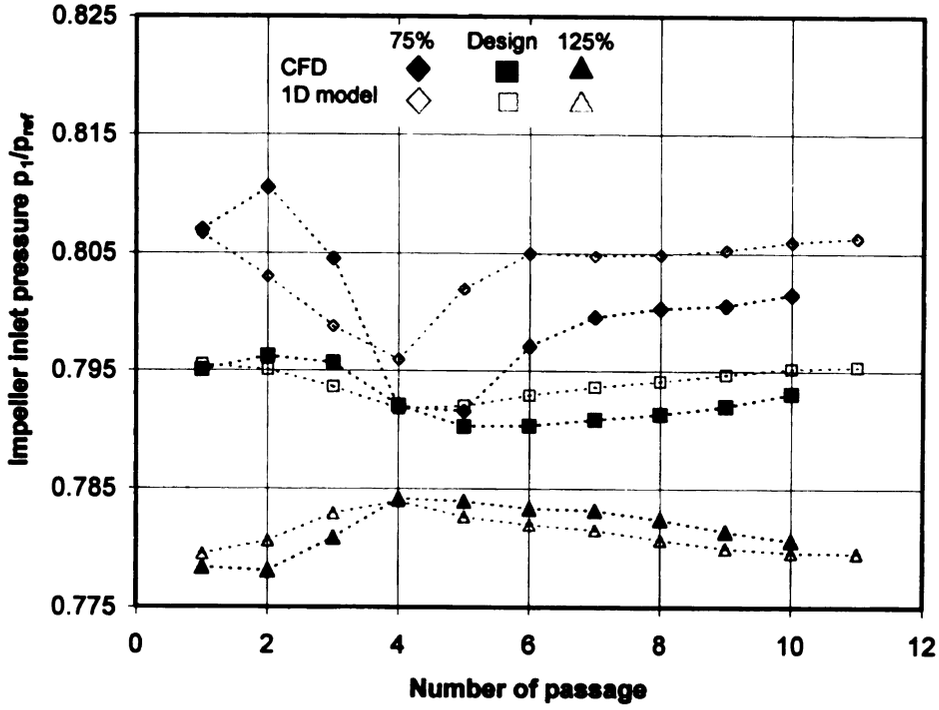

Figure 7.5 Inlet static pressure

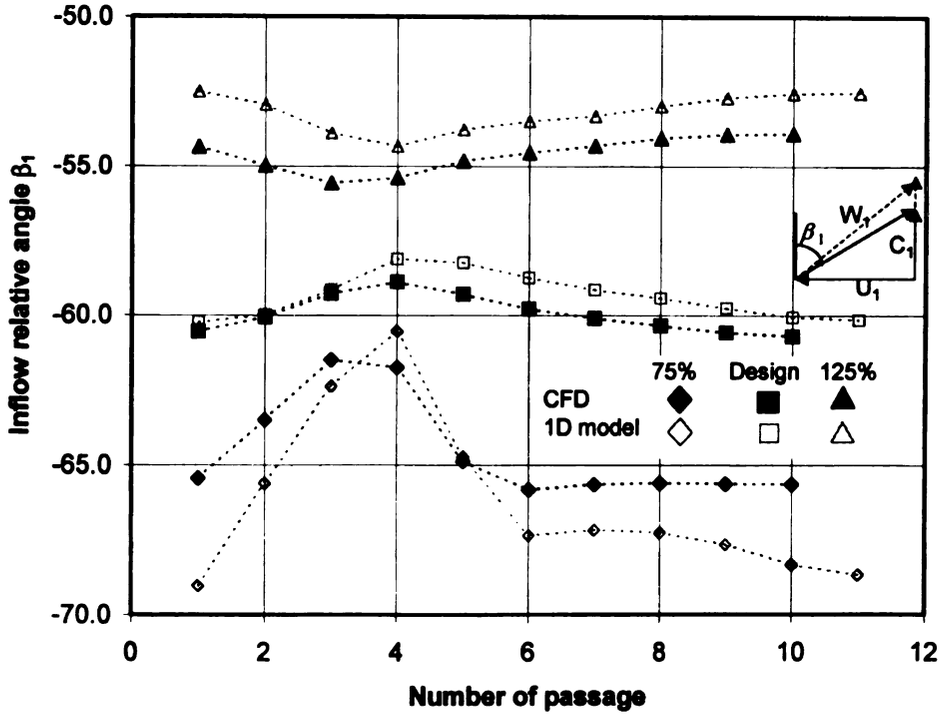

Figure 7.6 Inlet relative flow angle

curves are located above the ones from CFD. This is due to the fact that at these operation points the inducer of the impeller works as a diffuser (Japikse 1996), resulting in thicker boundary layers on the blade walls. The aerodynamic blockage, which is not considered by the model, is therefore higher.

The model calculates the inlet relative flow angle at the radius of root mean square

$$r_1 = \sqrt{r_{1h}^2 + r_{1s}^2} \tag{7.51}$$

Figure 7.6 shows that at this radius the flow angle from the model agrees with the one from CFD.

7.3.2 Impeller Outlet

The three-dimensional flow field from the CFD simulations is mass-weighted averaged at the station immediately downstream of the impeller with its radius being 0.5% higher than the impeller. The model uses the Wiesner's correlation of slip factor, because this correlation gives the result closest to the CFD one. In Van den Braembussche' model (1999), the response of the impeller to the distorted downstream pressure is represented by the distorted total pressure. The outlet total temperature and tangential velocity are assumed to be uniform, based on experimental observations. To be consistent to the Frozen rotor model of the CFD analysis, this model represents the response by the variations of mass flow and efficiency in different segments. Therefore, no aerodynamic parameter remains uniform at the exit under distorted exit pressures.

The exit absolute flow angle is compared in figure 7.7. It can be seen that Wiesner correlation accurately predicted the flow angle at the design point, slightly over-predicted

it at lower mass flow, and under-predicted it at higher mass flow. But the maximum difference is less than 2 degrees. Therefore, it is not surprising to find that the isentropic head coefficient is in very good agreement with the CFD one as shown in figure 7.8. The static pressure (figure 7.9) is slightly over-predicted by the model for all the mass flows, because the model ignores the thickness of boundary layers in the impeller passage

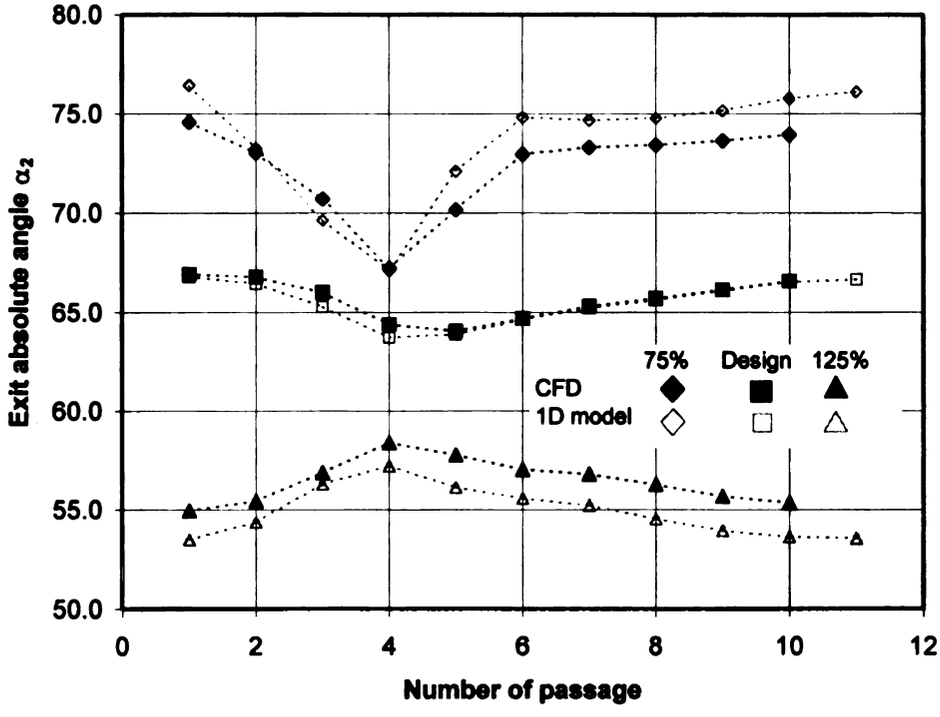

Figure 7.7 Exit absolute flow angle

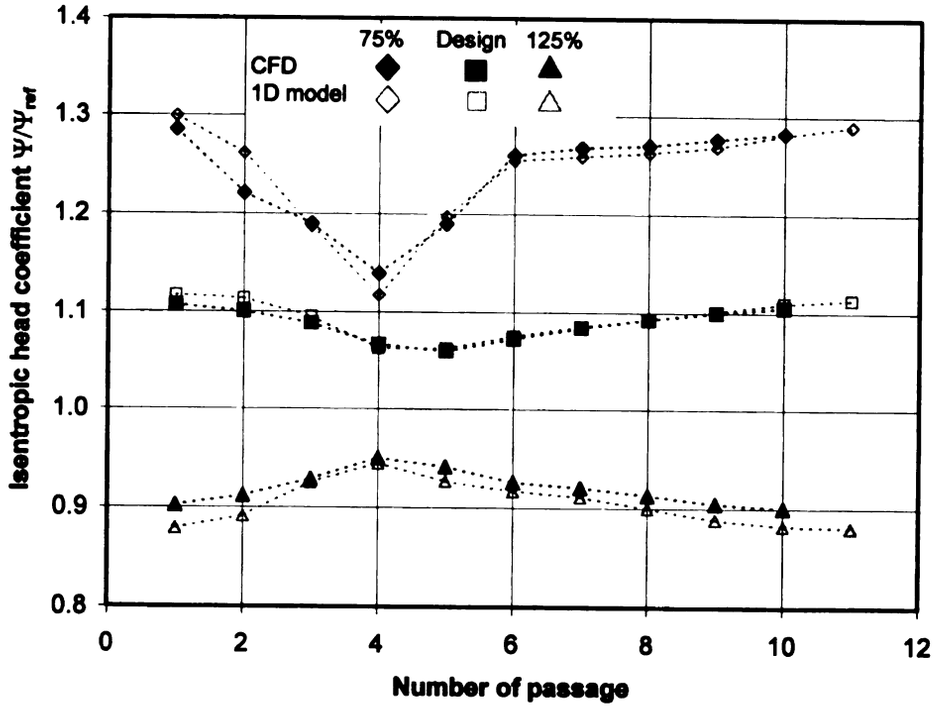

Figure 7.8 Isentropic head coefficient

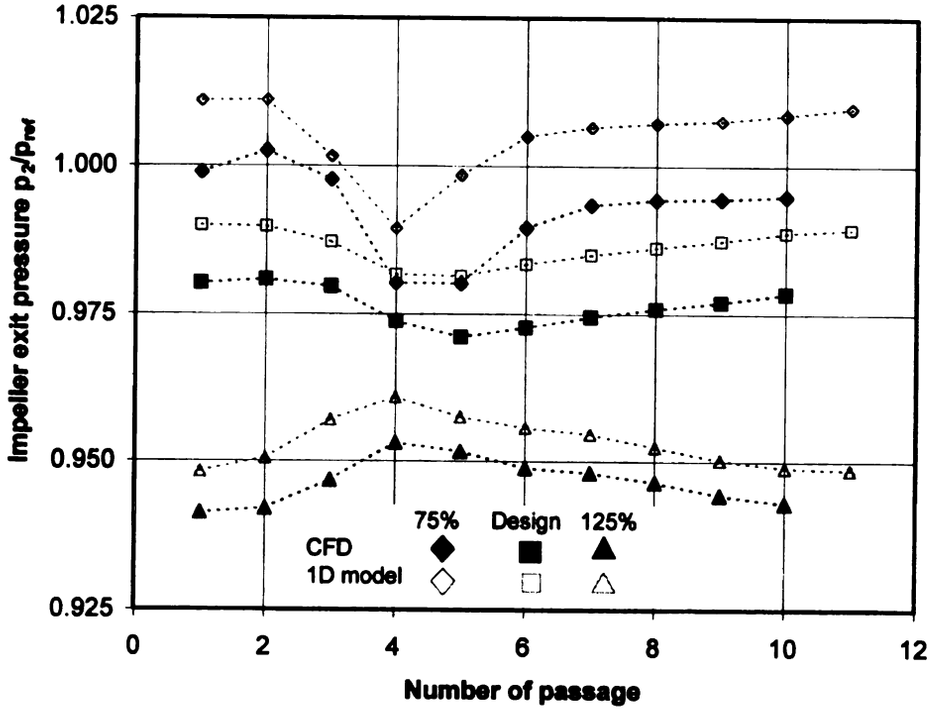

Figure 7.9 Impeller exit static pressure

7.3.3 Vaneless Diffuser Exit

The flow filed in the vaneless diffuser is obtained by integrating the equations of Stanitz (1952) for each stream tube. The interaction between neighboring stream tubes are neglected. The total and static pressures at the vaneless diffuser exit are shown in figure 7.10. The agreement between CFD and model is satisfactory. However, for all the mass flow the model consistently gives slightly higher pressures. This can be explained by figure 7.11, which compares the accumulative mass flow at the exit of the vaneless diffuser. Because each stream tube expends inside the vaneless diffuser at its own rate, the mass conservation is damaged, resulting in less mass flow. The static pressure is therefore over-estimated. The other problem with the model is that it falsely predicted a phase shift for the static pressure. It has been experimentally observed by Ayder et al. (1993) and Hagelstein et al. (1999) and numerically captured by Gu et al. (2001) that there is a significant phase shafting for the total pressure as the flow moves in the vaneless diffuser, but the static pressure distortion does not exhibit any phase change; the violent static pressure variation sticks to the tongue section.

The swirl factor λ at the vaneless diffuser exit is compared in figure 7.12. For both design and higher mass flow, the prediction of the model is in reasonable good agreement with the CFD result. But for the lower mass flow, the prediction of model oscillates much stronger than the CFD result. For the lower mass, the inlet of the vaneless diffuser is most distorted, resulting in stronger streamline interactions, which the model failed to predict. For volute design, the swirl factor at the vaneless diffuser exit/volute inlet plays a significant role because the continuity says for incompressible flows

$$A_5 C_{m5} = A_7 C_{t7} \tag{7.52}$$

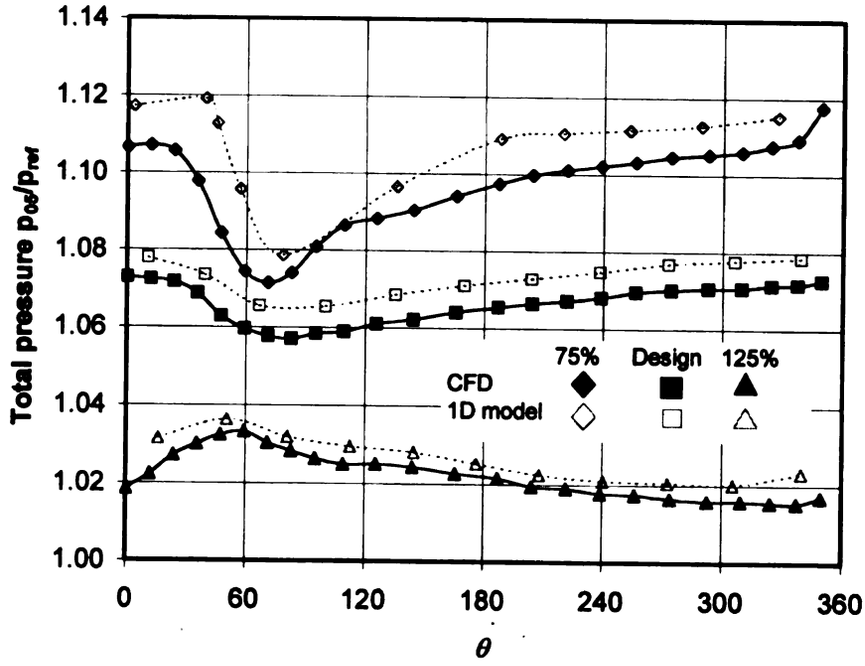

(a) Total pressure

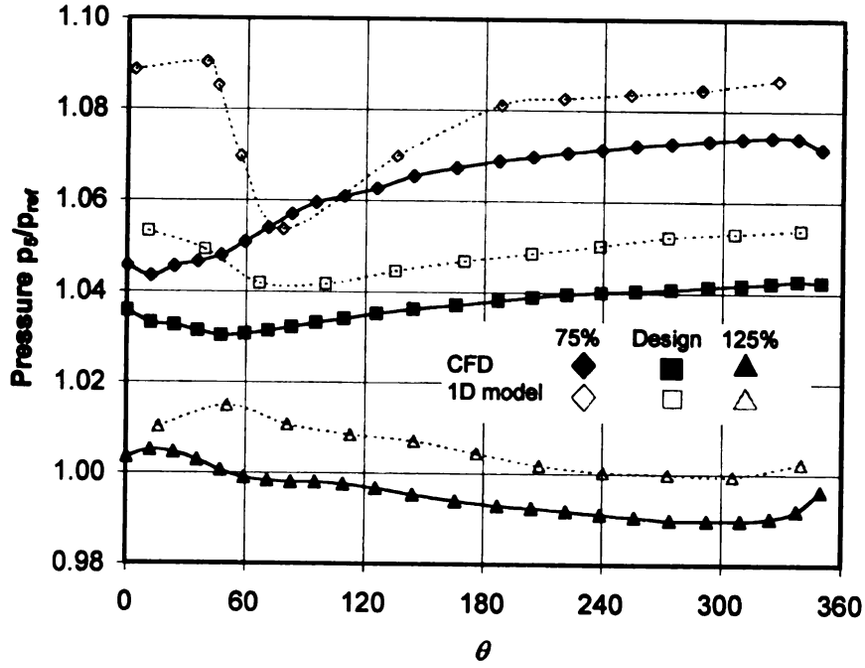

(b) Static pressure

Figure 7.10 Total and static pressure at vaneless diffuser exit

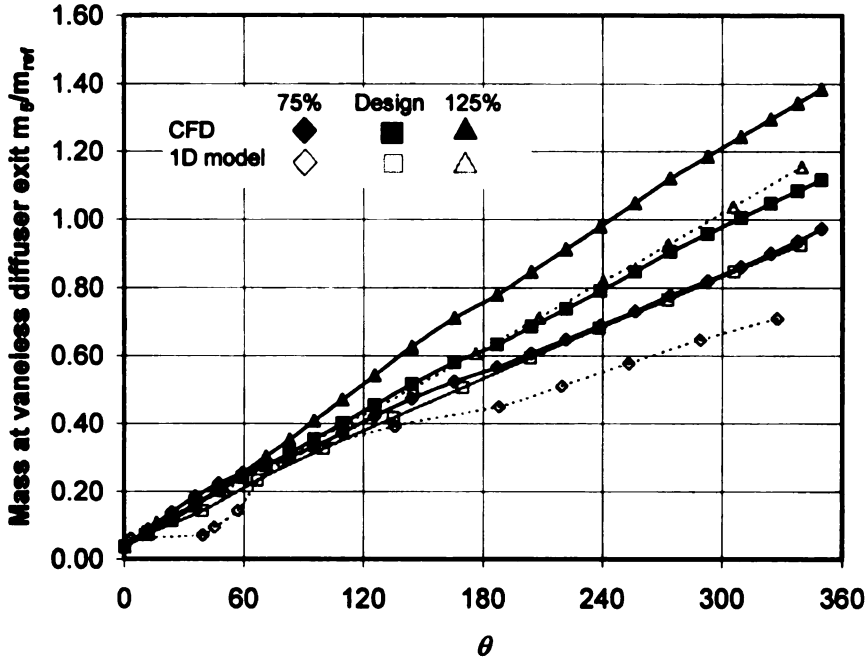

Figure 7.11 Accumulative mass at vaneless diffuser exit

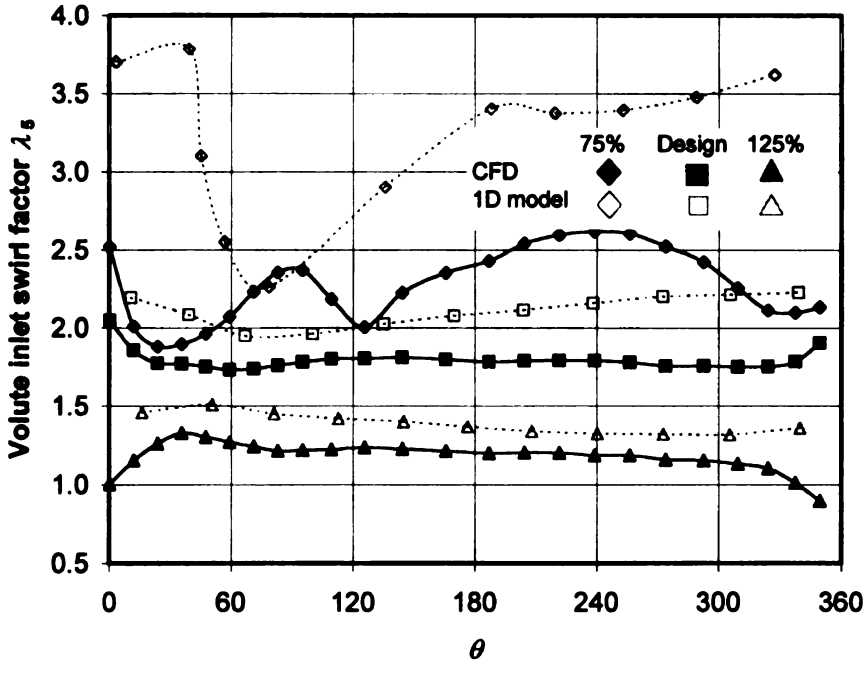

Figure 7.12 Swirl factor at vaneless diffuser exit

At the design point of a volute with constant centroid radius equal to the radius at the vaneless diffuser exit, it is reasonable to assume $C_{t7} = C_{t5}$. Therefore

$$\lambda_5 = \frac{C_{t5}}{C_{m5}} = \frac{A_5}{A_7} \tag{7.53}$$

It indicates that the critical area of the volute is determined by the inflow swirl factor. With the larger difference of swirl factor for the lower mass flow, it is suspicious whether the model can go on to predict the volute flow.

7.3.4 Volute Flow

The volute is a unique component in compressors because if the flow is decelerated or accelerated inside the volute, the pressure circumferential distortion will be created. The flow in the vaneless diffuser and impeller therefore will be distorted. In other words, the circumferential pressure distortion is an indication of whether the machine is running at its design point. The sectional area and centroid radius of the volute used for this study are plotted in figure 7.13. The sectional area contains the 90 degree bend starting from the exit of the vaneless diffuser (r_5). The area is therefore not zero at the beginning of the volute. The centroid radius is calculated by

$$r_k = \frac{\int r dA}{\int dA} \tag{7.54}$$

It increases up to 95 degrees and then decreases consistently because this volute has a constant outer diameter. The non-dimensional radius is always larger than 1, indicating that this is an external volute.

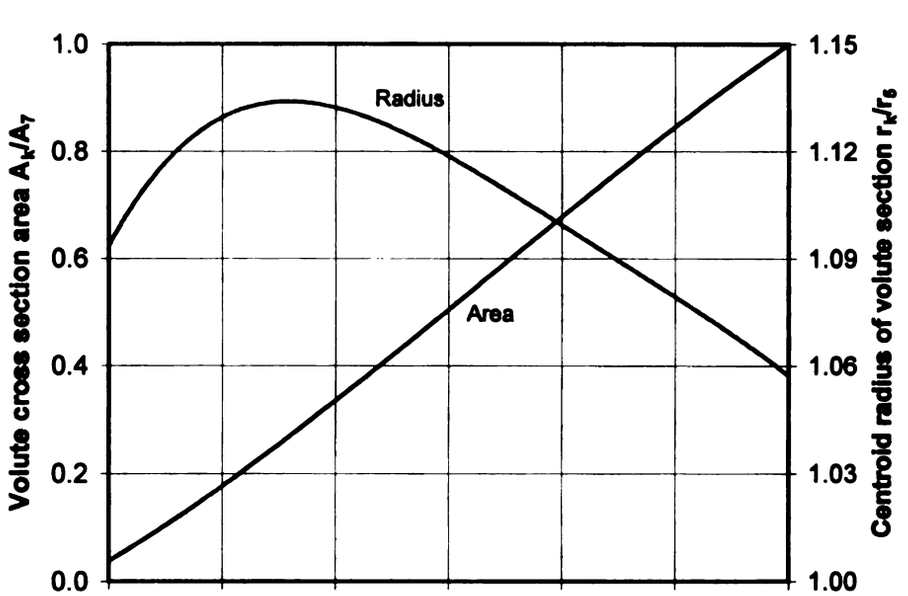

Figure 7.13 Volute sectional area and radius

Because the prediction of the vaneless diffuser exit flow is not accurate enough, it is feasible for the model to use the CFD result to begin the volute flow calculation. Both coefficients $\varepsilon_1, \varepsilon_2$ in equations 7.36 and 7.42 are arbitrarily chosen to be zero. The through-flow velocity is compared in figure 7.14. It can be seen that the model predicts the tendency correctly. In the tongue region, the model predicted less over-shooting for the design and lower mass flows. The model over-estimated the velocity for the off-design conditions because the CFD curves are mass-averaged. It is known that the mass averaged value is smaller than the one from the one dimensional calculation. The centroid static pressure is calculated by both momentum approach and energy approach as shown in figure 7.15. The momentum approach failed to predict the pressure variation, even in tendency. It seems that this approach over-accounts for the role of centroid radius. The angular momentum equation (7.34) suggests that pressure p_o increases as radius r_o

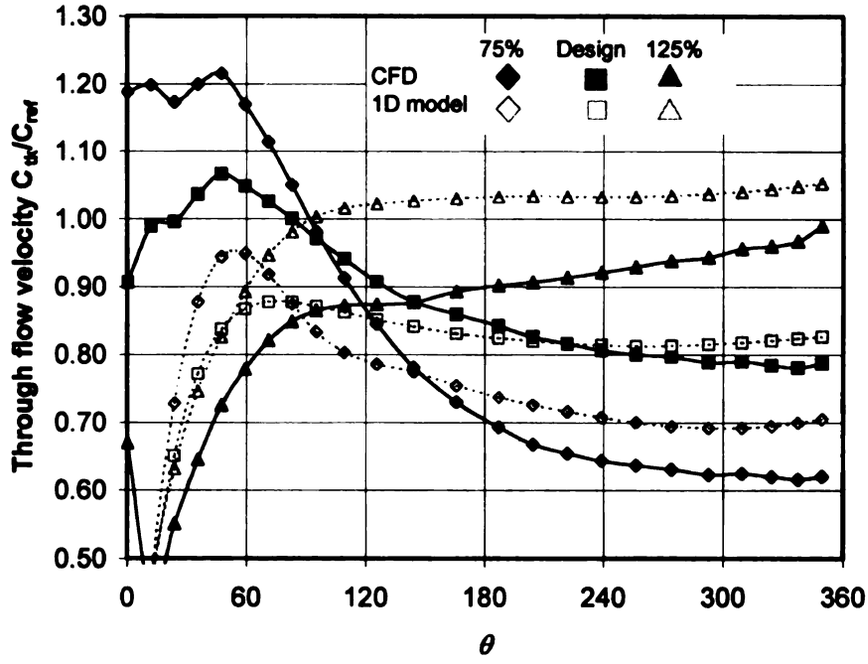

Figure 7.14 Volute through-flow velocity

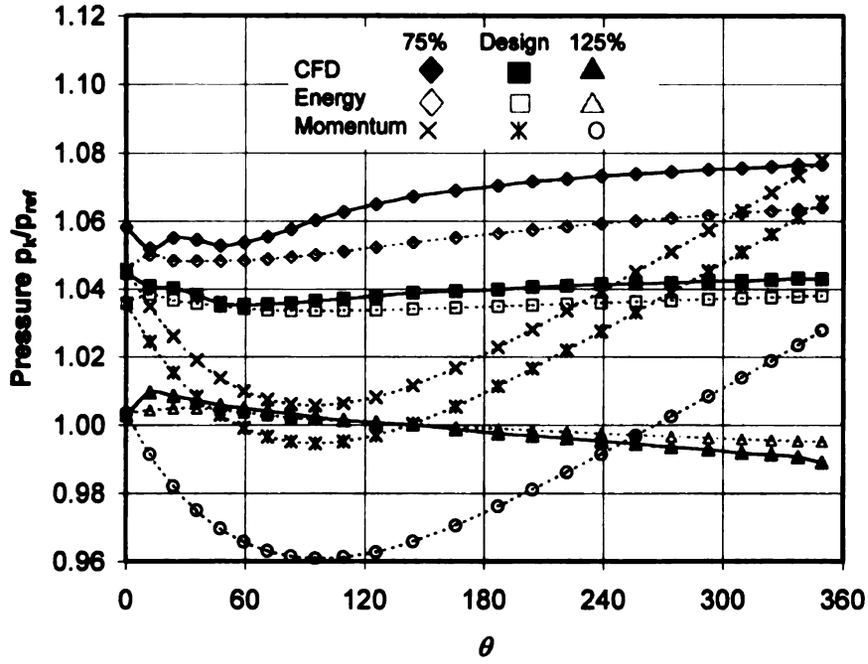

Figure 7.15 Volute centroid pressure

decreases and vice versa. This is exactly what the curves say. On the other side, the energy approach successfully predicted the pressure variation; the agreement with CFD results is exceptionally good for the design and higher mass flows. For the lower mass flow, the tendency is correctly predicted.

7.3.5 Discussion on Centroid Radius

After the centroid pressure in the volute passage is calculated, it is supposed to compare it with the one at the vaneless diffuser exit and updating the inlet mass flow using equations (7.49) and (7.50). Because of the poor accuracy in vaneless diffuser prediction, this mass iteration process is not completed currently. However, the role of equation (7.49) in the volute design can still be discussed. It indicates that

- For a volute with constant centroid radius, the pressure difference is constant. If the radius is equal to the one at the vaneless diffuser exit, the pressure difference is 0. If the radius is larger than the one at the vaneless diffuser exit, the centroid pressure is larger than the pressure at the vaneless diffuser exit and vice versa.
- If the centroid radius of the volute is a function of the azimuth angle, so is the pressure difference. If the volute is designed to target at a constant centroid pressure, the pressure at the vaneless diffuser will be distorted and the impeller will work under a distorted exit pressure condition. The performance of the machine will be deteriorated. This is one aspect of how the volute affects the machine performance.

A volute optimization approach can be derived from this discussion. Define the problem as: a uniform inlet at vaneless diffuser exit is give, and the volute area as a function of azimuth angle is given. The centroid radius is to be optimized. The optimization process is:

(1) The centroid velocity is calculated from equation (7.33).

(2) The centroid pressure ($p_k = p_o$) is calculated from equation (7.41).

(3) The centroid is optimized by equation (7.49)

7.4 CONCLUSION

A one dimensional model was developed for a centrifugal compressor to simulate the response of the impeller to the pressure distortion due to the volute at off-design conditions. The centrifugal compressor is divided into several segments; each segment has its own mass flow rate. This model consists of the impeller inlet and outlet calculations, vaneless diffuser calculation, and the volute flow calculation. The comparison with CFD results shows that:

- This model successfully estimated the parameter distribution for each component with different accuracy.
- Stanitz equations for the vaneless diffuser flow, when applied to isolated streamlines, produced a mass reduction and an incorrect phase shift of static pressure distortion.
- The momentum approach predicted the pressure variation in the volute passage with significant errors because it over-accounts the role of the centroid radius. The energy approach successfully predicted the pressure variation in the volute passage.
- This model can be used to optimize the match of the volute with the impeller because it can predict the pressure distortion in the volute if the volute size is incorrect or the variations of the area and centroid radius are not appropriate.

Future work is needed to improve the accuracy of the model. A two-dimensional Navier-Stokes equation solver can be a promising approach to improve the vaneless diffuser calculation.

Chapter 8

CONCLUSIONS

This dissertation has carried out a numerical study on the volute design and flow analysis for centrifugal compressors with one chapter devoted to turbine volutes. It begins from one-dimensional design approaches, goes over the complicated three-dimensional flow field and volute/impeller interaction, and ends up with a one-dimensional analysis model.

A volute design system for both turbines and compressors was developed first, which converts design parameters into volute geometries. The flexibility of the geometry representation is implemented by Bezier polynomials. An interface with commercial CFD solver is built to generate grids and boundary conditions for the simulation. This system greatly reduces the cost of volute design by reducing the interaction between autoCAD systems and CFD solvers.

One-dimensional design concepts apply to both turbine and compressor volutes, but the turbine volute design is of more interest because the flow is compressible. Therefore, One-dimensional conceptual design of a turbine volute is assessed by the means of theoretical analysis and numerical simulation. It is proved that the incompressible approach gives a volute with larger A/r, resulting in a smaller average exit flow angle for compressible flows. Chapple's compressible design approach is extended to take into account the total pressure losses. A numerical simulation is conducted on a previously designed volute to investigate the deviation of the flow from the free vortex design. It is shown that when the ratio of area to radius of the volute is smaller than the

free vortex design, the Mach numbers of the centroid flow are higher and the centroid flow angle is distorted at both ends. The wake flow of the tongue and the recirculation flow under the tongue are among the factors contributed to the angle distortion. It is also observed that the wake flow of the tongue causes the deficit of the tangential velocity component near the discharge surface downstream of the tongue; the thicker boundary layer causes the deficit of the tangential velocity component near the outer wall upstream of the tongue. The radial velocity component at first lies above the free vortex design, then consistantly goes below the free vortex design. A possible reason is that the ratio of area to radius of the volute is slightly smaller than the free vortex design.

The compressor volute flow structure was investigated by numerical simulations using stage model from commercial CFD package CFX-TASCflow. This model removes the circumferential distortion at the impeller exit, so the effect of axial distortion at impeller exit was studied on the volute flow structure at off-design conditions. The following conclusions have been reached:

- At all mass flow rates, the losses occurred in the volute accounts for a large portion of the total losses in the stationary components. As the mass flow rate increases up to the design point, the loss in the vaneless diffuser is reduced; after that the loss stays constant. On the contrary, the loss in the volute decreases before the mass flow rate reaches the design point; then it consistently increases faster as the mass flow increases.
- The upstream effect of volute is indicated by the higher static pressure rise and higher total pressure loss on the shroud side of the vaneless diffuser.

- In the vaneless diffuser, the inlet distortion is always exaggerated at all mass flows.

- In the volute, the flow basically follows Van den Braembussche's model. A new model is proposed to take into account the axial distortion at the vaneless diffuser inlet and the circumferential pressure distortion at off-design conditions. At lower mass flow, the lower total pressure fluids from the hub side upstream of the tongue cannot exit the volute. Instead, they move into the force vortex center, resulting in recirculation. At higher mass flow, a twin vortex structure is found at downstream of the tongue. The recirculation and the twin vortex structure are attributed to the increase of total pressure losses at off-design conditions.

The steady-state volute/impeller interaction is numerically studied using the frozen rotor model provided by the commercially available CFD software, CFX-TASCflow. The pressure distortion due to the volute at off-design conditions is traced from the tongue to the impeller inlet. The following conclusions have been reached:

- The frozen rotor model is applicable to the compressor flow where the acoustic Strouhal number is close to zero. It cannot predict the response of the impeller to pressure perturbation of higher frequency.
- In the volute passage the pressure gently increases circumferentially at lower mass flow, and gently decreases at high mass flow. The radical pressure variation around the tongue is caused by the incidence to the tongue at off-design conditions.
- The frozen rotor model failed to predict the decay of the pressure perturbation when it propagates upstream from the vaneless diffuser exit to the inlet. It

indicates that the decay of the perturbation is a response of the impeller to the perturbation of higher frequency.

- The performance drop of the compressor at off-design conditions is mainly due to the performance drop of the impeller. The circumferentially increased pressure at the impeller exit is detrimental to the impeller flow. Therefore, at higher mass flow, the impeller efficiency deterioration comes from these passages upstream of the tongue in the range of about 150°. At lower mass flow, all the passages but the two around tongue are responsible for the lower impeller efficiency.

The volute/impeller frozen model study suggests that the undersized volute is beneficial to the impeller due to the fact that the impeller is experiencing the exit pressure of negative slopes.

At last a one dimensional model was developed for the centrifugal compressor to simulate the response of the impeller to the pressure distortion due to the volute at off-design conditions. The centrifugal compressor is divided into several segments; each segment has its own mass flow rate. This model consists of the impeller inlet and outlet calculations, vaneless diffuser calculation, and the volute flow calculation. The comparison with CFD results shows that:

- This model successfully estimated the parameter distribution for each component with different accuracy.
- Stanitz equations for the vaneless diffuser flow when applied to isolated streamlines produced a mass reduction and a wrong phase shift of static pressure distortion.

- The momentum approach predicted the pressure variation in the volute passage with significant errors, because it over-accounts the role of the centroid radius. The energy approach successfully predicted the pressure variation in the volute passage.
- This model can be used to optimize the match of the volute with the impeller, because it can predict the pressure distortion in the volute if the volute size is incorrect or the variations of the area and centroid radius are not appropriate.

Future work is needed to improve the accuracy of the model. A two-dimensional Navier-Stokes equation solver can be a promising approach to improve the vaneless diffuser calculation.

BIBLIOGRAPHY

Bibliography

Ayder, E., 1993, "Experimental and Numerical Analysis of the Flow in Centrifugal Compressor and Pump Volutes," Dissertation of Von Karman Institute.

Ayder, E., Van den Braembussche, R. and Brasz, J. J. 1993, "Experimental and Theoretical Analysis of the Flow in a Centrifugal Compressor Volute," ASME Journal of Turbomachinery, Vol. 115, pp. 582-589.

Ayder, E. and Van den Braembussche, R., 1994, "Numerical Analysis of the Three-dimensional Swirling Flow in Centrifugal Compressor Volutes," ASME Journal of Turbomachinery, Vol. 116, pp. 462-468.

Benisek, E.F., 1987, "Laser velocimeter Measurements at the Rotor Inlet of A Turbocharger Radial Inflow Turbine," ASME FED-Vol 55

Brown, W. B. and Bradshaw, G. R., 1947, "Design and Performance of family of Diffusing Scrolls with Mixed-Flow Impeller and Vaneless Diffuser," NACA 936.

Chapple, P. M., Flynn, P. F. and Mulloy, J. M., 1980, "Aerodynamic Design of Fixed and Variable Geometry Nozzleless Turbine Casing," ASME, Journal of Engineering for Power, Vol. 102, pp141-147

Chen, H., 1996, "Design Methods of Volute Casings for Turbocharger Turbine Applications," ImechE, Vol. 210, pp.149-156.

Di Liberti, J., 1998, "Design and Development of Low-Flow Coefficient Centrifugal Compressors for Industrial Application," Dissertation of Department of mechanical Engineering at Michigan State University.

Escudier, M., 1979, "Estimation of Pressure Loss in Ring Type Exit Chambers," ASME Journal of Fluids Engineering, Vol. 101, pp. 511-516.

Fatsis, A, Pierret, S. and Van den Braembussche R. A., 1997, "Three-Dimensional Unsteady Flow and Forces in Centrifugal Impellers with Circumferential Distortion of the Outlet Static Pressure," ASME Journal of Turbomachinery, Vol. 119, pp. 94-102.

Flathers, M. B. and Bache, G. E., 1999, "Aerodynamically Induced radial Forces in a Centrifugal Gas Compressor: Part 2—Computational Investigation," ASME Journal of Engineering for Gas Turbines and Power, Vol. 121, pp. 725-734.

Flathers, M. B., Bache, G. E., and Rainsberger, R., 1994, "An Experimental and Computational Investigation of Flow In a Radial Inlet of An Industrial Pipeline Centrifugal Compressor," ASME 94-GT-134.

Gu, F., and Engeda, A., 2001, "A Numerical Investigation on the Volute/Impeller Steady-State Interaction due to the Circumferential Distortion," Submitted to ASME IGTI'2001.

Hagelstein, D., Hasemann, H., Keiper, R. and Rautenberg, M., 2000, "Comparison of Flow Field and Performance of Internal and External Volutes for Centrifugal Compressors," JSME 2000-GT-.

Hagelstein, D., Hillewaert, K, Van den Braembussche, R. A., Engeda, A., Keiper, R. and Rautenberg M., 1999, "Experimental and Numerical Investigation of the Flow in a Centrifugal Compressor Volute," ASME 99-GT-79.

Hawthorne, W. R., ed., 1964, "Aerodynamics of Turbines and Compressors," Vol. 10, Princeton University Press, N. J., pp.533-538.

Hillewaert, K. and Van den Braembussche, R. A., 1999, "Numerical Simulation of Impeller-Volute Interaction in Centrifugal Compressors," ASME Journal of Turbomachinery, Vol. 121, pp. 603-608.

Hussain, M., Ilyas, M., and Bhinder, F. S., 1982, "A Contribution to Designing a Nozzle-less Volute casing for the inward flow radial gas turbine," ImechE, C35/82

Inoue, M., Hara, K. and Furukawa, M., 1987, "Experimental Study on the Three-Dimensional Flow Field in a Turbine Scroll," 87-TOKYO-IGTC-9

Japikse, David, 1996, "Centrifugal Compressor Design and Performance," Concepts ETI Inc.

Khalil, I. M., Tabakoff, W. and Hamed, A., 1976, "Losses in Radial Inflow Turbines," ASME Journal of Fluids Engineering, Vol. 98, pp. 364-373.

Kim Won Joong, 1998, "Design and Development of Low Solidity Vaned Diffusers for Centrifugal Compressors," Ph.D. dissertation of Michigan State University.

Krain H., 1988, "Swirling Impeller Flow," ASME Journal of Turbomachinery, Vol. 110, pp.122-128.

Lopez Pena, F., 1987, "Study of Volutes for Centrifugal Compressors with Constant Cross Sectional Area and Simple Geometry," VKI PR 1897-05.

Lorett, J. A. and Gopalakrishnan, S., 1986, "Interaction between Impeller and Volute of Pumps at off Design Conditions," ASME Journal of Fluids Engineering, Vol. 108, pp. 12-18.

MacGregor, S. A., Whitfield, A. and Mohd Noor, A. B., 1994, "Design and Performance of Vaneless Volutes for Radial Inflow Turbines, Part 3: Experimental

Investigation of the Internal Flow Structure," IMechE, Proc. Instn Mech Engrs, Part A: Journal of Power and Energy, Vol. 208, pp.295-302.

Miller E. C., L'Ecuyer, M. R., and Benisek, E. F., 1987, "Flowfield Surveys at the Rotor Inlet of A Radial Inflow Turbine," ASME 87-ICE-52.

Mishina, H. and Gyobu, I., 1978, "Performance Investigations of Large Capacity Centrifugal Compressors," ASME paper 78-FT-3.

Owarish, H. O., Ilyas, M. and Bhinder, F. S., 1992, "A Two-Dimensional Flow Analysis Model for Designing a Nozzle-less Volute Casing for Radial Flow Gas Turbines," ASME Journal of Turbomachinery, Vol. 114, pp.402-410.

Schlichting, H., 1979, "Boundary-layer Theory," McGraw-Hill Book Company, pp. 626.

Stiefel, W. (1972), "Experiences in the Development of Radial Compressors," in Advanced Radial Compressors, VKI LS 50.

Sideris, M. and Van den Braembussche, R., 1986, "Experimental Study of the Flow in a Vaneless diffuser with Circumferential Pressure distortion," VKI TN 157.

Sorokes, J. M., Borokes, C. and Koch, J. M., 1998, "Investigation of the Circumferential Static Pressure Non-Uniformity Caused by a Centrifugal Compressor discharge Volute," ASME Paper No. 98-GT-326.

Tabakoff, W., Sheoran, Y., and Kroll, K., 1980, "Flow Measurements in a Turbine Scroll," ASME Journal of Fluids Engineering, Vol. 102, pp.290-296.

Tabakoff, W., Vittal, B. and Wood, B., 1984, "Three-dimensional Flow Measurements in a Turbine Scroll," ASME Journal of Engineering for Gas Turbines and Power," Vol. 106, pp.516-522.

TASCflow Version 2.9 Users Manual, 1999, Advanced Engineering Computing.

Van den Braembussche, R. A. and Hande, B. M., 1990, "Experimental and Theoretical Study of the Swirling Flow in Centrifugal Compressor Volutes," ASME Journal of Turbomachinery, Vol. 112, pp. 38-43.

Van den Braembussche R. A., Ayder, E., Hagelstein, D., Rautenberg, M. and Keiper, R., 1999, "Improved Model for the Design and Analysis of Centrifugal Compressor Volutes," ASME Journal of Turbomachinery, Vol. 121, pp. 619-625.

Van den Braembussche R. A., 2000, Private Communication.

Watson, N. and Janota, M. S., 1993, "Turbocharging the Internal Combustion Engine," MacMillan Press.

Weber, C. R. and Koronowski, M. E., 1986, "Meanline Performance Prediction of Volutes in Centrifugal Compressors," ASME Paper 86-GT-216.

Whitfield, A. and Mohd Noor, A. B., 1990, "Investigation of the Flow Characteristics of Radial Inflow Turbocharger Volutes," IMechE. C405/023.

Whitfield, A. and Mohd Noor, A. B., 1994, "Design and Performance of Vaneless Volutes for Radial Inflow Turbines Part 1: Non-dimensional Conceptual Design Considerations," ImechE, Vol. 208, pp.199-211

Whitfield, A., MacGrego, S. A., and Mohd Noor, A. B., 1994, "Design and Performance of Vaneless Volutes for Radial Inflow Turbines Part 2: Experimental Investigation of the mean line Performance-Assessment of Empirical design Parameters," ImechE, Vol. 208, pp.213-224

Wilson, D. G., 1993, "The Design of High-Efficiency Turbomachinery and Gas Turbines," The MIT Press, Sixth printing.

Wislicenus, G. F., 1965, "Fluid Mechanics of Turbomachinery," 2nd Ed., Vol.1, Dover Publication, New York, pp.561-564.

APPENDIX

Appendix

Publications during the Study

Maguire, J. M., Bruce, G. J., Engeda, A., and Gu, F., 2000, "Compressor and Turbine Volute Design System," ASME Paper 2000-GT-0537

Gu, F., Engeda, A., and Edward Benisek ,2000 "A Comparative Study of Incompressible and Compressible Design Approaches of Radial Inflow Turbine Volutes," submitted to Proceedings of the Institution of Mechanical Engineering, Part A Journal of Power and Energy, UK.

Gu, F., Engeda, A., Mike Cave, and Jean-luc Di Liberti, 2000 "A Numerical Investigation on the Volute/Diffuser Interaction due to the Axial Distortion at the Impeller Exit," Presented at The 2000 ASME International Mechanical Engineering Congress and Exposition, Nov. 5-10, 2000. Orlando, Florida. PID-Vol.5, pp.71-80. Accepted by ASME Journal of Fluids Engineering.

Gu, F., and Engeda, A., 2001, "A Numerical Investigation on the Volute/Impeller Steady-State Interaction due to the Circumferential Distortion," Submitted to ASME IGTI'2001.

Gu, F., and Engeda, A., 2001, "One Dimensional Modeling of Volute/Impeller Interaction at off-design", Submitted to ASME IGTI'2001.